Fábio Emanuel de Sousa Ferreira

PROCESS-PROPERTIES RELATIONS IN DEEP OSCILLATION MAGNETRON SPUTTERING

Doctoral Thesis in Mechanical Engineering, Surface Engineering, supervised by Doctor João Carlos Barbas de Oliveira and submitted to the Mechanical Engineering Department of the Faculty of Sciences and Technology of the University of Coimbra.

September 2017

UNIVERSIDADE DE COIMBRA

Fábio Emanuel de Sousa Ferreira

PROCESS-PROPERTIES RELATIONS IN DEEP OSCILLATION MAGNETRON SPUTTERING

Doctoral Thesis in Mechanical Engineering, Surface Engineering, supervised by Doctor João Carlos Barbas de Oliveira and submitted to the Mechanical Engineering Department of the Faculty of Sciences and Technology of the University of Coimbra.

September 2017

UNIVERSIDADE DE COIMBRA

ACKNOWLEDGMENTS

I would like to thank all the people who would somehow contribute to making this work possible.

To all my colleagues in CEMMPRE, especially to Ricardo Serra, Manuel Evaristo, Filipe Fernandes, Nuno Figueiredo, Maria João Madeira, without forgetting also those who have already left Noora Manninen, Ana Escudeiro, André Cavaleiro, Melkamu Awoke and Silvia Godinho, who along these years have made this work an immense joy. Without forgetting during this moments also Professor Sandra Carvalho and Carla Lopes.

Thank IPN (Instituto Pedro Nunes) by making available laboratorial equipment for the characterization of the samples produced for this work. Especially to Carlos Patacas, who helped me in SEM characterization.

To FLAD Foundation who gave me the amazing opportunity to make an internship at Lawrence Berkeley Lab in USA.

To Berkeley Lab by a very kind reception in the USA, and in special to my American boss André Anders who was amazing for me.

To SVC foundation by the financial support that gave me the opportunity to attend one of the best conferences in my field.

To all my close friends, especially to Antonio Tomás, Bruno Figueiredo, Ivo Ferreira, Anselmo Santos, Luis Marques, Claudio Sousa, Pedro Correia and Vera Barbosa they were present on this journey, but above all, they were present in the bad and good moments of almost all of my lifetime.

To my entire family, especially to my Mother and to Daniela, they are my strength to live.

Last but not least, I would like to thank to two persons that I admire a lot.

To Professor Albano Cavaleiro, thank you for giving me this fantastic opportunity to work with this fantastic group, for all the knowledge given and inspiration to try to be always better in each passing day. A Professor, a co-worker, a friend. Thanks for all the travel and moments we share together on and off work.

To Dr. João Carlos Oliveira, thank you for having believed me since the beginning of this work, without a doubt the key of this thesis. My supervisor but most of all a friend,

there are no words to describe what I learned from you. Thank you so much for all the unconditional support, good advice, professionalism and all the opportunities given to attend excellent conferences and work in other laboratories. This thesis is entirely dedicated to this great Man.

ABSTRACT

In the last decade, new magnetron sputtering deposition techniques have been developed to produce highly ionized fluxes of sputtered material and, consequently, allow greater control over the energy and direction of the sputtered species. One of such techniques is Deep Oscillations Magnetron Sputtering (DOMS). The main objectives of the present work are to develop an accurate understanding of the new deposition mechanisms that the DOMS technology brings about and to evaluate the potential of this technology for industrial application. In the first part of this work four well-known deposition systems (Cr, Ta, CrN and TiSiN) were investigated. In each case, thin films were deposited by DOMS and Direct current Magnetron Sputtering (DCMS) in order to compare their microstructural, structural and mechanical properties. In the second part of this work, the knowledge previously acquired was applied to the development of a state of the art thin film with technologically relevant properties. The DOMS process was applied to the development of hydrogen-free hard carbon films for application in piston rings of internal combustion engines.

This work was carried out at the Surface Engineering Group (SEG) of the Centre for Mechanical Engineering, Materials and Processes (CEMMPRE) of the University of Coimbra. All the thin films were deposited using a Cyprium power supply form Zpulser™ LLC, operated in DOMS mode. In all the deposition systems, a detailed study of the effect of the peak power (Pp) on the films properties was carried out. The deposited thin films were characterized by Scanning Electron Microscopy, Atomic Force Microscopy, X-ray Diffraction and Nanoindentation. In selected cases, the flux of ions generated in the plasmas was studied by Energy-Resolved Mass Spectroscopy. Carbon films were additionally characterized by UV Raman spectroscopy and their tribological properties were evaluated by pin-on-disc tests. Simulations of the sputtering process were carried out using Monte Carlo programs (SRIM 2013 and SIMTRA 2008 software packages).

A new strategy aiming at taking advantage of the ionization of the sputtered species for thin film deposition by HiPIMS was identified in this work. It is shown that in DOMS the shadowing effect can be effectively controlled and, thus, dense and homogeneous films can be deposited at low peak power without the need of energetic bombardment. On the other hand, it is shown that the backscattered nitrogen neutrals formed upon CrN films deposition by DOMS are responsible for an energetic “background bombardment”

independent of the peak power and ultimately responsible for the high compressive stresses found in the films. It is also shown that the DOMS process allows a much greater independence of the films properties on the specific geometry and dimensions of the deposition system. This constitutes an important technological advantage as up-scaling of the films deposition processes from the deposition system used for development to those used for mass production is facilitated.

Keywords HiPIMS, DOMS, High power, ionization, thin films.

RESUMO

Na última década, foram desenvolvidas novas técnicas de deposição por pulverização catódica para produzir fluxos altamente ionizados de material pulverizado e, consequentemente, permitirem um maior controle sobre a energia e a direção das espécies pulverizadas. Uma dessas técnicas é o *Deep Oscillations Magnetron Sputtering* (DOMS). Os principais objetivos do presente trabalho consistem em desenvolver uma compreensão precisa dos novos mecanismos de deposição que a tecnologia DOMS facilita e em avaliar o potencial desta tecnologia para aplicação industrial. Na primeira parte deste trabalho, foram investigados quatro sistemas clássicos de deposição (Cr, Ta, CrN e TiSiN). Para cada caso, foram depositados filmes finos por DOMS e *Direct current Magnetron Sputtering* (DCMS) com o objetivo de comparar as suas propriedades microestruturais, estruturais e mecânicas. Na segunda parte deste trabalho, o conhecimento anteriormente adquirido foi utilizado para desenvolver um filme fino de última geração com propriedades tecnologicamente relevantes. O processo DOMS foi aplicado no desenvolvimento de filmes de carbono não hidrogenados com elevadas durezas para aplicação em anéis de pistão de motores de combustão interna.

Este trabalho foi realizado no Grupo de Engenharia de Superfícies (SEG) do Centro de Engenharia Mecânica, Materiais e Processos (CEMMPRE) da Universidade de Coimbra. Todos os filmes finos foram depositados usando uma fonte de potência Cyprium da Zpulser™ LLC, operada em modo DOMS. Em todos os sistemas de deposição, realizou-se um estudo detalhado do efeito da potência de pico (Pp) nas propriedades dos filmes. Os filmes finos depositados foram caracterizados por Microscopia Eletrónica de Varrimento, Microscopia de Força Atômica, Difração de Raios-X e Nanoindentação. Em casos selecionados, o fluxo de iões gerados no plasma foi estudado por Espectroscopia de Massa Resolvida em Energia. Os filmes de carbono foram adicionalmente caracterizados por espectroscopia UV Raman e as suas propriedades tribológicas foram avaliadas por testes de pino-disco. As simulações do processo de pulverização catódica foram realizadas utilizando programas de Monte Carlo (*software* SRIM 2013 e SIMTRA 2008).

Foi identificada neste trabalho uma nova estratégia visando aproveitar a ionização das espécies pulverizadas para deposição de filmes finos por HiPIMS. Mostra-se que, em DOMS, o efeito de sombra pode ser efetivamente controlado e, assim, possibilitar a

deposição de filmes densos e homogêneos a baixas potências de pico evitando assim a necessidade de um bombardeamento energético. Por outro lado, mostra-se que os neutros de azoto retro-difundidos formados na deposição de filmes de CrN por DOMS são responsáveis por um "bombardeamento de fundo" energético independentemente da potência de pico usada e, em última instância, responsável pelas altas tensões de compressão formadas nos filmes. Foi também comprovado que o processo DOMS permite uma maior independência das propriedades dos filmes sobre a geometria específica e as dimensões do sistema de deposição. Isso constitui uma importante vantagem tecnológica, pois é facilitada a passagem dos processos de deposição dos filmes do sistema de deposição utilizado para o desenvolvimento para aqueles utilizados para produção em massa.

Palavras-chave: HiPIMS, DOMS, alta potência, ionização, filmes finos.

INDEX

Acknowledgments i

Abstract iii

Resumo v

Index vii

List of figures ix

list of tables xii

Nomenclature and Acronyms xiii
- Nomenclature xiii
- Acronyms xv

1. Introduction 17

LIST OF PUBLISHED PAPERS 21

2. Backround information 23
   - 2.1. Introduction 23
   - 2.2. HiPIMS 23
     - 2.2.1. Modulated Pulse Power Magnetron sputtering 29
     - 2.2.2. Deep Oscillations Magnetron Sputtering 31
     - 2.2.3. Morphology of films produced by HiPIMS 32
   - 2.3. Hard DLC films 34
     - 2.3.1. Carbon-based thin films 34
     - 2.3.2. Stresses in DLC/ta-C thin films 37
     - 2.3.3. Deposition of ta-C thin films 38
     - 2.3.4. Carbon ionization in HiPIMS 39

3. Experimental 41
   - 3.1. Introduction 41
   - 3.2. Deposition chamber 41
   - 3.3. Metal systems (Cr and Ta) 42
     - 3.3.1. Effect of the peak power (Cr and Ta) 42
     - 3.3.2. Detailed study of Cr films (Pp and P) 45
   - 3.4. Nitride systems (CrN and TiSiN) 47
   - 3.5. Carbon system 49
     - 3.5.1. General experimental conditions 49
     - 3.5.2. Depositions as a function of substrate bias 49
     - 3.5.3. Depositions as a function of Ne content in the gas 51
     - 3.5.4. Experimental conditions for the tribological characterization 52

4. Comparison of DOMS across diferent depostion systems 53
   - 4.1. Introduction 53
   - 4.2. Metallic deposition systems (Cr and Ta) 55
     - 4.2.1. Plasma analysis 55
     - 4.2.2. Films properties 58
   - 4.3. Systematic study of the Cr system 64
     - 4.3.1. Surface properties 64
     - 4.3.2. Bulk properties 65
   - 4.4. Nitride systems (CrN and TiSiN) 73

5. Deposition mechnisms in DOMS 81
5.1. Introduction 81
5.2. Additional degree of freedom in DOMS 83
5.3. Backscattered nitrogen neutrals in DOMS 86
5.4. Overcoming asymmetrical deposition conditions in DOMS 90
5.5. Atomic Shadowing in DOMS 94
5.6. General overview of DOMS 100
5.6.1. Deposition rate in DOMS 100
5.6.2. Energetic ions bombardment in DOMS 100
5.6.3. Control of the shadowing mechanism in DOMS 101
5.6.4. Backscattered species in DOMS 102
5.6.5. Industrial advantages of DOMS 103

6. Hard hydrogen-free Diamond like carbon coatings deposited by DOMS 105
6.1. Introduction 105
6.2. Influence of substrate biasing 106
6.3. Influence of Ne content in discharge gas 107
6.4. Tribological properties of the DLC films 112
6.5. Potential of the DOMS for C deposition 116

7. Conclusions and future developments 117
7.1. Conclusions 117
7.2. Future developments 119

References 121

Annex A 128

Annex B 137

Annex C 146

Annex D 158

Annex E 169

Annex F 181

Annex G 195

LIST OF FIGURES

Figure 2.1. a) Charge circuit diagram of a HiPIMS source and b) a typical voltage-current characteristic from a HiPIMS discharge [9]. 25

Figure 2.2. I-V characteristics from a DCMS and HiPIMS discharge [2]. 26

Figure 2.3. The ionized flux fraction dependence on plasma density for different materials [11]. 26

Figure 2.4. Schematic of the target material pathway model. The letters G and M stand for gas and metal ions, respectively [13]. 27

Figure 2.5. Relative deposition rate in HiPIMS compared to deposition rate in DCMS [16]. 28

Figure 2.6. Typical MPP pulse [7]. 30

Figure 2.7. Different work regimes based on the peak power density at the target, combined with the duty cycle [8]. 31

Figure 2.8. Typical I-V waveforms of a DOMS pulse and, b) oscillation pulses within one long pulse. 32

Figure 2.9. Structure zone diagram applicable to energetic deposition proposed by Anders [41]. 33

Figure 2.10. Thermodynamic Phase diagram of Carbon. 34

Figure 2.11. The sp^3, sp^2, sp^1 hybridised states of carbon valence orbitals. [43]. 35

Figure 2.12. Phase diagram for amorphous Carbon [44]. 36

Figure 2.13. Fraction of SP3 carbon in the thin film against the energy of ions [48]. 37

Figure 2.14. SEM analyses of film deposited By CVA [50]. 38

Figure 2.15. Pulsed laser deposition technique. 39

Figure 2.16. The ion energy distributions for carbon ions obtained from different gas composition discharges at the pressures of 2 Pa and 4.66 Pa [52]. 40

Figure 3.1 Deposition Chamber used in this work. 42

Figure 3.2. HiPIMS-DOMS power supply. 42

Figure 3.3. Typical I-V waveforms of a DOMS pulse and associated oscillations during a), b) Cr depositions and c), d) Ta depositions. 44

Figure 3.4. Typical I-V waveforms of a DOMS pulse and associated oscillations during), b) Cr films deposition at low P_p and c), d) Cr films deposition at high P_p. 46

Figure 3.5. Typical I-V waveforms of a DOMS pulse and associated oscillations during of a), b) CrN films depostion and c), d) TiSiN films deposition. 48

Figure 3.6. a) The target voltage and current oscillation waveforms measured during the DLC coatings depositions. b) Oscillations within a pulse. 50

Figure 3.7. a) The target voltage and current oscillation waveforms measured during the DLC coatings depositions in Ar-Ne discharge. b) Oscillations within the pulses. 51

Figure 3.8. Pin on Disc scheme used for measurement of friction for DLC films with different substrate bias. 52

Figure 4.1. Ion energy distributions (IEDs) of Ar^{+}; Ar^{2+}; Ta^{+} and Ta^{2+} species measured from a) DCMS and b), c) DOMS plasma with different peak powers during sputtering a Ta target in pure Ar atmosphere. Ion energy distributions (IEDs) of Ar^{+}; Ar^{2+}; Cr^{+} and Cr^{2+} species measured from d) DCMS and e), f) DOMS plasma with different peak powers during sputtering a Cr target in pure Ar atmosphere. 57

Figure 4.2. Deposition rate of the Cr and Ta films deposited by DOMS as a function of peak power (Pp). 59

Figure 4.3. SEM cross-section and surface micrographs of the a) to d2) Cr and e) to h2) Ta thin films deposited by DCMS and DOMS. 60

Figure 4.4. Hardness of the Cr and Ta thin films deposited by DOMS. 61

Figure 4.5. Young's modulus of the Cr and Ta thin films deposited by DOMS. 62

Figure 4.6. Deposition rate of the Cr films deposited by DCMS without and with substrate bias and by DOMS at low Pp and high Pp at different deposition pressures. 66

Figure 4.7. Young Modulus of the Cr films deposited by DCMS without and with substrate bias and by DOMS at low Pp and high Pp at different deposition pressures. 67

Figure 4.8. XRD structure of the Cr films deposited by DCMS without and with substrate bias and by DOMS at low Pp and high Pp at different deposition pressures. 68

Figure 4.9. Normalized relative intensity of the (110) and (222) diffraction peaks of the Cr films deposited by DCMS without and with substrate bias and by DOMS at low Pp and high Pp at different deposition pressures. 69

Figure 4.10. Hardness of the Cr films deposited by DCMS without and with substrate bias and by DOMS at low Pp and high Pp at different deposition pressures. 70

Figure 4.11. Deposition rate of the CrN and TiSiN films deposited by DOMS as a function of peak power (Pp). 73

Figure 4.12. SEM cross-section and surface micrographs of the a) to c2) CrN and d) to f2) TiSiN thin films deposited by DCMS and DOMS at low and high peak power. 75

Figure 4.13. Grain size of the CrN and TiSiN films deposited by DOMS calculated from the GIXRD patterns using the (220) diffraction peak. 76

Figure 4.14. Lattice parameter of the CrN and TiSiN films deposited by DOMS calculated from the XRD patterns using the (220) diffraction peak. 77

Figure 4.15. Hardness of the CrN and TiSiN thin films deposited by DOMS. 78

Figure 4.16. Young's modulus of the CrN and TiSiN thin films deposited by DOMS. 79

Figure 5.1. Morphological zone model for nc-TiN/a-Si_3N_4 as function of the silicon content. The dark areas represent nanocrystals, the lighter zones stand for the amorphous phase [69]. 83

Figure 5.2. SEM surface and cross-section micrographs (inset) of the Cr films deposited by a); b) DCMS without and with bias and by c); d) DOMS at low and high Pp at 0.4 Pa. The arrow approximately indicates the substrate rotation direction (X direction). 90

Figure 5.3. Double logarithmic representation of the Height-Height correlation functions calculated for the Cr films deposited at a) 0.4 Pa and b) 0.8 Pa. The HHCFs are represented with linear scales in the inset. 92

Figure 5.4. IEDFs of the Cr+ ions obtained from the DOMS and DCMS plasmas normalized to unit area. 96

Figure 5.5. Simulation of the angle distributions of the thermalized and energetic a) neutrals and b) ions upon impinging on the growing film at 1.0 Pa. 97

Figure 5.6. Schematic of Cr species trajectories as a function of their energy and initial impingement angle at the substrate. In this figure is also plotted the equation that gives the angle of impingement of the ion at the substrate surface (β) as a function the angle of the ion trajectory when arriving at the sheath (α). 98

Figure 6.1. Cross section micrographs of DLC coatings with different Ne content in the discharge gas. 108

Figure 6.2. Deposition rate of DLC coatings with different Ne content in the discharge gas. 108

Figure 6.3. Raman spectra of the DLC films as a function of the Ne content in the plasma. 109

Figure 6.4. Eovolution of the I_G/I_D ratio as a function of the Ne content in the plasma. ... 110

Figure 6.5. Hardness of DLC coatings with different Ne content in discharge gas. 111

Figure 6.6. Young's modulus for DLC coatings with different Ne content in discharge gas. 111

Figure 6.7. Friction coefficient graphs for DLC coatings with different substrate bias.... 112

Figure 6.8. Coefficient of friction for last 50 m of sliding of the DLC coatings deposited with different substrate biasing. 113

Figure 6.9. Wear track for DLC coatings with different substrate bias in pin-on-disc; a) Floating; b) -40V; c) -60V; d) -80V; e) -100V; with the magnification of 200X114

Figure 6.10. Coefficient of friction for DLC coatings with different Ne content. 115

Figure 6.11. Coefficient of friction for last 50 m of sliding for DLC with Ne content..... 115

LIST OF TABLES

Table 2.1. Comparison of major properties of amorphous carbons with diamond, graphite, ta-C and polyethylene [46]. 36

Table 3.1. Deposition conditions for the Cr and Ta films deposited by DOMS. 43

Table 3.2. Deposition conditions for the Cr and Ta films deposited by DCMS. 45

Table 3.3. Deposition conditions of the Cr films deposited by DOMS with different deposition pressures. 45

Table 3.4. Deposition conditions used to deposit CrN and TiSiN films by DOMS........ 47

Table 3.5. Deposition conditions for the CrN and TiSiN films deposited by DCMS. 49

Table 3.6. Deposition conditions for HiPIMS-DOMS DLC coating with different substrate bias........ 50

Table 3.7. Deposition conditions for HiPIMS-DOMS DLC coating with different Ne content. 51

Table 3.8. Experimental conditions for pin-on-disc. 52

NOMENCLATURE AND ACRONYMS

Nomenclature

Ar – Argon

Ar^+ – Argon ion

Ar^{2+} – Argon ion doubly charged

C – Capacitor

C – Carbon

C^+ - Carbon ion

Cr – Chromium

Cr^+ – Chromium ion

Cr^{2+} – Chromium ion doubly charged

CrN – Chromium nitride

D – Pulse duration

DC_{int} – Internal DC power supply

E_0 – Initial energy of the ions

F – Pulse frequency

I – Current

I_p – Peak current

k – Waists constant

k_{miz} – Ionization rate co-efficient

L – Inductor

n_e – Plasma density

Ne – Neon

N – Atomic nitrogen

N^+ – Atomic nitrogen ion

N_2 – Nitrogen molecule

N_2^+ - Nitrogen cation

P – Pressure

P_a – Average power

P_p – Peak power

Q – Ion charge state

Si – Silicon

T – Period

Ta – Tantalum

Ta^{+} – Tantalum ion

Ta^{2+} – Tantalum ion doubly charged

t_{dep} – Deposition time

T_e – Electron temperature

T_h – Homologous temperature

Ti – Titanium

$TiSiN$ – Titanium silicon nitride

t_{on} – Oscillations ON time

t_{off} – Oscillations Off time

V – Voltage

V_b – Bias voltage

V_p – Peak voltage

V_s – Velocity of the sputtered neutrals

λ_{miz} – Ionization mean free path

α – Sheath impinging angle

β – Substrate impinging angle

ΔV – Potential drop at the substrate

Acronyms

AFM – Atomic Force Microscopy

CEMMPRE – Centre for Mechanical Engineering, Materials and Processes

CVD – Chemical Vapor Deposition

CVA – Cathodic Vacuum Arc

DC – Direct Current

DCMS – Direct Current Magnetron Sputtering

DLC – Diamond Like Carbon

DOMS – Deep Oscillation Magnetron Sputtering

FCVA – Filtered Cathodic Vacuum Arc

ERMS – Energy-Resolved Mass Spectroscopy

HHCF – Height-Height Correlation Function

HiPIMS – High Power Impulse Magnetron Sputtering

HPPMS - High Power Pulsed Magnetron Sputtering

ICE – Internal Combustion Engine

IPVD – Ionized Physical Vapour Deposition

MPPMS – Modulated Pulse Power Magnetron Sputtering

MSIBD – Mass Selected Ion Beams Deposition

PLD – Pulsed laser Deposition

PMS – Pulsed Magnetron Sputtering

PO – Preferential Orientation

PVD – Physical Vapour Deposition

RFMS – Radio Frequency Magnetron Sputtering

SCCM – Standard Cubic Centimeters per Minute

SEM – Scanning Electron Microscopy

SRIM – Stopping and Range of Ions in Matter

SZD – Structure Zone Diagram

XRD – X-ray diffraction

Chapter I

1. INTRODUCTION

The advent of magnetron flat cathodes in the 70s of the previous century gave rise to an intense development of thin film deposition by sputtering. Nowadays, several variants of magnetron sputtering, such as direct current magnetron sputtering (DCMS) and pulsed magnetron sputtering (PMS) are widely used at industrial level, being integrated into the manufacturing of a great diversity of products. However, the demand for films with higher performance and application tailored properties is incessant and continuously drives the development of new process developments. In the last decade, new magnetron sputtering deposition techniques have been developed to produce highly ionized fluxes of sputtered material and, consequently, allow greater control over the energy and direction of the sputtered species. High-power Impulse Magnetron Sputtering (HiPIMS) and Modulated Pulsed Power Magnetron Sputtering (MPPMS), a variant of HiPIMS, are two of the most recent of these developments. Both deposition techniques rely on the application of very high target power densities to achieve higher plasma densities and subsequent ionization of the sputtered material. As the ionization degree of the sputtered species increases with the increase of peak power, then it becomes possible to influence the direction of the species impinging on the film, since the metal ions are deflected to trajectories close to the normal of the substrate due to the self-biasing or the substrate biasing. As in DCMS, independent control of the average impinge angle and the average energy of the sputtered species is not possible. In fact, the increase of peak power also leads to an increase in the discharge voltage and, consequently, an increase in the average energy of the species arriving at the substrate. However, the nature of the interdependence between the energy and the impinge direction of the particles that bombard the growing film is substantially different in HiPIMS and DCMS. Thus, HiPIMS allows generating bombardment conditions that are not available in

DCMS process.

This work was carried out at the Surface Engineering Group (SEG) of the Centre for Mechanical Engineering, Materials and Processes (CEMMPRE) of the University of Coimbra. In the last three decades, a large body of experience and know-how has been developed at SEG concerning the deposition of thin films by magnetron sputtering. The main area of expertise is the production of thin films for mechanical applications, including hard and high temperature coatings and wear and corrosion resistant thin films. Prior to the present work, most of the development work at SEG was based on DCMS and PMS, although radio frequency magnetron sputtering (RFMS) was also routinely used. This work arises from the strategic option made at the SEG to extend the group know-how to HiPIMS. For this purpose, a new generation HiPIMS power supply (ZPulser Cyprium) was acquired prior the beginning of this work. This power supply operates in Deep Oscillating Magnetron Sputtering (DOMS) mode, a variant of HiPIMS characterized by the use of oscillatory pulses of voltage. In spite of the vast experience acquired in the CEMMPRE over the years regarding the deposition of thin films by magnetron sputtering, the use of a DOMS power supply presupposes the development of new experimental procedures and know-how. On the other hand, the use of ionized film forming species makes available new deposition mechanisms, as compared to DCMS, that influence not only the films properties but also the control of the deposition process. New knowledge, ranging from the most basic aspects of the deposition process to the most complex ones have to be acquired and new concepts specifically tailored to the DOMS process have to be developed. Thus, the main objectives of the present work are to develop an accurate understanding of the new deposition mechanisms that the DOMS technology brings about, in comparison to DCMS, and to evaluate the potential of this technology to meet the constant technological demand for thin films with improved performances.

Taking into account the two main objectives refereed above, this research work was structured based on two main parts. In the first part, which corresponds roughly to the two first years of the work, four deposition systems already well-known at SEG were investigated. In each case, thin films were deposited by DOMS and DCMS in order to compare their microstructural, structural and mechanical properties and to identify the main differences resulting from the DOMS process. Initially, two metallic systems, Cr and Ta, were investigated as the deposition of metals by magnetron sputtering is less complex than that of compounds and thus it allows a greater focusing on the deposition process itself. Then, two nitride system were studied, CrN and TiSiN. In both cases, the results were

systematically analyzed and discussed in order to identify the new experimental capabilities and/or new deposition mechanisms that result from the DOMS process.

The four deposition systems studied in the first part of this work were chosen because they were already well studied at SEG regarding their deposition by DCMS. This allowed for a greater focus on the main differences introduced by the DOMS process both on the films properties and deposition mechanisms. Although new interesting results were obtained by using DOMS instead of DCMS, all the selected deposition systems were already well-known in the literature at the time of start of this work. In the second part of this work, which corresponds roughly to the third year, the knowledge previously acquired was applied to the development of a state of the art thin film with technologically relevant properties. The main objective was to demonstrate the added value of the DOMS process for the development of solutions that correspond to actual needs of the thin film industry. For this purpose, the DOMS process was applied to the development of hydrogen-free hard carbon films for application in piston rings. The main motivation for the selection of the carbon system was the start of new European project at SEG, the TANDEM project, which aims to develop a new generation of significantly improved DLC films deposited by HiPIMS for piston rings in internal combustion engines (ICE). The current trends in ICE development such as downsizing, start-stop engines, turbo-charging and the use of lower viscosity oils, all have similar effects on requirements for engine parts: operating temperatures and loading densities on components are getting increasingly higher. Although classical DLC coatings already account for more than 50 % of the coatings applied in internal combustion engines, their application in future piston rings require improved wear resistance and higher temperature stability (up to 500 ºC) than they can currently deliver. The propose solution to meet this demand in the TANDEM project is the development of hard hydrogen-free tetrahedral DLC coatings (ta-C coatings).

Most of the research carried out in the first part of this work has been presented in papers published in scientific journals in the field of thin film and surface science technology (see list of papers at the end of this chapter). Each of the studied deposition systems has been individually discussed and analyzed in a corresponding publication (Cr system: Cr01, Cr02, Cr03; Ta system: Ta01; CrN system: CrN01; TiSiN system: TiSiN01; C system: C01). Detailed information about the experimental setups used for thin film deposition and characterization, as well as results and discussions for each the individual systems can be found in the corresponding paper and which are an integral part of this thesis. The main body of this thesis aims at developing an overall synthesis of the results obtained for each

individual system and to highlight the most important outcomes of the work taking into account the proposed objectives. A comparison of the evolution of the properties of the thin films deposited by DOMS with increasing peak power is made in chapter IV for both the metallic (section 4.2) and metal nitride systems (section 4.4). Although many of the results resented in this chapter were already published, new characterization results were added in order to achieve a more complete comparison between the deposition systems. Additionally, a section dealing with the effect of the deposition pressure in Cr films deposition by DOMS is also included in this chapter (section 4.3). The most important conclusions concerning the technological capabilities of the DOMS process and the new deposition mechanisms involved in DOMS, in comparison with DCMS, are summarized in sections 5.2 to 5.6 of chapter V. A comprehensive discussion about the conclusions presented in each of these sections can be found in papers TiSiN01, CrN01, Cr02 and Cr03, respectively. The goal of chapter V is to congregate the most relevant conclusions obtained in this work in a single place in order to facilitate the discussion of the overall potential of the DOMS process for thin film deposition, which is discussed in the last section of the chapter (section 5.6).

The initial results obtained in this work regarding the deposition of hard hydrogen-free DLC films were published in the journal Surface and Coatings Technology (C01). In this paper the effect of substrate biasing on the deposition of DLC films by DOMS is discussed. The mass density, structure, temperature stability, morphology and mechanical properties of the DLCs films are presented in the paper as well as a preliminary study of their temperature resistance. A Cr interlayer was used in all depositions in order to enhance the films adhesion. However, it was found that the adhesion of the films was not adequate for tribological testing and that the DLC films peeled off the substrate almost immediately at the beginning of pin-on-disk tests. In chapter VI, new results concerning the deposition of DLC films by DOMS obtained from films deposited using a more complex adhesive interlayer (based on Cr and CrN layers) which allowed for tribological testing of the films are presented. Besides the effect of substrate biasing (section 6.2), the influence of adding Ne to the discharge gas (section 6.3) and the tribological properties of the films (section 6.4) are also presented and discussed. Chapter VI ends with a discussion about the potential of the DOMS process for the deposition of hard hydrogen-free DLC (section 6.5).

As stated above, a detailed account of the experimental conditions used in this work regarding thin films deposition and characterization can be found in the papers published in the aim of this work. Nevertheless, an experimental chapter was included in the thesis (chapter III) aiming at facilitating the understanding of the results and discussion carried in

the thesis main body. The most important deposition parameters are collected in this chapter according to each of the sections of chapters IV to VI. Additionally, detailed experimental conditions regarding the deposition and characterization results not included in the published papers are also presented. Finally, background information regarding the HiPIMS deposition process and the deposition of hard hydrogen-free DLC films (ta-C) is presented in chapter II. In section 2.2, an introduction to the main characteristics of the HiPIMS process is first presented and is then followed by a more in depth discussion of the main aspects of this deposition process relevant for chapters IV and V. A general introduction to the deposition of hard DLC films for mechanical applications is first presented in section 2.3 and is then followed by the a more specific state of the art regarding DLC films deposition by HiPIMS.

LIST OF PUBLISHED PAPERS

Cr01 (Annex A): F. Ferreira, R. Serra, J. Oliveira, and A. Cavaleiro, "Effect of peak target power on the properties of Cr thin films sputtered by HiPIMS in deep oscillation magnetron sputtering (DOMS) mode," Surface and Coatings Technology, vol. 258, pp. 249-256, 2014.

Ta01 (Annex B): F. Ferreira, C. Sousa, A. Cavaleiro, A. Anders and J. Oliveira, “Phase tailoring of tantalum thin films deposited in deep oscillation magnetron sputtering mode.” Surface and Coatings Technology, vol. 314, pp.97-104, 2017.

CrN01 (Annex C): F. Ferreira, J. Oliveira, and A. Cavaleiro, "CrN thin films deposited by HiPIMS in DOMS mode," Surface and Coatings Technology, vol. 291, pp. 365-375, 2016.

TiSiN01 (Annex D): J. Oliveira, F. Fernandes, F. Ferreira, and A. Cavaleiro, "Tailoring the nanostructure of Ti–Si–N thin films by HiPIMS in deep oscillation magnetron sputtering (DOMS) mode," Surface and Coatings Technology, vol. 264, pp. 140-149, 2015.

Cr02 (Annex E): F. Ferreira, R. Serra, A. Cavaleiro, and J. Oliveira, "Additional control of bombardment by deep oscillation magnetron sputtering: Effect on the microstructure and topography of Cr thin films," Thin Solid Films, vol. 619, pp. 250-260, 2016.

Cr03 (Annex F): J. C. Oliveira, F. Ferreira, A. Anders, and A. Cavaleiro, "Reduced atomic shadowing in HiPIMS: Role of the thermalized metal ions," Applied Surface Science, vol. 433, pp. 934-944, 2018.

C01 (Annex G): F. Ferreira, A. Aijaz, T. Kubart, A. Cavaleiro, and J. Oliveira, "Hard and dense diamond like carbon coatings deposited by deep oscillations magnetron sputtering," Surface and Coatings Technology, 2017.

Reprints of the papers were made with the written consent of the Publisher and can be found in annex.

Chapter II

2. BACKROUND INFORMATION

2.1. Introduction

The first part of this chapter aims at an outline of HiPIMS and its main characteristics. Rather than making a thorough and detailed description of HiPIMS, section 2.2 focuses on the main aspects of HiPIMS relevant within the aim of the present work. Besides an initial general introduction, selected topic encompassing concepts and results discussed in the main body of this work are presented in a more in depth approach. This section ends with a summary of the main characteristics of the DOMS process. As already mentioned in the general introduction, four well-known deposition systems were studied in the first part of this work (Cr, Ta, CrN, TiSiN) in order to evaluate the potential of DOMS for thin film deposition. For each deposition system, the relevant literature references in light of the present work have been given and discussed in the corresponding published papers and, thus, they are not included in this chapter. The second part of this chapter is, thus, focused on the deposition of carbon by magnetron sputtering based processes. Besides a general introduction to carbon hybridization and to the mechanisms responsible for sp^3 formation in carbon thin films, a special attention is given to the effect of adding Ne to the plasma during carbon deposition by HiPIMS in pure Ar.

2.2. HiPIMS

In the last decades, the demand for films with higher performance and optimized properties has driven the development of sputtering techniques that allow direct control of

the sputtered material flux. These techniques are referred as ionized PVD (IPVD) when the deposition flux consists of more ions than neutrals [1]. Control of the sputtered material allows, for example, filling the cavities interior with a uniform thickness, a very important technological aspect in the microelectronic industry. However, most of IPVD techniques require additional equipment as compared to DCMS and thus their interested has been mostly academical. In the last fifteen years, a new magnetron sputtering deposition technique has been developed to produce highly ionized fluxes of sputtered material while using essentially the same equipment as in DCMS except for the power supply. This technique, known as High-power Impulse Magnetron Sputtering (HiPIMS) [1-4], and some of its variants, such as Modulated Pulsed Power Magnetron Sputtering (MPPMS) [5-7], are now on the verge of industrial application. Although they rely on similar physical processes as DCMS, they bring about new opportunities in thin film deposition.

In DCMS the plasma density can be increased by increasing the power applied to the target. However, the maximum power that can be applied to the target is limited by its melting point and by its cooling efficiency by the cathode. In HiPIMS the power is applied in very short pulses and, thus, the instantaneous value of the power can be significantly increased without increasing the average power. This technique was introduced by Kouznetsov et al. in 1999 [3] and, since then an extensive body of research has been focused on its development.

The power sources used in HiPIMS basically consist of a load circuit formed by a DC source which charges a capacitor (C) through a solid state switch and by a discharge circuit which discharges the capacitor through an inductor (L) whose objective is to protect the source components from abrupt current variations (figure 2.1a)) [8]. The capacitor capacitance (C) is typically between 1 to 50 μF while the inductance (L) is 20 to 50 μH. In HiPIMS, power pulses with a typical duration (or on time) between 5 –5000 μs are applied to the cathode such that the duty cycle is kept low (<5%), providing sufficient time for the target cooling. The pulse frequency is in the range between 100 Hz to 10 kHz. A voltage-current characteristic of a HiPIMS discharge is shown in figure 2.1b). The typical discharge voltage in HiPIMS is two or more times higher than in DCMS while typical target current densities are of the order of many tens of Acm^{-2}, i.e, several orders of magnitude higher as compared to DCMS technique [1]. The exact shape of the pulses depends not only on the power source but also on the discharge formed in the deposition system, i.e., the target material, the magnetic field configuration, the gas used and the deposition pressure.

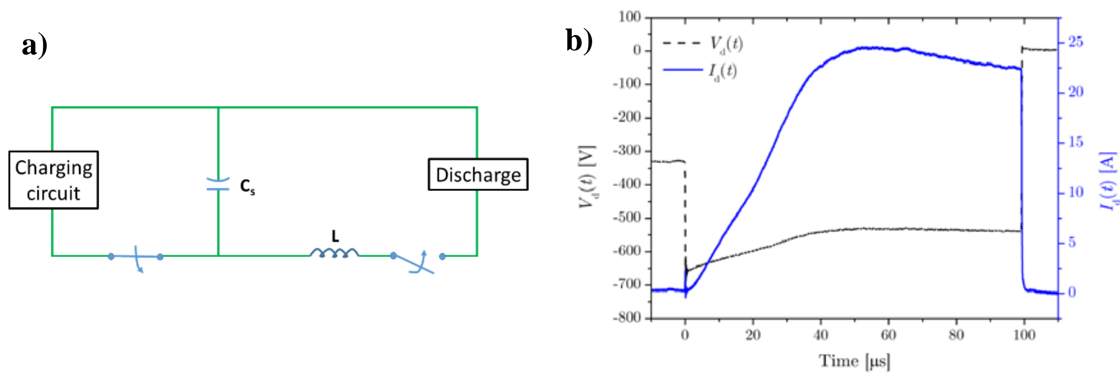

Figure 2.1. a) Charge circuit diagram of a HiPIMS source and b) a typical voltage-current characteristic from a HiPIMS discharge [9].

Conventional magnetron discharges follow the empirical power law $I = k \times V^n$ where I is the discharge current, V the discharge voltage, and n is in the range between 5 and 15 [10]. The constant k depends on the geometry of the discharge, magnetic field shape, gas type, gas pressure, and the target material. The exponent n depends on the efficiency of the electron trapping in the plasma. The more efficient the electron trapping is the higher is the n value. A high value of n shows that the discharge can provide a significant increase in discharge current with a relatively small variation in target voltage, i.e., it shows that the plasma is rather weakly ionized. Figure 2.2 shows the I-V characteristics from a DCMS and HiPIMS discharge [2]. The n value for the DCMS discharge is 8, a typical value for this type of discharge. The HiPIMS discharge clearly shows two operating modes. For lower current densities, the discharge has a value of n = 7, similar to the value obtained for the DCMS discharge. For higher current densities values, n assumes a value close to unity typical for a HiPIMS discharge. This variation translates to a sudden increase in the plasma impedance with the transition into HiPIMS mode, which may be due to a decrease of the electrons entrapment efficiency in the plasma [2]. In DCMS, the probability of the sputtered species being ionized during their travel towards the substrate is quite small due to the low electron density in the discharge. Thus, typically only 1% of the sputtered material reaches the substrate in the form of ions. The high instantaneous power densities used during the HiPIMS pulses allow a significant increase in the plasma electron density (more than two orders of magnitude), and, therefore, the probability of the sputtered species being ionized increases greatly. Typically, a HiPIMS discharge has an electron density in the order of 10^{19}

electrons per cubic meter. Therefore, as predicted in the simulation shown in figure 2.3, in many materials more than 50 % of the sputtered species are ionized during their travel towards the substrate, reaching the fraction of almost 100% ionized material in the case of Al and Ti [11]. For this reason, the plasma produced by HiPIMS is often referred to as a highly ionized metal plasma.

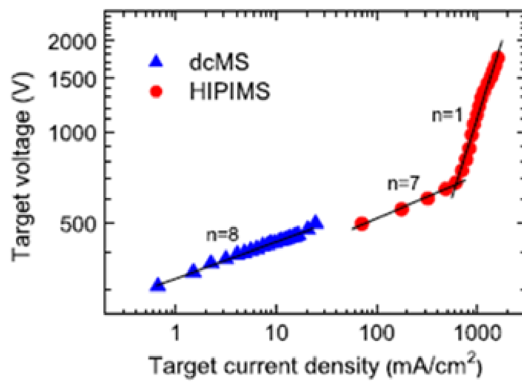

Figure 2.2. I-V characteristics from a DCMS and HiPIMS discharge [2].

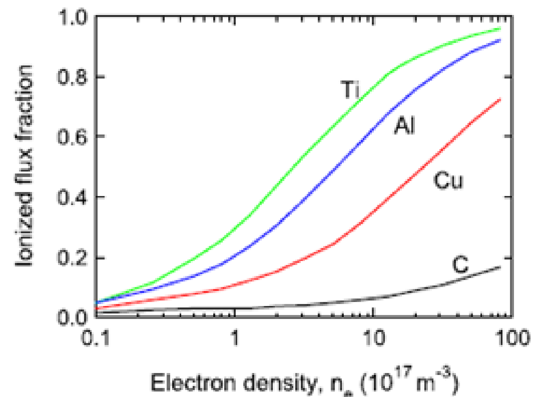

Figure 2.3. The ionized flux fraction dependence on plasma density for different materials [11].

Christie et al. developed a phenomenological model in order to determine the ionized fraction of the sputtered material arriving at the substrate and to explain the low deposition rate reported in HiPIMS discharges [12]. Since then, several authors modified this model in order to add the feature of evaluating the fraction of the sputtered species returned to the target [13, 14]. A schematic of the phenomenological model is presented in figure 2.4. The sputtering of the target surface is performed by both the argon and the metal ions present in the plasma since both are accelerated by the target negative potential (processes I and II). These two types of ions have different sputtering coefficients, whereby the amount of sputtered material from the target will be different (III). During their travel towards the substrate, the sputtered material crosses the ionization zone of the discharge, still in the vicinity of the target, where it can be ionized (IV). A fraction of those ions created in this zone can return to the target if they do not have sufficient kinetic energy to overcome the potential barrier (V) and thus contribute to target sputtering. The remaining ions escape from the ionization zone (VI) and may ultimately be lost to the chamber walls or end up at the substrate position (VII) where they contribute to the film growth. The sputtered neutral species that have not been ionized in the ionization zone continue their journey through the

plasma where they can still be ionized (VIII), while being too far away to be affected by the negative potential drop at the target. They may also reach the substrate where they contribute to the film growth (VII) or be lost to the chamber walls. The sputtered neutral species that are not ionized in the plasma can also reach the substrate (IX) or be lost to the chamber walls. Finally, both the sputtered metal species and the Ar atoms resulting from the neutralization and reflection of some of the Ar^+ ions on the target surface (XI) may collide with the discharge gas (X, XII). These collisions cause a decrease in the gas density in front of the target, usually referred to as gas rarefaction.

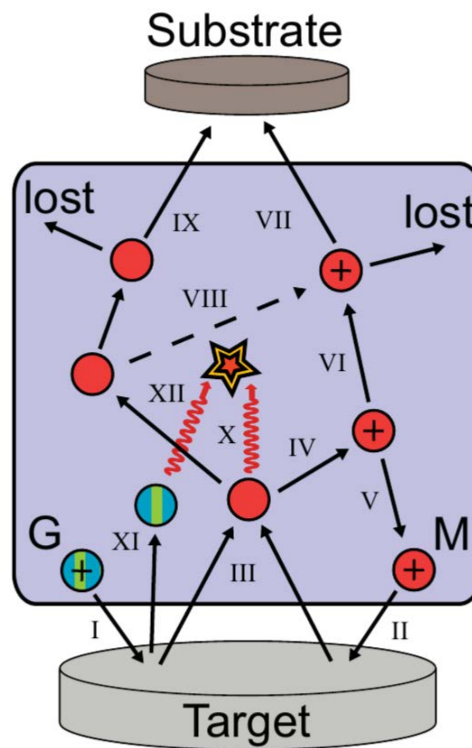

Figure 2.4. Schematic of the target material pathway model. The letters G and M stand for gas and metal ions, respectively [13].

The major drawback of HiPIMS is the significant reduction in deposition rate compared to DCMS. Typically, metal deposition rates by HiPIMS vary between 30 and 80% of the deposition rates obtained by DCMS (see figure 2.5) under the same deposition conditions [15-17]. This topic has been intensively investigated within the scientific community of HiPIMS and has given rise to several publications in recent years that the most interested reader can consult [15, 16, 18, 19]. Here, only the two main causes of loss of deposition rate will be presented in a summarized way. As already mention before, if the

ionization of a sputtered atom occurs sufficiently close to the target in such a way that the created ion is under the influence of the target negative potential and if the kinetic energy of that ion is not sufficient to overcome the potential barrier, then, the ion will be back-attracted to the target surface. Back-attracted ions do not contribute to the film growth and, thus, they contribute to decrease the deposition rate (known as return effect). When these metal ions impinge on the target with enough kinetic energy, they also contribute to target sputtering, i.e., self-sputtering occurs. However, their sputtering efficiency is typically lower than that of Ar^+ ions (their sputtering coefficient is lower as compared to the Ar^+ ions). Thus, they bring about a reduction of the sputtered material, contributing once again to the decrease of deposition rate.

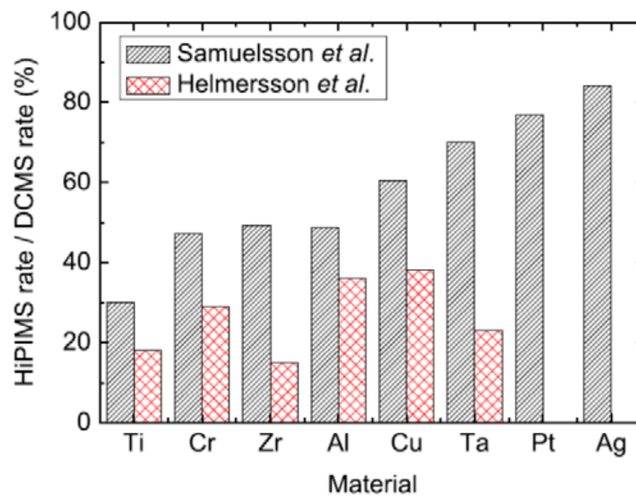

Figure 2.5. Relative deposition rate in HiPIMS compared to deposition rate in DCMS [16].

Another important cause for the decrease in deposition rate is the higher voltages required to operate a HiPIMS discharge as compared to DCMS discharge. The sputtering coefficient increases with the energy of the incident ions, i.e., with the potential difference between the plasma and the target. However, this increase follows a sub-linear trend. Thus operating at higher voltages and, thus, at lower currents, results in a loss of efficiency of the sputtering process and therefore in a decrease of the deposition rate (known as yield effect). Anders et al. estimated that for a discharge with a Cu target, which is typically operated at 350 V in DCMS and at 700 V in HiPIMS, this effect was responsible for a 30% loss in deposition rate [15].

The use of very high peak powers results in HiPIMS discharges with highly energetic metal ions, which have been shown to have a densifying effect on thin films [20, 21]. In order to understand this phenomenon, HiPIMS plasmas have been investigated by several researchers by monitoring the ion fluxes at the substrate or target [22-25]. On the other hand, fast optical diagnostics revealed a pattern formation in HiPIMS plasmas, namely the formation of the so-called spokes [26, 27]. In the spokes regime the homogeneous plasma torus known from DCMS plasmas changes to a determinate number of plasmoids which are rotating over the racetrack. The number of plasmoids is referred to as quasi-mode number. However, the origin of the energetic metal species generated by HiPIMS is still an open issue [28]. Numerous mechanisms have been proposed to explain the presence of energetic metal species in HiPIMS such as: i) the high-energy tail of the Thompson distribution [24]; ii) reflected ions at the target [29]; iii) negative ions that are generated in front of the target and then are accelerated towards the substrate by the full target potential [30-32]; iv) acceleration of metal species by a two-stream instability induced by localized ionization zones on the target [33] and v) formation of a double layer when the HiPIMS plasma is in the spokes regime [34, 35].

The generation mechanism of the spokes and their influence on the species transport towards substrate are not yet completely understood. Regarding to the spokes region, Lundin et al. observed energetic ions in lateral directions to the target [33]. The authors explained these energetic species by a generation mechanism based on a two-stream instability interacting with the spoke region, Andersson et al. [35] and Anders et al. [34] proposed a model which incorporates a double layer when the HiPIMS plasma is in the spokes regime witch explains both the deconfinement and the acceleration of the metallic ions to high energies,

2.2.1. Modulated Pulse Power Magnetron sputtering

In the last decade a new variant of HiPIMS, Modulated Pulse Power Magnetron Sputtering (MPPMS), has been developed in the United States. This technique uses longer pulses than the classic HiPIMS, with a duration up to 3 ms, each pulse being divided into segments with different voltage and current characteristics [5-7, 36]. Typically, two segments are used, one of low peak voltage whose purpose is to pre-ionize the discharge gas and another one of much higher peak voltage in which the HiPIMS regime occurs. The

applied voltage in each segment is controlled by the application of micro-pulses (between 2 and 16 µs) with a frequency of the order of kHz. By modulating the pulse duration (up to 3000 µs), its frequency (4 to 400 Hz), the duration of the micro-pulses and their frequency, this technique allows to generate in a controlled way peak powers up to 360 kW, average powers up to 20 kW and peak currents up to 550 A at the target during the high ionization segment. A typical MPPMS pulse is shown in figure 2.6. Note that in the simplest case where a pulse consists of a single segment it is necessary to define five parameters to establish the exact pulse shape to be used: the applied voltage (DC_{int}), duration and pulse frequency (D and F) and the times when the micro-pulses are on (t_{on}) and off (t_{off}).

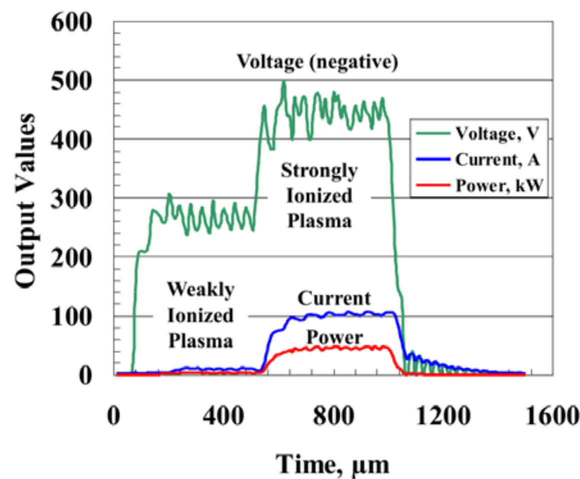

Figure 2.6. Typical MPP pulse [7].

As referred above the instantaneous power density applied to the target in HiPIMS is two orders of magnitude higher than in DCMS. One of the advantages of MPPMS is that it can operate in a large range of power densities. The operating regimes of HiPIMS, MPPMS and DCMS taking into account the power density at the target and the duty cycle (the percentage of the time that the pulse is on) are shown in figure 2.7**.** The power density in MPPMS can be varied from DCMS-like values up to the typical HiPIMS values, i.e., the ionization degree of the sputtered material can be tuned from very low DCMS-like values to the very high degrees found in typical HiPIMS.

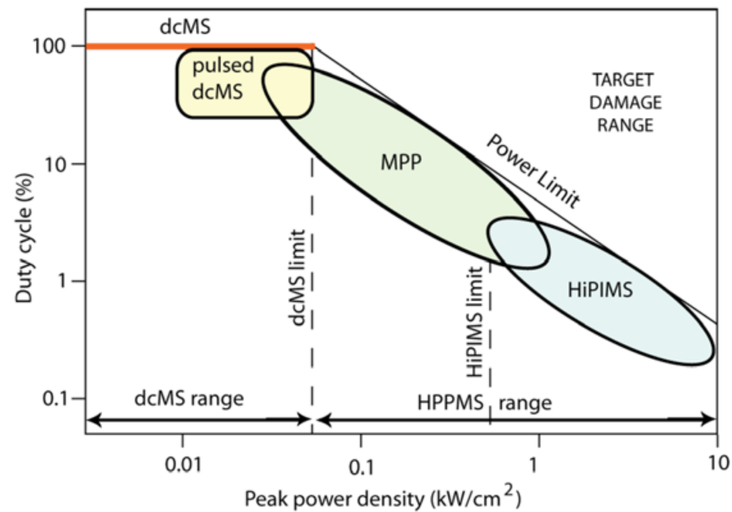

Figure 2.7. Different work regimes based on the peak power density at the target, combined with the duty cycle [8].

2.2.2. Deep Oscillations Magnetron Sputtering

Both HiPIMS and MPPMS discharges present a serious disadvantage when operated in a reactive mode: a significant number of arcs are generated, which negatively influence the quality of the deposited films. More recently, a variant of MPPMS has been developed in which the voltage pulses are designed in order to avoid abrupt voltage variations and thus reduce the amount of produced arcs. This operation mode is known as deep oscillation magnetron sputtering (DOMS) and is still in an exploratory phase of its potentialities [37, 38]. In DOMS, the voltage pulses are constituted by a set of oscillations as can be seen in figure 2.8. In each oscillation, both the voltage and the current gradually increase during the on-time (t_{on}) until they reach their maximum value (V_p and I_p). Then, both the voltage and current gradually decay, reaching zero before the end of the oscillations period (T). The power supply is powered by an internal d.c. power supply (DC_{int}). The applied voltage is controlled by the application of oscillations (between 2 and 16 μs) with a frequency of the order of kHz. By varying the pulse duration (100 to 3000 μs), its frequency (1 to 1400 Hz), the duration of the oscillations and their frequency, this technique allows to generate in a controlled way peak powers up to 510 kW, average powers up to 5 kW and peak currents up to 300 A at the target. Therefore, it is necessary to define five parameters to establish the exact pulse shape to be used: the applied voltage (DC_{int}), duration pulse (D) and the times when the oscillations are on (t_{on}) and off (t_{off}). The power supply software automatically

adjusts the pulse frequency (F) in order to keep a constant average power (P_a). The peak power (P_p) is defined as the product $V_p \times I_p$. In this work, a power supply operating in DOMS mode (Zpulser CYPRIUM III) was used for the deposition of thin films. Like MPPMS, the DOMS technique allow varying the ionization degree of the sputtered material from very low DCMS-like values to typical HiPIMS values.

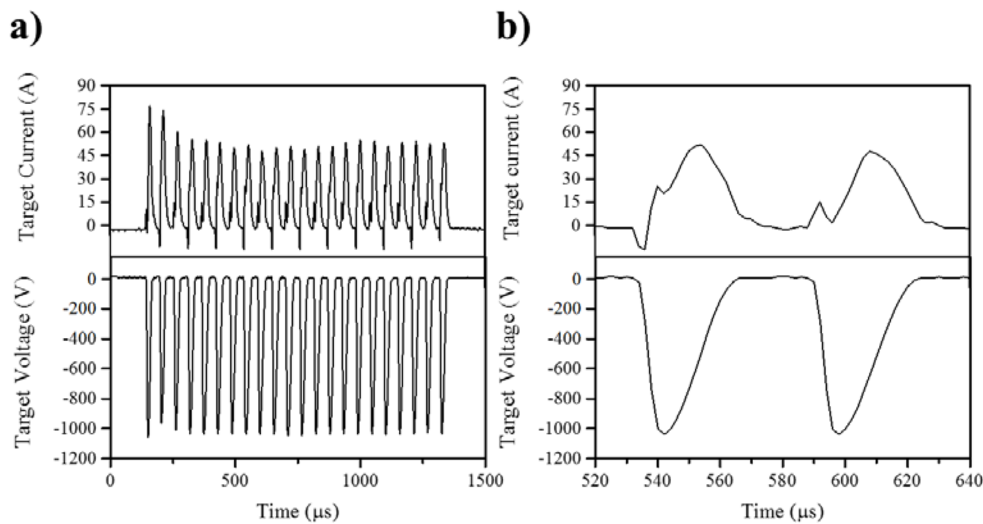

Figure 2.8. Typical I-V waveforms of a DOMS pulse and, b) oscillation pulses within one long pulse.

2.2.3. Morphology of films produced by HiPIMS

The Structure Zone Diagram (SDZ) proposed by Thornton [39] summarizes the dependency of the microstructure of magnetron sputtered thin films on both the homologous temperature and the process pressure. This SZD has become a classic and is reproduced in many papers and textbooks concerned with physical vapor deposition. However, the Thornton diagram does not incorporate the effect of additional ion bombardment when deposition is ion assisted (such as substrate biasing). This effect was added by Messier et al. who proposed a modified diagram in which the pressure axis was replaced by an energy axis of the ions [40]. In turn, this diagram does not take into account the atoms/ions ratio reaching the substrate, the mass difference between ions and atoms that contribute to film growth and that the ions can have a broad energy distribution. More recently, Anders [41] proposed a new SDZ specifically considering HiPIMS. For this purpose, three modifications were proposed to the Thornton diagram:

- A term was added to the axis of the homologous temperature that takes into account the effect of the potential energy of the particles arriving at the substrate, thus obtaining a generalized temperature axis.
- The linear pressure axis has been replaced by a normalized logarithmic energy axis which takes into account the displacement and heating effects due to the kinetic energy of the bombarding particles.
- A Z-axis has been defined as the net film thickness to indicate the thickness reduction due to the film densification and sputtering, it also allows the incorporation of ion etching zone (negative thickness).

The SDZ presented by Anders is shown in figure 2.9. In this diagram are present the familiar zones of the SZD proposed by Thornton et al. with the same meaning [39]. A detailed description of the SZD proposed by Anders can be found in the respective paper [41].

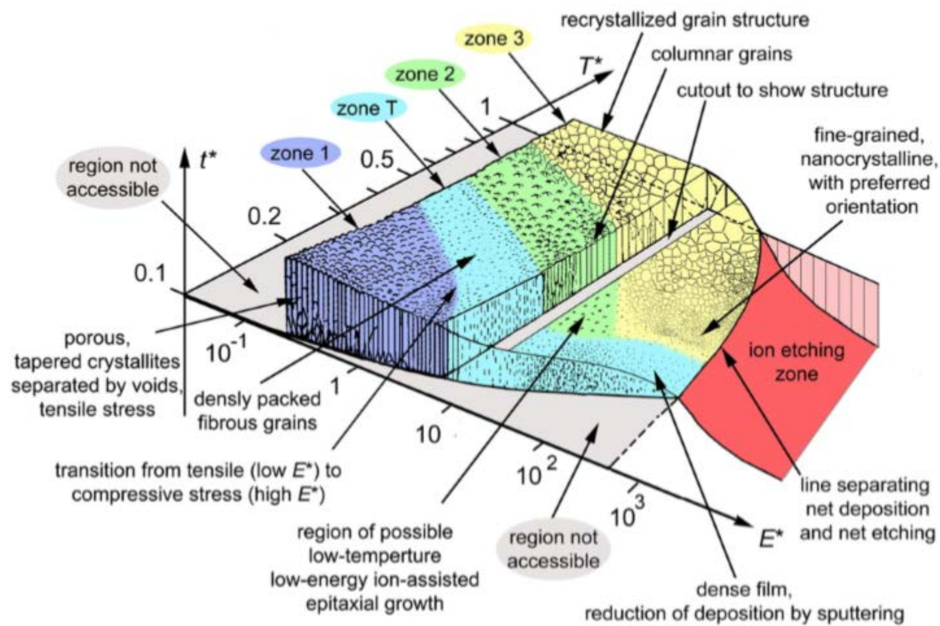

Figure 2.9. Structure zone diagram applicable to energetic deposition proposed by Anders [41].

Here, we will only highlight two important aspects. On one hand, we note the significant decrease in film thickness to higher values of the normalized energy axis and the existence of an etching zone when these values exceed a critical value. On the other hand,

the extension of the both zone T and zone 3 to higher normalized energy values giving rise to the deposition of denser nanocrystalline films with low grain size and preferential orientation. Another interesting feature of the SDZ is the proposed existence of a region of possible low-temperature low-energy ion-assisted epitaxial growth near the conjunction of zones T, 2 and 3.

2.3. Hard DLC films

2.3.1. Carbon-based thin films

Carbon is the essential ingredient of numerous essential engineering materials possessing an exceptionally wide range of properties. C is also an abundant and environmentally friendly element. Graphite and Diamond are the most stables phase of Carbon (figure 2.10). Depending on the bonding type, the properties of C materials may range from that of diamond, standing out for its hardness, optical properties as well as high thermal conductivity, to graphite, a soft, lubricating and electrical conductor. However, thin films of carbon consist mainly in amorphous carbon (a-C), which possess a unique and adjustable combination of properties, such as high hardness and wear resistance, chemical resistance and good tribological performances in different operating environments [42]. Carbon-based thin films are thus used as protective coatings in areas such as optical windows, magnetic storage, car components, biomedical tools or micro-electromechanical devices.

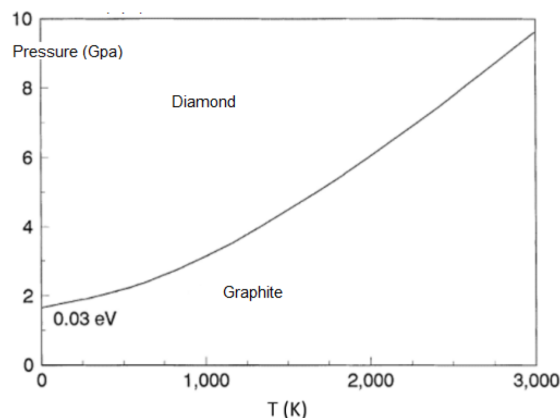

Figure 2.10. Thermodynamic Phase diagram of Carbon.

The wide range of properties that can be achieved with amorphous carbon thin films is mainly due to the different hybridization states (sp^1, sp^2 and sp^3, see figure 2.11) that are formed upon C bonding. Each carbon atom possesses four valance electrons available for bonding. In sp^1 hybridization, two of the four available valence electrons form σ (sigma) bonds with neighboring carbon atoms, while the remaining two electrons form π (pi) bonds. In the sp^3 hybridization, as in diamond, each of the four carbon valence electrons are assigned to tetrahedrally directed orbitals, making four strong σ bond with neighboring C atoms. In the sp^2 hybridization, as in graphite, three of the four valence electrons are assigned to trigonally directed orbitals, which participate in three σ bonds on the same plane. The fourth electron is assigned to a carbon p orbital, oriented perpendicularly to the σ bonding plane. This electron participates in a weaker π bond with one or more similar electrons in neighboring atoms [43].

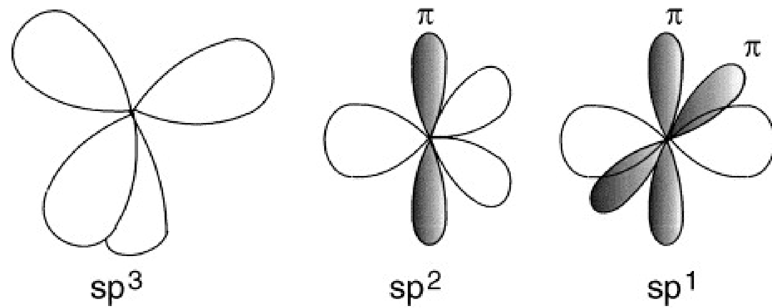

Figure 2.11. The sp^3, sp^2, sp^1 hybridised states of carbon valence orbitals. [43].

Two widely used forms of DLC coatings are hydrogen-free DLC (ta-C, and a-C denoting tetrahedral amorphous, and amorphous carbon, respectively) and hydrogenated DLC (ta-C: H and a-C:H) that are typically distinguished by their hydrogen content. Hydrogenated DLC films are relatively soft but exhibit low friction and wear coefficients. Dense hydrogen-free DLCs can approach the properties of diamond with extremely high hardness, good thermal conductivity and high density. The deposition phase diagram of amorphous carbon thin films is shown in figure 2.12. Hydrogen-free films are deposited in the regions close to the sp^2-sp^3 axis. Besides the graphitic films consisting of almost only sp^2 bonds, a-C thin films deposited by sputtering have close to 20 % sp^3 while the sp^3 content of ta-C films ranges from close to 40 % to almost 90 % sp^3. Since the sigma bonds are

stronger in comparison to π bond, the ta-C films which are rich in sp^3 (like Diamond) exhibit higher hardness than the other carbon hybridization states [44]. The properties of different carbon thin films are shown in table 2.1.

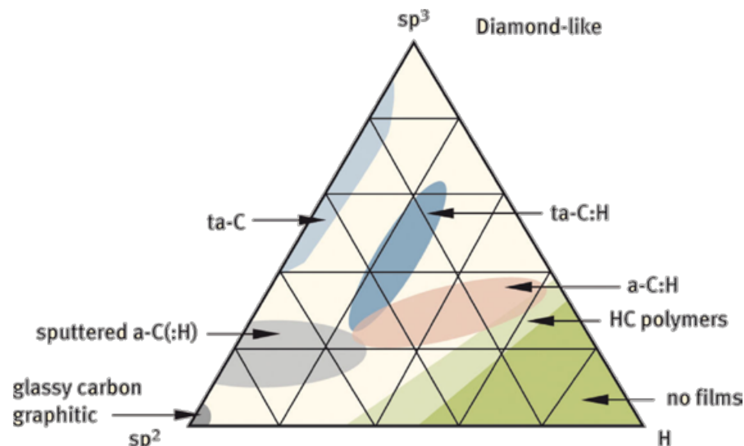

Figure 2.12. Phase diagram for amorphous Carbon [44].

Besides the sp^3 to sp^2 ratio and the hydrogen content, the properties of the C films can be modified by doping with other elements. Common dopants are light elements (B, Si, N, O or F), metals and combinations thereof to modify properties such as hardness, coefficient of friction, internal stress, adhesion, electrical conductivity or biocompatibility [45]. For example, by adding some metallic elements like Cr, W and Ti the tribological performance of the surface are enhanced.

Table 2.1. Comparison of major properties of amorphous carbons with diamond, graphite, ta-C and polyethylene [46].

	sp^3 (%)	H (at. %)	Density (g/cm^3)	Gap (eV)	Hardness (GPa)
Diamond	100	0	3.515	55	100
Graphite	0	0	2.267	0	
ta-C	80-88	0	3.1	2.5	80
a-C:H hard	40	30-40	1.6-2.2	1.1-1.7	10-20
a-C:H soft	60	40-50	1.2-1.6	1.7-4	<10
ta-C:H	70	30	2.4	2.0-2.5	50
Polyethylene	100	67	0.92	6	0.01

2.3.2. Stresses in DLC/ta-C thin films

The major problem inhibiting the development of ta-C coatings are the high internal compressive stresses, which can be in excess of 10 GPa. Unfortunately, these very high stress values limit the maximum film thickness to a few hundreds of nanometers as delamination occurs when the internal stress exceeds a critical value. The stress is generally considered an intrinsic property of DLC films arising from the deposition mechanism creating the sp^3 bonds. Several models have been proposed to explain this relation. McKenzie et al. [47] proposed that the compressive stress originated from C ion bombardment lead to subsequent formation of sp^3 sites. On the contrary, in the model proposed by Robertson et al. [48] the sp^3 bonding is directly related to the densification produced by subplantation of C ions. The dominant picture about DLC deposition is that local increase of the density is required to a C-C bond rearrangement from sp^2 to sp^3**.** In thin film deposition, the formation of sp^3 sites is achieved by shallow C atom implantation (subplantation) is employed and the optimum energy of the impinging species is about 100 eV (see figure 2.13). Subplantation, however, results in a highly compressed structure accompanied by large compressive stresses. The high stresses are generally considered a prerequisite for high sp^3 content and relaxation of the compressed structure is expected to lead to sp^3 bonds converting back to sp^2 (see figure 2.13). However, whether the stress in DLC coatings are a consequence of the mechanism of sp^3 formation or just a by-product of the deposition processes still remains an open question [49].

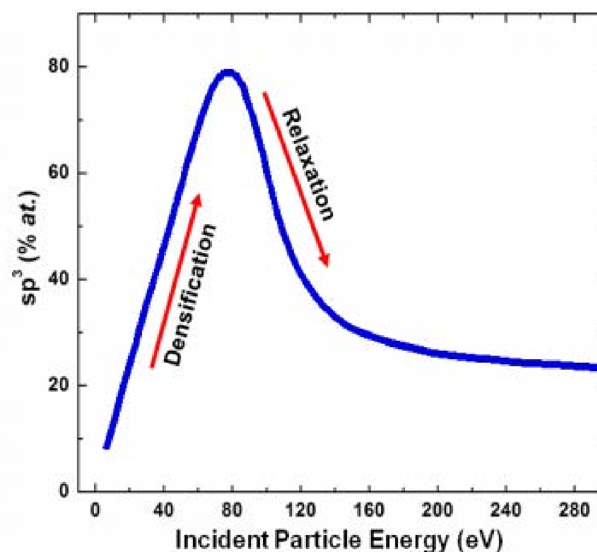

Figure 2.13. Fraction of SP3 carbon in the thin film against the energy of ions [48].

2.3.3. Deposition of ta-C thin films

Cathodic vacuum ARC (CVA) is one of the well-established technologies at industrial level for the deposition of ta-C coatings. This deposition process produces an energetic plasma with a high ion density of up to 10^{13} cm^3 and a large ion energy distribution (between 20 and 200 eV). The advantages of the CVA are that it produces a highly ionized plasma with an energetic species and high growth rates for a low capital cost. The main drawback is the ejection of "macro-particles" from the target (figure 2.14) which end in the film degrading its mechanical properties and increasing the surface roughness beyond industry acceptable standards. This can be overcome by filtering the plasma in Catholic ARC (FCVA). However, this solution limits the industrial scalability of the process and increases the production costs.

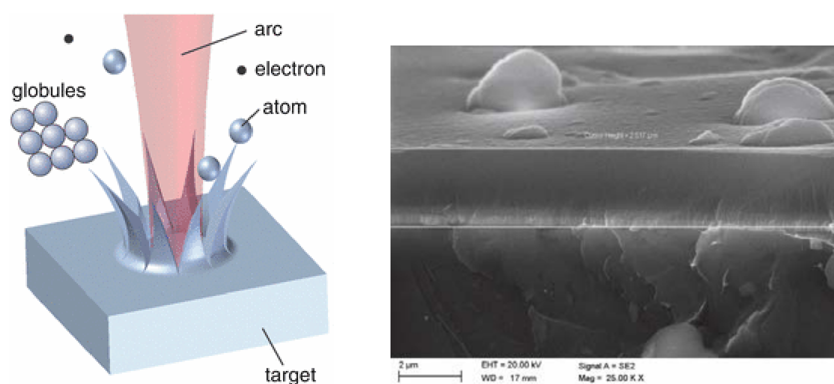

Figure 2.14. SEM analyses of film deposited By CVA [50].

Pulsed excimer lasers such as KrF produce very short, intense energy pulses, which can be used to vaporize materials as an intense plasma (figure 2.15). The plasma tends to extend towards the substrate. The kinetic energy of this expansion gives broad ion energy distributions analogous to CVA. Hence, pulsed laser deposition (PLD) produces ta-C films similar to those from FCVA methods and similar dependencies of the films properties on ion energy are observed. However, costly setup, lack of lateral uniformity of the grown films as well as difficulty in making large area depositions.

Magnetron Sputtering is preferred for industrial applications, including DLC coatings, because of its versatility, its widespread use to sputter many materials, and its ease of scale up. However, it is not suitable for synthesis of dense and sp^3 rich DLC coatings. This is a direct result of the low plasma densities in magnetron sputtering ($\sim 10^{16}$ m^{-3}) as

compared to CVA and PLD (~10^{21} m^{-3}) and thus negligible ionization fraction of the carbon atoms.

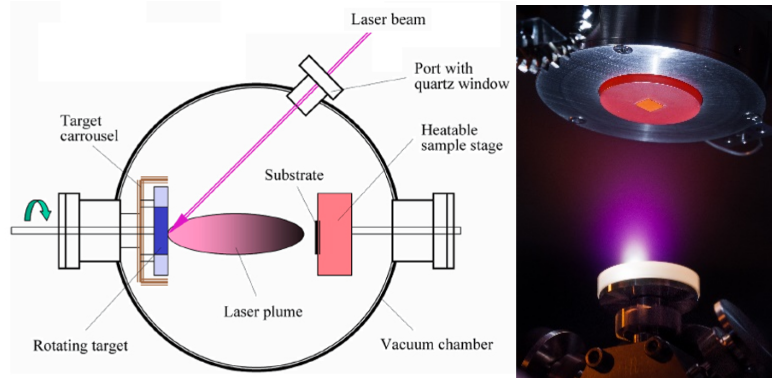

Figure 2.15. Pulsed laser deposition technique.

2.3.4. Carbon ionization in HiPIMS

In magnetron sputtering-based processes, the most common ionization mechanisms of the sputtered species are collisions with energetic electrons (electron impact ionization) and interactions with excited sputtering gas atoms (Penning ionization). The main strategy in HiPIMS to achieve highly ionized fluxes of the sputtered species is to increase the plasma density and, thus, promote the electron impact ionization mechanism. The ionization mean free path, λ_{miz}, is determined by the velocity of the sputtered neutrals, v_s, the plasma density, n_e, and the ionization rate co-efficient, k_{miz}, through the expression [51],

$$\lambda_{miz}=v_s/(k_{miz}n_e) \qquad (2.1)$$

Thus, increasing n_e decreases λ_{miz}, i.e., it increases the ionization efficiency by electron impact. However, the high ionization energy of C and its low cross section for electron impact ionization means that high ionization flux fraction can only be obtained at electron densities above those available even in HiPIMS [44]. As proposed by Aijaz et al. [51], an alternative strategy for enhancing the impact ionization is to increase the rate coefficient k_{miz}. This coefficient is given by,

$$k_{miz}(T_e)=k_0\exp(-E_0/T_e), \qquad (2.2)$$

where k_0 and E_0 are material dependent constants which can be extracted from experiments or computer simulations and T_e is the electron temperature. The electron temperature term, residing in the exponential expression, provides a more efficient means for increasing the ionization probability as compared to linearly dependent n_e. Thus, increasing T_e by substituting Ar by gases with higher ionization energy, such as Neon and Helium, is a possible route to increase C ionization in HiPIMS. Aijaz et al. tested this strategy using Neon [52]. As shown in figure 2.16, the authors found an overall increase of the C^+ ion current with increasing Ne fraction, which clearly demonstrated that the degree of carbon ionization had increased.

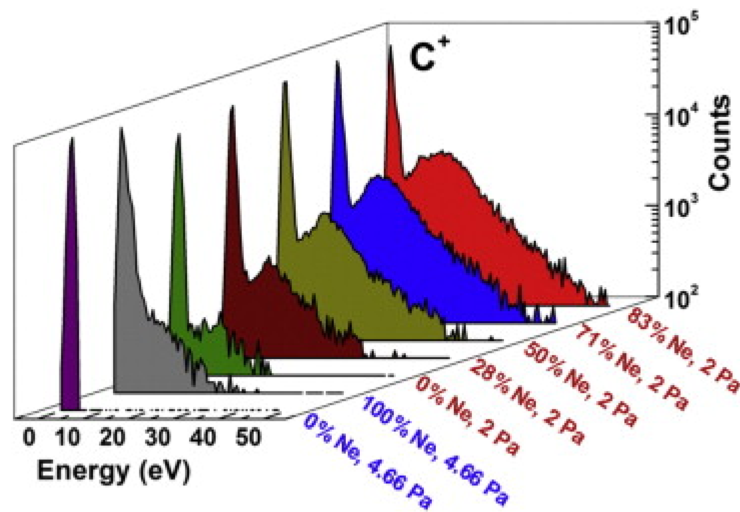

Figure 2.16. The ion energy distributions for carbon ions obtained from different gas composition discharges at the pressures of 2 Pa and 4.66 Pa [52].

Chapter III

3. EXPERIMENTAL

3.1. Introduction

A full account of the experimental conditions used for the deposition and characterization of thin films in the Cr, Ta, CrN and TiSiN systems can be found in the respective papers published in the aim of this work. The main aim of this chapter is to facilitate the analysis and discussion of the results presented in chapters IV to V of this theses. As all the films studied in this work were deposited using the same equipment, a brief description of the configuration and of main characteristics of the deposition chamber used in this work is first given in section 3.2. The most important deposition parameters used for the deposition of the films discussed in chapters IV to V are then collected in sections 3.3, for the metallic deposition systems, and 3.4, for the nitride deposition systems. In each case, the typical waveforms of the voltage and current in DOMS are also presented. Complementary experimental conditions associated to experimental results not published and to film deposition by DCMS were also added, where appropriate. Finally, a detailed account of the experimental conditions used for deposition of C films is given in section 3.5 as the results associated with the deposition of C films by DOMS using a mixed Ar + Ne plasma where not published.

3.2. Deposition chamber

All the films studied in the aim of this work were deposited at SEG-CEMPPRE using a modified commercial deposition chamber from HARTEC. The chamber (figure 3.1) is made of high-grade stainless steel made and has a cubic shape with dimensions of 400 x 400

x 400 mm. The chamber has two cathodes, one with fixed position and one with adjustable position, which are placed along two adjacent walls. The cathodes are water cooled through a set of flexible tubes. Inside the chamber, there is also a shutter, which acts as a barrier between the target and the substrates in order to clean the target before the depositions. The deposition chamber is also fitted with an ion-gun for substrates surface treatment before deposition. All the targets used in this work have the same dimensions (150 x 150 mm and 10 mm of thickness). Only the fixed cathode was used for studying the metal and nitride deposition systems while both cathodes were used for carbon deposition as an adhesion enhancement interlayer was deposited before the carbon films. Both cathodes are at a distance of 8 cm from the substrates. A base pressure lower than $5x10^{-4}$ Pa was achieved before all depositions using a system constituted by a rotary and a turbomolecular pump. The films were deposited by HiPIMS in DOMS mode using a Cyprium™ III plasma generator from Zpulser Inc. (figure 3.2) and by DCMS using a PFG 7500 d.c. power supply from Hüttinger.

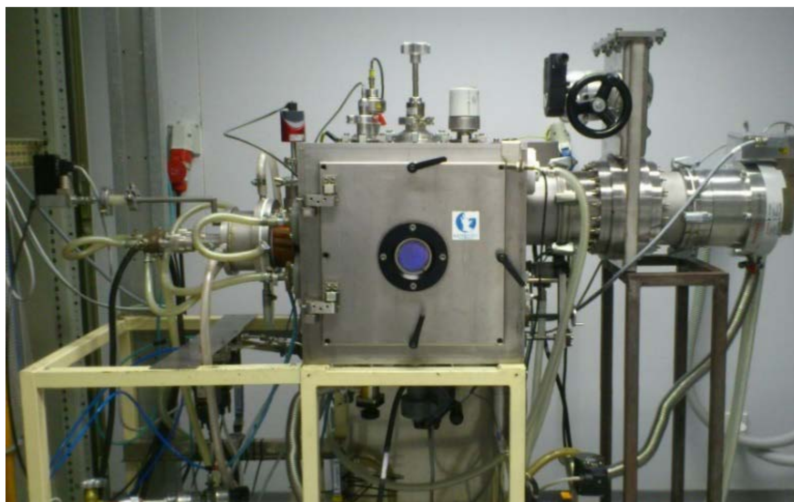

Figure 3.1 Deposition Chamber used in this work.

Figure 3.2. HiPIMS-DOMS power supply.

3.3. Metal systems (Cr and Ta)

3.3.1. Effect of the peak power (Cr and Ta)

The main deposition conditions used for the study of the effect of the Pp on the properties of Cr and Ta films deposited by DOMS, as discussed in section 4.2, are compiled

in table 3.1. Note that in this work the P_p is defined as the maximum value of the V_p x I_p products calculated for each oscillation in a single pulse.

Table 3.1. Deposition conditions for the Cr and Ta films deposited by DOMS.

System	Pressure (Pa)	V_p (V)	I_p (A)	P_P (kW)	P_a (kW)	F_i (Hz)
Cr	0.8	-860	45	39	1.2	310
		-1011	62	63		215
		-1225	83	102		156
		-1314	98	129		117
Ta	0.7	-909	54	49	1.2	271
		-987	66	66		219
		-1084	76	82		180
		-1172	90	105		148
		-1296	101	130		120

Typical voltage and current waveforms corresponding to Cr and Ta films deposited by DOMS and the respective parameters used to drive the DOMS power supply are shown in figure 3.3.

The ion energy distributions (IEDs) of the chromium plasma presented in section 4.2.1 were measured using a combined particle spectrometer combining an energy and mass filter (EQP 300 by Hiden Ltd.) at the Lawrence Berkeley National Laboratory. This equipment can measure up to 1 kV/charge and is differentially pumped by a 70 l/s turbo pump. A chromium target with a diameter of 7.6 cm was mounted in front of the EQP at a distance of 2 cm from the EQP entrance orifice (100 µm diameter). An average target power of 600 W was used for both DOMS and DCMS. The IEDs scans were measured from 0 to 100 V with a step size of 0.5 V and a 1000 ms dwell time. The raw data were corrected for the double charged ions by multiplying the scan voltage by two and dividing the count rate by two to account for the energy bin width and height.

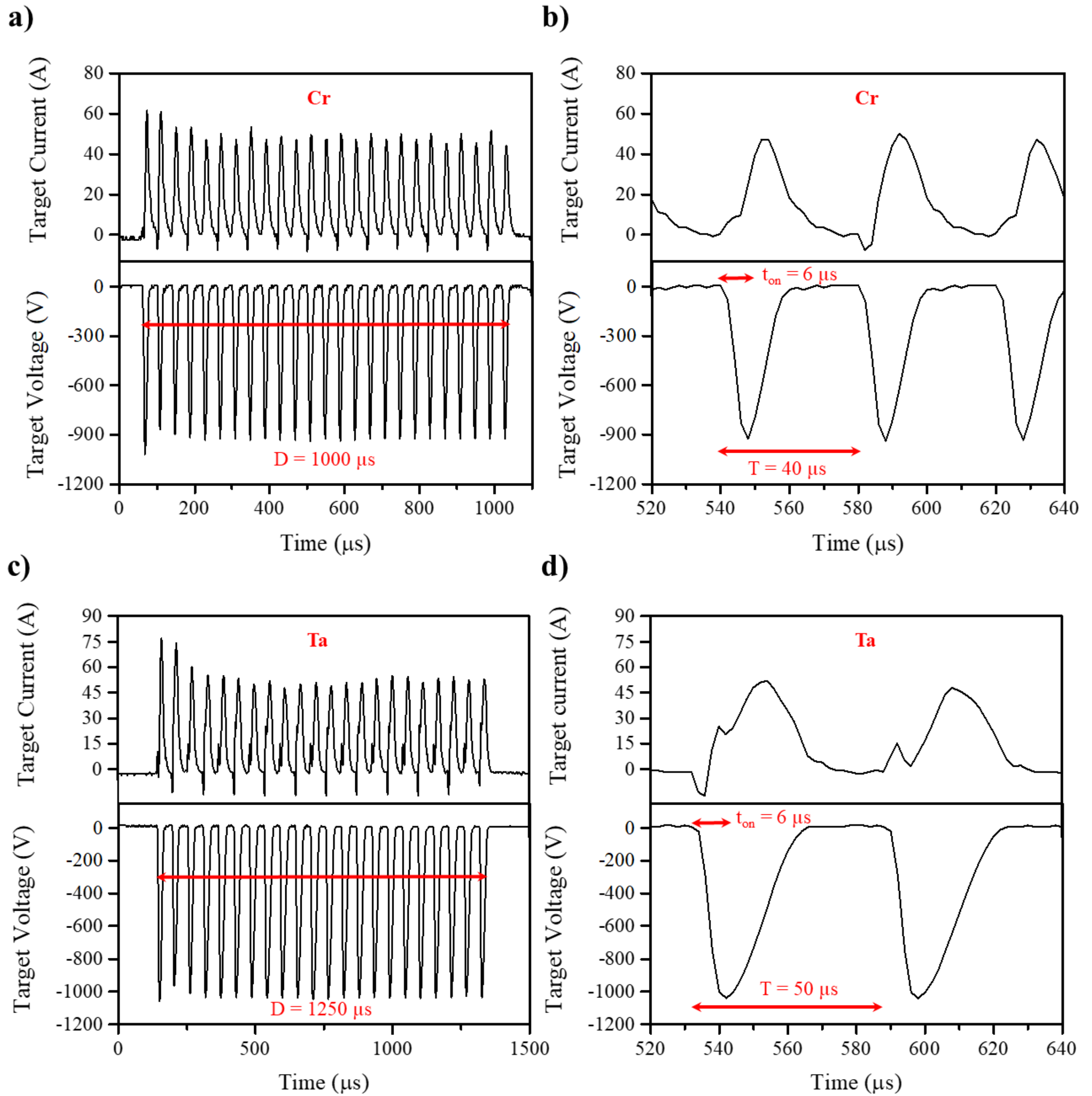

Figure 3.3. Typical I-V waveforms of a DOMS pulse and associated oscillations during a), b) Cr depositions and c), d) Ta depositions.

The main deposition conditions used for the deposition of the reference Ta and Cr films deposited by DCMS, referred in section 4.2, are shown in table 3.2.

Table 3.2. Deposition conditions for the Cr and Ta films deposited by DCMS.

System	Pressure (Pa)	V (V)	I (A)	P_a (kW)	Bias (V)
Cr	0.8	-368	3.41	1.2	-
		-368	3.40		-110
Ta	0.7	-333	3.75	1.2	-30
		-332	3.76		-120

3.3.2. Detailed study of Cr films (Pp and P)

Two series of depositions were carried out in DOMS mode. First Cr films were deposited at deposition pressures from 0.2 to 1.0 Pa at low peak power (Low Pp serie), i.e., by applying a voltage of 300 V to the internal DC power supply of the Cyprium plasma generator. The same procedure was then repeated using a higher peak power, i.e, by applying a voltage of 400 V to the internal DC power supply of the Cyprium plasma generator (High Pp serie). The deposition conditions used for the deposition of the Cr are shown in table 3.3.

Table 3.3. Deposition conditions of the Cr films deposited by DOMS with different deposition pressures.

Regime	Pressure (Pa)	V_p (V)	I_p (A)	P_p (kW)	P_a (kW)	F_i (Hz)
Low P_p (DC_{int} = 300 V)	0.2	-1058	33	35	1.2	236
	0.4	-1006	38	38		217
	0.6	-945	43	41		217
	0.8	-916	50	46		220
	1.0	-899	56	50		216
High P_p (DC_{int} = 400 V)	0.2	-1384	65	90	1.2	124
	0.4	-1290	71	92		118
	0.6	-1241	77	96		119
	0.8	-1164	88	102		117
	1.0	-1183	92	109		116

Typical voltage and current waveforms corresponding to Cr films deposited by DOMS at low and high P_p and the respective parameters used to drive the DOMS power supply are shown in figure 3.4.

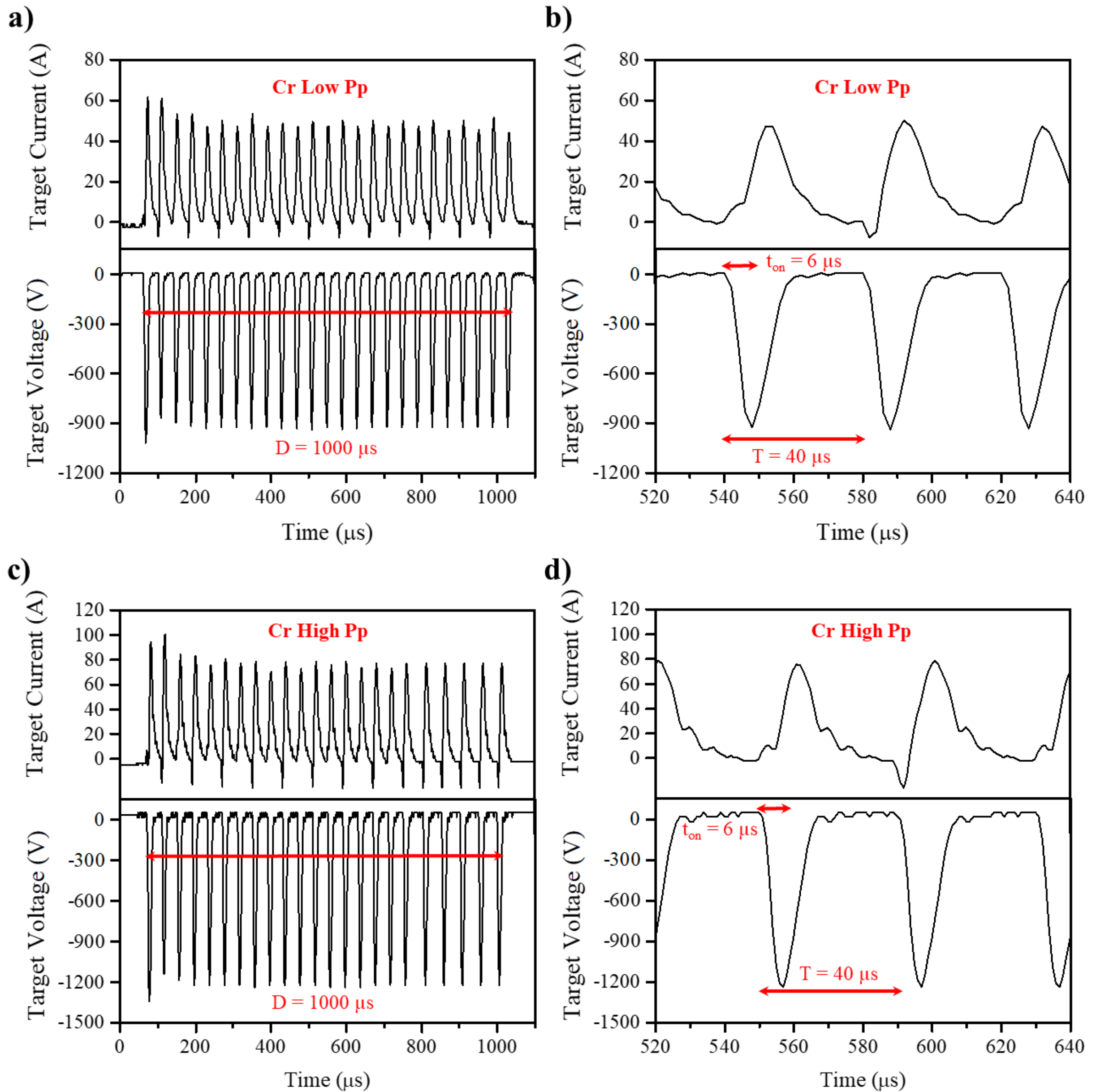

Figure 3.4. Typical I-V waveforms of a DOMS pulse and associated oscillations during), b) Cr films deposition at low P_p and c), d) Cr films deposition at high P_p.

3.4. **Nitride systems (CrN and TiSiN)**

The main deposition conditions used for the study of the effect of the Pp on the properties of CrN and TiSiN films deposited by DOMS, as discussed in section 4.4, are compiled in table 3.4.

Table 3.4. Deposition conditions used to deposit CrN and TiSiN films by DOMS.

System	Pressure (Pa)	V_p (V)	I_p (A)	P_P (kW)	P_a (kW)	F_i (Hz)
CrN	0.7	-773	44	34	1.2	287
		-878	72	63		233
		-940	88	83		194
		-1012	102	103		167
		-1119	129	144		114
TiSiN	0.9	843	31	26	0.8	312
		939	47	44	1	290
		1023	63	65	1.2	312
		1137	90	102	1.2	258
		1247	119	148	1.2	198

Typical voltage and current waveforms corresponding to CrN and TiSiN films deposited by DOMS and the respective parameters used to drive the DOMS power supply are shown in figure 3.5.

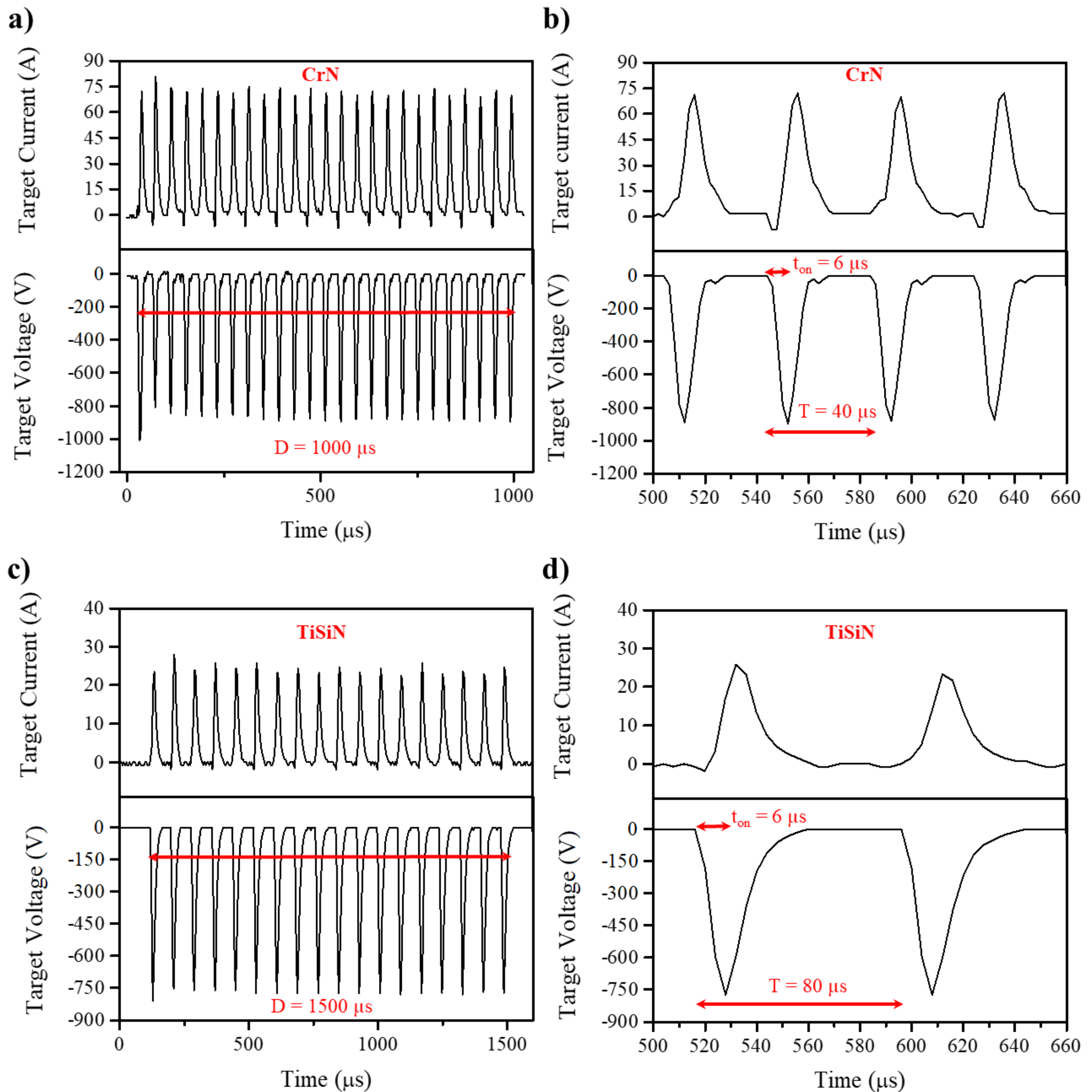

Figure 3.5. Typical I-V waveforms of a DOMS pulse and associated oscillations during of a), b) CrN films depostion and c), d) TiSiN films deposition.

The main deposition conditions used for the deposition of the reference CrN and TiSiN films deposited by DCMS, referred in section 4.4, are shown in table 3.5.

Table 3.5. Deposition conditions for the CrN and TiSiN films deposited by DCMS.

System	Pressure (Pa)	V (V)	I (A)	P_a (kW)	Bias (V)
CrN	0.3	-412	3	1.2	-80
TiSiN	0.3	-415	2.97	1.2	-70

3.5. Carbon system

3.5.1. General experimental conditions

In each deposition, Silicon [100] 1.5 x 1.5 cm and High Speed Steel disc (2.5 cm diameter) are mounted in sample holder. Steel sample were polished with sandpapers in order to reach smooth surface for deposition, then steel and silicon samples were cleaned in a sequence of Acetone and Ethanol ultrasonic bath for 15 minutes each. They were then glued with silver glue (99.9% purity) onto a rotating aluminium substrate holder which revolved at 23.5 rev/min around the central axis of the deposition chamber. Prior to all depositions an etching treatment (using the ion gun) was done in order to increase the film adhesion. The voltage and current used in the ion gun was equal to 36 V and 20 A, respectively. This process was done during 40 minutes by attracting the Ar ions into the substrate using – 120 V of bias. An adhesion enhancing interlayer consisting of a Cr sub-layer and a CrN sub-layer was deposited prior the main DLC layer.

3.5.2. Depositions as a function of substrate bias

The main deposition conditions used for the study of the effect of the substrate bias on the properties of DLC films deposited by DOMS are compiled in table 3.6. All depositions were carried out in pure Ar discharge.

Table 3.6. Deposition conditions for HiPIMS-DOMS DLC coating with different substrate bias.

Pressure (Pa)	V_b (V)	V_p (V)	I_p (A)	P_P (kW)	P_a (kW)	F_i (Hz)
	floating	1400	64	90		250
	-40	1399	63	88		252
0.8	-60	1398	65	91	1.3	251
	-80	1401	63	88		250
	-100	1400	66	92		253

Typical voltage and current waveforms corresponding to DLC films deposited by DOMS and the respective parameters used to program the DOMS power supply are shown in figure 3.6.

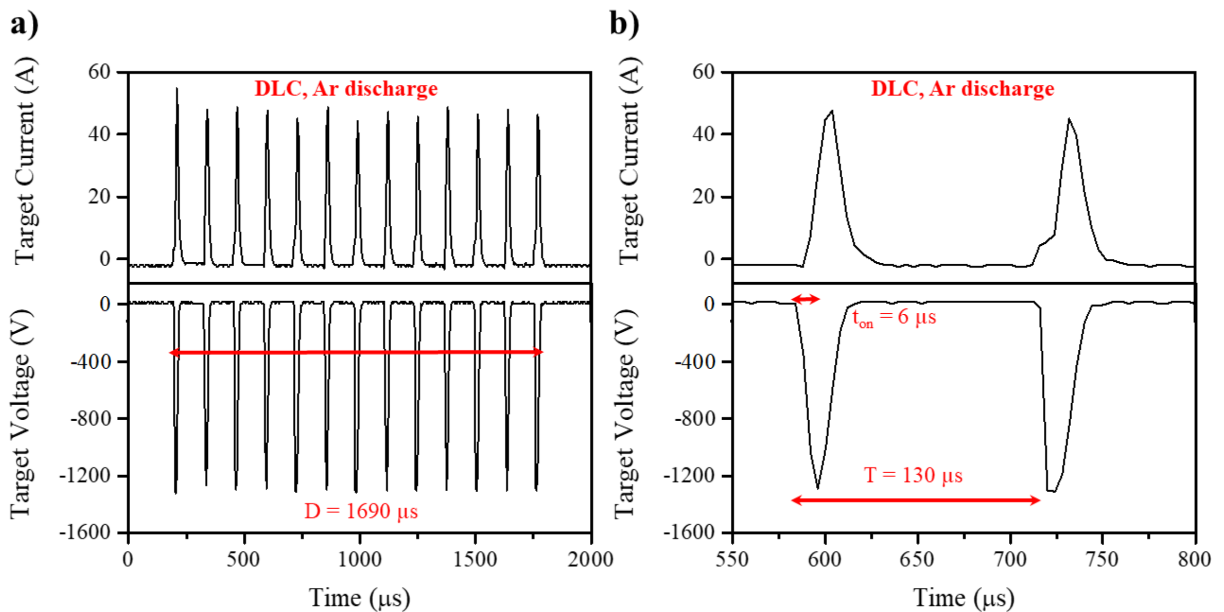

Figure 3.6. a) The target voltage and current oscillation waveforms measured during the DLC coatings depositions. b) Oscillations within a pulse.

3.5.3. Depositions as a function of Ne content in the gas

The effect of adding Ne to the discharge gas was studied by depositing several DLC coatings using different Ne contents in the plasma. The films deposition conditions are shown in table 3.7. Neon gas was gradually introduced in the deposition chamber while the Argon flux was reduced to keep the deposition pressure at 0.8 Pa.

Table 3.7. Deposition conditions for HiPIMS-DOMS DLC coating with different Ne content.

Pressure (Pa)	V_b (V)	Ne (%)	V_p (V)	I_p (A)	P_P (kW)	P_a (kW)	F_i (Hz)
	-80	0	1401	63	88		250
	-80	11	1396	70	98		253
0.8	-80	25	1398	72	101	1.3	254
	-80	36	1395	78	109		252
	-80	50	1395	80	112		250

Typical voltage and current waveforms corresponding to DLC films deposited by DOMS in mix Ar-Ne discharge and the respective parameters used to program the DOMS power supply are shown in figure 3.7.

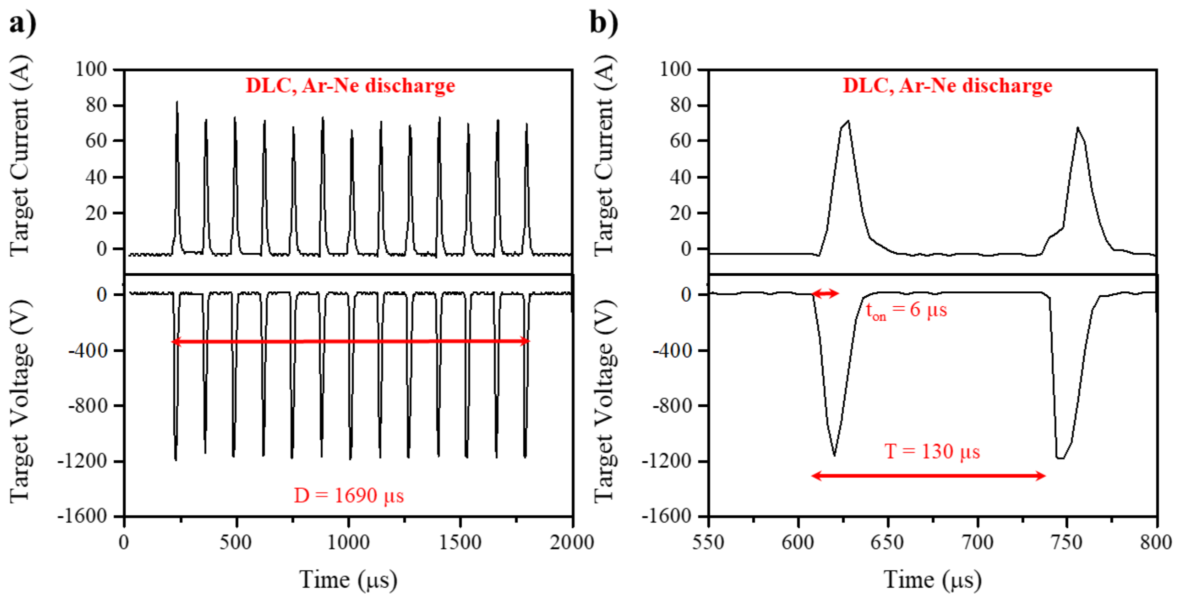

Figure 3.7. a) The target voltage and current oscillation waveforms measured during the DLC coatings depositions in Ar-Ne discharge. b) Oscillations within the pulses.

3.5.4. Experimental conditions for the tribological characterization

The tribological tests were carried out using a pin-on-disc setup (homemade) in ambient air as shown in figure 3.8. All coatings were deposited on AISI M2 Steel disc and tested with 100Cr6 counterbody machined as a ball with a diameter of 8 mm. The friction coefficient was measured during the sliding tests using a load-cell and the results were transferred to a computer. All tests were carried out with a normal load of 1 N and a distance of 200 m. The wear of the ball was evaluated by scanning electron microscopy (SEM). More experimental conditions are shown at table 3.8.

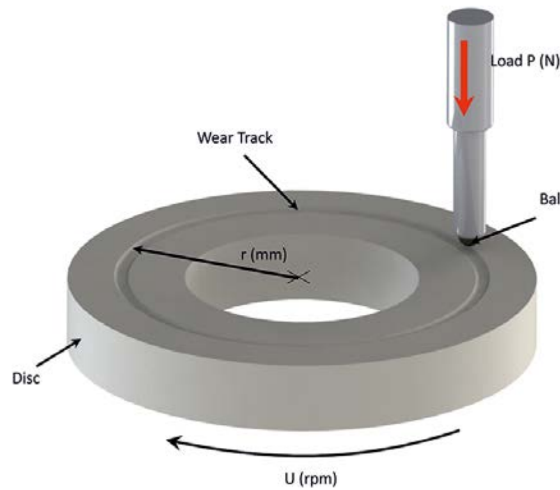

Figure 3.8. Pin on Disc scheme used for measurement of friction for DLC films with different substrate bias.

Table 3.8. Experimental conditions for pin-on-disc.

Normal Load (N)	Rotation Speed (RPM)	Frequency of data acquisition (Hz)	Ball material	Relative humidity (%)	Temperature (ºC)	Rotation radius (mm)
1	136	10	100Cr6	65	26	7

Chapter IV

4. COMPARISON OF DOMS ACROSS DIFERENT DEPOSTION SYSTEMS

4.1. Introduction

As referred in the introduction, two metallic (Cr and Ta) and two metal nitride deposition systems (TiSiN and CrN) have been studied in this work. For each system, the microstructure, the structure and the mechanical properties of the films deposited by DOMS were characterized and compared with those of reference coatings deposited by DCMS. Detailed results and analysis about each individual system have been published and the corresponding papers are available as annexes in this thesis. The main aim of the present chapter is to develop a more general understanding of the DOMS process by performing a comparative study of the deposition system studied in this work. For this purpose, the results obtained by DOMS for the two metallic systems as well as those obtained for the two metal-nitride systems are compared and discussed. As the effect of the peak power on the films properties has been systematically studied in all the deposition systems under consideration, this process parameter is used in this chapter as a probe to compare the different deposition systems.

The metallic deposition systems, Cr and Ta, are discussed in the second section of the chapter. The microstructure, structure and mechanical properties of the films deposited by DOMS in each metallic system are compared to each other and to corresponding reference films deposited by DCMS. New results, not previously published, regarding the plasma analysis by EMRS of the Cr plasma were incorporated in this section in order to achieve a more complete comparison between the two metallic systems. A more comprehensive study of the properties of Cr films deposited by DOMS,

including the study of the effect of the deposition pressure in addition to the peak power, is presented in the third section of this chapter. This study was motivated by the results presented in the second section of this chapter and aimed at a detailed characterization of the anisotropy of the Cr films surface morphology. Finally, the comparison of the two metal-nitride systems is performed in the fourth section of the chapter based on the results already published individually for each system. The evolution of the microstructure, structure and mechanical properties with the peak power are directly compared and discussed.

4.2. **Metallic deposition systems (Cr and Ta)**

This section aims at comparing both the plasmas generated in DOMS and DCMS during sputtering of Cr and Ta targets and the properties of the resulting films. In the first part of the section, the IEDFs obtained by ERMS from the DCMS plasma and from two conditions representative of the DOMS plasma at low and high peak power are analyzed. The experimental setup and conditions used to generate the IEDFs are presented in details in paper Ta01 for the Ta system and section 3.1.1 for the Cr system. In the second part of the section, the evolution of the deposition rate, microstructure and the mechanical properties of the deposited films as a function of the peak power are studied. The experimental system and the experimental parameters used to deposit the films are presented in papers Cr01 and Ta01. In order to facilitate the reading of this section, the main experimental parameters used to deposit the Cr and Ta films are also listed in section 3.1.1.

4.2.1. Plasma analysis

The time averaged ion energy distributions (IEDFs) for Cr^{+}, Cr^{2+}, Ta^{+}, Ta^{2+}, Ar^{+} and Ar^{2+} ion species obtained from DCMS and DOMS plasmas with different peak powers during Cr and Ta sputtering are displayed in figure 4.1. All the IEDFs reveal only a narrow low energy peak for Ar^{+} centred near 5 eV corresponding to thermalized Ar^{+} ions after being accelerated over the sheath from the plasma to the EQP collecting orifice. The energetic position of the peak corresponds to the plasma potential. Lin et al. found a similar result for a MPPMS discharge [53]. The Ar^{2+} IEDFs also exhibit a low energy peak corresponding to thermalized ions. As expected the low energy peak is located at higher energy (close to 10 eV) and it is close to twice broader than for Ar^{+} due to the higher charge of the Ar^{2+} ions. The IEDFs of the Ar^{2+} ions in DOMS exhibit an additional high energy tail with increasing maximum energy (from around 30 to 48 eV) with increasing peak power. Hecimovic et al. observed that the Ar^{2+} IEDF in their system (HiPIMS) with a Cr target consisted of high energy ions (up to 25 eV) during the HiPIMS pulse whereas only a low energy Ar^{2+} peak was noticed in post-discharge conditions [54]. The authors suggested that the high energy Ar^{2+} ions were possibly generated through collisions with high energy Cr ions. Momentum transfer through collisions with either the highly energetic Cr or Ta species could also explain the high energy Ar^{2+} ions generated within the DOMS discharge. Note, nevertheless,

that the energy of the vast majority of the Ar^{2+} ions is within the low energy peak and thus that energetic Ar^{2+} ions only have small influence on the film growth in both systems.

Both Cr^{+} and Ta^{+} IEDFs in DCMS show a low energy peak centered close to 6 eV. As for Ar, this peak originates from the thermalized ions after acceleration in the substrate sheath. Additionally, both distributions also display an additional high energy tail which extends up to 28 eV and 20 eV for Cr and Ta, respectively. The energy distribution of the sputtered atoms follows a Thompson distribution upon leaving the target, with a most probable value of only a few electrons volts and a high energy tail [55]. The high energy tails in the Cr^{+} and Ta^{+} IEDFs in DCMS derive from the high energy tail in the original Thompson distribution of neutral sputtered atoms [55]. Note however that, after ionization, the energy distribution of the ions is modified by interactions with the electric field of the target sheath, by collisions in the gas phase and finally trough acceleration over the sheath at the EQP collecting orifice.

The IEDFs of the singly charged metal ions found in DOMS also consist of a low energy peak corresponding to the thermalized ions (centered close to 6 eV) and a high energy tail. However, the high energy tail extends to much higher energies than for the IEDFs obtained in DCMS. The maximum energy of the Cr^{+} ions reaches 60 eV at low peak power (28 kW) and 70 eV at high peak power (129 kW). On the other hand, the maximum energy of the Ta^{+} ions is 65 eV regardless of peak power. In both cases, the number of metal ions decreases by one order of magnitude with increasing the peak power. The DOMS discharge produces highly energetic singly charged metal ions with much higher energies than those generated in DCMS and MPPMS discharges [53]. This effect is partly caused by the larger cathode sheath voltage which develops in DOMS as the higher energy of the Ar^{+} ions bombarding the target will translate to higher average energy of the sputtered atoms. Nevertheless, the origin of the energetic metal species produced by HiPIMS is still an open issue [28]. Anders et al. suggested that ionization zones in HIPIMS are zones of locally enhanced potential, integrating double layers which result in potential humps that might explicate the relatively high energy of the ions at the substrate [34]. Furthermore, Maszl et al. concluded that energetic Ti^{+} ions are generated in the spokes region and then accelerated inside the double layers nearby the spoke [28]. A similar mechanism could also explain the highly energetic singly charged metal ions created by the DOMS discharges in this work. The doubly charged metal ions in DCMS exhibit a peak at 8 eV and a tail extending up to 35 eV and 25 eV for Cr and Ta, respectively. In both cases, the amount of doubly charged metal ions is much lower than the singly charged metal ions. In the DOMS discharge the

Ta^{2+} IEDF exhibits a peak close to 10 eV and a tail extending to even higher energy than for the Ta^{+} ions, i.e., reaching 95 eV at low peak power (37 kW) and 120 eV at high peak power (114 kW). Furthermore, at high peak power the amount of Ta^{2+} ions is larger than the amount of Ta^{+} ions. The Cr^{2+} IEDF at low peak power (28 kW) exhibits a similar maximum energy (60 eV) as for the Cr^{+} ions, while increasing the peak power to 129 kW results in a much higher energy tail reaching up to 105 eV.

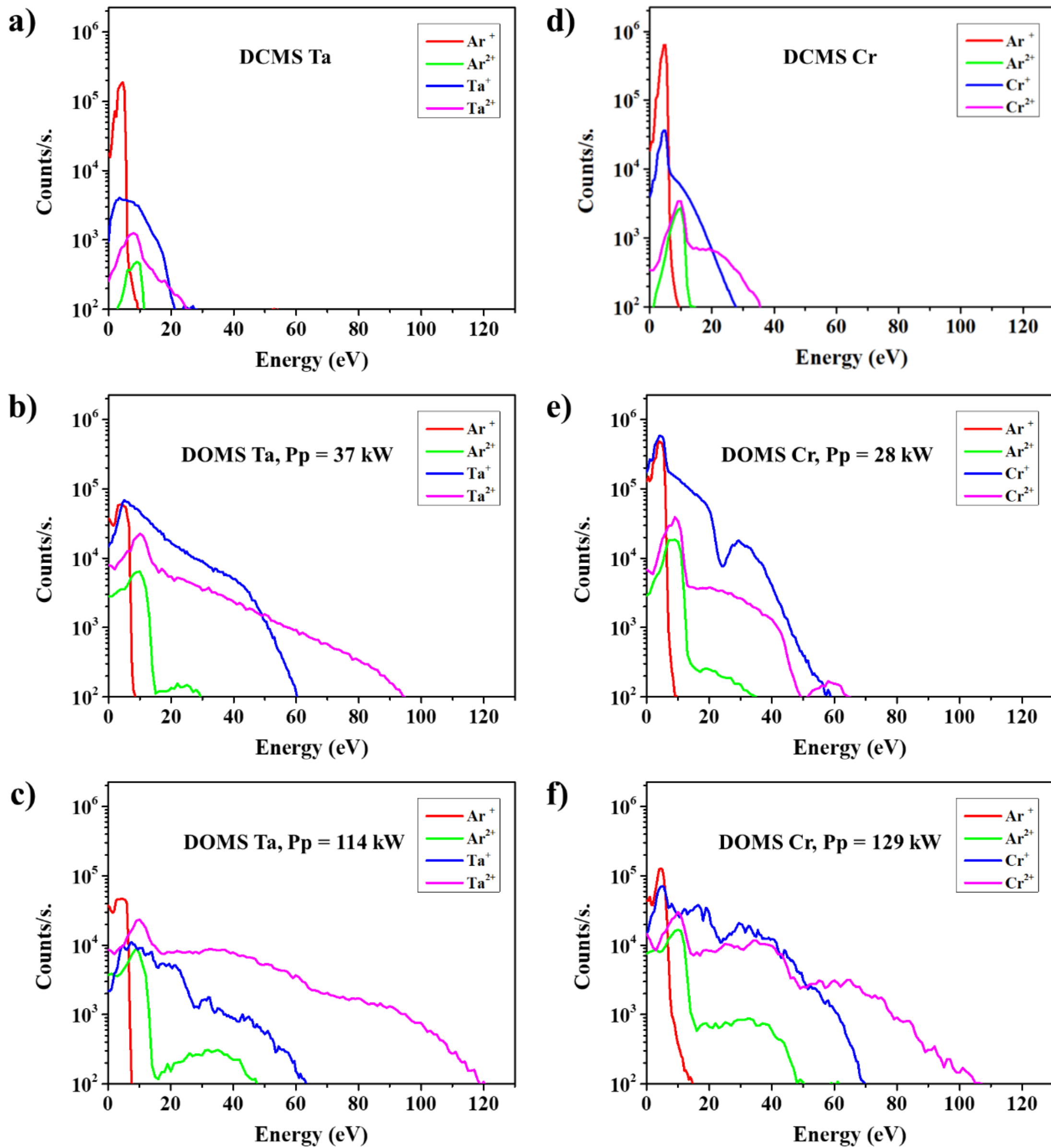

Figure 4.1. Ion energy distributions (IEDs) of Ar^{+}; Ar^{2+}; Ta^{+} and Ta^{2+} species measured from a) DCMS and b), c) DOMS plasma with different peak powers during sputtering a Ta target in pure Ar atmosphere. Ion energy distributions (IEDs) of Ar^{+}; Ar^{2+}; Cr^{+} and Cr^{2+} species measured from d) DCMS and e), f) DOMS plasma with different peak powers during sputtering a Cr target in pure Ar atmosphere

The DCMS plasma is dominated by gas ions, which account for 88% of the ion flux in the Cr system and 91% in Ta system. On the other hand, the DOMS plasma is dominated by metal ions which account for between 62 and 77% of the ion flux regarding the system and the peak power used. As expected many more metal ions are generated in DOMS than in the DCMS. During a DOMS deposition the growing film will be under intense and energetic bombardment of metal ions while in DCMS most of the ions reaching the substrate are process gas ions with much lower energy.

At low peak power (28 kW for Cr and 37 kW for Ta) more metal ions are generated in Cr system than in the Ta system. However, the inverse is observed at high peak power. Furthermore, the Ta system at high peak power (114 kW) is the only regime where the double charged metal ions have the major contribution to the metal ion flux.

4.2.2. Films properties

The deposition rate of the Cr and Ta thin films deposited by DOMS is shown in figure 4.2. The deposition rate was calculated for both systems by dividing the film thickness (measured by SEM) by the deposition time. For both systems, the deposition rate decreases with increasing peak power. In the Cr system, an increase of the peak power by a factor of three results in a loss of 49 % in deposition rate. The deposition rate of the Ta films deposited by DOMS shows a similar trend (43 % loss) with increasing peak power as was observed for the Cr films, although with a shift to lower deposition rates. Increasing the peak power in the DOMS discharge simultaneously increases I_p and V_p, i.e., simultaneously increases the ionized fraction of the sputtered material and the energy of the sputtered species bombarding the film. It is well established in the literature that increasing the fraction of ionized sputtered flux results in a loss of deposition rate due to increasing metallic ion back-attraction to the target ("return effect") [12]. Moreover, the increase of V_p with increasing peak power also contributes to the loss of deposition rate due to the sub-linear evolution of the sputtering yield with discharge voltage ("yield effect") [56].

Depending on the peak power, the deposition rate of the Cr films deposited by DOMS lies between 38 and 74 % of the deposition rate of the Cr film deposited by DCMS with a substrate bias of – 110 V (66 nm/min). On the other hand, the deposition rate of the Ta films deposited by DOMS lies between 36 and 63 % of the deposition rate of the Ta film deposited by DCMS with a substrate bias of – 120 V (44 nm/min.). The loss of deposition rate in

DOMS/HiPIMS, as compared to DCMS, is well documented in the literature and several possible causes have been identified. Besides the "return effect" and the "yield effect" already mentioned above, Panjan et al. and Franz et al. also described an increased flux of the sputtered species sideways, i.e., to higher angles with respect to target surface normal in HiPIMS than in DCMS [57, 58].

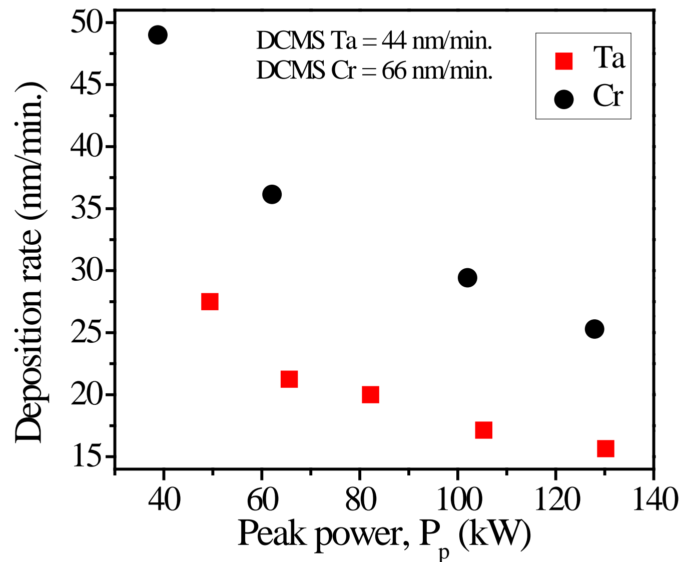

Figure 4.2. Deposition rate of the Cr and Ta films deposited by DOMS as a function of peak power (Pp).

The cross-section and surface morphology of Cr and Ta thin films deposited by DOMS, as well as those of a Cr film deposited by DCMS without substrate biasing and a Ta film deposited by DCMS with a – 30 V bias, are displayed in figure 4.3. Both DCMS films show well-developed columns extending from the substrate to the top of the film with dome-like endings on the film surface (figure 4.3 a) and e)). The well-defined columnar microstructure of the films is characteristic of deposition regimes under the influence of the atomic shadowing effect. The surface morphology of the Cr films is anisotropic as the column tops are preferentially elongated along a direction perpendicular to the rotation direction. In this work, the Cr films were deposited using a rotating substrate holder which introduces a geometrical anisotropy in the deposition configuration. As a result, more atoms will impinge on the substrate at shallow angles in the substrate rotation direction than in the perpendicular direction. Therefore, the shadowing effect is more intense in the rotation direction, giving rise to anisotropic surface morphologies as well as anisotropic stresses in the plane of the film [59, 60]. This effect is not observed for the Ta films deposited by

DCMS.

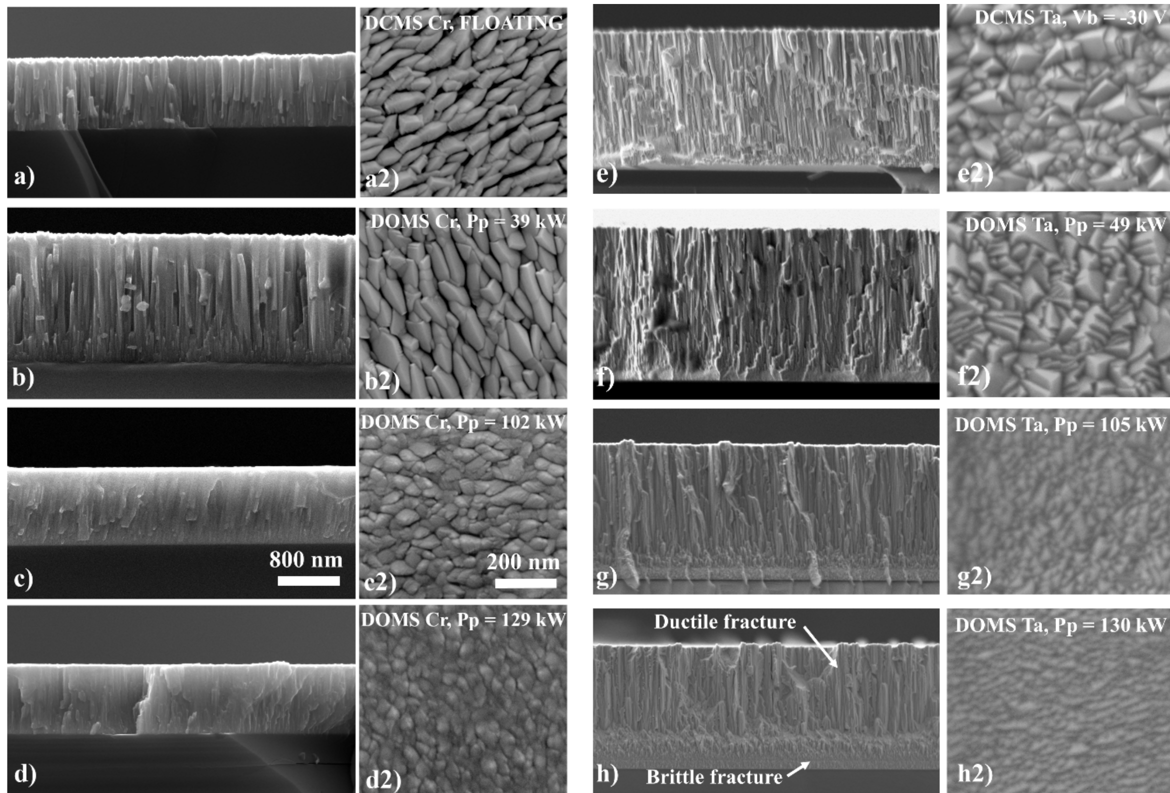

Figure 4.3. SEM cross-section and surface micrographs of the a) to d2) Cr and e) to h2) Ta thin films deposited by DCMS and DOMS.

The DOMS films deposited with the lowest peak power show a columnar growth, with columns also extending from the bottom to the top of the film, although the Ta film exhibit a more compact microstructure. The surface of the Cr film is still anisotropic as was already observed for the Cr films deposited by DCMS. The surface of the Ta film displays dense, regularly spaced grain facets similar to the ones described by Ren et al. [61].

Increasing the peak power in the Cr system results in the deposition of more compact microstructures. The well-defined columnar microstructure obtained at the lowest peak power is progressively replaced by a featureless one, while the dimensions of the surface features decreases significantly. Furthermore, the surface morphology is much less anisotropic than at lower peak powers. Increasing the peak power in the Ta system also results in a significant decrease of the surface features of the Ta films. However, the cross-section micrographs still reveal a well-defined columnar growth similar to the ones observed in the Ta films deposited with the lowest peak power. The cross-section micrograph of Ta film deposited at the highest peak power reveals two different types of fracture, the lower

part of film (close to the substrate) displays a brittle fracture whereas the upper part displays a ductile fracture. Myers et al. obtained a similar result in Ta films deposited by MPPMS and associated these different fractures types to the existence of different Ta phases [62].

Figure 4.4 shows the hardness of the DOMS Cr and Ta films deposited at different peak powers. The hardness of the Cr films deposited by DOMS increases with increasing peak power from 9.8 GPa to 17.7 GPa. This result is due to the increasing fraction of ionized Cr species generated with increasing peak power and the consequent increase of bombardment during film growth (Cr01). This effect is even more pronounced at higher peak power as a larger number of energetic Cr^{2+} ions are produced (see figure 4.1). On the contrary, the hardness of the Ta films remains constant (close to 11.5 GPa) up to 105 kW and only slightly increases to 12.7 GPa at the highest peak power.

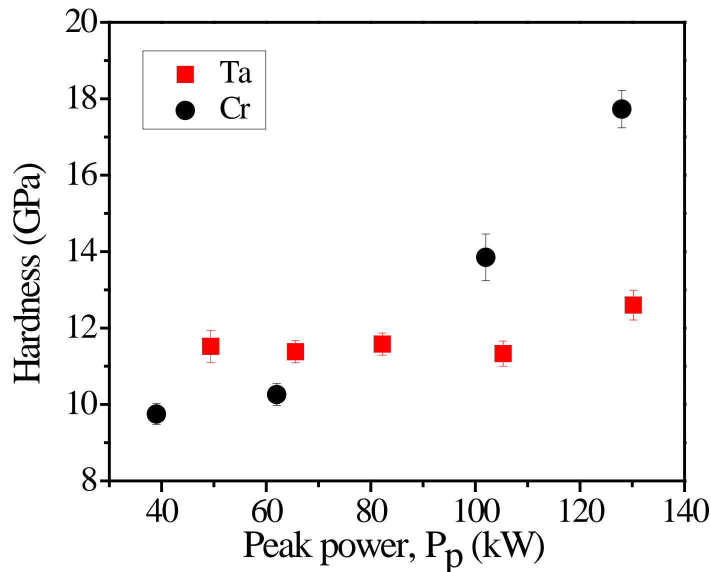

Figure 4.4. Hardness of the Cr and Ta thin films deposited by DOMS.

This last result agrees well with the phase composition of the Ta films as observed by X-ray diffraction (Ta01). The higher hardness of the film deposited at the highest peak power results from the co-deposition of both the α-Ta and β-Ta phase while at lower peak powers only the softer α-Ta is deposited.

Figure 4.5 shows the Young´s modulus of the DOMS Cr and Ta films deposited at different peak powers. The Young´s modulus referred in literature for bulk Cr and Ta are equal to 279 and 200 GPa, respectively. The Young's modulus of the deposited films is independent of the peak power as all the films have a Young's modulus close to the value

referred in the literature for bulk material. Lintymer et al. reported that the Young's modulus of sputtered Cr films increases with decreasing porosity following a perfect mixture rule [63]. Therefore, this result shows either for Cr or Ta system, bombarding the growing film with metal ions allows a complete elimination of the porosity in the film, i.e., overcoming the shadowing effect.

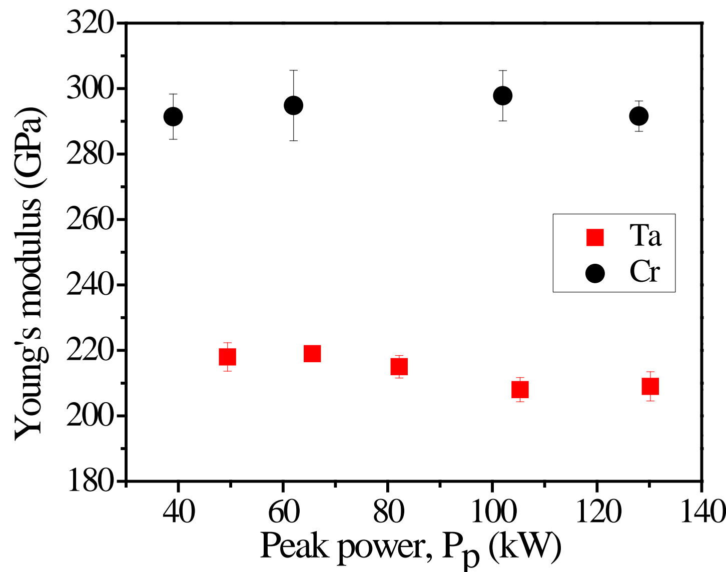

Figure 4.5. Young's modulus of the Cr and Ta thin films deposited by DOMS.

The properties of the Cr films deposited by DOMS show a clear correlation with the peak power used during the deposition process. Both the microstructure and the hardness of the films continuously change with increasing peak power, which is consistent with the deposition of more compact films as the peak power is increased. This correlation shows that the properties of the Cr films are mostly determined by the bombardment of the sputtered species during film growth. On the contrary, the properties of the Ta films deposited by DOMS are much less influenced by the peak power. Although the surface morphology of the films evolves in a similar fashion as for the Cr films, both the deposited columnar microstructure and the hardness of the Ta films remain almost unchanged as the peak power is increased. These results suggest the existence of one or more deposition mechanisms operating in parallel with the bombardment of the sputtered species, which mask the effect of the latter on the film properties. Such a mechanism could be, for example, the bombardment of the film with energetic Ar atoms resulting from the backscattering of Ar^+ ions upon impinging on the target. The subplantation of such energetic Ar neutrals during

film growth could explain the contrast between the evolution of the bulk properties of the films and the evolution of their surface morphology with increasing peak power.

As stated in the introduction, one of the main objective of this work was to understand the new deposition mechanisms that the DOMS technology brings about. As the ionization of the sputtered species is the main differentiating feature of the DOMS process in comparison to the DCMS, and as the Cr films properties are much more sensitive to the peak power that the Ta ones, the Cr system was selected for further investigation. In the following section the influence of the peak power on the properties of Cr films deposited by DOMS using different deposition pressures is studied and compared with their DCMS counterparts.

4.3. Systematic study of the Cr system

As shown in the previous section, the effect of the peak power on the properties of Cr films is a good proxy to investigate the effect of the ionization of the sputtered species in DOMS. In this thesis a systematic study of the properties of Cr films deposited by DOMS was carried out not only as a function of the peak power but also as a function of the deposition pressure, one of the most influential deposition parameters in DCMS. This investigation aimed at identifying and understanding the additional features specific to DOMS in comparison to DCMS, i.e., those that result from the ionization of the sputtered species. Therefore, for comparison purposes, Cr films deposited by DCMS with and without substrate biasing were also included in this investigation.

The first part of the systematic study of the Cr deposition system focused on the films surface properties and their evolution with both the peak power and the deposition pressure. The films surface was thoroughly investigated by SEM and AFM and the obtained results were published in paper Cr02. The main conclusions originating from this work are summarized in the first sub-section of this section. The second sub-section is concerned with the bulk properties of the Cr films and their evolution with the peak power and the deposition pressure. Both the DCMS and DOMS films were characterized with respect to their structure, as determined by X-ray diffraction, and their mechanical properties. This section ends with a discussion of the relation between the surface and the bulk properties of the films.

4.3.1. Surface properties

As seen in the Annex E (paper Cr02) and summarized here, all of the deposited DCMS Cr films (with or without bias) have a columnar microstructure. On the overall, the surface morphology (without bias) is anisotropic since most of the voids channels are preferentially oriented along the same direction. The microstructure of the Cr films deposited with bias is similar to the microstructure of the films deposited without bias at low pressure. Although the overall anisotropy of the surface remains mostly unchanged, bombarding the substrate with Ar ions results in slightly thinner columns separated by thinner valleys of voids. These kind of microstructures have been described in the literature for Cr films deposited by magnetron sputtering. On the other hand, the Cr films deposited by DOMS at low (pressures below 0.6 Pa) and high Pp (all pressures) presents a much denser columnar

microstructure. The surface of the films is isotropic and consists of fine and highly compacted features.

The surface roughness (in Annex E) of the films deposited by DCMS with and without bias increases significantly with increasing pressure. This is consistent with the formation of deeper grooves and higher hills on the films surface, as observed by SEM analyses, due to the increasing strength of the shadowing effect. Bombarding the growing film with argons ions extracted from the plasma and accelerated at -80 V only has a small influence on the surface roughness, excepting for the films deposited at 1.0 Pa. The surface roughness of the films deposited by DOMS is much lower and much less influenced by the deposition pressure than that of the films deposited by DCMS. This is more evident at high deposition pressures, showing that the shadowing effect is effectively counterbalanced and/or prevented both at low and high Pp. On the other hand, increasing the peak power decrease the surface roughness at all deposition pressures.

The surface properties of all films deposited by DCMS are governed by the atomic shadowing effect. Although both the deposition pressure and the substrate bias have some influence on the film surface properties, allowing to deposit smoother films by decreasing the former and increasing the latter, all the films present a surface morphology consisting of well-defined pyramidal-like features resulting from the shadowing effect. On the contrary, most of the films deposited by DOMS have a globular or featureless surface morphology, which indicates a much lower influence of the atomic shadowing effect or even no influence at all. The only exceptions are the films deposited at high pressure (0.8 and 1.0 Pa) which still display a surface morphology consisting of pyramidal-like shapes. However, these two films have a much lower surface roughness than all the films deposited by DCMS, similar to the remaining Cr films deposited by DOMS. On the overall, the surface properties of the films clearly distinguish the films deposited by DCMS from those deposited by DOMS and show that a significant reduction of the atomic shadowing is achieved in DOMS.

4.3.2. Bulk properties

The deposition rate of the Cr films deposited by DCMS without substrate biasing increases exponentially with increasing deposition pressure (figure 4.6). In Annex E, the deposition of Cr thin films by DCMS was simulated using the SRIM and SIMTRA software

packages. The simulation results showed that the total amount of Cr species arriving at the substrate should decrease by almost 15 % with increasing pressure from 0.2 to 1.0 Pa. It is well known that the deposition of metallic thin films at relatively high pressure results in the formation of porous films with interconnected void channels due to the shadowing effect. For example, Drüsedau et al. have shown that in the case of W deposition the film density is only weakly dependent on pressure up to a critical pressure (1.3 Pa) and then decreases with the logarithm of pressure [64]. As Cr is a lighter element than W, porous films should be deposited at even lower pressures than for W. Lintymer et al. [63] have shown that porosity is the dominant microstructural feature influencing the Young's modulus of sputtered Cr thin films. All the Cr films deposited by DCMS without substrate biasing have a much lower Young's Modulus than the bulk material (280 GPa) as shown in figure 4.7. Furthermore, the Young's modulus decreases with increasing pressure thus confirming that the exponential increase of the deposition rate is due to a corresponding increase of the Cr films porosity.

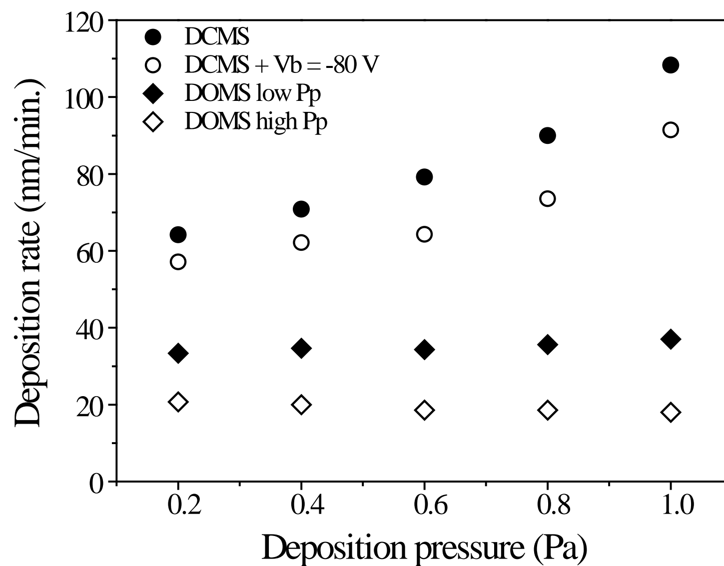

Figure 4.6. Deposition rate of the Cr films deposited by DCMS without and with substrate bias and by DOMS at low Pp and high Pp at different deposition pressures.

The deposition rate of the films deposited by DCMS with a substrate bias of – 80 V shows a similar trend with increasing pressure as was observed for the unbiased films, although with a shift to lower deposition rates (figure 4.6). On the other hand, applying a substrate bias increases the Young's modulus of the films at all pressures by an average of

30 GPa (figure 4.7). However, the maximum Young's Modulus value (260 GPa) is still lower than the value of the bulk material while the Young's modulus decreases with increasing pressure as for the unbiased films. Porous films are still deposited even with substrate biasing showing that the films properties are still dominated by the shadowing effect. The exponential-like increase in the deposition rate with increasing pressure is no longer observed for the two series of Cr films deposited by DOMS (figure 4.6). The deposition rate of the films deposited with low Pp is almost constant between 0.2 and 0.6 Pa while their Young's modulus is similar to the value of the bulk material (figure 4.7). These results show that almost porosity-free Cr films are deposited. The deposition rate slightly increases above 0.6 Pa while the Young's modulus decreases showing that at higher pressure the Cr films are no longer porosity-free. However, the Young's modulus of the Cr films deposited above 0.6 Pa is higher than that of the films deposited by DCMS and is in fact similar to the Young's modulus of the films deposited by DCMS with bias at lower pressure. All the films deposited by DOMS at high Pp have bulk-like young's modulus while their deposition rate slightly decreases with increasing pressure as was predicted by the simulations of the deposition process. Fully porosity-free films are deposited by DOMS at high Pp irrespectively of the deposition pressure.

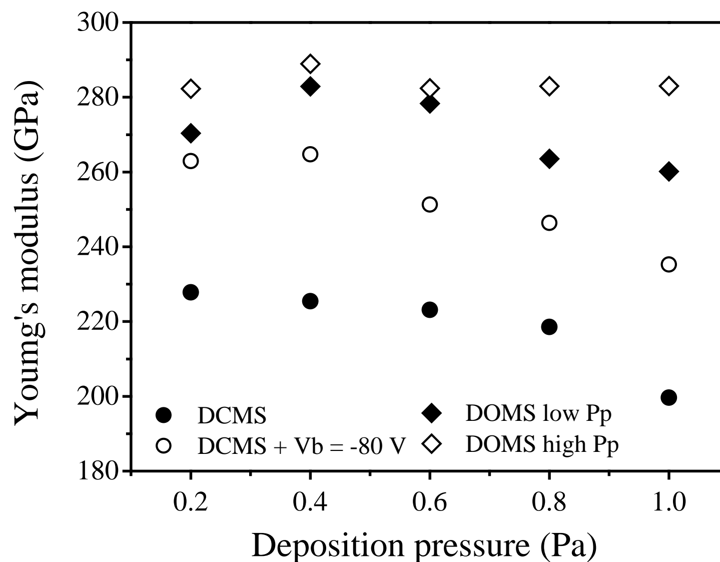

Figure 4.7. Young Modulus of the Cr films deposited by DCMS without and with substrate bias and by DOMS at low Pp and high Pp at different deposition pressures.

The XRD patterns of the Cr films deposited by DCMS and DOMS are shown in figure 4.8 as a function of the deposition pressure. All the XRD peaks could be indexed to the b.c.c. Cr phase. The Cr (110) and/or (222) peaks are dominant in all the diffractograms although low intensity (211) and (220) were also detected. The (110) diffraction peak is the most intense peak in the diffraction patterns of the films deposited by DCMS with and without bias up to 0.6 Pa. The peak intensity decreases with increasing pressure while the intensity of the (222) diffraction peak, which appears at 0.4 Pa and 0.8 Pa in the films deposited with and without bias, respectively, follows the opposite trend. The (110) peak is also the most intense diffraction peak in the diffractograms of the Cr films deposited by DOMS at low Pp. In fact the (111) peak is only detected in the diffractograms of the films deposited at higher pressures. The (110) peak is the only diffraction peak detected in all the diffractograms of the films deposited by DOMS at high Pp, irrespectively of the deposition pressure.

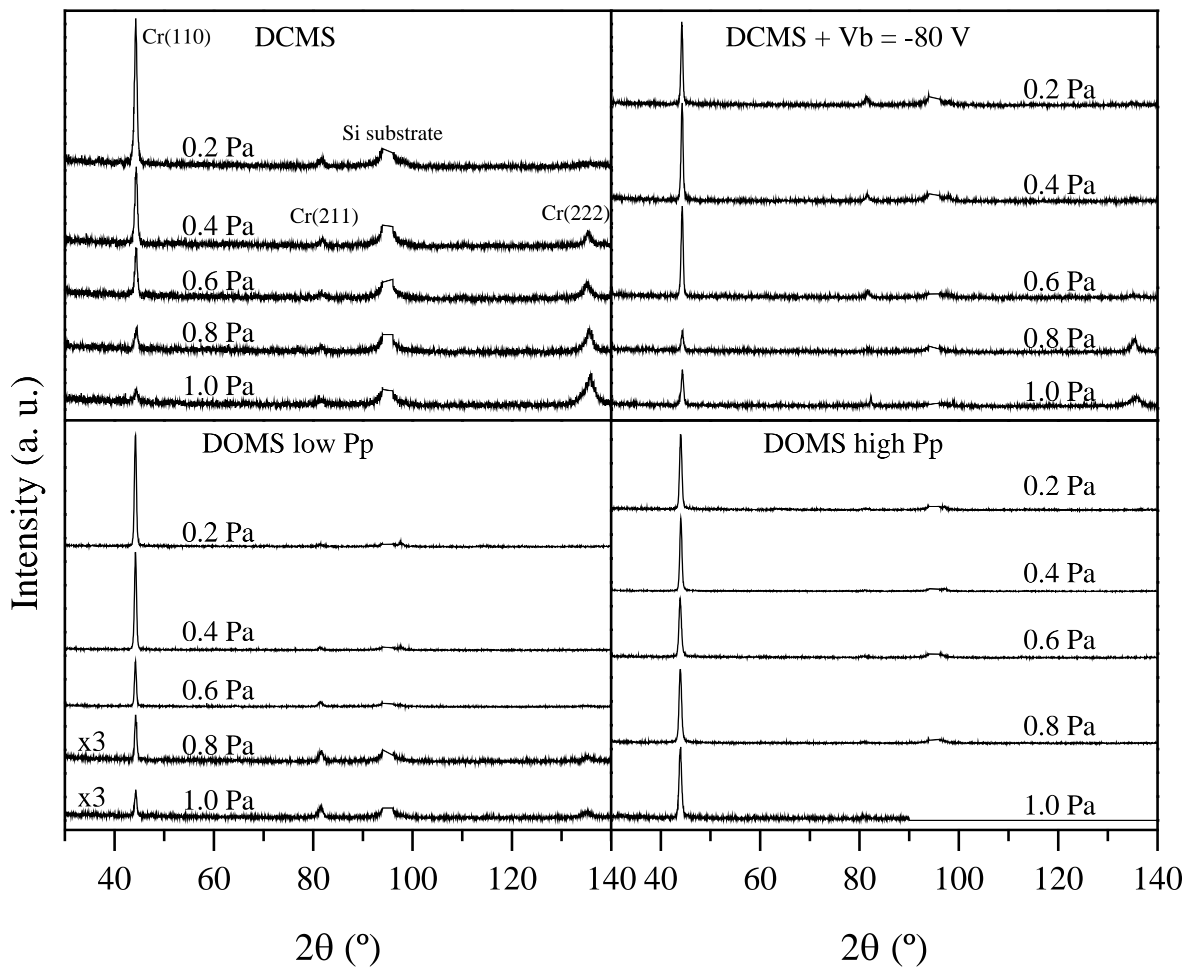

Figure 4.8. XRD structure of the Cr films deposited by DCMS without and with substrate bias and by DOMS at low Pp and high Pp at different deposition pressures.

On the overall, increasing the deposition pressure decreases the intensity of the (110) peak and favours the formation of the (222) peak. On the other hand, the formation of the (222) diffraction peak is undermine by increasing the film bombardment during deposition, whether by biasing the substrate or by using DOMS. The intensities of the (110) and (222) diffraction peaks in the diffraction patterns of the Cr films are proportional to the amount of grains oriented with the (110) and (222) planes parallel to the substrate, respectively. However, in order to compare the relative amount of grains with each orientation the intensity of the diffraction peaks has to be corrected taking into account the intensities of both peaks in the ICCD card of Cr. The corrected relative intensity calculated from the diffraction patterns in figure 4.8 are shown in figure 4.9 as a function of the deposition pressure. A value of 100% in the Y axis means that all the grains that contribute to diffraction have the (110) planes oriented parallel to the substrate. On the other hand, a value of 0% means that all the diffracting grains have the (222) planes oriented parallel to the substrate surface, i.e., all the diffracting grains are [111] oriented. Most of the diffracting grains in the film deposited by DCMS at 0.2 Pa (around 75 %) are [110] oriented. Increasing the deposition pressure to 0.4 Pa abruptly changes the dominant orientation to [111] which then account for around 75 % of the total diffracting grains.

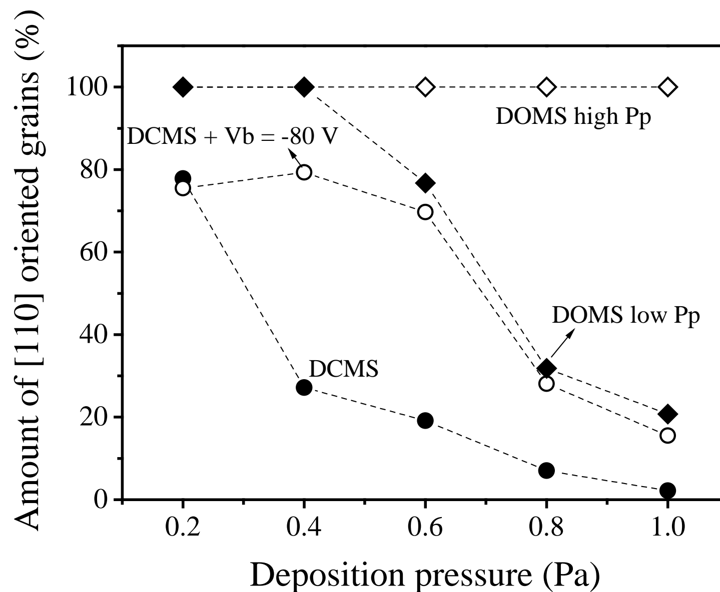

Figure 4.9. Normalized relative intensity of the (110) and (222) diffraction peaks of the Cr films deposited by DCMS without and with substrate bias and by DOMS at low Pp and high Pp at different deposition pressures.

Further increasing the deposition pressure slowly increases the relative amount of [111] oriented grains up to almost 100 % at 1.0 Pa. An abrupt transition from the [110] to [111] PO is also observed for the films deposited by DCMS with bias and by DOMS at low Pp although it is shifted to a higher deposition pressure (between 0.6 and 0.8 Pa). However the films deposited by DOMS at low Pp display a complete [110] PO at low pressures while [111] oriented grains are always detected in the films deposited by DCMS. Finally, only [110] oriented grains are detected in the diffractograms of the films deposited by DOMS at high peak power, i.e., the films have a complete [110] PO irrespectively of the deposition pressure.

The hardness of the Cr films deposited by DCMS without bias decreases from 12 GPa to 8 GPa as the deposition pressure is increased from 0.2 to 1 Pa (figure 4.10). A similar trend is observed for the films deposited by DCMS with bias although the hardness values at high pressure are higher (10 GPa). Although the hardness of thin films also depends on their porosity, the relationship between both properties is not as straightforward as in the case of the Young's modulus. In fact the hardness of the films is also strongly influenced by the microstructure of the films. It is well known, for example, that the hardness of thin films increases with decreasing grain size. The hardness of Cr sputtered thin films deposited by DCMS ranges from 4 to 12 GPa as found in the literature [65, 66].

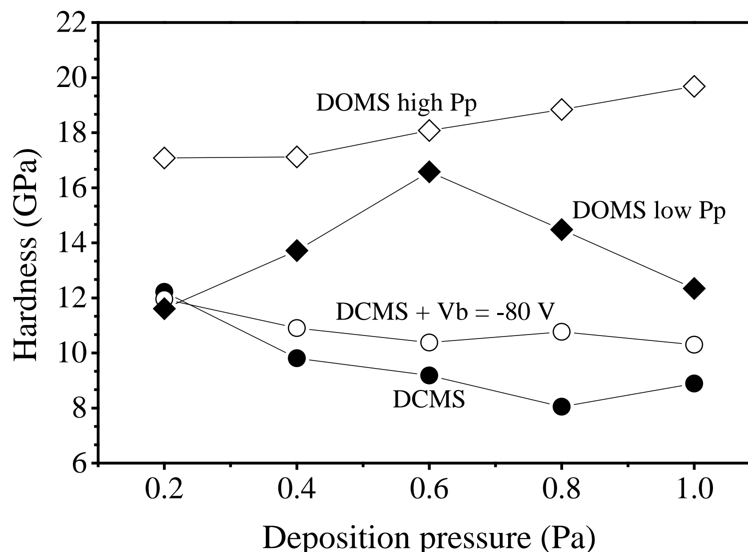

Figure 4.10. Hardness of the Cr films deposited by DCMS without and with substrate bias and by DOMS at low Pp and high Pp at different deposition pressures.

However, the highest hardness values (above 9 GPa) are due to the significant incorporation of Ar in the coatings when high bias values are used. In this work, the highest hardness value of the DCMS coating was found at the lowest pressure (0.2 Pa) and no Ar was found in the films by EDS (not shown here). This high hardness values is due to the high energy of the impinging Ar species which allow to obtain denser films. As shown by Hoffman et al. [67], the Cr films tend to form compressive stresses when the deposition is carried out below 0.3 Pa which are responsible for the high hardness value. Note also that the films deposited by DCMS at 0.2 Pa have similar hardness values although their Young's modulus differs by almost 30 %. This clearly shows the influence of microstructure on the hardness. The hardness of the films deposited by DOMS with low Pp show a distinct evolution with deposition pressure. First it increases from 12 to 16 GPa at 0.6 Pa and then decreases to close to 12 GPa. Clearly, the Hardness and Young's modulus of these coatings show very different dependencies on deposition pressure. Finally, the hardness of the films deposited by DOMS at high Pp values is much higher than for all the other films, increasing from 17 to 19 GPa with increasing deposition pressure.

The bulk properties of the deposited Cr films correlate well with their surface properties. Increasing the deposition pressure in DCMS increases the films porosity and promotes a texture turnover from a [110] to a [111] PO. These results agree well with the increasing surface roughness of the films and with the increasing size of the pyramidal-like features that are form on the films surface. Substrate biasing in DCMS decreases the surface roughness of the films while increasing their density and shifting the texture turnover to higher deposition pressure. On the other hand, using DOMS instead of DCMS allows to deposit much smoother films and to prevent the formation of pyramidal-like features at the film surface. Correspondingly, the Cr films deposited by DOMS are much denser and do not change their PO with increasing deposition pressure. The good correlation between the surface and bulk properties of the Cr films deposited in this work shows that the films can be viewed as the sum of the surfaces that develop with increasing thickness during film growth. In other words, the bulk properties of the films are the result of the evolution of their surface during film growth. This result is mostly due to the low mobility of the Cr ad-atoms on the film surface during growth, which allows the films to preserved the bombardment history.

As was already concluded from the surface properties of the films in the previous sub-section, the evolution of the bulk properties of the films with deposition pressure and peak power show that the films properties are mainly governed by the atomic shadowing

effect and that in DOMS the atomic shadowing effect is largely reduced and even completely avoid in certain deposition conditions. The mechanism underpinning these results will be discussed in detail in the next chapter of this work.

4.4. **Nitride systems (CrN and TiSiN)**

This section aims at comparing the influence of the peak power used during deposition on the properties of CrN and TiSiN films deposited by DOMS. The evolution of the deposition rate, microstructure and mechanical properties of the deposited films as a function of the peak power are presented and discussed. The experimental system and the experimental parameters used to deposit the films under study in this section are presented in papers CrN01 and TiSiN01. In order to facilitate the reading of this section, the main experimental parameters used to deposit the CrN and TiSiN films are also listed in section 3.4.

The deposition rate of the CrN and TiSiN films deposited by DOMS normalized to the time average power is shown in figure 4.11. In both systems, the normalized deposition rate steadily decreases with increasing peak power, as was already observed in section 4.2 for the metallic systems. The deposition rate loss with increasing peak power is due to the same causes as for the metallic systems, which include the aforementioned back-attraction of the metallic ions to the target [12] and sub-linear evolution of the sputtering yield with discharge voltage [56].

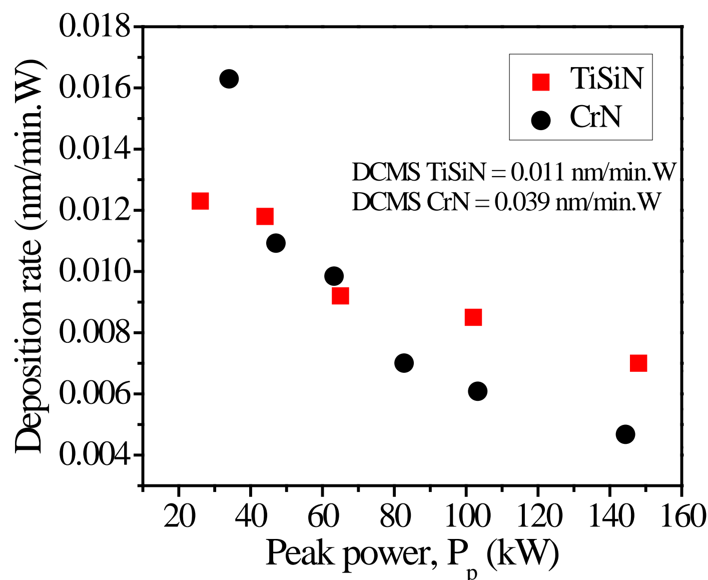

Figure 4.11. Deposition rate of the CrN and TiSiN films deposited by DOMS as a function of peak power (Pp).

Within the range of studied values of the peak power, the normalized deposition rate decreases by 71 % for the CrN system and by 43 % for the TiSiN system. Although both Cr

and Ti allow to achieve high ionization fractions of the sputtered species in HiPIMS, a higher ionization fraction is reported for Ti species in the literature [16]. Thus, a higher deposition rate loss with increasing peak power is to be expected in DOMS using a pure Ti target as compared to a pure Cr target. However, in this work, the racetrack of the Ti target during TiSiN films deposition was partially covered with Si pellets. As the ionization fraction in HiPIMS for Si is substantially lower than for both Ti and Cr [68], the amount of back-attracted ions is lower in the TiSiN system than in the CrN one, and, thus, a lower deposition rate loss with increasing peak power is found in the TiSiN system.

The cross-section and surface morphology of CrN and TiSiN thin films deposited by DCMS and DOMS are displayed in figure 4.12. The CrN film deposited by DCMS has a compact microstructure with columns extending from the substrate to the top of the film (figure 4.12a)). The film surface consists of elongated features with different sizes resulting from the stacking of several columns (figure 4.12a2)). Both the microstructure and the surface morphology of the CrN film deposited by DOMS at the lowest peak power (34 kW) are very similar to those of the CrN film deposited by DCMS (figure 4.12b) and 4.12b2)). Increasing the peak power results in the deposition of denser films with a less defined columnar structure and even featureless films at the highest peak power (figure 4.12d)). The characteristic size of the film´s surface features also decreases with increasing peak power, which is consistent with the deposition of denser films (figure 4.12d2)). As was observed for the CrN film deposited by DCMS, the TiSiN film deposited by DCMS also displays a compact microstructure with columns extending from the substrate to the top. The top-view micrographs show the characteristic dome-like endings of the columns although with a preferential elongation along one direction. However, the TiSiN film deposited by DCMS has a denser microstructure, the columnar microstructure is much less defined and the surface features have considerably smaller dimensions. This result is due to the co-deposition of the SiN_x phase, which leads to an encapsulation of the growing TiN crystallites and, thus, hinders their further [69]. The TiSiN films deposited by DOMS with the two lowest peak power also show a compact columnar microstructure (figure 4.12f)). However, the top-view micrographs show that the top of the columns have an equiaxed geometry, i.e., no preferential orientation is observed (figure 4.12f2)). The surface morphology of the film resembles a cauliflower-type morphology with protruding structures, which consists of grains, 15–25 nm wide, that agglomerate to form larger structures, 70–120 nm wide. These types of structures are associated with unstable growth under surface diffusion limited conditions. Increasing the peak power still results in the formation of cauliflower-type

morphology but the characteristic dimensions of the agglomerates are considerably reduced due to increased surface diffusion (figure 4.12g) and g2)). The film deposited at the highest peak power has a completely dense morphology, without any columnar remains, while a granular surface morphology develops (figure 4.12h) and h2)). Increasing the peak power results in the deposition of denser films both in the CrN and TiSiN systems. Although this effect is much more evident for the CrN system, in both cases the microstructure continuously evolves with increasing peak power, i.e., the columnar microstructure is gradually replaced by a featureless one with finer surface morphology.

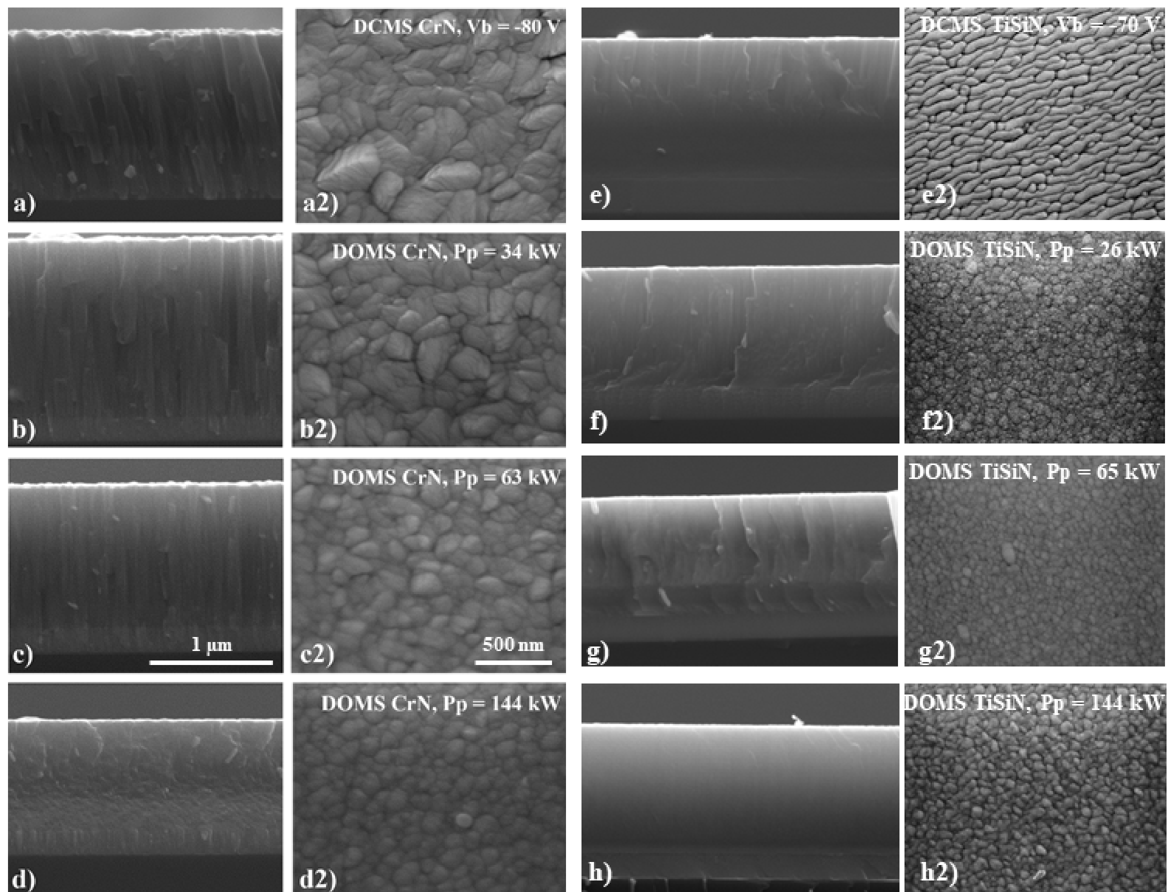

Figure 4.12. SEM cross-section and surface micrographs of the a) to c2) CrN and d) to f2) TiSiN thin films deposited by DCMS and DOMS at low and high peak power.

The dependence of the CrN and TiSiN films grain size on the peak power is shown in figure 4.13. The grain size of the TiSiN films is close to 25 nm at the lowest peak power and continuously decreases with increasing peak power down to values close to 5 nm. On the contrary, the grain size of the CrN films is already below 10 nm and remains fairly constant (close to 5 nm) as the peak power is increased. For both CrN and TiSiN grain sizes

below 10 nm are an indication of an intense bombardment during film growth. For example, Gautier at al. also found that CrN thin films deposited at higher bias voltage had a grain size below 10 nm while a higher grain sizes, up to 45 nm, were found at low bias [70]. On the other hand, Chang et al. found that the grain size of HIPIMS TiN films deposited under intense ion bombardment, i.e, low duty cycle, was less than 5 nm [71]. Moreover, TiN films with reasonably large grain size (25 nm) were also deposited by Lattemann et al. using HIPIMS under intense low-energy ion irradiation of the growing film [72]. The rest of the films (for both systems) have a grain size below 10 nm, including the films deposited by DCMS. The lower grain sizes found when more intensive ion bombardment is used is generally explained by the generation of more defects, which leads to secondary nucleation and interrupts epitaxial crystal (homoepitaxy). The evolution of the grain size of the TiSiN films is thus an indication of the transition from o low bombardment intensity at low peak power to a high bombardment intensity at high peak power. On the contrary, the evolution of the grain size of the CrN films shows that these are subjected to a high intensity bombardment even at low peak power.

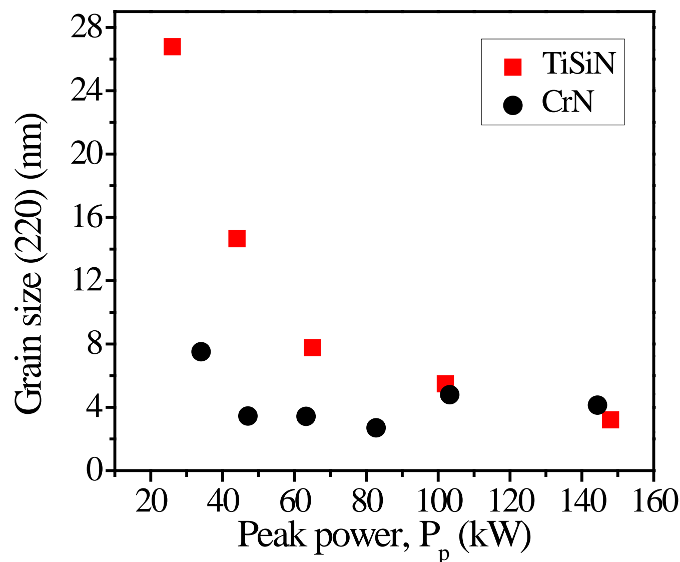

Figure 4.13. Grain size of the CrN and TiSiN films deposited by DOMS calculated from the GIXRD patterns using the (220) diffraction peak.

The lattice parameter of the CrN and TiSiN films is shown in figure 4.14 as a function of the peak power. For comparison, the lattice parameter of both materials in the unstressed state is also shown in the figure. The lattice parameter of the TiSiN film deposited at the lowest peak power is lower than the lattice parameter of the unstressed material. This result

is due to the incorporation of Si in the TiSiN grains as demonstrated in the paper TiSiN01. The lattice parameter of the TiSiN almost linearly increases with increasing peak power up to significantly higher values. These results are consistent with the formation of compressive stresses in the TiSiN films with increasing peak power. On the contrary, the lattice parameter of the CrN films is well above the unstrained value even at low peak power and remains mostly unchanged as the peak power is increased. As was concluded above from the grain size measurements, the evolution of the lattice parameters of the CrN and TiSiN films show clearly different dependencies on the peak power. In the case of the TiSiN films the evolution of the lattice parameter is consistent with an increase of the bombardment intensity during growth, from low to a high intensity bombardment. On the contrary, the evolution of the lattice bombardment of the CrN films is consistent with a similar and intense bombardment at all peak powers studied in this work.

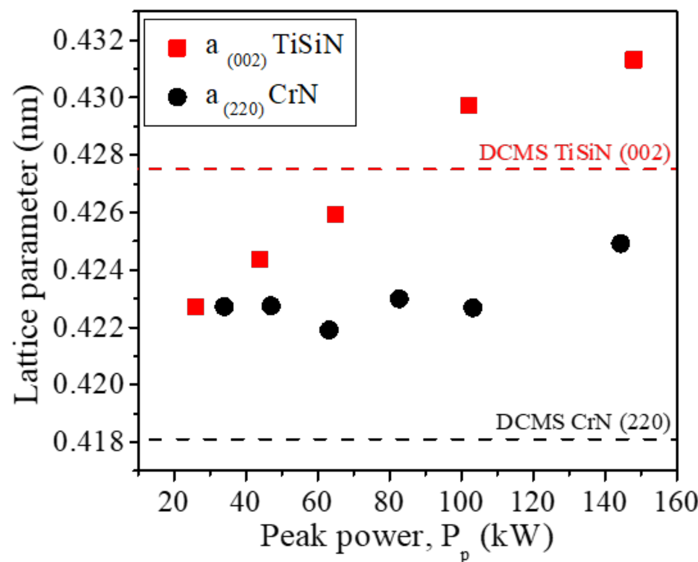

Figure 4.14. Lattice parameter of the CrN and TiSiN films deposited by DOMS calculated from the XRD patterns using the (220) diffraction peak.

Figure 4.15 shows the hardness of the DOMS CrN and TiSiN films deposited at different peak powers. As reference, the hardness of the CrN and TiSiN film deposited by DCMS is equal to 17 GPa. All the films deposited by DOMS have hardness above 21 GPa, i.e., much higher than the films deposited by DCMS. The hardness of the CrN films increases (from 21 to 29 GPa) with increasing peak power. Similarly, the hardness of the TiSiN films increases from 24 to 31 GPa with increasing peak power. In both systems, a continuous

increase in hardness with increasing peak power is observed. The hardness of the TiSiN films is always higher as compared to the hardness of the CrN films deposited at similar peak powers. All the TiSiN films deposited by DOMS have a nanocomposite microstructure consisting of two phases: f.c.c TiN and a-SiN (described in paper TiSiN01). This kind of microstructure is associated to extremely high mechanical properties [73]. Therefore, the results obtain in this work agrees well with the literature.

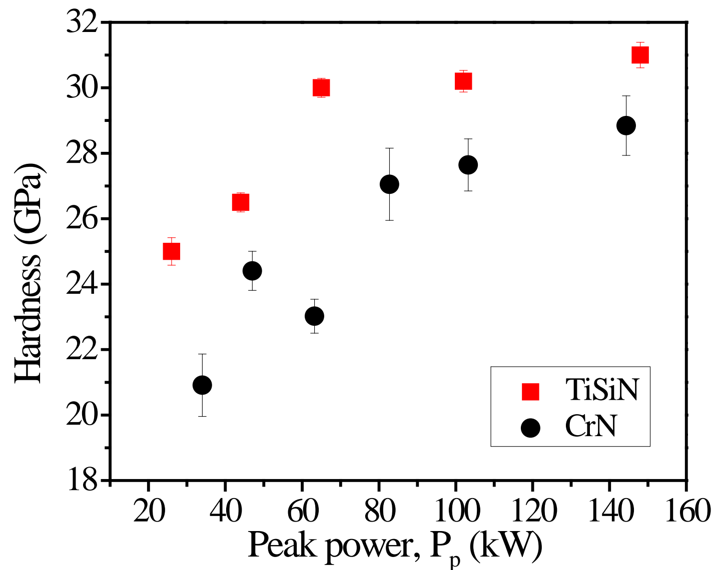

Figure 4.15. Hardness of the CrN and TiSiN thin films deposited by DOMS.

Figure 4.16 shows the Young's modulus of the DOMS CrN and TiSiN films deposited at different peak powers. As reference, the Young's modulus of the CrN film deposited by DCMS with a substrate bias of – 80 V is equal to 271 GPa and the TiSiN film (with a substrate bias of – 70 V) is equal to 238 GPa. The Young's modulus of the CrN films deposited by DOMS is always close to 295 GPa regardless of peak power, while in TiSiN system the Young's modulus increases with peak power up to values similar to the those obtained for the CrN films.

All the properties of the TiSiN films display a continuous variation with increasing peak power. The hardness, Young´s modulus and lattice parameter of the films steadily increases with increasing peak power, while the grain size of the films follows the opposite trend. These results are well in agreement with the deposition of denser and more compacts films, as observed by SEM analyses, and are consistent with an also continuous increase of the bombardment intensity during film growth with increasing peak power. As was already found for the Cr systems in sub-section 4.3, the properties of the TiSiN films are well

correlated with the peak power used during deposition.

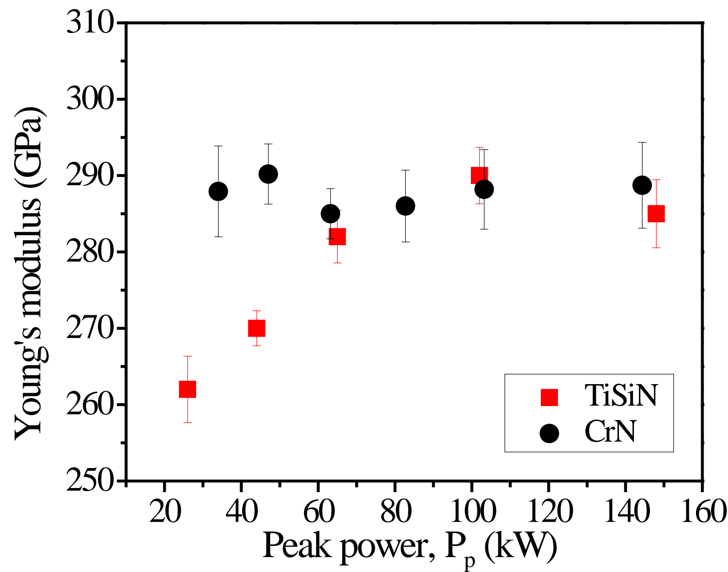

Figure 4.16. Young's modulus of the CrN and TiSiN thin films deposited by DOMS.

In the CrN system two different kinds of evolution of the film's properties with increasing peak power were found. On one hand, the microstructure of the films continuously evolves toward the deposition of denser films with increasing peak power while their hardness continuously increases. On the other hand, the grain size, lattice parameter and Young's modulus show almost no correlation with the peak power. While the microstructure and hardness evolution with increasing peak power are consistent with the transition from a low intensity to a high intensity bombardment regime, the remaining properties point to a constant high intensity bombardment independent of the peak power. Although a vast number of publications about the deposition of CrN is available, no references to similar contradictory results could be found in the literature. In the next chapter, the origin of the different types of evolution of the CrN films properties with increasing power is discussed and explained in section 5.3.

Chapter V

5. DEPOSITION MECHNISMS IN DOMS

5.1. Introduction

As already referred in the state of the art, the main difference of the DOMS deposition process, and more generally of HiPIMS, as compared to DCMS, is the ionization of the sputtered material by electron impact near the ionization zone of the magnetron discharge. Thus, in DOMS, the flux of sputtered material arriving at the substrate during deposition is at least partly influenced by the electric field which develops at the substrate sheath, even without intentional substrate biasing, while in DCMS the sputtered neutral species are not affected. On the other hand, the deposition conditions in DOMS (voltage, current …) are substantially different than in DCMS which can potentially influence the films properties. In this chapter, some of the more interesting results pointed out in the previous chapter are analyzed and discussed in light of the specific characteristics of the DOMS process sated above. The main aim is to develop a more general understanding of the process-properties relationships in the DOMS deposition process, both from the technological and scientific point of views.

In the second section of this chapter, the use of DOMS to tailor the phase composition and improve the structure and properties of TiSiN films is analyzed. This section is a summary of the results and discussion published in the corresponding paper (TiSiN01). In the third section of this chapter, the origin of the energetic "background bombardment" always present during the deposition of CrN films by DOMS is examined and its implications for the deposition process are discussed (based on paper CrN01). In the fourth section, the origin of the anisotropic surface morphology of the Cr films deposited by DCMS and by DOMS at low peak power and high pressure is firstly discussed. This section is mostly based on the results published in paper Cr02**.** Then the

advantage of using DOMS in order to avoid the deposition of films with anisotropic properties, even in complex industrial deposition system, is discussed. In the fifth section, the impact of the ionization of the sputtered material on the shadowing effect is analyzed. It is concluded that the shadowing effect in DOMS is mostly independent of the deposition pressure, in opposition to the DCMS deposition process, and that the main deposition parameter that influence the shadowing effect is the fraction of ionized sputtered material. This section corresponds to the results and discussion published in the Cr03. Finally, in the last section, a general overview of all DOMS characteristics observed in the previous sections of this chapter are discussed together in order to evaluate the DOMS potential in a more technological point of view.

5.2. Additional degree of freedom in DOMS

Depending on the deposition conditions, TiSiN films have been reported consisting of: i) nano-sized TiN crystallites surrounded by an amorphous matrix of Si_3N_4 [69, 73-77], or ii) substitutional solid solution of Si in TiN structure (not predicted by the Ti–Si–N phase diagram) [78-80]. In the first case, the hardness of the nanocomposite films has been shown to increase with increasing silicon content up to an optimal concentration. Following the model proposed by Patscheider et al. [69], reproduced in figure 5.1, the maximum hardness corresponds to the formation of the nanocomposite phase with optimized values of both the TiN crystallites and the inter-crystallites thickness of the Si_3N_4 amorphous matrix. In DCMS the ratio between the TiN grains size and thickness of the Si_3N_4 matrix is controlled by the Si content in the films. The size of TiN crystallites decreases with increasing Si content while the inter-crystallites thickness of the Si_3N_4 amorphous matrix follows the opposite trend. Thus, in DCMS, the TiN grains size and the inter-grain thickness of the Si_3N_4 matrix cannot be controlled independently. As a result, the optimized values of the TiN crystallites and the inter-crystallites thickness of the Si_3N_4 amorphous matrix may or may not be reached in a given deposition system depending on the specific deposition conditions inherent to the geometrical configuration of the system.

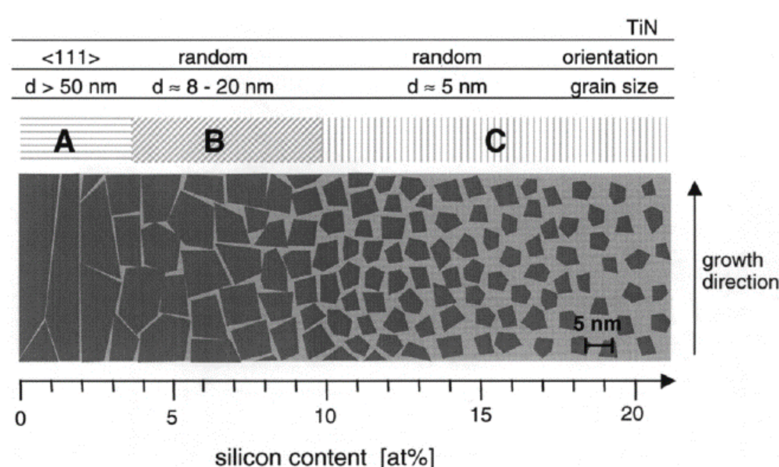

Figure 5.1. Morphological zone model for nc-TiN/a-Si_3N_4 as function of the silicon content. The dark areas represent nanocrystals, the lighter zones stand for the amorphous phase [69].

As was shown in paper TiSiN01, all the films deposited by DOMS have a nanocomposite microstructure consisting of two phases: f.c.c TiN and a-SiN. Although

similar amounts of SiN were detected in the DOMS films, both the phase distribution and the properties of the f.c.c phase depend on the peak power. At low peak power the nanocomposite is formed by a solid solution of Si in TiN and a-SiN. The columnar micro-structure of the films and the cauliflower-like surface morphology suggest that this film is formed by nano-columnar TiN based grains while the a-SiN phase fills the inter-columnar spaces. The microstructure of the TiSiN films is similar to that obtained for TiSiN films deposited by DCMS at low silicon content (region A in figure 5.1). Increasing the peak power suppresses the formation of the solid solution while decreasing the grain size. The higher peak power decreases the size of the TiN nano-columns although the nano-columnar nanocomposite microstructure still holds. The lower size of the nano-columns in the film is responsible for the hardness increase in spite of the solid solution suppression. The properties of the films are similar to those of region B in figure 5.1, and, thus increasing the peak power as a similar effect in DOMS as increasing the Si content in DCMS. Further increasing the peak power increases the bombarding species energy above the TiN critical threshold for implantation [72]. The high energy ions are able to penetrate to the subsurface of the growing films leading to the start of compressive stresses and defect formation. The morphology of the film is denser and globular structures are observed in the surface. Secondary nucleation starts and the film microstructure consists of equiaxed nanocrystalline TiN grains in an a-SiN matrix. Thus, the microstructure of the TiSiN films is similar to that obtained for TiSiN films deposited by DCMS at high silicon content (region C in figure 5.1).

The above results show that increasing the peak power in DOMS allows to tailor the microstructure of the TiSiN coatings within a range of microstructures similar to that achieved in DCMS upon increasing the Si content. Thus, in DOMS, the size of TiN crystallites and the inter-crystallites thickness of the Si_3N_4 amorphous matrix can be controlled independently of the films Si content. As a consequence, the existence of optimized values of the TiN crystallites and the inter-crystallites thickness of the Si_3N_4 amorphous matrix can be investigated for each Si content, irrespectively of the specific deposition conditions inherent to the geometrical configuration of the deposition system. Thus, DOMS brings about a new degree of freedom for the TiSiN films deposition as compared to DCMS.

The grain size of the TiSiN films deposited by DOMS at the highest peak power is similar to that of the film deposited by DCMS at lower pressure and with substrate biasing. Furthermore, high compressive stresses were found in both films. These results indicate that both films were subjected to an energetic bombardment during growth. The denser

microstructure of the film deposited by DOMS and the presence of higher compressive stresses can be attributed to an even higher bombardment intensity in DOMS, in agreement with most of the literature about HiPIMS, which stresses that HiPIMS brings about an increase of the energy of the film forming species. However, the properties of the TiSiN films deposited at low peak power cannot be justified just by assuming that the bombardment intensity is lower than at high peak power. The TiSiN films deposited by DOMS at low peak power has a high grain size (35 nm) and almost no compressive stresses, which indicates a low bombardment intensity during growth. On the other hand, the microstructure of this film is similar to that of the film deposited by DCMS with substrate biasing and its hardness is even higher (22 GPa against 17 GPa), which indicates a high bombardment intensity during growth. As will be shown in section 5.5, these apparently contradictory results can be explained by assuming that ionization of the sputtered species in DOMS has additional effects on the deposition process beyond influencing the energy of the bombarding species.

5.3. Backscattered nitrogen neutrals in DOMS

In section 4.4 it was shown that the evolution of the properties of CrN thin films deposited by DOMS with increasing peak power displayed somewhat contradictory results: while the microstructure and hardness evolution are consistent with the gradual transition from a low intensity to a high intensity bombardment regime, the lattice parameter and preferred orientation of the films are consistent with an energetic bombardment during growth regardless of the deposition conditions.

The main sources for substrate bombardment during CrN deposition by reactive magnetron sputtering are the sputtered (Cr and N) and backscattered species (Ar and N). Sarakinos et al. [81] found high compressive stresses in CrN films deposited by DCMS. Using both simulation and experimental techniques the authors showed that the compressive stresses could not be explained either by bombardment of the sputtered species or by formation of thermal stresses upon cooling of the films after the deposition stage. This conclusion agrees well with the result obtained in this work for Cr deposition by DOMS. The lattice parameter of Cr thin films deposited by DOMS at low peak power (39 kW) is close to the corresponding ICCD card value (0.288 nm). In other words, at low peak power the Cr film was only subjected to a weak bombardment unable to induce subplantation of the impinging species and consequent high compressive stress formation. On the other hand, Sarakinos et al. [81] also rule out the bombardment of Ar neutral backscattered from the target as the origin of the high compressive stresses in the CrN films. In fact, only a small amount of backscattered Ar neutral are formed upon impingement of Ar ions on a Cr target (close to 3%), as was confirmed in this work by simulation with the SRIM software. Sarakinos et al. finally concluded that the out-of-plane lattice strain and compressive stresses in the CrN films were due to the subplantation of the backscattered N species resultant from neutralization and dissociation of the N_2^+ ions impinging on the target.

Greczynski et al. reported the occurrence of energetic N neutrals on HiPIMS discharge [82]. They used mass spectroscopy to investigate the energy and composition of the ion flux in a HiPIMS discharge. A Cr target was used in both metallic (Ar) and reactive mode (Ar + N_2). The authors reported that the IEDF of singly charge Cr ions was comparable to the one acquired in metallic mode, regardless of N_2/Ar ratios in the discharge gas. In contrast, the IEDF of the N^+ ions revealed not only the predictable flux increase but also an increasing high energy tail. They established that an energetic stream of N^+ ions was

generated through the electron-impact ionization of the N atoms, either resulting from sputtering of the nitride portion of the target or being the result of dissociation of back-attracted N_2^+ ions at the target surface.

The peak voltage during CrN films deposition by DOMS (above −773 V) is higher than the deposition voltage reported by Sarakinos et al. (−504 V) [81]. The energy of the N neutrals impinging on the growing film is proportional to the acceleration of N_2^+ ions from the plasma upon falling into the cathode potential. Thus, it is to be expected that bombardment with energetic nitrogen neutrals have an even stronger impact on the properties of CrN films deposited by DOMS. In this study, it is argued that the CrN thin films deposited by DOMS are subjected to a strong bombardment by energetic nitrogen atoms, regardless of the deposition conditions used. Note however that the energetic flux of N species impinging on the growing film is unable to prevent the columnar growth at low peak power, showing that bombarding the growing films with energetic N species is ineffective at overcoming the shadowing effect.

Increasing the peak power has a significant effect on both the microstructure and the hardness of the CrN films deposited by DOMS. The bombardment by energetic backscattered nitrogen neutrals discussed above can be viewed as a "background" bombardment, almost independent of the deposition conditions, and thus cannot explain the observed microstructural transformation. One possible cause for this transformation could be the increase of the mean energy of the species impinging on the growing film. It is well known that the development of columnar structures is primarily due to the shadowing effect. Although the columnar growth can be overcome by increasing the energy and/or the flux of the bombarding species, and, on the other hand, it can be avoided by decreasing or preventing the shadowing effect.

Increasing the deposition voltage increases the energy gain by the plasma ions upon acceleration in the cathode fall. However, most of the additional energy contributes to an increase of the sputtering yield rather than to an increase of the mean energy of the sputtered species. Therefore, although the peak voltage increases with sputtered species is to be expected with increasing peak power. On the other hand, the energy gain upon acceleration in the vicinity of the substrate by both the ionized sputtered species and the Ar ions extracted from the plasma is small, as the self-bias is in the order of a few eVs only. Accordingly, Alami et al. [83] found that for CrN films deposited by HIPIMS the energy of the species arriving at the substrate is not significantly increased by increasing the peak power. However, as shown in figure figure 4.1, the average energy of Cr ions in a DOMS discharge

using a Cr target increases with increasing peak power. A similar trend of the average energy of the Cr ions is thus expectable during CrN films deposition by DOMS carried out in this work. Thus, the microstructure evolution of the CrN with increasing peak power could be due to the activation of the re-deposition mechanism at higher peak power, which could efficiently counteract the shadowing mechanism and thus result in denser/less columnar films with higher hardness.

Increasing the peak power increases the ionization fraction of the Cr species, which in turn increases their mean angle of incidence on the substrate, i.e., decreases the shadowing effect. Greczynski et al. have shown that this can have a striking influence on the microstructure of Cr films by HiPIMS as the trajectory of the ions impinging on the substrate can be influenced significantly [84]. In this study, the transition from columnar to columnar-free microstructures occurs at lower peak power for the CrN films deposited by DOMS at 0.7 Pa than for those deposited at 0.3 Pa. In fact at both deposition pressures the transition from the columnar to the columnar-free growth occurs at similar values of Ip (just above 80 A), although the peak voltage is higher by more than −200 V at low pressure. This result shows that the microstructure transformation is most probably triggered by an increase in the ionization fraction of the sputtered species and consequent weakening of the shadowing effect as the mean incidence angle of the species impinging on the growing film is shifted to values closer to the normal of the film.

In light of the preceding discussion, the evolution of the properties of the CrN films deposited by DOMS in this work with increasing peak power can thus be understood by considering that the films are subjected to two almost independent bombardments by metallic ions and energetic monoatomic nitrogen neutrals. The lighter monoatomic nitrogen neutrals are unable to efficiently transfer their moment to the metallic adatoms on the film surface, due to the mass mismatch, and thus they do not influence significantly their mobility. As a result, bombarding the growing film with energetic N species does not efficiently change the microstructure of the films. Most of the N species are subplanted below the film surface, much like the energetic carbon ions used to deposited ta-C mainly contributing to the creation of defects, such as interstitials and vacancies, and ultimately to the formation of high compressive stresses and loss of crystallinity of the films (i.e., lower grain size) [48]. On the other hand, the moment transfer of the Cr species to the growing film is much more efficient, as they are themselves film forming species. More importantly, increasing the peak power increases the ionization fraction of the Cr sputtered species and thus considerably weakens the shadowing mechanism, as concluded above. Thus, the

bombardment by metallic ions is responsible the microstructural evolution from columnar to featureless as the peak power is increased.

5.4. Overcoming asymmetrical deposition conditions in DOMS

As shown in paper Cr02, all the Cr films deposited by DCMS have a highly anisotropic surface morphology. The films surface consists of three sided pyramidal-like column tops which are preferentially elongated and align along the Y direction. The surface morphology is well described as ridges of columns separated by deep valleys of continuous voids oriented along the Y direction. Examples of such kind of surface morphologies are shown in figure 5.2 for Cr films deposited at 0.4 Pa. Decreasing the deposition pressure reduces the size of the pyramid-like tops and inter-columnar voids, resulting in shallower and thinner valleys and ridges, although the morphology of the surface remains mostly the same. Using a substrate bias during deposition, i.e, bombarding the substrate with Ar ions results in slightly thinner columns tops separated by thinner valleys of voids, but the overall anisotropy of the surface remains mostly unchanged as exemplified in figure 5.2b) in the case of the Cr films deposited at 0.4 Pa.

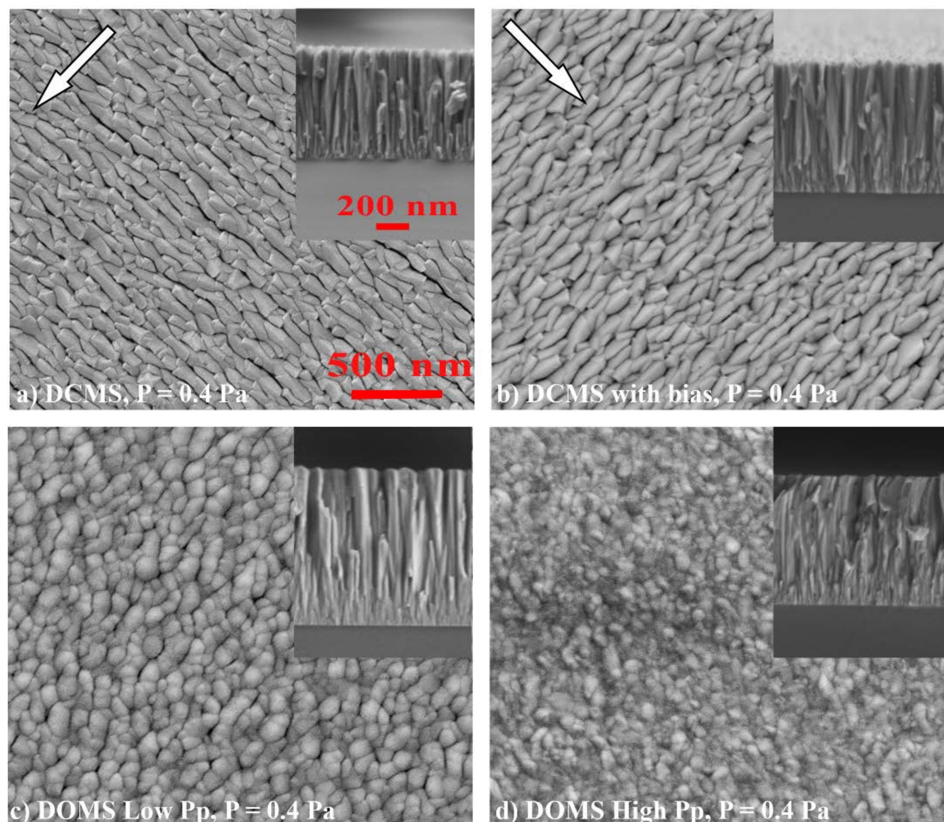

Figure 5.2. SEM surface and cross-section micrographs (inset) of the Cr films deposited by a); b) DCMS without and with bias and by c); d) DOMS at low and high Pp at 0.4 Pa. The arrow approximately indicates the substrate rotation direction (X direction).

Anisotropic surface morphologies have been described in the literature for Cr films deposited by magnetron sputtering. Cr films were deposited by Whitacre et al. onto silicon wafers fixed on a platen which rotated under the sputter target [85]. The obtained Cr films presented a faceted surface morphology with grain elongation in the plane of growth normal to the direction of substrate motion. They associated the anisotropic morphology of those films to the asymmetric deposition system as there was on average more oblique flux in the rotation direction above any other. Equivalent results were found for Ta, Mo and CrN films. Zhao et al. study the evolution of anisotropic microstructure and residual stress in sputtered Cr coatings [60]. The authors also used a rotating substrate holder, in such a way that the center of the substrates passed under the sputter target in each revolution. The resulting films presented well-organized microstructures formed by elongated grains separated with preferentially aligned inter-columnar voids. The direction of grain elongation matched with direction perpendicular to substrate rotation. The thicker Cr film deposited by the authors has a very similar surface morphology to the one observed in the films deposited by DCMS in this work. Zhao et al. deposited Mo films by DCMS onto moving and static substrates [86]. The authors found that anisotropic stresses and elongated grains were only developed in the first deposition case. A twofold rotation geometry with the substrates and target vertically aligned was used by Jansen et al. to deposit Cr films [59]. The authors also reported an anisotropic microstructure. In direction perpendicular to substrate rotation, the grains formed ridges separated by large grain boundaries whereas they were separated by deep grooves in the opposite direction.

The HHCFs in the X and Y directions obtained from the surface of Cr film deposited in this work at 0.4 and 0.8 Pa are shown in figure 5.3. All the HHCFs behave as a power-law for small values of r, i.e., a linear behavior in the log-log graph is always observed. On the other hand, all HHCFs stabilize at the same value at higher values of r. At intermediate values of r, the HHCF calculated along the X direction display an oscillatory behavior before stabilizing, which is typical of mounded surfaces and indicates that the shadowing effect is shaping the films morphology in the rotation direction [87]. On the contrary, the HHCF calculated along the Y direction monotonically increase up to its maximum value and do not display an oscillatory behavior at intermediate values of r. Thus the atomic indicating that the shadowing effect has no or little influence on the films morphology along the Y direction. In all the depositions of Cr films carried out in this work, the substrates were mounted on a rotating substrate holder placed in front of the target in the vertical direction. Thus, the substrates were revolved in front of the Cr target along the X direction during deposition.

Although the average impinging angle of the incoming species should be the same in the rotation direction (X direction) and the vertical direction (Y direction), the spread of the angle distribution is considerably higher along the rotation direction. In this direction, glancing angle impingement is achieved both when the substrate enters and leaves the field of view of the target. Consequently, the impinging flux has a higher angle component in the rotation direction and, thus, the atomic shadowing effect is stronger in this direction as was concluded from the HHCFs.

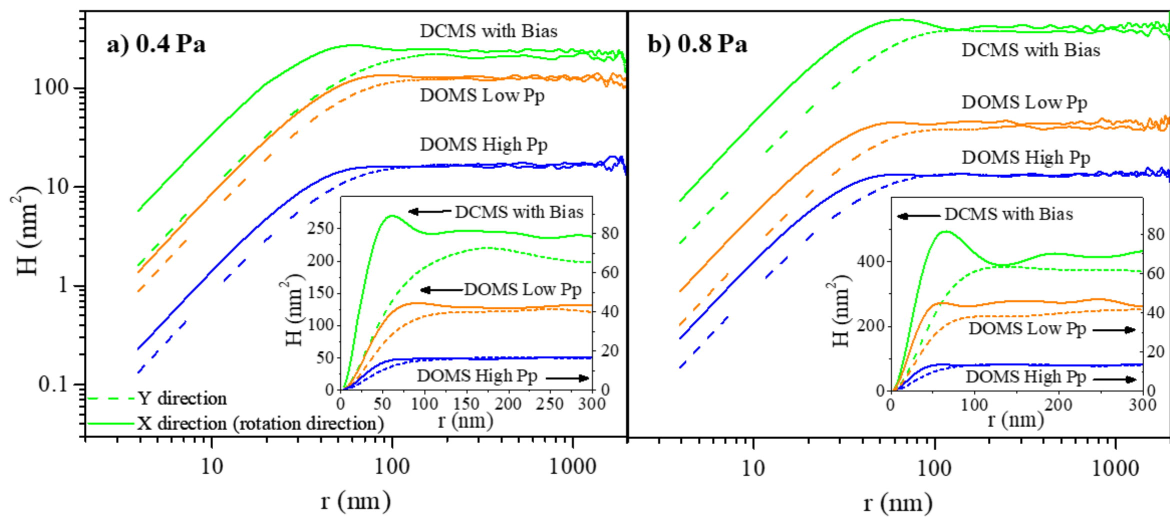

Figure 5.3. Double logarithmic representation of the Height-Height correlation functions calculated for the Cr films deposited at a) 0.4 Pa and b) 0.8 Pa. The HHCFs are represented with linear scales in the inset.

The three sided pyramidal-like column tops found on the surface of Cr films deposited by DCMS are elongated in the direction perpendicular to the substrate rotation. Karpenko et al. reported that high-angle ion bombardment of a growing film will result in grain elongation along the direction perpendicular to the bombardment direction [88]. The grains whose fast crystallographic growth directions are aligned with the fast geometric growth direction have a growth benefits over grains of other orientations. This model explains why the Cr films deposited by DCMS in this work have an elongation of the columns along the Y direction, as they are exposed to a flux of impinging species with a stronger high-angle component along the X direction. The extra material deposited along the Y direction as a result of the stronger shadowing effect along the X direction contributes to fill the inter-columnar voids otherwise formed by the shadowing effect along the Y direction.

As shown in paper Cr02, the surface morphology of Cr film deposited by DOMS at low Pp and 0.6 is quite different from that of the films deposited by DCMS. The surface of the film consists of fine equiaxed features instead of faceted pyramid-like shapes. The features are randomly distributed and the resulting surface morphology is almost isotropic. Increasing the peak power results in a completely isotropic surface morphology with fine and highly compacted features. The HHCFs of the film deposited by DOMS at 0.4 Pa (figure 5.3a)) are shifted to lower values of the vertical scale confirming that lower roughness surfaces are formed as compared to DCMS with or without bias. The oscillatory behaviour of the HHCF in the X direction is much less evident for the samples deposited by DOMS at low Pp and almost inexistent for the sample deposited by DOMS at high Pp. The HHCF show that in DOMS the shadowing effect in the rotation direction is much weaker than in DCMS at low peak power and event completely prevented at high peak power, which explains the isotropic surface morphologies of the films. Thus, in DOMS, the effect of the asymmetrical deposition conditions due to the substrate rotation during deposition is minimized and even completely prevented at high peak power. Even though the average energy of the film forming species is higher in DOMS than in DCMS, as shown in figure 4.1, this result cannot be due exclusively to the higher bombardment intensity in DOMS. On one hand, almost isotropic surface morphologies are already obtained in DOMS at low peak power, i.e., at low energetic bombardment. On the other hand, applying a substrate bias of –80 V during deposition in DCMS, i.e., bombarding the growing films with highly energetic Ar ions did not result in a significant decrease of the films surface anisotropy. As was concluded in the previous section, the properties of the Cr films deposited by DOMS as compared to their DCMS counterparts clearly indicate that DOMS brings about additional deposition mechanisms besides an increased energy of the impinging film forming species. This issue will be discussed in detail in the next section.

5.5. **Atomic Shadowing in DOMS**

In magnetron sputtering-based deposition processes the ability to tailor the properties of a thin film deposited under conditions of low temperature and low mobility of the ad-atoms depends primary on the effective control of the flux of particles arriving at the growing film surface. The flux intensity and composition, as well as the energy and impinging direction of the particles can trigger different deposition mechanisms to different extents [89, 90]. The so-called shadowing effect promotes the formation of rougher surfaces and porous columnar microstructures [91, 92]. This film formation mechanism is non-local as the capture of particles at the top of the hills also influence the film growth in the shadowed area, i.e., at considerable distance from their capture location [93, 94]. If the energy of the bombarding particles is high enough, i.e., above the sputtering threshold, the film material will be re-sputtered. The re-sputtered species may then be directly re-deposited on the valleys of the surface and thus contribute to fill the underdense regions resulting from the atomic shadowing effect [93, 94]. This so-called re-deposition process is also a non-local film formation mechanism as some of the re-sputtered particles end up being re-captured at a significant distance of their emission location. The bombarding particles can also influence the films properties through other film formation mechanisms that increase the ad-atoms mobility in the vicinity of the impingement location, such as atomic peening [95] and atomic scale heating [96]. However these mechanisms are local, i.e., they only operate in the vicinity of the impingement location and, thus, they are unable to counteract the atomic shadowing effect.

In the previous discussions the term “shadowing effect” has been used in this work to indicate both the deposition mechanism in charge for column formation, which does not change during film growth, and the actual shadowing effect by the hills on the film surface which increases during film growth as the height of the hills increases. In the following discussions, the first one will be explicitly denoted as “shadowing mechanism” whereas the later one will be denoted as “shadowing effect”, as is habitually the case. Therefore, the shadowing effect at any film growth stage is the consequence of the interplay between the shadowing mechanism and the bombardment-induced deposition mechanisms, as for instance re-deposition.

In the previous section it was shown that DOMS process allowed us to overcome the shadowing effect and, consequently, to deposit Cr coatings with much smoother surfaces

and densely packet columns even at relatively high pressure. This result is well illustrated by comparing the properties of the Cr films by DOMS at relatively high pressure (1.0 Pa) and DCMS at relatively low pressure (0.2 Pa). Both films have well-packed columnar microstructures with similar distances between column centres. They also have similar values of the $a_{(110)}$ lattice parameter, which are higher than in unstrained Cr. Finally, the films have similar hardness (close to 12 GPa), higher than most values reported in the literature for Cr films deposited by DCMS [65, 66]. These results show that the shadowing effect in the films is not much different despite the much higher pressure of the film deposited by DOMS. Furthermore, taking into account the significantly greater thickness of the Cr film deposited by DOMS the strength of the shadowing mechanism is even lower in DOMS at high pressure as confirmed by the lower surface roughness and the higher Young's modulus. The lower atomic shadowing effect in the film deposited by DOMS at high pressure can be explained either by an increased energy of the species bombarding the substrate during growth in DOMS, as compared to DCMS, or by a decrease of the strength of the atomic shadowing mechanism.

The occurrence of re-deposition depends mainly on two factors: the sputtering threshold of the material being deposited and the average energy of the energetic species imping on the growing films. The time-averaged ion energy distributions functions (IEDFs) of Cr^+ ions normalized to unit area obtained from the DCMS plasma at 0.2 Pa and from the DOMS plasma at 1.0 Pa during Cr sputtering are shown in figure 5.4. Both normalized IEDFs extend up to 20 eV and in both cases the vast majority of ions have energies less than 15 eV. The average energy of the Cr^+ ions are 6.8 and 9.2 eV for DOMS and DCMS, respectively. Assuming a similar potential drop at the EQP and substrate sheath, the average energy of the Cr^+ ions may be taken as the average energy of the Cr^+ ions impinging on a substrate placed at 2 cm from the target, the distance between the location of EQP collection orifice and the target. Since the chromium ions loose energy upon travelling inside the deposition chamber due to collisions with the process gas, their average energies upon impinging on the substrate placed at 8 cm from the target during the deposition process are considerably lower than those reported above. Therefore, they are also considerably lower than the threshold energy for Cr self-sputtering (which is close to 22 eV [97]) and thus the Cr^+ ions impinging on the growing film cannot trigger the re-sputtering mechanism. The same conclusion applies to the Cr neutrals as they are not sensitive to the electric field at the substrate sheath and thus they do not gain energy upon acceleration in the substrate sheath like the Cr^+ ions do. Since the substrates were not biased during deposition and the flux of

neutralized Ar ions reflected at the target is less than 3% of the sputtered Cr flux, as shown in the SRIM simulations (in paper Cr03), none of the species impinging on the growing film can trigger the re-sputtering mechanism.

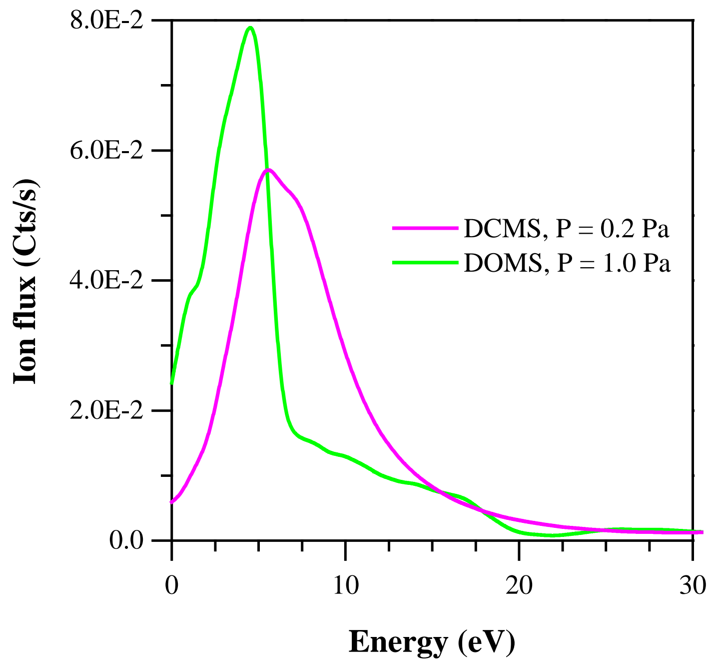

Figure 5.4. IEDFs of the Cr+ ions obtained from the DOMS and DCMS plasmas normalized to unit area.

In DCMS the flux of particles arriving at the substrate can be viewed as the sum of two fluxes: a ballistic flux comprising of the particles that travelled by line-of-sight to the substrate, and a diffusive flux, encompassing particles that were thermalized due to collisions in the gas phase and subsequently travelled to the substrate by diffusion [98]. The angle distributions of the Cr species impinging on the substrate at 1.0 Pa obtained by simulation of the DCMS depositions are shown in figure 5.5a). The impinging angle distribution of the thermalized and energetic (non-thermalized) Cr species are also shown in this figure. The angle distribution of the thermalized Cr neutrals which account for 37 % of the total Cr species, is symmetrical and peaks close to 45º, in accordance to their diffusive path to the substrate. Even at high pressure, the Cr species flux is dominated by particles that travel along the line-of-sight between the racetrack and the substrate. For these particles, the impinging angle relative to the substrate normal (α) is limited by the dimensions and relative positions of the substrate and racetrack, varying between 5.5 and 45.5º due to the off-axis

positioning of the substrate in relation to the racetracks in the deposition system used in this work.

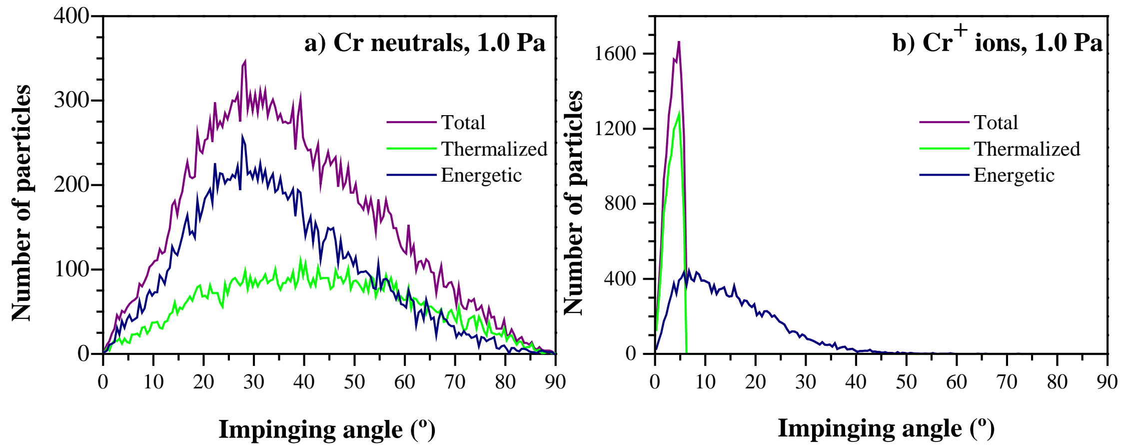

Figure 5.5. Simulation of the angle distributions of the thermalized and energetic a) neutrals and b) ions upon impinging on the growing film at 1.0 Pa.

In DCMS the vast majority of the Cr species arriving at the substrate are neutrals and thus they are not influenced by the potential difference across the substrate sheath. In DOMS, in contrast, a substantial part of the Cr species is ionized by electron impact near the ionization zone, and, thus, the resulting ions are attracted towards the growing film in the substrate sheath and arrive at the substrate at angles β such that $\beta < \alpha$. As illustrated in figure 5.6, the direction of the ions arriving at the substrate sheath edge is most significantly influenced for high values of α, i.e., for ions impinging at small angles relative to the substrate surface, and for ions with low energy.

In order to investigate the effect of the sheath acceleration on the Cr^+ ions trajectory, their impinging angle distribution was calculated by assuming that (i) they arrive at the substrate's sheath edge with identical energy and impinging angle as the Cr neutrals and that (ii) they are then accelerated in a collisionless sheath. The resulting impinging angle distribution at 1.0 Pa, assuming that the potential drop at the substrate is equal to the plasma potential in DOMS (ΔV= 3.5 V, see in paper Cr03), is shown in figure 5.5b).

As can be observed in Figure 5.5b), the acceleration in the substrate's sheath has dramatic effect on the angle distribution of thermalized ions. Their impinging angle after acceleration is close to 5° irrespectively of their initial trajectories and, thus, they are

responsible for the intense and narrow peak in the overall ions angle distributions. This is due to their very low initial velocity that give rise to a longer acceleration period.

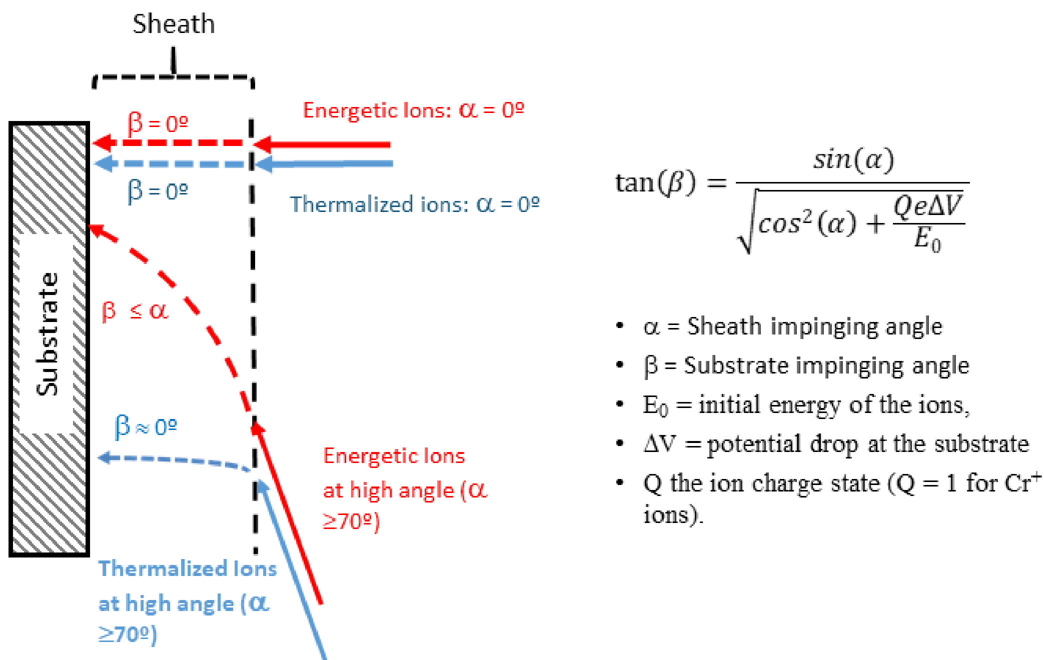

Figure 5.6. Schematic of Cr species trajectories as a function of their energy and initial impingement angle at the substrate. In this figure is also plotted the equation that gives the angle of impingement of the ion at the substrate surface (β) as a function the angle of the ion trajectory when arriving at the sheath (α).

The angle distribution of the non-thermal ions is also considerably compressed to lower impinging angles although it still extends to slightly greater than 50º. Thus, the acceleration of the Cr^+ ions at the substrate sheath significantly reduces the high angle component of the ions impinging angle distribution and, thus, efficiently reduces the atomic shadowing mechanism strength. The atomic shadowing effect, which develops during film growth, is thus prevented not by counteracting the atomic shadowing mechanism, as is usually the case in DCMS upon substrate biasing or upon another kind of high energy particle bombardment, but rather by decreasing the strength the atomic shadowing mechanism itself. Although both the energetic (ballistic) Cr ions and the thermalized ones contribute to weaken the shadowing mechanism, the later assume a much more prominent role. On one hand, thermalized neutrals are the primary particles influencing the strength of the atomic shadowing mechanism since the majority of particles impinging on the growing film at high angles in DCMS are thermalized. On the other hand, the thermalized ions are most efficiently influenced by the electric field at the substrate sheath. They end up

impinging on the substrate at angles close to the substrate normal, and thus, they have almost no contribution to the shadowing effect. As a result, ionizing the sputtered species is an efficient way of decreasing the shadowing mechanism, especially at higher pressure since the sputtered flux arriving at the substrate substrate's sheath edge has a higher diffusive (thermalized) component and lower energy ions.

5.6. General overview of DOMS

5.6.1. Deposition rate in DOMS

The lower deposition rate for HiPIMS as compared to DCMS at the same average power is one of the main drawbacks of this process. One of the main reasons for the successful implantation of magnetron sputtering-based processes at industrial level is the high mass productivity, which is mainly determined by the deposition rate. Therefore, the lower deposition rate usually found in HiPIMS threatens its market penetration and limits its potential applications in industry. This issue is one of the most discussed topics in the field of HiPIMS and has motivated many publications [15-19]. A similar loss of deposition rate in comparison to DCMS was found in this work for the DOMS process. At high peak power, the deposition rate is much lower than in DCMS in all the systems studied in this work, which makes the DOMS technique less attractive for industrial use. As the loss of deposition rate increases with increasing peak power, one possible solution to mitigate this issue is to use low peak powers during deposition. In DOMS, the deposition rate at low Pp is typically twice higher than the deposition rate at high Pp. Although using low peak powers brings about a lower degree of ionization of the sputtered species, this does not necessarily compromise the films properties and may even be beneficial as is shown in this work.

5.6.2. Energetic ions bombardment in DOMS

One of the most important advantages of HiPIMS as compared to DCMS is the increased ion bombardment. On one hand, the energy of the sputtered species impinging on the film during growth in HiPIMS is higher than that of the neutral sputtered atoms in DCMS. On the other hand, the momentum transfer of the incoming sputtered ions in HiPIMS is much more efficient than that of the Ar ions used in DCMS to bombard the growing film upon substrate biasing. As a result, many publications report on the deposition of denser films with less columnar microstructures in HiPIMS as compared to DCMS [20, 21]. The generation of highly energetic metal ions and the subsequent densifying effect on the thin film microstructure was also found in this work for the DOMS deposition process. In all the deposition system studied in this work, dense and almost featureless microstructures were

deposited at high peak power, even at high pressure and without substrate biasing. As in substrate biasing in DCMS, increasing the peak power in HiPIMS allows counteracting the atomic shadowing effect and thus results in the deposition of much smoother films. However, increasing the peak power leads to the generation of defects such as voids and interstitials and consequent re-nucleation processes. Thus, increasing the peak power brings about a compromise between the film properties and the formation of compressive stresses in a similar way as increasing the substrate bias in DCMS.

5.6.3. Control of the shadowing mechanism in DOMS

A new strategy aiming at taking advantage of the ionization of the sputtered species for thin film deposition by HiPIMS was identified in this work. Rather than relying on the increased energy of the sputtered species to counteract the shadowing effect, it was shown that in DOMS the shadowing mechanism could be effectively controlled. Thus dense and homogeneous films could be deposited at low peak power by decreasing the shadowing mechanism, or even by completely prevent it, rather than by decreasing its effectiveness, as is usually the case in magnetron sputtering when using highly energetic bombardment. Thus, in DOMS dense and tightly packed microstructures can be deposited even without the need of highly energy particles bombardment during growth, avoiding defect formation and compressive stresses development that are usually associated with high bombardment energy. In DOMS, the shadowing effect is regulated by the ionization degree of the sputtered material instead of process pressure and substrate biasing as is usually the case in DCMS. Thus, the shadowing mechanism can even decrease with increasing pressure, as both the fraction of thermalized ions and the degree of ionization of the sputtered material increase. Consequently, substrate biasing may even be superfluous with regard to controlling the atomic shadowing effect as the shadowing mechanism is already efficiently prevented.

As noted in section 2.2.3, the SDZ proposed by Anders [41] for HiPIMS encompasses the existence of a region of possible low-temperature low-energy ion-assisted epitaxial growth near the conjunction of zones T, 2 and 3. As referred by the author, this deposition region corresponds to a very narrow energy window where the impinging particles at the substrate have enough energy to promote surface diffusion of ad-atoms without creating defects in film bulk. Although the films deposited by DOMS at low peak

power in this work are not epitaxial, they have much higher grain sizes and lower compressive stresses than their high peak power counterparts do. It is thus argued in this work that these films correspond to the low-temperature low-energy ion-assisted growth proposed by Anders. Note, however, that this result is only achieved because there is an intrinsic reduction of the strength of the shadowing mechanism in the HiPIMS process.

5.6.4. Backscattered species in DOMS

Besides the bombardment of sputtered species and discharge gas ions upon substrate biasing (usually Ar^+), thin films deposited by magnetron sputtering-based processes are also subjected to the bombardment of backscattered neutrals atoms coming from the target. Depending on the target materials and composition of the discharge gas, these backscattered species can have a preponderant effect on the deposited films properties. In this work it was shown that the backscattered nitrogen neutrals formed upon CrN films deposition by DOMS were responsible for an energetic "background bombardment" independent of the peak power and ultimately responsible for the high compressive stresses found in the films. The main reason for this is the high voltage characteristic in DOMS depositions, as compared to DCMS depositions, which directly increases the energy of the backscattered nitrogen atoms impinging on the growing film. Note, however, that the bombardment by energetic N can also occur in DCMS as demonstrated by Sarakinos et al. [81]. Nevertheless, the energetic bombardment with nitrogen neutrals is more prone to occur in DOMS or, for that matter, in HiPIMS. The bombardment by energetic backscattered neutrals is not restricted to the CrN system or even to nitride-based deposition systems. In a study about the deposition of TiN films by DOMS, Oliveira et al. [99] also reported that the properties of the films were significantly influenced by nitrogen neutrals backscattered at the target. On the other hand, it is well known that in DCMS backscattered Ar neutrals may have a decisive influence on the films properties. In the latter case, this effect is most important when sputtering from target composed of heavy elements. In fact, the backscattered Ar neutrals may be at the origin of the properties of the Ta films deposited in this work by DOMS, as suggested in section 4.2. On the overall, the characteristically higher voltages of DOMS and HiPIMS will amplify the effect of the energetic backscattered species that bombard the films during growth in comparison to DCMS. However, the importance of this effect will depend on the

particular deposition systems and background gas composition and, namely, on the probability of backscattering of the ions impinging on the target in each particular system.

One possible solution for overcoming the effect of the energetic backscattered neutrals is to increase the deposition pressure. If the latter is high enough, most of the species travelling in the deposition chamber will be thermalized, including the backscattered species It could then be possible to extract these ions from the plasma and control their energy by biasing the substrate. This solution could not be tested in the deposition system used in this study due to severe arcing above 0.8 Pa, mainly due to the occurrence of corona discharges at the back of the cathode. Another alternative is use HiPIMS power supplies that operate at lower deposition voltages and thus reduce the energy of the backscattered species.

5.6.5. Industrial advantages of DOMS

One of the main advantages reported in the literature for HiPIMS over other IPVD deposition process is that it allows generating highly ionized fluxes of sputtered material while using essentially the same equipment as in DCMS except for the power supply. This "plug and Play" characteristic of HiPIMS has been confirmed in this work. The Cyprium power supply was used to deposit thin films in five different deposition systems without the need of any modification or adaptation in the deposition system. The only limitation found in this work was the severe arching at deposition pressures above 1.0 Pa that was attributed to the formation of corona discharges due to the high deposition voltages. Note however that this limitation was not found upon testing the DOMS power supply in a deposition chamber in which the cathodes were fitted in the chamber walls, in opposition to the deposition system used in this work in which the cathodes are placed inside the deposition chamber.

In a DCMS deposition systems the average intensity of the shadowing effect is firstly determined by the deposition geometry and depends on the average angle of the sputtered atoms coming from the racetrack and reaching the substrate without collisions with the gas phase. In DCMS, this "intrinsic" shadowing mechanism can only be counteracted to a certain degree by changing the deposition pressure. In DOMS, the "intrinsic" shadowing mechanism can be significantly decreased or even prevented. Thus, the DOMS process allows a much greater independence of the films properties on the specific geometry and dimensions of the deposition system. This constitutes an important technological advantage as up-scaling of

the films deposition processes from the deposition system used for development to those used for mass production is facilitated.

Another important technological feature of DOMS is that the additional control of the impinging flux allows minimizing the effects of geometrical asymmetries of the deposition system, such as substrate rotation and asymmetric targets, in the films properties. As pointed out by Greczynski et al. [84], this is an important issue at the industrial level as thin films are usually deposited in large batches and several degrees of rotations are necessary to expose the substrate surface to the impinging flux of atoms coming from the target. On the other hand, typical targets used for mass production are highly asymmetric. In these conditions, the DOMS process, and more generally the HIPIMS process, allows depositing thin films with much more uniform and similar properties.

Chapter VI

6. HARD HYDROGEN-FREE DIAMOND LIKE CARBON COATINGS DEPOSITED BY DOMS.

6.1. Introduction

In this chapter, the results obtained regarding the development of hydrogen-free hard carbon films for application in piston rings of internal combustion engines (ICE) are presented and discussed. The effect of substrate biasing was first studied as the formation of sp^3 links is directly correlated with the energy of the film forming species that impinge on the growing film during deposition. The morphology, mass density, structure and mechanical properties of the DLCs films were studied and discussed as well as a preliminary study of their temperature resistance. This study was published in the journal Surface and Coatings Technology (C01) and only a brief summary of the main conclusions is presented in section 6.2 of the present chapter.

The main strategy to achieve ionization of the sputtered species in HiPIMS is to promote electron impact ionization trough increasing the plasma density. However, this route is not effective for C which exhibit a low electron-impact ionization cross-section [44]. An alternative strategy to increase the ionization reaction of the sputtered carbon species is to increase the electron temperature of the discharge. This can be achieved by using gases with higher ionization energy than Ar (15.6 eV), such as Ne (21.56 eV). In the third section of this chapter, the effect of adding Ne to the discharge gas on the properties of hard DLC films is investigated and discussed.

As state in paper C01, a Cr and/or soft C adhesion interlayer was deposited before the DLC films in all the depositions carried out in the study of the effect of substrate biasing. However, it was found that the adhesion of the films was not adequate for tribological testing and that the DLC films peeled off the substrate almost immediately at the beginning of pin-

on-disk tests. In order to measure the tribological properties of the films a new adhesive interlayer (based on Cr and CrN layers) was developed in the aim of the TANDEM project. In section 6.4 of this chapter the results obtained from the pin-on-disk test of DLC films deposited using the improved adhesive interlayer are presented both as a function of substrate biasing and the addition of Ne to the discharge gas. Finally, this chapter ends with a discussion about the potential of the DOMS process for the deposition of hard hydrogen-free DLC films (section 6.5).

6.2. Influence of substrate biasing

The effect of substrate biasing on the properties of hard hydrogen-free DLC films was studied within the range from - 40 to - 100 V (C01). The main deposition condition used in this study are shown in table 3.6. On the overall, increasing the substrate bias results in the deposition of smoother and denser DLC films. The surface morphology of the films gradually changes from a cauliflower-type at lower biases to a smooth surface with almost imperceptible structures. On the other hand, the columnar microstructure observed at lower biases is transformed into a much more compact one with featureless cross section. Both the mass density and the hardness of the films increase with increasing bias voltage, from 1.8 to 2.5 g/cm^3 and from 15 to 23 GPa, respectively.

As shown by Robertson et al. [100], the mass density of DLC films is directly correlated to their sp^3 content (linear relationship). The formation of sp^3 bonds in DLC films is achieved by subplantation of energetic carbon species into the subsurface region of the growing film which promotes the formation of dense amorphous films [101, 102]. Thus, the increase in film density with increasing bias is consistent with the formation of an increasing number of sp^3 bonds. This conclusion agrees well with the results obtained by Raman spectroscopy as the I_D/I_G ratio obtained from the fitting of the Raman spectra exhibits a decrease with increasing bias voltage which in accordance with the Ferrari three-stage model indicates an increasing sp^3 content [103]. The most plausible explanation for the formation of sp^3 bonds in the films is the ionization of the sputtered carbon species in DOMS and the consequent bombardment by both C and Ar ions with hyper thermal energy. The strong and directional sp^3 bonding of carbon atoms results in the formation of a three-dimensional (tetrahedral) network of σ bonds which increases the hardness of DLC films [104, 105].

Thus, the increasing hardness of the DLC films deposited by DOMS with increasing substrate biasing correlates well with the increasing sp^3 content in the films previously inferred from the mass density measurement

6.3. Influence of Ne content in discharge gas

The cross sectional micrographs from the DLC coatings deposited with a – 80 V substrate bias and a Ne content from 0 to 50 % in the discharge gas are shown in figure 6.1. A Cr + CrN interlayer was deposited over the Si and steel substrates. As can be observed in all the cross section micrographs, the Cr + CrN interlayer has an open columnar microstructure, which is known to form tensile stresses that contribute to counteract the compressive stress formed upon DLC films deposition. All the DLC films display compact microstructures similar to the one observed for the DLC film deposited in pure Ar discharge (figure 6.1a)). However, increasing the Ne content in the discharge gas results in microstructures less influenced by the microstructure of the adhesion interlayer. This conclusion is more evident for the film deposited with – 80V of bias and with a Ne content of 50 % as the DLC layer microstructure seems to be completely independent of the columnar structure of the adhesion layer.

The deposition rate of the DLC films as calculated from the thickness of the films SEM micrographs is shown in figure 6.2 as a function of the Ne content in the discharge gas. Although the deposition rate seems to present a small decreasing trend with increasing Ne content, the deposition rate variations are close to the error limit of the measurements. On the overall adding Ne to the plasma does not significantly influences the deposition rate.

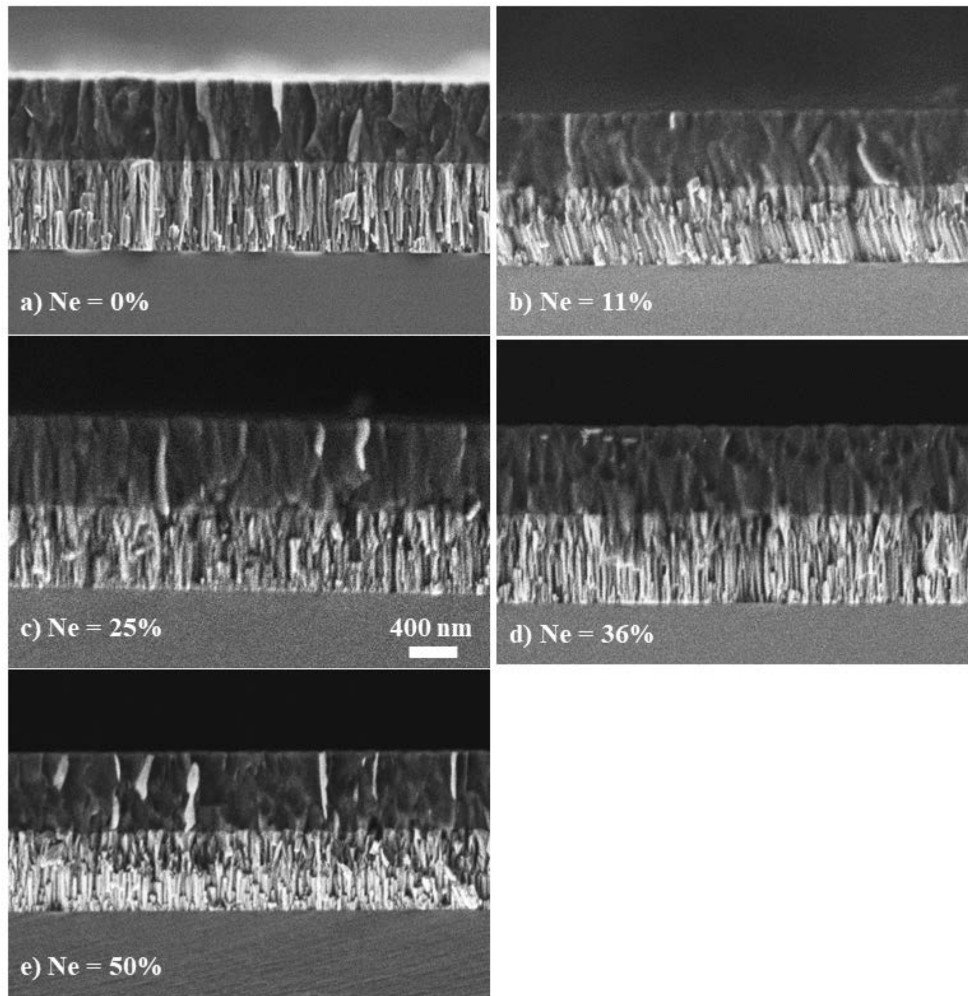

Figure 6.1. Cross section micrographs of DLC coatings with different Ne content in the discharge gas.

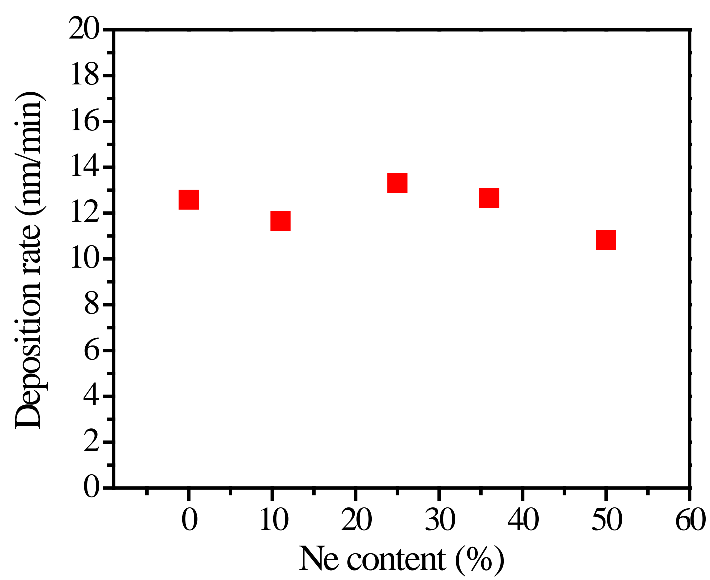

Figure 6.2. Deposition rate of DLC coatings with different Ne content in the discharge gas.

Raman spectra of DLC usually exhibit at least two distinct broad bands, the "graphitic carbon" (G) band located above 1500 cm^{-1} and the "disordered carbon" (D) band, located at lower Raman shifts than the G band. The absolute and relative features of these bands, such as position and full with at half maximum, can be used to gain information about the structure of the films. However, both bands convey information mainly about sp^2-bonded carbon atoms and only indirect information about sp^3-bonded carbons can be inferred. The main advantage of using UV radiation instead of visible light in Raman spectroscopy is that the higher energy photons are able to directly probe the sp^3-bonded carbon atoms and thus originate a third broad band located near 1040 cm^{-1}, the so-called T band.

The Raman spectra for DLC coatings deposited by DOMS with increasing Ne in the plasma measures using UV radiation are shown in figure 6.3. Each spectrum can be deconvoluted into only two Raman peaks, located close to 1438 and 1580 cm^{-1}, which were identified as the D and G bands, respectively. The so-called T band is not observed in the measured Raman spectra, irrespectively of Ne content. Therefore, only indirect information about the sp^3-bonded carbons, inferred from the characteristics of the D and G peaks, can be extracted from the Raman spectra of the deposited films.

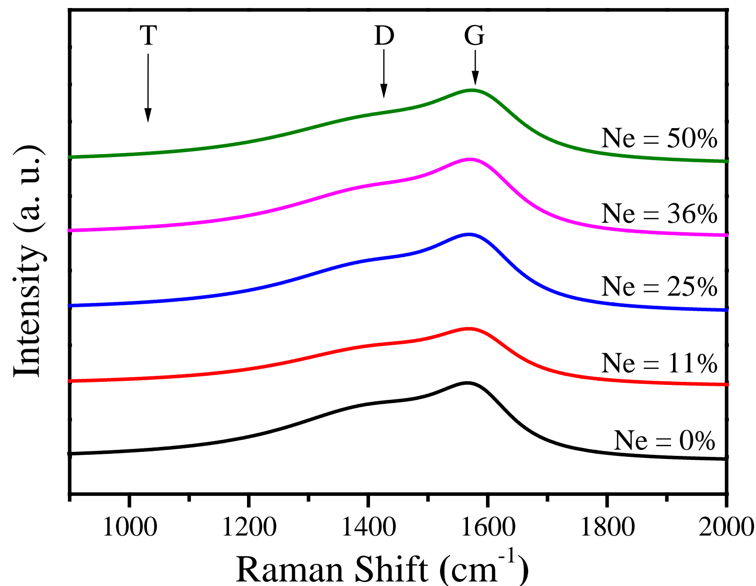

Figure 6.3. Raman spectra of the DLC films as a function of the Ne content in the plasma.

In this work, the intensity ratio I_D/I_G was used to probe the sp^3 to sp^2 ratio in the DLC films following the Ferrari three-stage model [103]. The D and G peaks were fitted using

Lorentzian and Breit-Wigner-Fano (BWF) line shapes respectively. The I_D/I_G ratio obtained from the fitted spectra (see figure 6.4) exhibit an initial decrease with increasing Ne content up to 25 % and stabilizes at the highest Ne contents. According to the Ferrari three-stage model, the initial decreasing of the I_D/I_G ratio can be interpreted as an increase of the sp^3/sp^2 ratio in the films up to ~ 20 %. The stabilization of the I_D/I_G ratio at higher Ne contents is also compatible with an increasing sp^3/sp^2 ratio in the films as the deposition of a-C films is gradually substituted by ta-C films.

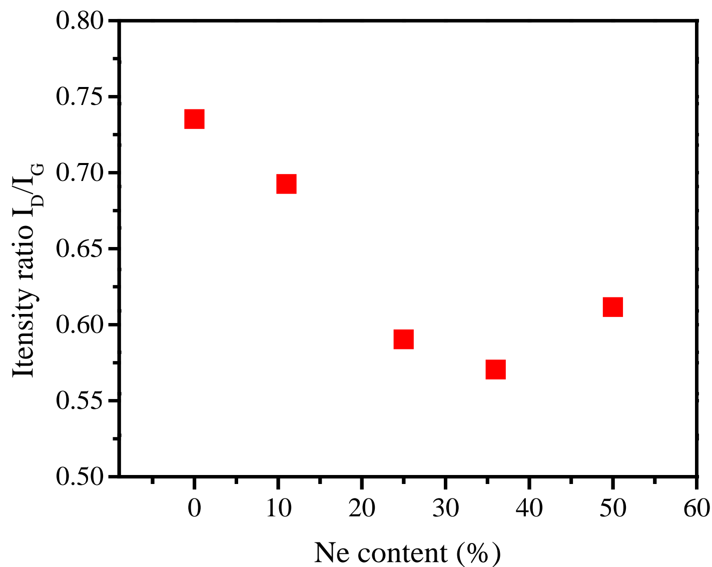

Figure 6.4. Eovolution of the I_G/I_D ratio as a function of the Ne content in the plasma.

The hardness of the DLC films is shown in figure 6.5 as a function of the Ne content in the discharge gas for two different indentation loads, 3 and 5 mN. By increasing Ne content from 0 to 50%, while keeping substrate bias at -80V, the hardness of the coating increases approximately from 14 to 25 GPa.

The Young's modulus of the DLC films is shown in figure 6.6 as a function of the Ne content in the discharge gas for two different indentation loads, 3 and 5 mN. The evolution of the Young's modulus with increasing Ne content in the discharge gas does not follow a monotonic trend. Although the Young's modulus of the films deposited at the two higher Ne contents in the discharge gas are tendentially higher than that of the films deposited with lower Ne contents, this trends cannot be conclusively established based on the available results.

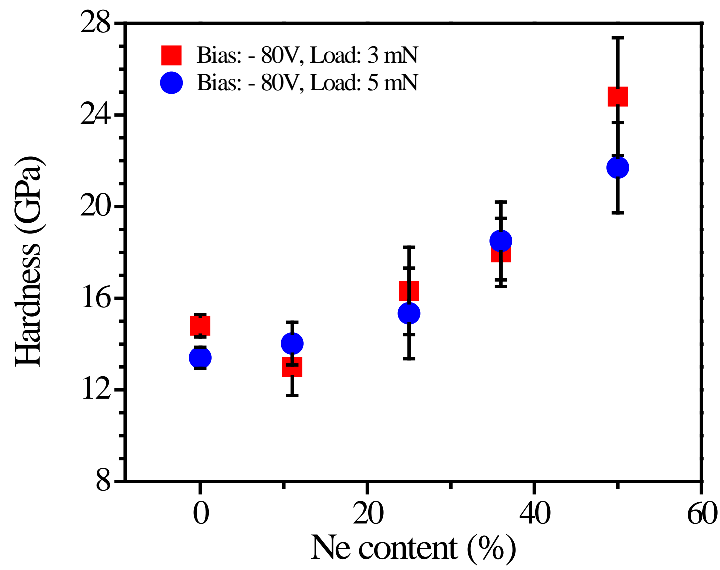

Figure 6.5. Hardness of DLC coatings with different Ne content in discharge gas.

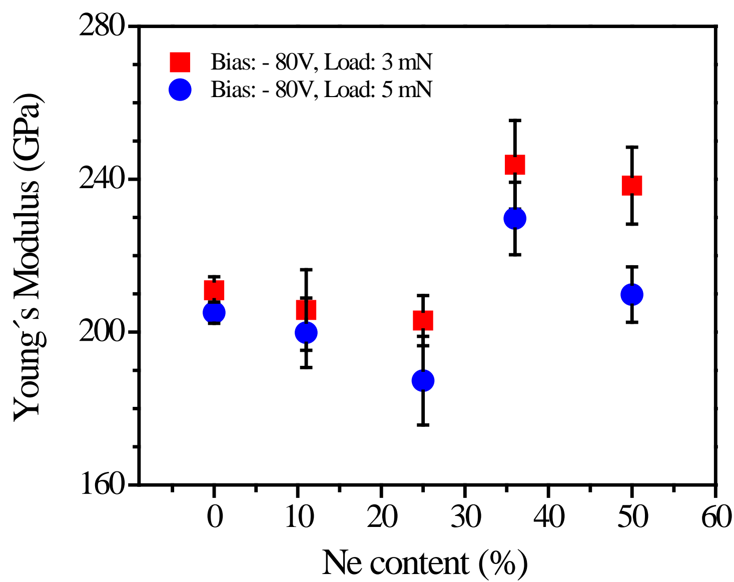

Figure 6.6. Young's modulus for DLC coatings with different Ne content in discharge gas.

6.4. **Tribological properties of the DLC films**

The evolution of the coefficient of friction during the pin-on-disc tests of the DLC coatings is shown in figure 6.7 as a function of the substrate bias. The experimental condition used to perform the pin-on-disc test are described in section 3.5. The raw data acquired during the tests was smoothened to facilitate the results analysis. A running-in period characterized by higher values of the friction coefficient is observed at the beginning of all tests. After this period, the pin-on-disk tests reach a steady state regime characterized by an almost constant friction coefficient. The friction coefficient averaged over the last 50 m of sliding, i.e., within the study state regime, is shown in figure 6.8 as a function of the substrate bias. The low friction coefficients measured for all the films (between 0.1 and 0.15) are typical of DLC films. The friction coefficient remains constant with increasing substrate bias.

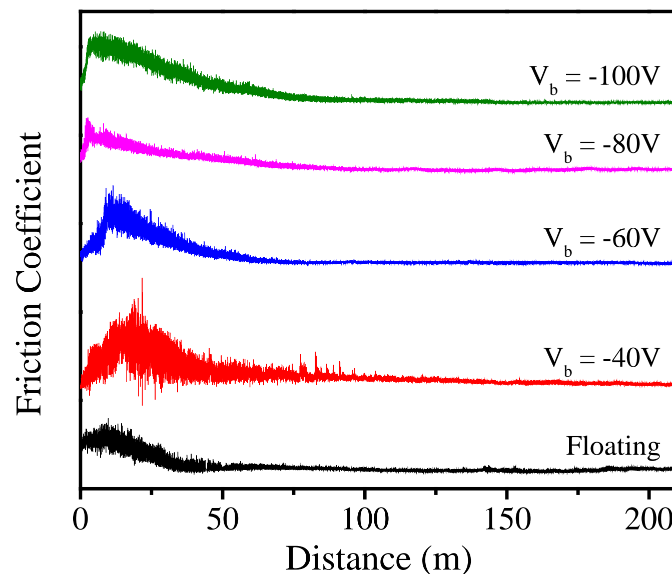

Figure 6.7. Friction coefficient graphs for DLC coatings with different substrate bias.

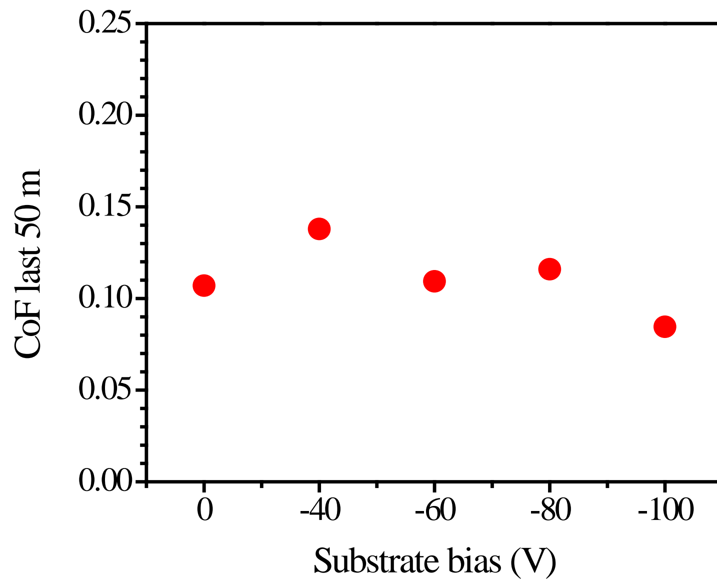

Figure 6.8. Coefficient of friction for last 50 m of sliding of the DLC coatings deposited with different substrate biasing.

SEM micrographs of the wear tracks resulting from the pin-on-disk test performed with different substrate biases are shown in figure 6.9. As can be observed in this figure, the wear-tracks of the films deposited with a substrate bias up to – 60 V display large wear tracks characteristic of significantly worn surfaces. On the other hand, the surface of the films deposited at higher substrate biases is much less worned, as can be concluded from the much lower width of the wear tracks. These results agree well with the increasing hardness of the films as measured by nano-indentation.

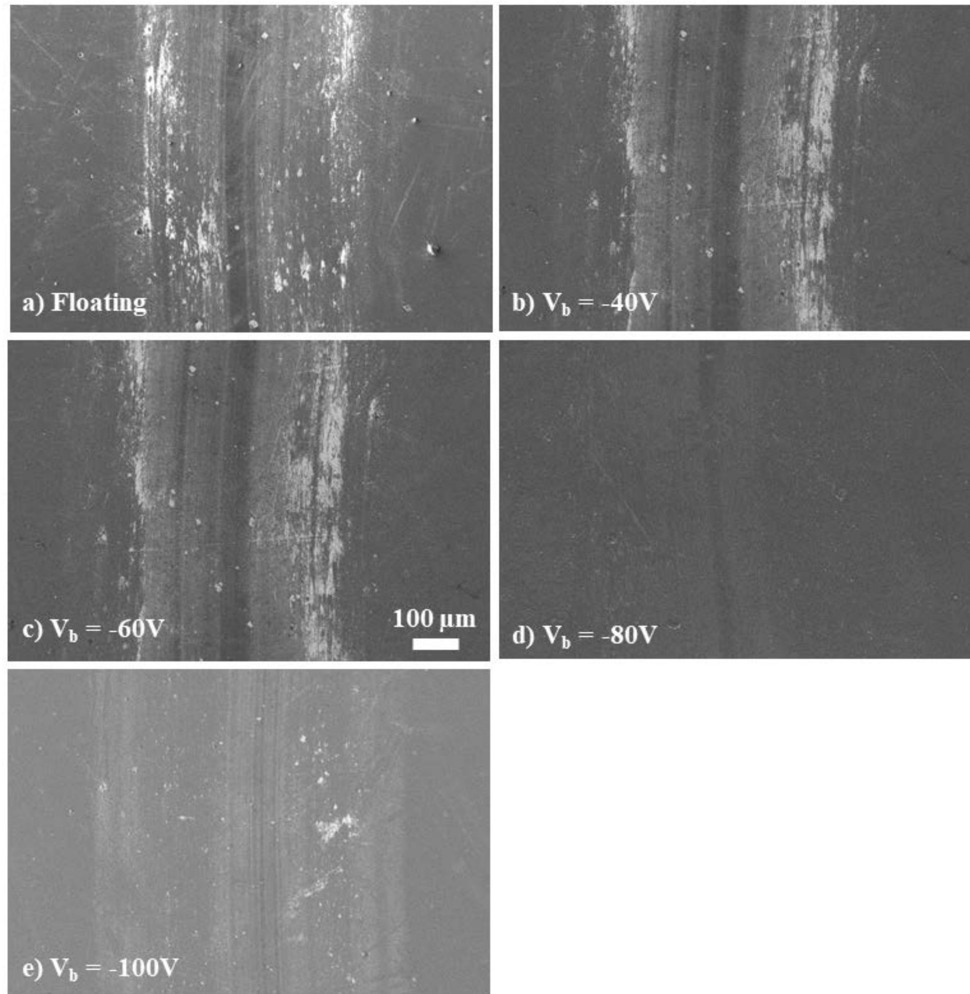

Figure 6.9. Wear track for DLC coatings with different substrate bias in pin-on-disc; a) Floating; b) -40V; c) -60V; d) -80V; e) -100V; with the magnification of 200X

The evolution of the coefficient during the pin-on-disk tests of DLC coatings deposited with a substrate bias of – 80 V and with different Ne content in the discharge gas is shown in figure 6.10. The experimental condition are the same as used for the pin-on-disc performed as a function of substrate bias. The raw data acquired during the tests was smoothened to facilitate the results analysis. Once again, the results show a running in period at the beginning of the tests followed by a steady state regime of the friction coefficient. The friction coefficient averaged over the last 50 m of sliding is shown in figure 6.11 as a function of the Ne content in discharge gas. Once again, the low friction coefficients measured for all the films (between 0.1 and 0.15) are typical of DLC films. On the overall, the addition of Ne to the discharge gas does not significantly influence the friction coefficient during the pin-on-disks tests.

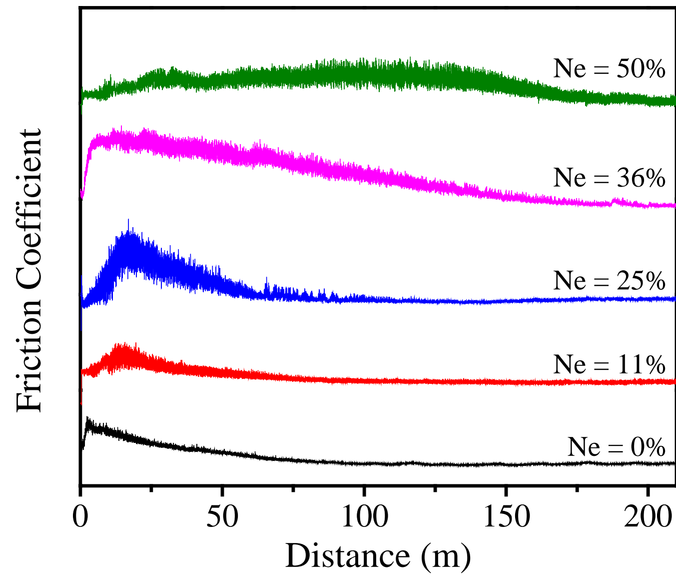

Figure 6.10. Coefficient of friction for DLC coatings with different Ne content.

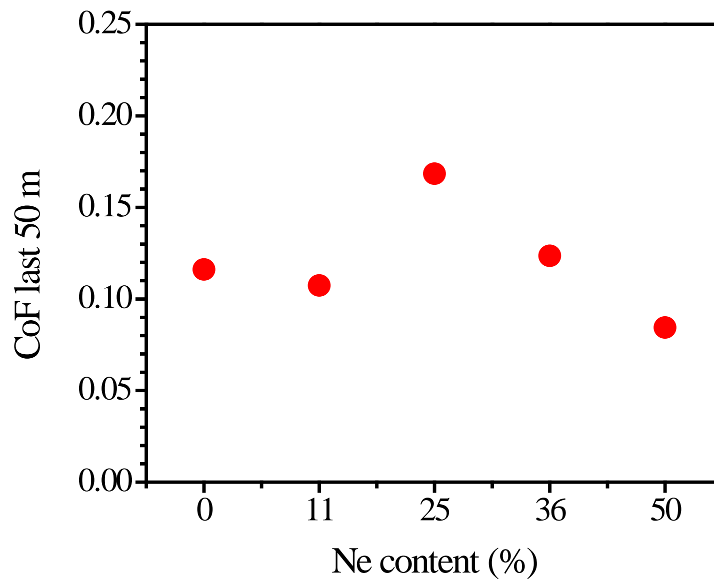

Figure 6.11. Coefficient of friction for last 50 m of sliding for DLC with Ne content.

6.5. Potential of the DOMS for C deposition

As already referred in the general introduction, the main objective of the last part of this work was to use the DOMS process for the development of solutions that correspond to actual needs of the thin film industry. The selected challenge was to deposit hydrogen-free hard carbon films by DOMS for application in piston rings. Taking advantage of the DOMS capabilities identified in the previous chapters for the deposition of carbon-based films by DOMS is a challenging task as the degree of ionization of C in HiPIMS is much lower than that of the sputtered metallic species previously studied. As the formation of sp^3 links in DLC films relies on the subplantation of hyper-thermal carbon ions, the addition of Ne to the plasma was tested in this work as a strategy to increase the C ionization degree by increasing the electronic temperature of the plasma. Although the addition of Ne to the plasma resulted in a consistent increase of hardness of the films without degrading its tribological properties, the results indiciate that the ionization degree of the carbon species was not substantially increased. Thus, the performance of the DLC films deposited in this work fall short of that required for application in piston rings of internal combustion engines. Although several other strategies to increase the ionization degree of the sputtered carbon atoms in HiPIMS are foreseen in the TANDEM project, the results obtained in this work highlight a crucial limitation of HiPIMS and DOMS: both processes rely crucially on the high ionization degree of the sputtered material. This limitation restricts the range of materials that can be deposited by HiPIMS while taking advantage of the special capabilities of this deposition process.

Chapter VII

7. CONCLUSIONS AND FUTURE DEVELOPMENTS

7.1. Conclusions

As with others variants of HiPIMS, a loss of deposition rate in comparison to DCMS was found in this work for the DOMS process. At high peak power, the deposition rate is much lower than in DCMS in all the systems studied in this work, which makes the DOMS technique less attractive for industrial use. As the loss of deposition rate increases with increasing peak power, one possible solution to mitigate this issue is to use low peak powers during deposition.

The generation of highly energetic metal ions and the subsequent densifying effect on the thin film microstructure was also found in this work in DOMS. In all the deposition system studied in this work, dense and almost featureless microstructures were deposited at high peak power, even at high pressure and without substrate biasing.

A new strategy aiming at taking advantage of the ionization of the sputtered species for thin film deposition by HiPIMS was identified in this work. Rather than relying on the increased energy of the sputtered species to counteract the shadowing effect, it was shown that in DOMS the shadowing mechanism could be effectively controlled. Thus dense and homogeneous films could be deposited at low peak power by decreasing the shadowing mechanism, or even by completely prevent it, rather than by decreasing its effectiveness, as is usually the case in magnetron sputtering when using highly energetic bombardment.

In this work it was shown that the backscattered nitrogen neutrals formed upon CrN films deposition by DOMS were responsible for an energetic "background bombardment" independent of the peak power and ultimately responsible for the high compressive stresses found in the films. On the overall, the characteristically higher voltages in DOMS will

amplify the effect of the energetic backscattered species that bombard the films during growth in comparison to DCMS.

One of the main advantages reported in the literature for HiPIMS over other IPVD deposition process is that it allows generating highly ionized fluxes of sputtered material while using essentially the same equipment as in DCMS except for the power supply. This “plug and Play” characteristic of HiPIMS has been confirmed in this work. The Cyprium power supply used in this work allowed for the successful deposition of thin films in five different deposition systems without the need of any modification or adaptation in the deposition system.

In DOMS, the “intrinsic” shadowing mechanism associated to the deposition system configuration can be significantly decreased or even prevented. Thus, the DOMS process allows a much greater independence of the films properties on the specific geometry and dimensions of the deposition system. This constitutes an important technological advantage as up-scaling of the films deposition processes from the deposition system used for development to those used for mass production is facilitated. On the other hand, the additional control of the impinging flux allows minimizing the effects of geometrical asymmetries of the deposition system, such as substrate rotation and asymmetric targets, in the films properties.

The performance of the DLC films deposited in this work fall short of that required for application in piston rings of internal combustion engines. The main reason for this is the low ionization degree of C in HiPIMS. Although a adding Ne to the plasma was studied in this work as a strategy to increase the ionization degree of the sputtered carbon atoms in HiPIMS, the results obtained in this work highlight a crucial limitation of HiPIMS and DOMS: both processes rely crucially on the high ionization degree of the sputtered material. This limitation restricts the range of materials that can be deposited by HiPIMS while taking advantage of the special capabilities of this deposition process.

7.2. **Future developments**

Taking into account the results and conclusions obtained in this work, one fundamental question remains to be answered: does the DOMS process worth it?

As any other deposition process, the DOMS process has strong and weak points that than be exploited and must be avoided, respectively. Regarding the positive points of DOMS, the most exiting feature found in this work is the ability to deposit dense and smooth thin films without the need of energetic bombardment. This feature opens the door to the possibility of depositing thin films with much lower compressive stresses, and still preserve the excellent mechanical and tribological properties characteristic of many magnetron sputtered films. A project proposal regarding the deposition of TiAlN films by DOMS is currently being matured at SEG-CEMPPRE, in order to take advantage of this feature to developed hard stress free TiAlN films for mechanical and tribological applications. However, the ability to deposit dense and smooth thin films without the need of energetic bombardment has a great potential in many other thin film applications.

Another positive point of HiPIMS is its lower dependence of the films properties on the physical characteristics of the deposition system, including the size and geometry of both the deposition chamber and the targets. This feature can be very important both during the development process of a thin film and in its mass production in industry. Although the higher independence of the films properties on the deposition system was demonstrated at the laboratory scale in this work, its real impact in actual up-scaling and deposition in industrial system remains to be confirmed.

Besides the well-known loss of deposition rate in HiPIMS as compared to DMCS, the main drawback of the DOMS process is the increased influence of the bombardment by energetic neutrals backscattered from the target. This feature limits the use of DOMS in deposition systems were a high probability of backscattering exists, such as is the case of the CrN deposition system studied in this work. Although the deposition of oxide-based films was not studied in this work, it is anticipated that the energetic negative oxygen ions generated in the vicinity of the target in reactive magnetron sputtering with oxygen will also be responsible for a detrimental bombardment of the films during growth in DOMS.

One possible strategy to avoid any kind of detrimental energetic bombardment in DOMS is to take advantage of the higher limit of the deposition pressure window as compared to DCMS. As was shown for both Cr and TiSiN system in this work, the DOMS

process can be used to deposit thin films at higher pressures than conventional sputtering, while still achieving bulk-like densities and properties. At high pressure, the number of collisions in the gas phase is greatly increased and most of the plasma species are thermalized, including any energetic species coming from the target. It could then be possible to extract the metallic ions from the plasma and control their energy by biasing the substrates. This strategy could not be tested in the deposition system used in this work due to severe arcing above 0.8 Pa, mainly due to the occurrence of corona discharges at the back of the cathode.

On the overall, in spite of the inherent limitations of DOMS and HiPIMS, both processes bring about new solutions for thin film deposition that are not available in DCMS even with substrate biasing, while still preserving the technological and industrial flexibility characteristic of magnetron sputtering-based depositions processes. Therefore, both processes are worth it either from the technological or industrial point of view.

REFERENCES

[1] U. Helmersson, M. Lattemann, J. Bohlmark, A. P. Ehiasarian, and J. T. Gudmundsson, "Ionized physical vapor deposition (IPVD): A review of technology and applications," *Thin Solid Films,* vol. 513, pp. 1-24, 2006.

[2] A. Ehiasarian, A. Vetushka, Y. A. Gonzalvo, G. Sáfrán, L. Szekely, and P. Barna, "Influence of high power impulse magnetron sputtering plasma ionization on the microstructure of TiN thin films," *Journal of Applied Physics,* vol. 109, p. 104314, 2011.

[3] V. Kouznetsov, K. Macák, J. M. Schneider, U. Helmersson, and I. Petrov, "A novel pulsed magnetron sputter technique utilizing very high target power densities," *Surface and coatings technology,* vol. 122, pp. 290-293, 1999.

[4] D. Lundin and K. Sarakinos, "An introduction to thin film processing using high-power impulse magnetron sputtering," *Journal of Materials Research,* vol. 27, pp. 780-792, 2012.

[5] J. Lin, J. Moore, W. Sproul, B. Mishra, J. Rees, Z. Wu*, et al.*, "Ion energy and mass distributions of the plasma during modulated pulse power magnetron sputtering," *Surface and Coatings Technology,* vol. 203, pp. 3676-3685, 2009.

[6] J. Lin, J. J. Moore, W. D. Sproul, B. Mishra, and Z. Wu, "Modulated pulse power sputtered chromium coatings," *Thin Solid Films,* vol. 518, pp. 1566-1570, 2009.

[7] J. Lin, W. D. Sproul, J. J. Moore, Z. Wu, S. Lee, R. Chistyakov*, et al.*, "Recent advances in modulated pulsed power magnetron sputtering for surface engineering," *JOM Journal of the Minerals, Metals and Materials Society,* vol. 63, pp. 48-58, 2011.

[8] J. Gudmundsson, N. Brenning, D. Lundin, and U. Helmersson, "High power impulse magnetron sputtering discharge," *Journal of Vacuum Science & Technology A: Vacuum, Surfaces, and Films,* vol. 30, p. 030801, 2012.

[9] M. Bowes, "Plasma diagnosis of reactive high power impulse magnetron sputtering (HiPIMS) discharges," University of Liverpool, 2014.

[10] S. Rossnagel and H. Kaufman, "Current–voltage relations in magnetrons," *Journal of Vacuum Science & Technology A: Vacuum, Surfaces, and Films,* vol. 6, pp. 223-229, 1988.

[11] J. A. Hopwood, "The role of ionized physical vapor deposition in integrated circuit fabrication," *Thin Films,* vol. 27, pp. 1-7, 2000.

[12] D. Christie, "Target material pathways model for high power pulsed magnetron sputtering a," *Journal of Vacuum Science & Technology A: Vacuum, Surfaces, and Films,* vol. 23, pp. 330-335, 2005.

[13] D. Lundin, "The hipims process," Linköping University Electronic Press, 2010.

[14] J. Vlček, P. Kudláček, K. Burcalová, and J. Musil, "High-power pulsed sputtering using a magnetron with enhanced plasma confinement," *Journal of Vacuum Science & Technology A: Vacuum, Surfaces, and Films,* vol. 25, pp. 42-47, 2007.

[15] A. Anders, "Deposition Rates of High Power Impulse Magnetron Sputtering," in *Proc. 51th Annu. SVC Tech. Conf*, 2008, pp. 19-24.

[16] M. Samuelsson, D. Lundin, J. Jensen, M. A. Raadu, J. T. Gudmundsson, and U. Helmersson, "On the film density using high power impulse magnetron sputtering," *Surface and Coatings Technology,* vol. 205, pp. 591-596, 2010.

[17] K. Sarakinos, J. Alami, and S. Konstantinidis, "High power pulsed magnetron sputtering: A review on scientific and engineering state of the art," *Surface and Coatings Technology,* vol. 204, pp. 1661-1684, 2010.

[18] N. Brenning, C. Huo, D. Lundin, M. A. Raadu, C. Vitelaru, G. Stancu, *et al.*, "Understanding deposition rate loss in high power impulse magnetron sputtering: I. Ionization-driven electric fields," *Plasma Sources Science and Technology,* vol. 21, p. 025005, 2012.

[19] D. Lundin, C. Huo, N. Brenning, M. A. Raadu, and U. Helmersson, "Deposition rate loss in high power impulse magnetron sputtering: understanding through computational modeling," in *54th Annual Technical Conference Proceedings, Chicago, IL April 16-21, 2011*, 2011.

[20] J. Alami, P. Å. Persson, D. Music, J. Gudmundsson, J. Bohlmark, and U. Helmersson, "Ion-assisted physical vapor deposition for enhanced film properties on nonflat surfaces," *Journal of Vacuum Science & Technology A: Vacuum, Surfaces, and Films,* vol. 23, pp. 278-280, 2005.

[21] A. Ehiasarian, P. E. Hovsepian, L. Hultman, and U. Helmersson, "Comparison of microstructure and mechanical properties of chromium nitride-based coatings deposited by high power impulse magnetron sputtering and by the combined steered cathodic arc/unbalanced magnetron technique," *Thin Solid Films,* vol. 457, pp. 270-277, 2004.

[22] J. Bohlmark, M. Lattemann, J. Gudmundsson, A. Ehiasarian, Y. A. Gonzalvo, N. Brenning, *et al.*, "The ion energy distributions and ion flux composition from a high power impulse magnetron sputtering discharge," *Thin Solid Films,* vol. 515, pp. 1522-1526, 2006.

[23] G. Greczynski, J. Lu, J. Jensen, I. Petrov, J. E. Greene, S. Bolz, *et al.*, "Metal versus rare-gas ion irradiation during Ti1− x Al x N film growth by hybrid high power pulsed magnetron/dc magnetron co-sputtering using synchronized pulsed substrate bias," *Journal of Vacuum Science & Technology A: Vacuum, Surfaces, and Films,* vol. 30, p. 061504, 2012.

[24] A. Hecimovic and A. Ehiasarian, "Time evolution of ion energies in HIPIMS of chromium plasma discharge," *Journal of Physics D: Applied Physics,* vol. 42, p. 135209, 2009.

[25] S. Schmidt, Z. Czigány, G. Greczynski, J. Jensen, and L. Hultman, "Influence of inert gases on the reactive high power pulsed magnetron sputtering process of carbon-nitride thin films," *Journal of Vacuum Science & Technology A: Vacuum, Surfaces, and Films,* vol. 31, p. 011503, 2013.

[26] A. Anders, "Self-organization and self-limitation in high power impulse magnetron sputtering," *Applied Physics Letters,* vol. 100, p. 224104, 2012.

[27] A. Ehiasarian, A. Hecimovic, T. De Los Arcos, R. New, V. Schulz-Von Der Gathen, M. Böke, *et al.*, "High power impulse magnetron sputtering discharges: Instabilities and plasma self-organization," *Applied Physics Letters,* vol. 100, p. 114101, 2012.

[28] C. Maszl, W. Breilmann, J. Benedikt, and A. von Keudell, "Origin of the energetic ions at the substrate generated during high power pulsed magnetron sputtering of titanium," *Journal of Physics D: Applied Physics,* vol. 47, p. 224002, 2014.

[29] M. Palmucci, N. Britun, T. Silva, R. Snyders, and S. Konstantinidis, "Mass spectrometry diagnostics of short-pulsed HiPIMS discharges," *Journal of Physics D: Applied Physics,* vol. 46, p. 215201, 2013.

[30] M. Bowes, P. Poolcharuansin, and J. Bradley, "Negative ion energy distributions in reactive HiPIMS," *Journal of Physics D: Applied Physics,* vol. 46, p. 045204, 2012.

[31] S. Mráz and J. M. Schneider, "Energy distribution of O− ions during reactive magnetron sputtering," *Applied Physics Letters,* vol. 89, p. 051502, 2006.

[32] K. Sarakinos, D. Music, S. Mráz, M. To Baben, K. Jiang, F. Nahif*, et al.*, "On the phase formation of sputtered hafnium oxide and oxynitride films," *Journal of Applied Physics,* vol. 108, p. 014904, 2010.

[33] D. Lundin, P. Larsson, E. Wallin, M. Lattemann, N. Brenning, and U. Helmersson, "Cross-field ion transport during high power impulse magnetron sputtering," *Plasma Sources Science and Technology,* vol. 17, p. 035021, 2008.

[34] A. Anders, M. Panjan, R. Franz, J. Andersson, and P. Ni, "Drifting potential humps in ionization zones: the "propeller blades" of high power impulse magnetron sputtering," *Applied physics letters,* vol. 103, p. 144103, 2013.

[35] J. Andersson, P. Ni, and A. Anders, "Spectroscopic imaging of self-organization in high power impulse magnetron sputtering plasmas," *Applied Physics Letters,* vol. 103, p. 054104, 2013.

[36] L. Meng, A. Cloud, S. Jung, and D. Ruzic, "Study of plasma dynamics in a modulated pulsed power magnetron discharge using a time-resolved Langmuir probe," *Journal of Vacuum Science & Technology A: Vacuum, Surfaces, and Films,* vol. 29, p. 011024, 2011.

[37] R. Chistyakov, "HIPIMS Arc-Free Reactive Deposition of Non-conductive Films Using the Applied Material ENDURA 200㎜ Cluster Tool," *□□□□□□ 학술발표회초록집,* pp. 96-97, 2012.

[38] J. Lin, B. Wang, W. D. Sproul, Y. Ou, and I. Dahan, "Anatase and rutile TiO2 films deposited by arc-free deep oscillation magnetron sputtering," *Journal of Physics D: Applied Physics,* vol. 46, p. 084008, 2013.

[39] J. A. Thornton, "Influence of apparatus geometry and deposition conditions on the structure and topography of thick sputtered coatings," *Journal of Vacuum Science and Technology,* vol. 11, pp. 666-670, 1974.

[40] R. Messier, A. Giri, and R. Roy, "Revised structure zone model for thin film physical structure," *Journal of Vacuum Science & Technology A: Vacuum, Surfaces, and Films,* vol. 2, pp. 500-503, 1984.

[41] A. Anders, "A structure zone diagram including plasma-based deposition and ion etching," *Thin Solid Films,* vol. 518, pp. 4087-4090, 2010.

[42] C. A. Charitidis, "Nanomechanical and nanotribological properties of carbon-based thin films," *Journal of Refractory Metals & Hard Materials,* 2009.

[43] J. Robertson, "Diamond-like amorphous carbon," *Materials Science and Engineering: R: Reports,* 2002.

[44] J. A. Hopwood, "Thin Films: Ionized Physical Vapour Deposition, ," *Academic Press,* 2000.

[45] J. C. S.-L. a. A. Fernández, "Doping and Alloying Effects on DLC Coatings," ed, 2008.

[46] C. Ronning, E. Dreher, J.-U. Thiele, P. Oelhafen, and H. Hofsäss, "Electronic and atomic structure of undoped and doped ta-C films," *Diamond and Related Materials,* vol. 6, pp. 830-834, 1997.

[47] P. C. Ha, D. McKenzie, M. Bilek, S. Kwok, P. Chu, and B. Tay, "Raman spectroscopy study of DLC films prepared by RF plasma and filtered cathodic arc," *Surface and Coatings Technology,* vol. 201, pp. 6734-6736, 2007.

[48] J. Robertson, "Diamond-like amorphous carbon," *Materials Science and Engineering: R: Reports,* vol. 37, pp. 129-281, 2002.

[49] A. Ferrari, S. Rodil, J. Robertson, and W. Milne, "Is stress necessary to stabilise sp 3 bonding in diamond-like carbon?," *Diamond and Related Materials,* vol. 11, pp. 994-999, 2002.

[50] A. Anders, "Some applications of cathodic arc coatings," in *Cathodic Arcs*, ed: Springer, 2008, pp. 1-62.

[51] A. Aijaz, K. Sarakinos, D. Lundin, N. Brenning, and U. Helmersson, "A strategy for increased carbon ionization in magnetron sputtering discharges," *Diamond and related materials,* vol. 23, pp. 1-4, 2012.

[52] K. S. Asim Aijaz, Daniel Lundin, "A strategy for increased carbon ionization in magnetron sputtering discharges," *Diamond and related materials,* 2012.

[53] J. Lin, J. J. Moore, W. D. Sproul, S. L. Lee, and J. Wang, "Effect of negative substrate bias on the structure and properties of Ta coatings deposited using modulated pulse power magnetron sputtering," *IEEE transactions on plasma science,* vol. 38, pp. 3071-3078, 2010.

[54] A. Hecimovic and A. Ehiasarian, "Spatial and temporal evolution of ion energies in high power impulse magnetron sputtering plasma discharge," *Journal of Applied Physics,* vol. 108, p. 063301, 2010.

[55] M. Thompson, "II. The energy spectrum of ejected atoms during the high energy sputtering of gold," *Philosophical Magazine,* vol. 18, pp. 377-414, 1968.

[56] J. Emmerlich, S. Mráz, R. Snyders, K. Jiang, and J. M. Schneider, "The physical reason for the apparently low deposition rate during high-power pulsed magnetron sputtering," *Vacuum,* vol. 82, pp. 867-870, 2008.

[57] R. Franz, C. Clavero, J. Kolbeck, and A. Anders, "Influence of ionisation zone motion in high power impulse magnetron sputtering on angular ion flux and NbO x film growth," *Plasma Sources Science and Technology,* vol. 25, p. 015022, 2016.

[58] M. Panjan, R. Franz, and A. Anders, "Asymmetric particle fluxes from drifting ionization zones in sputtering magnetrons," *Plasma Sources Science and Technology,* vol. 23, p. 025007, 2014.

[59] G. Janssen, P. Alkemade, V. Sivel, S. Y. Grachev, and J.-D. Kamminga, "Anisotropic growth of chromium films during sputter deposition on substrates in planetary motion," *Journal of Vacuum Science & Technology A: Vacuum, Surfaces, and Films,* vol. 22, pp. 1773-1777, 2004.

[60] Z. Zhao, S. Yalisove, Z. Rek, and J. Bilello, "Evolution of anisotropic microstructure and residual stress in sputtered Cr films," *Journal of applied physics,* vol. 92, pp. 7183-7192, 2002.

[61] H. Ren and M. Sosnowski, "Tantalum thin films deposited by ion assisted magnetron sputtering," *Thin Solid Films,* vol. 516, pp. 1898-1905, 2008.

[62] S. Myers, J. Lin, R. M. Souza, W. D. Sproul, and J. J. Moore, "The β to α phase transition of tantalum coatings deposited by modulated pulsed power magnetron sputtering," *Surface and Coatings Technology,* vol. 214, pp. 38-45, 2013.

[63] J. Lintymer, N. Martin, J.-M. Chappe, J. Takadoum, and P. Delobelle, "Modeling of Young's modulus, hardness and stiffness of chromium zigzag multilayers sputter deposited," *Thin Solid Films,* vol. 503, pp. 177-189, 2006.

[64] T. Drüsedau, M. Löhmann, F. Klabunde, and T.-M. John, "Investigations on energy fluxes in magnetron sputter-deposition: implications for texturing and nanoporosity of metals," *Surface and Coatings Technology,* vol. 133, pp. 126-130, 2000.

[65] J. Lintymer, N. Martin, J.-M. Chappé, P. Delobelle, and J. Takadoum, "Nanoindentation of chromium zigzag thin films sputter deposited," *Surface and Coatings Technology,* vol. 200, pp. 269-272, 2005.

[66] C. Paturaud, G. Farges, M. Sainte Catherine, and J. Machet, "Correlation between hardness and embedded argon content of magnetron sputtered chromium films," *Thin Solid Films,* vol. 347, pp. 46-55, 1999.

[67] D. Hoffman and J. A. Thornton, "Internal stresses in sputtered chromium," *Thin Solid Films,* vol. 40, pp. 355-363, 1977.

[68] G. Greczynski, J. Patscheider, J. Lu, B. Alling, A. Ektarawong, J. Jensen*, et al.*, "Control of Ti 1− x Si x N nanostructure via tunable metal-ion momentum transfer during HIPIMS/DCMS co-deposition," *Surface and Coatings Technology,* vol. 280, pp. 174-184, 2015.

[69] J. Patscheider, T. Zehnder, and M. Diserens, "Structure–performance relations in nanocomposite coatings," *Surface and Coatings Technology,* vol. 146, pp. 201-208, 2001.

[70] C. Gautier and J. Machet, "Study of the growth mechanisms of chromium nitride films deposited by vacuum ARC evaporation," *Thin Solid Films,* vol. 295, pp. 43-52, 1997.

[71] C.-L. Chang, S.-G. Shih, P.-H. Chen, W.-C. Chen, C.-T. Ho, and W.-Y. Wu, "Effect of duty cycles on the deposition and characteristics of high power impulse magnetron sputtering deposited TiN thin films," *Surface and Coatings Technology,* vol. 259, pp. 232-237, 2014.

[72] M. Lattemann, U. Helmersson, and J. Greene, "Fully dense, non-faceted 111-textured high power impulse magnetron sputtering TiN films grown in the absence of substrate heating and bias," *Thin Solid Films,* vol. 518, pp. 5978-5980, 2010.

[73] S. Veprek and S. Reiprich, "A concept for the design of novel superhard coatings," *Thin Solid Films,* vol. 268, pp. 64-71, 1995.

[74] C.-L. Chang, C.-T. Lin, P.-C. Tsai, W.-Y. Ho, and D.-Y. Wang, "Influence of bias voltages on the structure and wear properties of TiSiN coating synthesized by cathodic arc plasma evaporation," *Thin Solid Films,* vol. 516, pp. 5324-5329, 2008.

[75] S. R. Choi, I.-W. Park, S. H. Kim, and K. H. Kim, "Effects of bias voltage and temperature on mechanical properties of Ti–Si–N coatings deposited by a hybrid system of arc ion plating and sputtering techniques," *Thin Solid Films,* vol. 447, pp. 371-376, 2004.

[76] K. H. Kim, S.-r. Choi, and S.-y. Yoon, "Superhard Ti–Si–N coatings by a hybrid system of arc ion plating and sputtering techniques," *Surface and Coatings Technology,* vol. 161, pp. 243-248, 2002.

[77] C. Zhang, X. Lu, H. Wang, J. Luo, Y. Shen, and K. Li, "Microstructure, mechanical properties, and oxidation resistance of nanocomposite Ti–Si–N coatings," *Applied surface science,* vol. 252, pp. 6141-6153, 2006.

[78] F. Fernandes, A. Loureiro, T. Polcar, and A. Cavaleiro, "The effect of increasing V content on the structure, mechanical properties and oxidation resistance of Ti–Si–V–N films deposited by DC reactive magnetron sputtering," *Applied surface science,* vol. 289, pp. 114-123, 2014.

[79] Z. Li, S. Miyake, M. Kumagai, H. Saito, and Y. Muramatsu, "Structure and Properties of Ti–Si–N Films Deposited by dc Magnetron Cosputtering on Positively Biased Substrates," *Japanese journal of applied physics,* vol. 42, p. 7510, 2003.

[80] Z. Li, Y. Wu, and S. Miyake, "High-flux ion irradiation with energy of∼ 20 eV affecting phase segregation and low-temperature growth of nc-Ti N∕ a-Si 3 N 4 nanocomposite films," *Journal of Vacuum Science & Technology A: Vacuum, Surfaces, and Films,* vol. 25, pp. 1524-1528, 2007.

[81] K. Sarakinos, J. Alami, P. Karimi, D. Severin, and M. Wuttig, "The role of backscattered energetic atoms in film growth in reactive magnetron sputtering of chromium nitride," *Journal of Physics D: Applied Physics,* vol. 40, p. 778, 2007.

[82] G. Greczynski and L. Hultman, "Time and energy resolved ion mass spectroscopy studies of the ion flux during high power pulsed magnetron sputtering of Cr in Ar and Ar/N 2 atmospheres," *Vacuum,* vol. 84, pp. 1159-1170, 2010.

[83] J. Alami, K. Sarakinos, F. Uslu, and M. Wuttig, "On the relationship between the peak target current and the morphology of chromium nitride thin films deposited by reactive high power pulsed magnetron sputtering," *Journal of Physics D: Applied Physics,* vol. 42, p. 015304, 2008.

[84] G. Greczynski, J. Jensen, and L. Hultman, "Mitigating the geometrical limitations of conventional sputtering by controlling the ion-to-neutral ratio during high power pulsed magnetron sputtering," *Thin Solid Films,* vol. 519, pp. 6354-6361, 2011.

[85] J. Whitacre, S. Yalisove, and J. Bilello, "In-plane Texturing in sputtered films," *Texture, Stress, and Microstructure,* vol. 34, pp. 91-103, 2000.

[86] Z. Zhao, S. Yalisove, and J. Bilello, "Stress anisotropy and stress gradient in magnetron sputtered films with different deposition geometries," *Journal of Vacuum Science & Technology A: Vacuum, Surfaces, and Films,* vol. 24, pp. 195-201, 2006.

[87] Y. Zhao, G.-C. Wang, and T.-M. Lu, *Characterization of Amorphous and Crystalline Rough Surface--Principles and Applications* vol. 37: Academic press, 2000.

[88] O. Karpenko, J. Bilello, and S. Yalisove, "Growth anisotropy and self-shadowing: A model for the development of in-plane texture during polycrystalline thin-film growth," *Journal of applied physics,* vol. 82, pp. 1397-1403, 1997.

[89] B. Movchan and A. Demchishin, "Investigation of the structure and properties of thick vacuum-deposited films of nickel, titanium, tungsten, alumina and zirconium dioxide," *Fiz. Met. Metalloved,* vol. 28, 1969.

[90] J. A. Thornton, "The microstructure of sputter-deposited coatings," *Journal of Vacuum Science & Technology A: Vacuum, Surfaces, and Films,* vol. 4, pp. 3059-3065, 1986.

[91] R. Karunasiri, R. Bruinsma, and J. Rudnick, "Thin-film growth and the shadow instability," *Physical Review Letters,* vol. 62, p. 788, 1989.

[92] K. H. Müller, "Molecular dynamics and collision cascade studies of ion-assisted thin film deposition," *Journal of Vacuum Science & Technology A,* vol. 5, pp. 2161-2162, 1987.

[93] T. Karabacak, "Thin-film growth dynamics with shadowing and re-emission effects," *Journal of Nanophotonics,* vol. 5, pp. 052501-052501-18, 2011.

[94] M. Pelliccione, T. Karabacak, C. Gaire, G.-C. Wang, and T.-M. Lu, "Mound formation in surface growth under shadowing," *Physical Review B,* vol. 74, p. 125420, 2006.

[95] G. Janssen and J.-D. Kamminga, "Stress in hard metal films," *Applied physics letters,* vol. 85, pp. 3086-3088, 2004.

[96] A. Anders, "Atomic scale heating in cathodic arc plasma deposition," *Applied physics letters,* vol. 80, pp. 1100-1102, 2002.

[97] R. Stuart and G. Wehner, "Sputtering yields at very low bombarding ion energies," *Journal of Applied Physics,* vol. 33, pp. 2345-2352, 1962.

[98] J. Keller and R. Simmons, "Sputtering process model of deposition rate," *IBM Journal of Research and Development,* vol. 23, pp. 24-32, 1979.

[99] J. Oliveira, F. Fernandes, R. Serra, and A. Cavaleiro, "On the role of the energetic species in TiN thin film growth by reactive deep oscillation magnetron sputtering in Ar/N2," *Thin Solid Films,* vol. 645, pp. 253-264, 2018.

[100] J. Robertson, "Plasma deposition of diamond-like carbon," *Japanese Journal of Applied Physics,* vol. 50, p. 01AF01, 2011.

[101] Y. Lifshitz, S. Kasi, J. Rabalais, and W. Eckstein, "Subplantation model for film growth from hyperthermal species," *Physical Review B,* vol. 41, p. 10468, 1990.

[102] J. Robertson, "Deposition mechanisms for promoting sp3 bonding in diamond-like carbon," *Diamond and related materials,* vol. 2, pp. 984-989, 1993.

[103] A. C. Ferrari, A. Libassi, B. K. Tanner, V. Stolojan, J. Yuan, L. Brown*, et al.*, "Density, sp 3 fraction, and cross-sectional structure of amorphous carbon films determined by X-ray reflectivity and electron energy-loss spectroscopy," *Physical Review B,* vol. 62, p. 11089, 2000.

[104] S. Chowdhury, M. Laugier, and I. Rahman, "Characterization of DLC coatings deposited by rf magnetron sputtering," *Journal of Materials Processing Technology,* vol. 153, pp. 804-810, 2004.

[105] Y. Lifshitz, "Diamond-like carbon—present status," *Diamond and Related materials,* vol. 8, pp. 1659-1676, 1999.

ANNEX A

F. Ferreira, R. Serra, J. Oliveira, and A. Cavaleiro, "Effect of peak target power on the properties of Cr thin films sputtered by HiPIMS in deep oscillation magnetron sputtering (DOMS) mode," Surface and Coatings Technology, vol. 258, pp. 249-256, 2014.

Surface & Coatings Technology 258 (2014) 249–256

Contents lists available at ScienceDirect

Surface & Coatings Technology

journal homepage: www.elsevier.com/locate/surfcoat

Effect of peak target power on the properties of Cr thin films sputtered by HiPIMS in deep oscillation magnetron sputtering (DOMS) mode

F. Ferreira *, R. Serra, J.C. Oliveira, A. Cavaleiro

SEG-CEMUC, Mechanical Engineering Department, University of Coimbra, Polo II, Rua Luís Reis Santos, 3030-788 Coimbra, Portugal

A R T I C L E   I N F O

Article history:
Received 11 March 2014
Accepted in revised form 11 September 2014
Available online 18 September 2014

Keywords:
Sputtering
DOMS
HiPIMS
DCMS
Chromium

A B S T R A C T

The advent of High-power Impulse Magnetron Sputtering (HiPIMS) and its variant Modulated Pulsed Power Magnetron Sputtering (MPPMS) allowed a new knob to control the flux of sputtered species, i.e., a new knob to control the kinetic effects of the growing film. Recently, a new design of the MPPMS pulses has been proposed to reduce arc generation. This form of high power pulses has been named deep oscillation magnetron sputtering (DOMS). In this work, the influence of the kinetic effects induced by a DOMS discharge on Cr sputtered thin films was studied and compared to direct current magnetron sputtering (DCMS) discharge. The Cr thin films were deposited with increasing peak power at the same average power (1.2 kW) in order to minimize changes in the thermal effects that also influence film growth. The influence of the peak power on the morphology, structure and mechanical properties of Cr thin films was studied. The Cr films deposited by DCMS have a columnar morphology, a [110] preferential orientation, hardness between 7.2 and 8.5 GPa and a maximum Young's modulus of 255 GPa, value always lower than that for bulk material. Although substrate bias potential up to −110 V was used, some porosity always remained in the DCMS films. The deposition rate of the Cr films deposited by DOMS with increasing peak power decreases from 60 to 30% of DCMS deposition rate. The films also have a [110] preferential orientation. Increasing the peak power changes the film morphology from columnar to dense, increases the hardness up to 17 GPa, increases the lattice parameter and decreases the grain size. The Young's modulus of the films is always close to the bulk material value showing that all the films are porosity free.
© 2014 Elsevier B.V. All rights reserved.

1. Introduction

In conventional direct current magnetron sputtering (DCMS), the vast majority of the sputtered species are electrically neutral [1] and the control of the energy and direction of the incoming material to the substrate is rather limited. Over the last decades, the increasing requirements on coating performance and the advent of new applications drive the development of deposition techniques allowing direct control of the sputtered flux by achieving a high degree of ionization of the sputtered material [2,3]. These techniques are referred as ionized PVD (IPVD) when the deposition flux consists of more ions than neutrals. However, in most cases, additional dedicated equipment has to be used as compared to DCMS. In the last decade, new magnetron sputtering deposition techniques have been developed to produce highly ionized fluxes of sputtered material while using essentially the same equipment as in DCMS except for the power supply. High-power Impulse Magnetron Sputtering (HiPIMS) [2–4], also known as High-power Pulsed Magnetron Sputtering (HPPMS), and Modulated Pulsed Power Magnetron Sputtering (MPPMS) [5–7], a variant of HiPIMS, are two of the most recent of these developments. Both deposition techniques rely on the application of very high target power densities to achieve higher plasma densities and subsequent ionization of the sputtered material. However, in order to maintain the cathode thermal load at acceptable levels, the high power densities are only applied in short periods of time (up to some ms). The large number of metallic ions generated by both techniques has already been shown to densify the deposited coatings [8,9], to improve adhesion [10,11], to allow homogeneous deposition on complex shape and high aspect ratio substrates [12], to tailor the phase of the coatings [13,14] and to allow hysteresis free reactive sputtering [15]. As conveniently summarized in an illustrative way by Anders [16], the use of a large flux of ions of sputtered species widens the range of achievable morphologies and properties in magnetron sputtered coatings.

The much higher target voltages and currents applied in both HiPIMS and MPPMS and the lack of a positive reversal voltage between the high-power pulses facilitate arc generation, especially for highly insulating reactive film deposition. As a result, more complicated electronics are needed for arc handling [17]. Recently, a new design of the MPPMS pulses has been proposed to reduce arc generation. The use of voltage oscillation packages with short-off time periods, instead of using very short rectangular voltage pulses to modulate the peak power, has been shown to allow virtually arc-free depositions for reactive deposition of insulating films [18]. This form of high power pulse

* Corresponding author.
E-mail address: fabio.ferreira@dem.uc.pt (F. Ferreira).

http://dx.doi.org/10.1016/j.surfcoat.2014.09.020
0257-8972/© 2014 Elsevier B.V. All rights reserved.

has been named deep oscillation magnetron sputtering (DOMS) [19]. In this work a DOMS power supply (CYPRIUM III from Zpulser) has been used to deposit Cr thin films.

It is well known that the properties of the impinging flux of species during film growth (nature of incoming species, energy distribution, direction distribution, ion to atoms ratio …) have a crucial influence on the deposited film morphology and properties [20]. In magnetron sputtering, the flux of sputtered species is traditionally tailored in two main ways: by changing the deposition pressure and by applying a substrate bias. In the former case, the energy and direction distribution of the incoming species are tailored through the number of collisions of the sputtered species with the background gas. Although ions may be involved, most of the incoming species to the substrate are neutral. In the latter case, Ar ion bombardment is promoted by applying a negative potential to the substrate. The energy distribution of the Ar ions and/or the ions to atoms ratio are tailored by changing the magnitude of the applied potential. The nature of the incoming species flux also depends on other parameters, such as the magnet configuration and the target to substrate distance, but usually these are fixed parameters for a particular deposition system. The advent of HiPIMS and MPPMS allowed an extra knob to control the flux of sputtered species, i.e., to control the kinetic effects on the growing film. The main objective of the present work was to evaluate the potential of the DOMS deposition technique, as compared to DCMS, by studying the influence of the kinetics effects induced by the DOMS discharge on the deposited films. The Cr thin films were deposited by DOMS, with increasing peak power, and DCMS with and without substrate biasing, at constant pressure (0.8 Pa). All depositions were carried out at the same average power (1.2 kW) in order to minimize changes in the thermal effects that also influence film growth.

2. Material and methods

An example of the discharge voltage and current oscillating wave forms used in this work is shown in Fig. 1. Each DOMS pulse consists of a packet of single oscillations. The voltage and current gradually increase to their maximum values (V_p and I_p) during the voltage on-time (t_{on}), and then gradually decay, reaching zero before the end of the oscillation period (T). In this work t_{on} and T were kept constant for all DOMS depositions at 6 and 40 μs, respectively. The pulse duration (D) was also kept constant (1000 μs) while the pulse frequency (F) was automatically adjusted by the DOMS power supply software in order to keep a constant average power (P_a). The DOMS power supply is powered by an internal d.c. voltage source. In this work the target peak power (P_p) was varied between 39 and 129 kW by changing the charging voltage (DC_{int}) between 250 and 400 V. Note that P_p is the maximum value of the $V_p \times I_p$ products calculated for each oscillation in a single pulse.

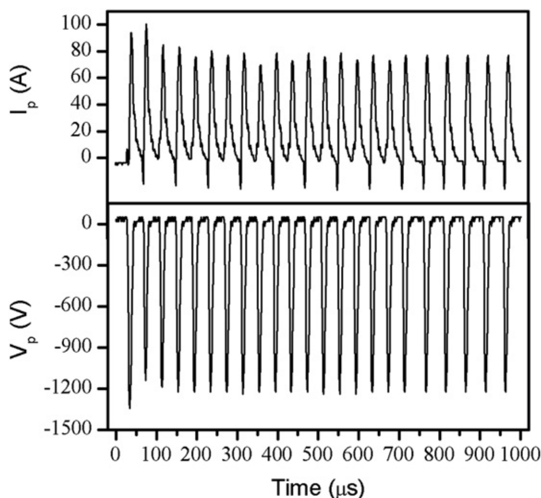

Fig. 1. Typical I–V waveforms of a DOMS pulse used on this work (P = 0.8 Pa; DC_{int} = 400 V; F = 117 Hz; D = 1000 μs; t_{on} = 6 μs; T = 40 μs).

The Cr films were deposited from a metal Cr target (99.99%) using a continuous d.c. power source (Hüttinger PFG 7500 DC) and a DOMS power supply (HIPIMS Cyprium™ III plasma generator, Zpulser Inc.). The target size was 150 mm × 150 mm. A base pressure lower than 5×10^{-3} Pa was achieved before all depositions. Plane glass slides and (100) Si wafers were used as substrates after cleaning in acetone and alcohol ultrasonic baths. The substrate-to-target distance was 80 mm and substrate rotation was kept at 23.5 rpm for all depositions. The Cr films were deposited for 35 min in DOMS mode with floating substrate potential. The DCMS deposition time was between 12 and 15 min depending on the substrate bias (floating, −50, −80 and −110 V). The Ar flow rate was kept constant at 15 sccm for all depositions, resulting in a working pressure of 0.8 Pa. The same average target power was used in all depositions (1.2 kW).

The crystal structure of Cr films was analyzed by X-ray diffraction (XRD) (PANalytical X'Pert PRO MPD) using Cu Kα radiation (45 kV and 40 mA) with a parallel beam in θ–2θ geometry. The incident beam optics consisted of a hybrid monochromator (with a Cu W/Si mirror and a double crystal Ge (220)). A parallel plate collimator (0.7°) and Soller slits (0.004°) were mounted on the path of the diffracted beam. A PIXcel detector in receiving slit mode was used for X-ray collection. The thickness and morphology of the films were studied by scanning electron microscopy (SEM) using a Quanta 400FEG ESEM. The film topography and roughness were examined by atomic force microscopy (AFM) using a Bruker Innova equipment in contact mode. The hardness of the films was measured by nano-indentation (MicroMaterialsNano Tester) using a Berkovich diamond indenter. The hardness was evaluated from load–displacement curve using the depth sensing method. Hardness measurements were done with 4 and 8 mN loads (16 measurements for each load) in order to evaluate possible influences of the substrate and/or indenter size effects. The hardness values agreed well within the experimental error and only the values obtained at 8 mN are presented in this work.

3. Results

3.1. Electrical characteristics of the DOMS discharge

The peak voltage (V_p) and peak current (I_p) are shown in Fig. 2 as a function of the voltage applied to the internal d.c. voltage source (DC_{int}) of the Cyprium III power supply. Both parameters increase linearly with the applied voltage, i.e., both the energy and ionization fraction of the sputtered species increase with the applied voltage. In this work the P_p parameter was varied by controlling the charging voltage (DC_{int}) while keeping constant all the other deposition parameters.

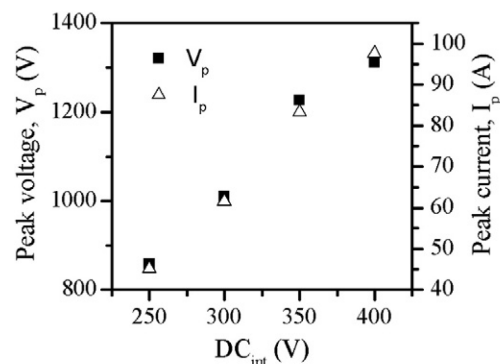

Fig. 2. Evolution of peak voltage (V_p) and peak current (I_p) as a function of the charging voltage (DC_{int}) (P_a = 1.2 kW; P = 0.8 Pa; $t_{dep.}$ = 35 min; D = 1000 μs; t_{on}/T = 6/40 μs).

The average power applied to the target (P_a) is shown in Fig. 3 also as a function of the DC_{int} voltage for three different pulse frequencies. In all cases the average power increases linearly with the d.c. voltage source in the range between 240 and 400 V, being the later value the maximum voltage of the source. The inset in Fig. 3 also shows that the average power increases linearly with the frequency. As expected, the energy supplied to the discharge increases linearly with both DC_{int} and F. At DC_{int} values below 240 V it is still possible to establish a stable discharge but the oscillation shape is irregular and the average power quickly tends to become zero. In this work all the depositions were carried out in average power control mode, or in other words, the average power was maintained constant in all depositions by the power supply software through automatic adjustments of the frequency (F).

Conventional magnetron discharges follow the empirical power law $I = k \times V^n$ with typical values for the exponent n between 5 and 15 [21]. Fig. 4 shows the I–V characteristics of the DCMS discharge operated in this work at 0.8 Pa. A value of n = 12.5 was calculated from the experimental data which is within the defined range. The I–V characteristics of the DOMS discharge are also represented in Fig. 4 considering the maximum values of voltage (V_p) and current (I_p) within each pulse. The DOMS discharges only operate at voltage values from 680 to 1300 V, well above the voltage values of the DCMS discharge. The n exponent for the DOMS discharge (2.7) is much lower than that for the DCMS discharge and lies well below the minimum value indicated for DCMS. Low values of n indicate that the discharge is already efficiently ionized, voltage increases result only in small amount of increase in the current, and are typical of HiPIMS discharges [22–24]. The DCMS like mode of operation observed by Ehiasarian et al. [22] for a Cr target sputtered by HiPIMS at 0.4 Pa between 500 and 650 V is not observed in this work as the DOMS discharge did not ignite below 680 V.

3.2. Cr films deposited by DCMS

The deposition conditions for the Cr films deposited by DCMS are shown in Table 1. As expected variation of the substrate bias did not significantly influence the voltage and current values during deposition. The deposited films have similar thicknesses as a result of deposition time adjustment. The roughness of the films, calculated from AFM topographic images, slightly decreases with increasing substrate biasing.

The deposition rate decreases with increasing substrate bias as is shown in Fig. 5. The loss of deposition rate with substrate bias is well documented in the literature [9,23,25] and results mainly from film densification by Ar ion bombardment ("Peening" effect) and/or resputtering of some of the deposited species. A maximum loss of deposition rate of nearly 20% was measures for the film deposited with the highest bias (−110 V).

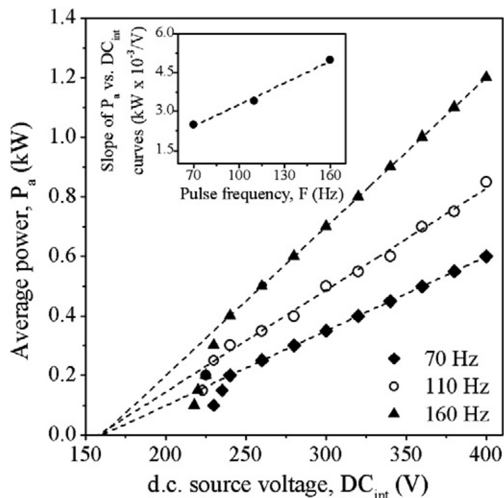

Fig. 3. Average power (P_a) as a function of the charging voltage (DC_{int}) for three pulse frequencies (F).

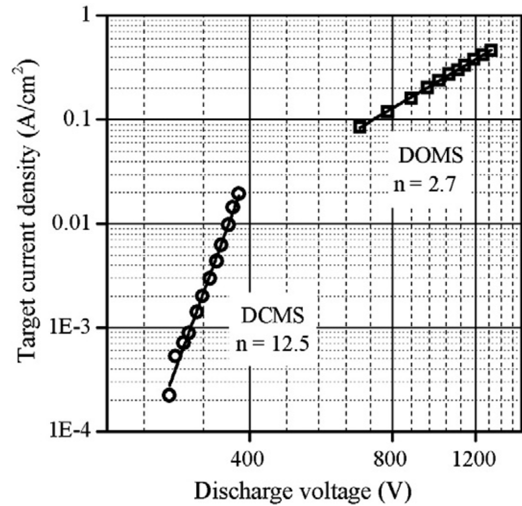

Fig. 4. I–V characteristics for the DCMS and DOMS discharges used in this work. The values for the DOMS discharge correspond to maximum voltage (V_p) and current (I_p) within each pulse.

Cr films deposited by DCMS at working pressure close to the one used in this work (0.8 Pa) and without substrate heating usually have a crystalline structure with preferential orientation along the <110> direction [26,27], as the (110) family of planes has the lowest surface energy in the b.c.c. structure [28]. The X-ray diffraction spectra of the Cr films deposited in this work are shown in Fig. 6. As expected, all the films are crystalline and show the preferential orientation of the (110) planes parallel to the substrate.

The lattice parameter of the Cr structure calculated from the 2θ value of the (110) diffraction peaks is shown in Fig. 7 as a function of the substrate bias. The lattice parameter of the film deposited without biasing is smaller than the value of the standard material (JCPDS no 01-085-1336) which indicates the formation of tensile stresses, as referred in the literature for films deposited in similar conditions [29,30]. The lattice parameter increases with increasing bias and is close to the value of the standard material at the highest bias. This result shows that the tensile stresses generated at the grain boundaries upon increasing energetic bombardment are increasingly counteracted by the compressive stresses generated by point defects. A grain size of 24 nm was calculated using the Scherrer formula for this film.

The Cr films deposited by DCMS have a columnar microstructure resulting from the low mobility of the Cr atoms and from the shadow effect (Fig. 8). The cross-section micrographs show columns extending from the substrate to the top of the film. The top-view micrographs show the characteristic dome-like endings of the columns, although with a preferential elongation along the rotation direction. In this work the Cr films were deposited using a rotating substrate holder which introduces an anisotropy in the deposition system which can induce anisotropic stresses in the plane of the film [32,33]. The spread of the incident angles of the sputtered species on the substrate surface is higher along the direction tangent to the substrate rotation than in

Table 1
Deposition conditions for the Cr thin films deposited by DCMS (Pa = 1.2 kW; P = 0.8 Pa).

V (V)	I (A)	Bias (V)	Dep. time (minutes)	Thickness (nm)	Ra (nm)
368	3.41	–	12	1000	14.8
377	3.31	−50	13	950	13.6
380	3.38	−80	14	1000	12.4
368	3.40	−110	15	1000	12.2

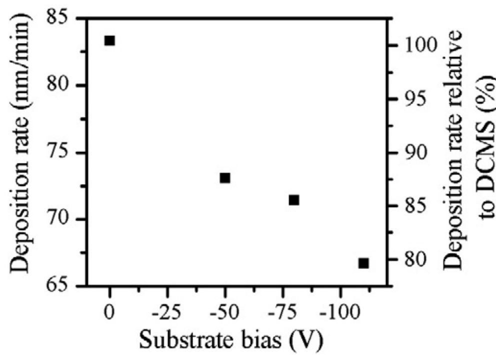

Fig. 5. Deposition rate of the Cr films prepared by DCMS ($P_a = 1.2$ kW; $P = 0.8$ Pa).

the perpendicular direction. On the other hand, the relatively high deposition pressure (0.8 Pa) is such that the mobility of the Cr atoms on the surface of the films is low and hence the anisotropy of the deposition system is preserved in the film microstructure (Fig. 8a). The anisotropy of the microstructure is smeared out by applying a bias (Fig. 8b) as the Ar ions bombard the film at incident angles close to the normal to the film surface and increase the mobility of the Cr atoms on the film surface. The film deposited without biasing is highly porous (Fig. 8a), as expected for films corresponding to zone 1 of Thornton structure zone diagram [31]. Applying a bias of −110 V decreases the porosity although some remaining pores are still observed (Fig. 8b).

The hardness and Young's modulus of the Cr films deposited by DCMS are shown in Fig. 9 with increasing substrate bias. The film deposited without substrate bias has a hardness of 7.2 GPa which lies in the upper limit of the hardness range values referred in the literature for sputtered Cr films [34,35]. Applying a substrate bias of −50 V increases the hardness to 8.5 GPa. Fernandes et al. [36] have shown that tensile stresses decrease the hardness measured by nano-indentation while compressive stresses have the opposite effect. The increased hardness obtained by biasing the substrate is due to the relaxation of the tensile stresses by Ar ion bombardment. Further increasing the substrate bias does not significantly influence the film hardness.

The Young's modulus of the Cr film deposited by DCMS without substrate bias (225 GPa) is lower than the value referred in the literature for bulk Cr (279 [37]). As shown by Lintymer et al. [38], the Young's modulus of sputtered Cr films decreases with increasing porosity following a perfect mixture rule. The low Young's modulus of the film deposited without bias agrees well with the high porosity already inferred from its cross-section micrograph (Fig. 8a). Applying a substrate bias of −50 V increases the film Young's modulus to 250 GPa which indicates that its porosity is reduced by the Ar ion bombardment. The film porosity is again reduced by increasing the bias to −80 V, resulting in a

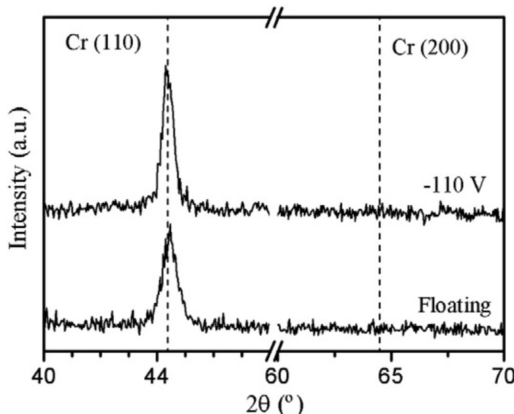

Fig. 6. X-ray diffraction patterns of the films prepared by DCMS ($P_a = 1.2$ kW; $P = 0.8$ Pa).

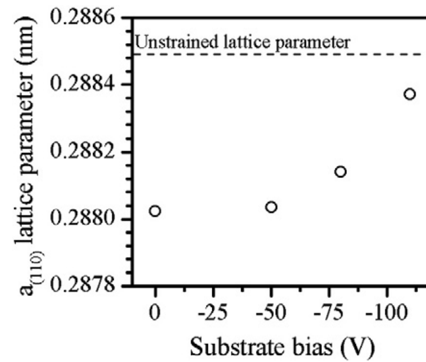

Fig. 7. Lattice parameter for the films deposited by DCMS as function of substrate bias ($P_a = 1.2$ kW; $P = 0.8$ Pa).

Young's modulus of 260 GPa. However, further increasing the bias to −110 V does not change the Young's modulus of the films.

3.3. Cr films deposited by DOMS

The deposition conditions of the films deposited by DOMS are shown in Table 2. Both I_p and V_p contribute to the increase in peak power (Pp) from 39 to 129 kW with increasing DC_{int}. The average power (P_a) was kept constant at 1.2 kW by decreasing the frequency of the pulses from 310 to 117, respectively. The thickness of the films decreases with increasing peak power, although the same deposition time was used in all depositions (35 min). At last the film surface smoothens with increasing peak power as the value of Ra, calculated from AFM topographic images, decreases by a factor of 4. Note also that the voltage values in the DOMS depositions are from 2.2 to 3.5 times higher than the voltage values shown for the DCMS depositions in Table 1.

The deposition rate of the films deposited by DOMS decreases with increasing peak power. As is shown in Fig. 10, increasing the peak power by three times results in a loss of 30% in deposition rate. The loss of deposition rate in HiPIMS is well documented in the literature [9,23,25] and several possible causes have been identified. Two of these are the return effect, resulting from back-attraction of the sputtered atoms after ionization, and the yield effect, related to the sub-linear energy dependence of the sputtering yield. Both effects contribute to the decrease of deposition rate observed in this work, as both the peak current, i.e., the fraction of ionized sputtered material, and the peak voltage contribute to the increase of the peak power (see Fig. 2). The relative deposition rate at the highest peak power is just above 30%. This value compares well with the results published by Helmersson et al. [39] although Samuelsson et al. [9] reported a relative deposition rate close to 50% for Cr films deposited by HiPIMS.

All the diffractograms of the deposited films have a single diffraction peak which was indexed to the (110) family of plans of the b.c.c. Cr crystalline structure (Fig. 11). All films have a [110] preferred orientation irrespective of the peak power used for deposition. A similar result was reported by Lin et al. [8] for chromium coatings deposited by MPPMS. The [110] preferred orientation was obtained even for peak power values higher than those used in this work. The (110) diffraction peak of the film deposited with the lowest peak power (39 kW) is close to the position referred for the standard material, i.e., the lattice parameter for this film is closed to the unstrained material. Increasing the peak power leads to gradual shift of the (110) peak position to lower 2θ values, which indicates the formation of compressive stresses with increasing intensity.

The grain size and the $a_{(110)}$ lattice parameter of the films calculated from the XRD spectra in Fig. 11 are shown in Fig. 12. The $a_{(110)}$ lattice parameter and the grain size have opposite trends with increasing P_p, the former increases while the latter decreases. The film deposited

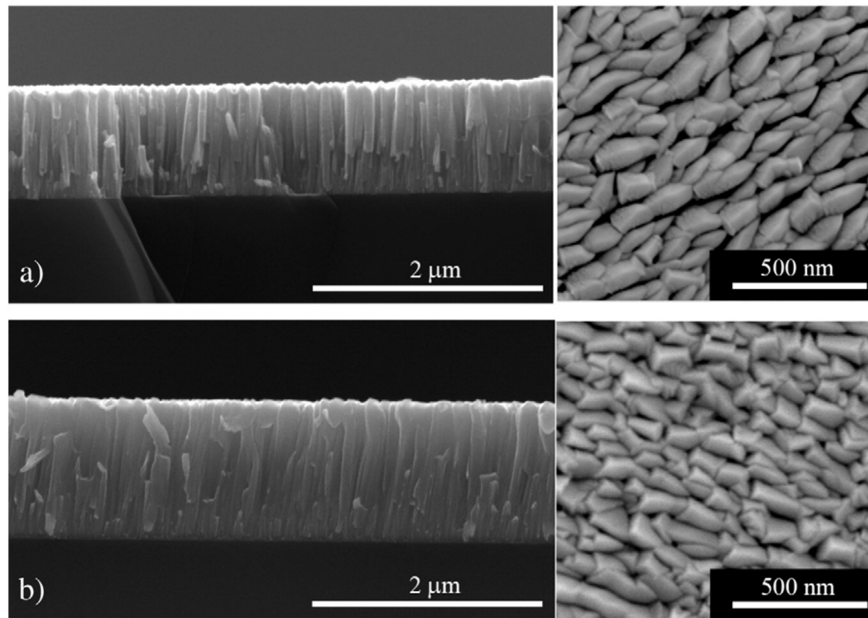

Fig. 8. SEM micrographs for the Cr films deposited by DCMS. a) Without substrate bias and b) with −110 V substrate bias.

with the lowest peak power has a lattice parameter (0.2884 nm) similar to the value reported for the unstrained standard material (JCPDS no 01-085-1336), as concluded above, and a grain size of 48 nm. Increasing the peak power to 63 kW slightly increases the lattice parameter while the grain size is only decreased by 4 nm. Further increasing the peak power to 102 kW has a much higher effect on the grain size, which drops to 33 nm, than on the lattice which follows the increasing trend observed at lower P_p. On the contrary, increasing the peak power to 129 kW only slightly decreases the grain size, by 2 nm, while the lattice parameter increases steeply to 0.2915 nm.

The Cr film deposited with the lowest peak power (39 kW) has a columnar morphology with columns extending from the bottom to the top of the film (Fig. 13a). The top of the columns shows a preferential elongation in one direction as was already observed for the film deposited by DCMS. The same type of morphology is observed for the film deposited with $P_p = 63$ kW (Fig. 13b). Increasing the peak power to 102 kW significantly changes the morphology of the film (Fig. 13c). Although some remains of columns are still observed, the morphology of the film is much more compact as can be observed in the cross-sectional micrograph. The preferential orientation of the surface features is still detected but with a much lower intensity. Further increasing the peak power to 129 kW confirms the previous trend (Fig. 13d). The Cr film has a completely dense morphology, without any columnar remains, and the preferential orientation of the surface features is completely lost. The roughness of the deposited films, as

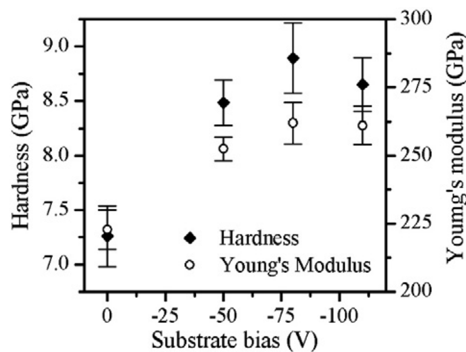

Fig. 9. Young's modulus and hardness of the Cr films deposited by DCMS as a function of the applied substrate bias.

measured by AFM, decreases with increasing P_p (see Table 2) in agreement with the SEM observations.

The hardness of the deposited films increases with increasing peak power (Fig. 14) from 9.8 GPa to 17.7 GPa. However, the hardness of the films deposited with the two lowest peak power is almost the same. Similar hardness results were found by Lin et al. [8] for modulated pulse power sputtered chromium coatings. The authors found that at the lowest powers (between 43 and 90 kW) the hardness of the film was close to 10 GPa while increasing the peak power to 125 and 135 kW increased the hardness to 12.8 and 15.2 GPa, respectively. Both the MPPMS films and the films deposited in this work have hardness values higher than those of the films deposited by DCMS even with substrate biasing. The Young's modulus of the deposited films is õ-independent of the peak power as all the films have a Young's modulus close to the value referred in the literature for bulk chromium (290 GPa).

4. Discussion

The Cr film deposited by DCMS without substrate biasing has a low hardness (7.2 GPa) and a smaller lattice parameter than the unstrained material (0.2880 nm). Both results are characteristic of Cr films deposited by DCMS at high pressure, as a type 1 columnar morphology with tensile stresses is formed. The low Young's modulus of the film, as compared to the bulk material (225 against 279 GPa), also reveals the high porosity levels typical of these structures. Applying a substrate bias of −110 V increases the hardness to 8.5 GPa and the lattice parameter to a value slightly smaller than the unstrained material (0.2884 nm). Substrate bombardment with Ar ions decreases the tensile stresses and increases the film density, although the columnar morphology is retained. However, the Young's modulus of the film is still significantly

Table 2
Deposition conditions for the Cr thin films deposited by DOMS (Pa = 1.2 kW; t = 35 min; P = 0.8 Pa; D = 1000 μs; t_{on} = 6 μs; T = 40 μs).

V_p (V)	I_p (A)	P_P (kW)	F_i (Hz)	Thickness (nm)	Ra (nm)
860	45	39	310	1720	10.4
1011	62	63	215	1270	7.9
1225	83	102	156	1030	4.4
1314	98	129	117	890	2.7

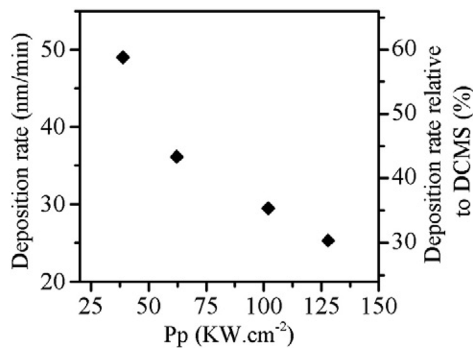

Fig. 10. Deposition rate of the films deposited by DOMS as a function of peak power (P_p) (Pa = 1.2 kW; t = 35 min; P = 0.8 Pa; D = 1000 μs; t_{on} = 6 μs; T = 40 μs).

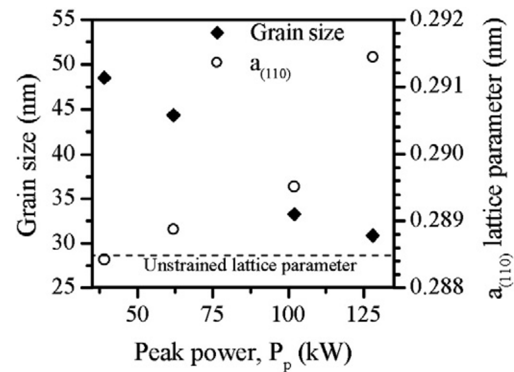

Fig. 12. Grain size and lattice parameter (P_a = 1.2 kW; t = 35 min; P = 0.8 Pa; D = 1000 μs; t_{on} = 6 μs; T = 40 μs).

lower than the bulk material (279 GPa) which shows that the film still has appreciable levels of porosity.

The porosity of Cr thin films deposited by sputtering consists of atomic scale intra-granular voids (mainly at grain boundaries) and macro-scale inter-columnar voids which result from the shadowing effect [32,40]. The structural relaxation of grain boundaries has been considered as the main source of tensile stress in sputtered films of metals with low atomic mobility such as Cr. On the contrary, inter-columnar voids are so wide that atomistic coupling between neighboring grains is almost impossible and these void regions cannot support stresses. Applying a substrate bias of −110 V resulted in the almost complete cancelation of the tensile stresses by the compressive stresses formed upon energetic bombardment, although some significant level of porosity still remained. This result indicates that the bombardment of the growing with Ar ions eliminates the intra-granular voids in the films, mainly thought the atomic peening effect, but does not overcome the formation of inter-granular voids due to the shadowing effect.

Following the technical definition proposed by Anders [41], the film deposited in this work at the highest peak power value was deposited in the HiPIMS regime, as the peak power (129 kW) exceeds the time-averaged power (1.2 kW) by more than two orders of magnitude. This conclusion is supported by the value of the n exponent of the discharge (n = 2.7) which is much lower than expected for DCMS and close to the value reported for Cr discharges by HiPIMS. Furthermore, the deposition rate of this film is close to 30% of the DCMS rate which agrees well with the values reported in the literature for Cr films deposited by HiPIMS.

The film deposited by DOMS with the lowest peak power (39 kW) also shows a columnar morphology similar to the one observed for the films deposited by DCMS with and without substrate biasing. However, both the hardness (9.8 GPa) and the Young's modulus (280 GPa) are higher than for the DCMS films. In fact, the Young's modulus of this film is the value of the bulk material. Bombarding the growing film with Cr ions allows a complete elimination of the porosity in the film, i.e., overcoming the shadowing effect, in opposition to the bombardment with Ar ions by substrate biasing in DCMS. The lattice parameter of the film is similar to the unstrained material (and close to the lattice parameter of the film deposited by DCMS with the highest substrate bias) indicating that in spite of the bombardment with Cr ions the formation of compressive stresses was avoided. Increasing the peak power to 63 kW does not significantly influence the morphology, hardness and Young's modulus of the film. However, the slight increase in lattice parameter shows that compressive stresses start to form.

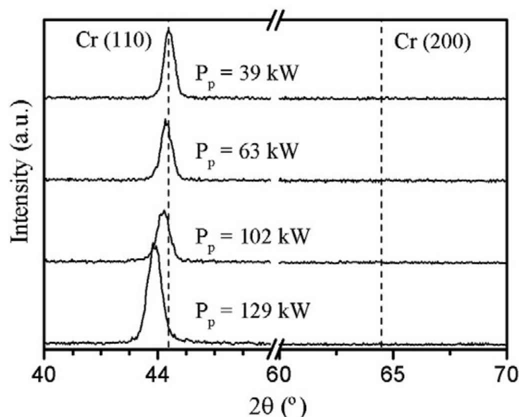

Fig. 11. Diffractograms of the Cr films deposited by DOMS as a function of the target peak power (Pa = 1.2 kW; t = 35 min; P = 0.8 Pa; D = 1000 μs; t_{on} = 6 μs; T = 40 μs).

Further increasing the peak power (to 102 kW) leads to abrupt change in all film properties, except for the Young's modulus which remains the value of bulk chromium. The morphology of the Cr film is much denser, although some remains of columns are still observed, the hardness increases to almost 14 GPa, the lattice parameter increases to 0.2895 nm and the grain size decreases from 44 to 33 nm. Finally, increasing the peak power to 129 kW confirms the previous trend: the film morphology is denser, the hardness increases up to 17.7 GPa, more compressive stresses are generated (a = 0.2915 nm) and the gain size decreases to 31 nm while the Young's modulus remains unchanged. These results point to a qualitative change in the nature of the substrate bombardment. Greczynski et al. [40] have shown that the most prominent change upon increasing the peak current in a Cr HiPIMS discharge is the number of generated Cr^{2+} ions which increased nearly twenty times and even surpassed the flux of Cr^{+} ions at the highest peak current. Lin et al. [5] reported a much more significant increase in the intensity signal of Cr^{2+} ion energy distribution than for Cr^{+} ions in a MPPMS discharge over a Cr target. The increased relative number of Cr^{2+} ions generated at higher peak powers may be the cause for the deposition of denser and harder films, with lower grain size and significant compressive stresses.

5. Conclusions

The Cr thin films were deposited with increasing peak power by DOMS with the same average power (1.2 kW) in order to minimize changes in the thermal effects that also influence film growth. The Cr films deposited by DCMS have a columnar morphology, a [110] preferential orientation, hardness between 7.2 and 8.5 GPa and a maximum Young's modulus of 255 GPa, always lower than the value of the bulk material. Although substrate polarization up to −110 V was used, some porosity always remained in the DCMS films. The deposition rate of the Cr films deposited by DOMS with increasing peak power decreases from 60 to 30% of the DCMS deposition rate. The films also have a [110] preferential orientation. Increasing the peak power changes the film morphology from columnar to dense, increases the hardness up to 17 GPa, increases the lattice parameter and decreases the grain size. The Young's modulus of the films is always the bulk material value.

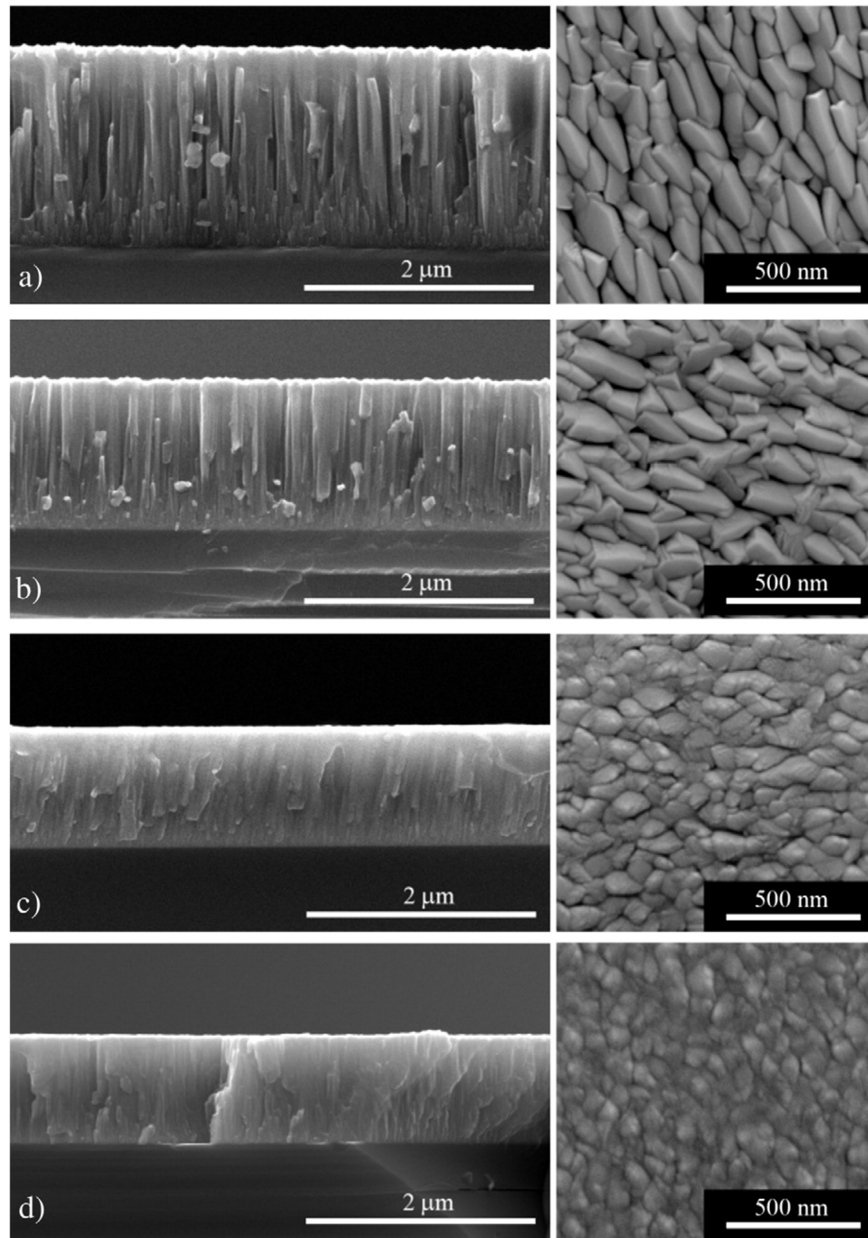

Fig. 13. SEM micrographs of the Cr films deposited by DOMS with increasing values of P_p: a) 39 kW; b) 62 kW; c) 102 kW; d) 128 kW (P_a = 1.2 kW; t = 35 min; P = 0.8 Pa; D = 1000 μs; t_{on} = 6 μs; T = 40 μs).

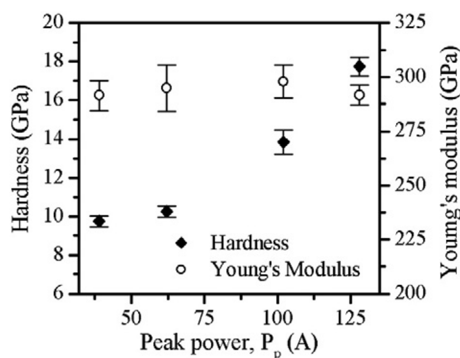

Fig. 14. Hardness and Young's modulus of the Cr films deposited by DOMS (P_a = 1.2 kW; t = 35 min; P = 0.8 Pa; D = 1000 μs; t_{on} = 6 μs; T = 40 μs).

Bombarding the growing film with Cr^{+} ions allows a complete elimination of the porosity in the film, i.e., overcoming the shadowing effect, in opposition to the bombardment with Ar ions by substrate biasing in DCMS. The increased relative number of Cr^{2+} ions generated at higher peak powers may be the cause for the deposition of denser and harder films, with lower grain size and significant compressive stresses.

Acknowledgments

This research is sponsored by FEDER funds through the program COMPETE – Programa Operacional Factores de Competitividade – and by national funds through Portuguese Foundation for Science and Technology (FCT), under the project PEst-C/EME/UI0285/2013 and through the Grant SSFRH/BPD 17382712010 (R.S.).

References

[1] S.M. Rossnagel, J. Hopwood, Appl. Phys. Lett. 63 (1993) 3285–3287.
[2] J.T. Gudmundsson, J. Phys. Conf. Ser. 100 (2008) 082002.
[3] U. Helmersson, M. Lattemann, J. Bohlmark, A.P. Ehiasarian, J.T. Gudmundsson, Thin Solid Films 513 (2006) 1–24.
[4] K. Sarakinos, J. Alami, S. Konstantinidis, Surf. Coat. Technol. 204 (2010) 1661–1684.
[5] J. Lin, J.J. Moore, W.D. Sproul, B. Mishra, J.A. Rees, Z. Wu, R. Chistyakov, B. Abraham, Surf. Coat. Technol. 203 (2009) 3676–3685.
[6] J. Lin, W. Sproul, J. Moore, Z. Wu, S. Lee, R. Chistyakov, B. Abraham, JOM 63 (2011) 48–58.
[7] J. Lin, W.D. Sproul, J.J. Moore, Mater. Lett. 89 (2012) 55–58.
[8] J. Lin, J.J. Moore, W.D. Sproul, B. Mishra, Z. Wu, Thin Solid Films 518 (2009) 1566–1570.
[9] M. Samuelsson, D. Lundin, J. Jensen, M.A. Raadu, J.T. Gudmundsson, U. Helmersson, Surf. Coat. Technol. 205 (2010) 591–596.
[10] M. Lattemann, A.P. Ehiasarian, J. Bohlmark, P.A.O. Persson, U. Helmersson, Surf. Coat. Technol. 200 (2006) 6495–6499.
[11] A.P. Ehiasarian, J.G. Wen, I. Petrov, J. Appl. Phys. 101 (2007).
[12] V. Kouznetsov, K. Macák, J.M. Schneider, U. Helmersson, I. Petrov, Surf. Coat. Technol. 122 (1999) 290–293.
[13] S. Konstantinidis, J.P. Dauchot, M. Hecq, Thin Solid Films 515 (2006) 1182–1186.
[14] J. Alami, P. Eklund, J.M. Andersson, M. Lattemann, E. Wallin, J. Bohlmark, P. Persson, U. Helmersson, Thin Solid Films 515 (2007) 3434–3438.
[15] E. Wallin, U. Helmersson, Thin Solid Films 516 (2008) 6398–6401.
[16] A. Anders, Thin Solid Films 518 (2010) 4087–4090.
[17] D.J. Christie, F. Tomasel, W.D. Sproul, D.C. Carter, J. Vac. Sci. Technol. A 22 (2004) 1415–1419.
[18] R. Chistyakov, B. Abraham, SVC Bull. (Spring 2012) 26–31.
[19] L. Jianliang, W. Bo, D.S. William, O. Yixiang, D. Isaac, J. Phys. D. Appl. Phys. 46 (2013) 084008.
[20] I. Petrov, P.B. Barna, L. Hultman, J.E. Greene, J. Vac. Sci. Technol. A Vac. Surf. Films 21 (2003) S117–S128.
[21] S.M. Rossnagel, H.R. Kaufman, J. Vac. Sci. Technol. A 6 (1988) 223–229.
[22] A.P. Ehiasarian, R. New, W.D. Münz, L. Hultman, U. Helmersson, V. Kouznetsov, Vacuum 65 (2002) 147–154.
[23] J. Alami, K. Sarakinos, G. Mark, M. Wuttig, Appl. Phys. Lett. 89 (2006).
[24] F. Papa, H. Gerdes, R. Bandorf, A.P. Ehiasarian, I. Kolev, G. Braeuer, R. Tietema, T. Krug, Thin Solid Films 520 (2011) 1559–1563.
[25] D.J. Christie, Czechoslov. J. Phys. 56 (2006) B93–B97.
[26] H. Li, B. Jiang, B. Yang, Appl. Surf. Sci. 258 (2011) 935–939.
[27] S.L. Duan, J.O. Artman, B. Wong, D.E. Laughlin, J. Appl. Phys. 67 (1990) 4913–4915.
[28] Y.C. Feng, D.E. Laughlin, D.N. Lambeth, J. Appl. Phys. 76 (1994) 7311–7316.
[29] D.W. Hoffman, J.A. Thornton, Thin Solid Films 40 (1977) 355–363.
[30] G.C.A.M. Janssen, A.J. Dammers, V.G.M. Sivel, W.R. Wang, Appl. Phys. Lett. 83 (2003) 3287–3289.
[31] J.A. Thornton, J. Vac. Sci. Technol. 11 (1974) 666.
[32] Z.B. Zhao, S.M. Yalisove, Z.U. Rek, J.C. Bilello, J. Appl. Phys. 92 (2002) 7183–7192.
[33] G.C.A.M. Janssen, P.F.A. Alkemade, V.G.M. Sivel, S.Y. Grachev, J.-D. Kamminga, J. Vac. Sci. Technol. A 22 (2004) 1773–1777.
[34] V. Guilbaud-Massereau, A. Celerier, J. Machet, Thin Solid Films 258 (1995) 185–193.
[35] J. Lintymer, J. Gavoille, N. Martin, J. Takadoum, Surf. Coat. Technol. 174–175 (2003) 316–323.
[36] N.A. Sakharova, P.A. Prates, M.C. Oliveira, J.V. Fernandes, J.M. Antunes, Strain 48 (2012) 75–87.
[37] J. Lintymer, N. Martin, J.M. Chappé, J. Takadoum, P. Delobelle, Thin Solid Films 503 (2006) 177–189.
[38] J. Lintymer, N. Martin, J.M. Chappé, P. Delobelle, J. Takadoum, Surf. Coat. Technol. 200 (2005) 269–272.
[39] U. Helmersson, M. Lattemann, J. Alami, J. Bohlmark, A.P. Ehiasarian, J.T. Gudmundsson, Proceedings of the 48th Annual Technical Conference of the Society of Vacuum Coaters, April 23–28, 2005, Denver, CO, USA, 2005, p. 458, (vol.).
[40] G. Greczynski, J. Jensen, L. Hultman, Thin Solid Films 519 (2011) 6354–6361.
[41] A. Anders, Surf. Coat. Technol. 205 (2011) S1–S9.

ANNEX B

F. Ferreira, C. Sousa, A. Cavaleiro, A. Anders and J. Oliveira, "Phase tailoring of tantalum thin films deposited in deep oscillation magnetron sputtering mode." Surface and Coatings Technology, vol. 314, pp.97-104, 2017.

Surface & Coatings Technology 314 (2017) 97–104

Contents lists available at ScienceDirect

Surface & Coatings Technology

journal homepage: www.elsevier.com/locate/surfcoat

Phase tailoring of tantalum thin films deposited in deep oscillation magnetron sputtering mode

Fábio Ferreira [a,b,*], Cláudio Sousa [a], Albano Cavaleiro [a], André Anders [b], João Oliveira [a]

[a] SEG-CEMUC - Department of Mechanical Engineering, University of Coimbra, Rua Luis Reis Santos, 3030-788, Coimbra, Portugal
[b] Lawrence Berkeley National Laboratory, 1 Cyclotron Road, Berkeley, CA 94720, USA

ARTICLE INFO

Article history:
Received 30 June 2016
Revised 4 August 2016
Accepted in revised form 6 August 2016
Available online 8 August 2016

Keywords:
Ta films
DOMS
HiPIMS
Film growth
Phase tailoring

ABSTRACT

The effect of energetic ion bombardment on the properties of tantalum thin films was investigated. To achieve such energetic ion bombardment during the process the Ta thin films were deposited by deep oscillation magnetron sputtering (DOMS), an ionized physical vapor deposition technique related to high power impulse magnetron sputtering. The peak power was between 49 and 130 kW and the substrate was silicon at room temperature and ground potential. The directionality and the energy of the depositing species was controlled by changing the ionization fraction of the Ta species arriving at the substrate at different peak powers. In this work, the surface morphology (AFM), microstructure (SEM), structure (XRD) and hardness and Young's modulus (nanoindentation) of the films were characterized. The ion energy distributions (IEDs) were measured using an electrostatic quadrupole ion energy and mass spectrometer (HIDEN EQP 300). The IEDs showed that the DOMS process applies a very energetic (up to 120 eV) ion bombardment on the growing tantalum films. Therefore, with such conditions it was possible to deposit pure α-Ta (of 2 μm of thickness) without the use of additional equipment, i.e., without substrate bias or substrate heating. Conditions are therefore significantly different than in previous works, offering a much simpler and cheaper solution to up-scale for industrial operation.
© 2016 Elsevier B.V. All rights reserved.

1. Introduction

Tantalum is a refractory metal with a number of unique characteristics and attractive properties such as low electrical resistivity, high melting point, and excellent chemical inertness at temperatures below 150 °C [1,2]. Due to these characteristics Ta has many applications, for instance as heat and wear resistant protective coatings, as-diffusion barriers in integrated circuits and magnetic disk drives [3–5]. Tantalum exists in two distinct phases: a stable α-phase with a body-centred cubic lattice structure and a metastable β-phase with a tetragonal lattice structure. The tough and ductile α-phase is required in most industrial applications, such as diffusion barrier layers, metallic corrosion protective layers, and in biomedical devices. Bulk Ta metal has the α-phase structure while the β-phase appears in thin films. The β-phase is hard and brittle, and its presence may compromise the film performance. According to the state of the art, formation of the β-phase in magnetron sputtered films can be prevented by manipulating the deposition parameters, such as sputtering gas, energetic ion bombardment, substrate temperature and substrate material [6–10]. Among these, it was found that the use of energetic ion bombardment on the growing film played an important role in the tantalum film structure and properties [11].

In direct current magnetron sputtering (DCMS) the most influential deposition parameter with respect to ion bombardment on the growing film is the substrate bias. However, applying a negative bias to the substrate only allows us to extract process gases (Ar) ions from the plasma as the ionization degree of the sputtered material is very low (e.g., 1%–3%). In recent years, new magnetron sputtering deposition techniques that allow producing highly ionized fluxes of sputtered material have been developed. High peak power is applied to the target for a short period of time causing much higher plasma densities than in DCMS by ionization of the sputtered species by electron impact. Two of these recent developments, called High-power Impulse Magnetron Sputtering (HiPIMS) [12–15], and Modulated Pulsed Power Magnetron Sputtering (MPPMS) [16–18], were already used for the deposition of tantalum thin films. Alami et al. [11] found that HiPIMS allowed us to control the Ta phase formation and established a bias voltage window for deposition of α-tantalum on Si. Lin et al. [19] found that all α-tantalum films are deposited by MPPMS when the negative bias voltage was – 50 V or greater. In both cases the energetic bombardment of the growing film was achieved by substrate biasing. Recently, a new HIPIMS process called deep oscillation magnetron sputtering (DOMS) [20–24] was developed. This process uses large voltage oscillation packets in long modulated pulses for achieving high peak target currents and voltages.

* Corresponding author at: SEG-CEMUC - Department of Mechanical Engineering, University of Coimbra, Rua Luis Reis Santos, 3030-788 Coimbra, Portugal.
E-mail address: fabio.ferreira@dem.uc.pt (F. Ferreira).

http://dx.doi.org/10.1016/j.surfcoat.2016.08.017
0257-8972/© 2016 Elsevier B.V. All rights reserved.

The authors have shown previously that the DOMS process allowed us to tailor the microstructure and properties of metal and nitride thin films without the need of substrate biasing [20,21,24]. Therefore, it is expected that the energetic ion bombardment in DOMS could also be used to tailor the phase composition and improve the structure and properties of tantalum thin films without the use of substrate bias and/or substrate heating.

In the current study, tantalum thin films were deposited on silicon by DOMS at different peak powers in order to have different levels of ion bombardment. The structure, morphology and mechanical properties of tantalum thin films were characterized. The ion energy distributions (IEDs) were measured using an electrostatic quadrupole plasma mass spectrometer (HIDEN EQP 300) both for DOMS or DCMS process. Five films were deposited by DCMS with the increase of the substrate bias for comparison purposes.

2. Experimental procedure

2.1. Film deposition

Tantalum thin films (of 2 μm of thickness) were deposited on Si (100) substrates using a continuous D.C. power source (Huttinger PFG 7500 DC) and a DOMS power supply (HiPIMS Cyprium™ plasma generator, Zpulser Inc.) at room temperature and ground potential. An example of the DOMS discharge voltage and current wave forms used in this work is shown in Fig. 1. The voltage on-time ($t_{on} = 6$ μs), oscillation period ($T = 50$ μs) and pulse duration ($D = 1250$ μs) were kept constant for all depositions, while the pulse frequency (F) was automatically adjusted by the DOMS power supply software in order to maintain a specified time-averaged power.

The 2 cm × 2 cm substrates were cut from Si (100) wafers. Prior to the depositions they were ultrasonically cleaned in a sequence of acetone and ethanol solutions baths, for 10 min each. They were then glued with silver glue (99.9% purity) onto an aluminium substrate holder and placed in the deposition chamber made from high grade stainless steel with 40 cm × 40 cm × 40 cm dimensions. In all depositions, the substrate-to-target distance and substrate rotation was kept at 80 mm and 23.5 rpm, respectively. The target used consisted of 99.95% pure Ta with an area of 150 mm × 15 mm and 7 mm thickness. A base pressure lower than 4×10^{-4} Pa was achieved before all depositions using a turbomolecular pump. A constant Ar (99.999%) flow rate of 15 sccm was used in all the depositions resulting in a discharge pressure of 0.7 Pa. A constant average target power of 1.2 kW was used for all depositions (DOMS and DCMS) in order to minimize variations of thermal effects during the deposition of the films. The deposition time was changed in order to achieve 2 μm of thickness.

The tantalum thin films were deposited by DOMS with the increase of the peak power (P_p) in order to increase the ionization of the sputtered material during the process. The P_p was varied between 49 and 130 kW by changing the charging voltage (DC_{int}) between 270 and 400 V. The peak power (P_p) is defined as the product $V_p \times I_p$. The main DOMS deposition parameters are compiled in Table 1. Five films were deposited by DCMS with increased negative substrate bias (−30 V, −50 V, −80 V and −120 V) for comparison purposes. In these depositions the voltage target and current target were 333 V and 3.75 A, respectively.

2.2. Ion energy distribution measurements

The ion energy distributions (IEDs) were measured using an electrostatic quadrupole plasma mass spectrometer (HIDEN EQP 300). This equipment can measure up to 1 keV/charge and is assisted by 70 l/s turbo pump for differential pumping of the instrument. The tantalum target with a diameter of 7.6 cm was mounted in front of the EQP orifice (100 μm diameter) with a 10 cm distance between them. An average target power of 600 W was used for both DOMS and DCMS. The IEDs were measured from 0 to 100 V scan voltage with a step size of 0.5 V and a 1000 ms dwell time. The extractor voltage used in EQP measurement was equal to 40 V. In accordance with the reference [25], after the measurements the raw data were corrected for the double charge ions by multiplying the scan voltage by two and dividing the count rate by two to account for the energy bin width. The following ions were analysed: Ta^{+}, Ta^{2+}, Ar^{+}, Ar^{2+}. It has to be mentioned that the here-presented distributions merely provide a semi-quantitative description of the energy distributions involved during the DOMS tantalum sputtering process because difficult-to-assess instrument functions such as the acceptance angle distort the measured functions.

2.3. Film characterization

The crystal structure of tantalum thin films was analysed by X-ray diffraction (XRD) (PANalytical X'Pert PRO MPD) using Cu Kα radiation (45 kV and 40 mA) with a parallel beam in θ–2θ geometry. The incident beam optics consisted of a hybrid monochromator (with a Cu W/Si mirror and a double crystal Ge (220)). A parallel plate collimator (0.7°) and Soller slits (0.004°) were mounted on the path of the diffracted beam. A

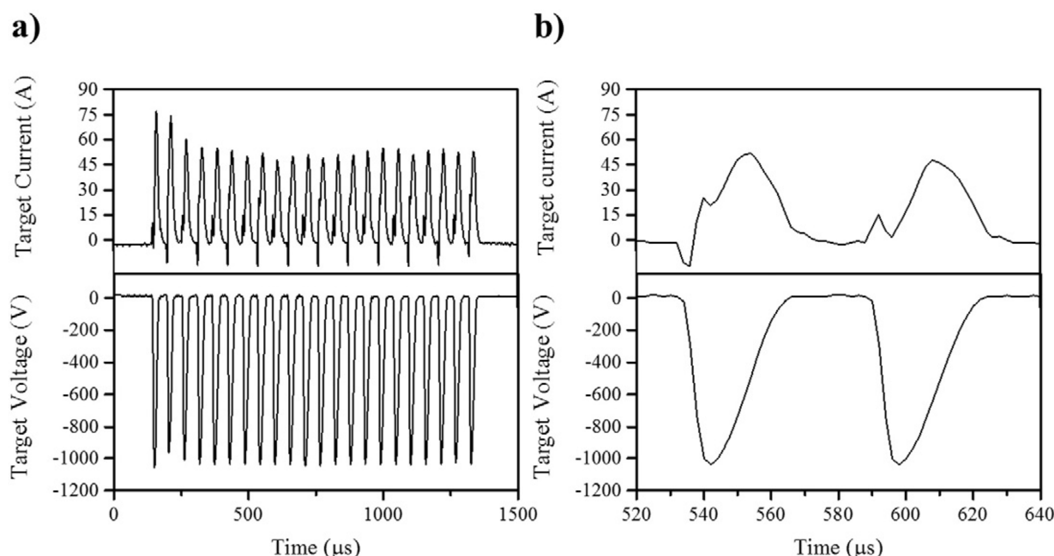

Fig. 1. a) The target voltage and current oscillation waveforms measured during the Ta thin film depositions. b) Small oscillation pulses within one long pulse.

Table 1
– Deposition conditions used to deposit tantalum thin films by DOMS.

DC_{int} (V)	V_p (V)	I_p (A)	P_p (kW)	F_i (Hz)	Dep. time (min.)
270	909	54	49	271	80
300	987	66	66	219	8
330	1084	76	82	180	95
360	1172	90	105	148	105
400	1296	101	130	120	115

PIXcel detector in receiving slit mode was used for X-ray collection. The thickness and morphology of the films were studied by scanning electron microscopy (SEM) using a Quanta 400FEG ESEM. The SEM images obtained for the cross section and surface area in this work were achieved with a 2 keV beam. The film topography and roughness were examined by atomic force microscopy (AFM) using a Bruker Innova equipment in contact mode. Images with a surface area of 2 μm × 2 μm resolution. The hardness of the films was measured by nano-indentation (MicroMaterialsNano Tester) using a Berkovich diamond indenter. The hardness was evaluated from load–displacement curves using the depth-sensing method. Hardness measurements were done with 10 mN loads in order to ensure an indentation depth less than 10% of the coating's thickness. 16 hardness measurements were performed on each specimen.

3. Results

3.1. Ion energy distribution functions

The time-averaged ion energy distributions (IEDFs) for $^{181}Ta^+$, $^{181}Ta^{2+}$, $^{40}Ar^+$ and $^{40}Ar^{2+}$ ion species measured from the DOMS plasma obtained at different peak powers (37, 52, 84 and 114 kW) during Ta sputtering are displayed in Fig. 2. The ion energy distributions obtained from the DCMS plasma are also displayed in Fig. 2 for comparison. All the regimes reveal a low energy peak for Ar^+ centred near 5 eV with a maximum energy close to 8 eV (Fig. 2a). This peak corresponds to thermalized Ar^+ ions after being accelerated over the sheath from the plasma to the substrate. The energetic position of the peak corresponds to the plasma potential. A similar IEDF for Ar^+ was found by Lin et al. [19] for a MPPMS discharge. The Ar^{2+} IEDs (Fig. 2b) exhibit a low energy peak centred close to 9 eV for both processes although the number of ions is almost one order of magnitude higher in DOMS than in DCMS. Once again, this peak corresponds to thermalized ions accelerated over the substrate (or detector entrance) sheath. However, the IEDFs of the DOMS process exhibit an additional high energy tail with increased maximum energy (from 30 to 48 eV) with increasing peak power. Hecimovic et al. [26] found that the Ar^{2+} IEDF in their HiPIMS discharge with a chromium target consisted of high energy ions (with maximum energy up to 25 eV) during the HiPIMS pulse while only a low energy Ar^{2+} peak was detected in post-discharge conditions. The authors proposed that the high energy Ar^{2+} ions were probably created through collisions with high energy Cr ions. Momentum transfer through collisions with the highly energetic Ta species also explains the high energy Ar^{2+} ions generated within the DOMS discharge. Note, however, that the energy of the vast majority of the Ar^{2+} ions is within the low energy peak and thus that energetic Ar^{2+} ions only have small influence on the film growth.

The Ta^+ IEDF in DCMS also show a low energy centred close to 6 eV but this peak extends up to 20 eV (Fig. 2c), i.e., up to higher energy than in DCMS. The higher energy Ta^+ ions result from the original Thompson distribution function of the sputter-ejected atoms [27]. Much broader Ta^+ IEDFs are found in DOMS. The maximum energy of the Ta^+ ions reaches 65 eV regardless of peak power. The DOMS discharge produces highly energetic single charged Ta ions with much higher energies than those generated in DCMS and MPPMS discharges [19]. This result is at least partly due to the larger cathode sheath voltage which develops

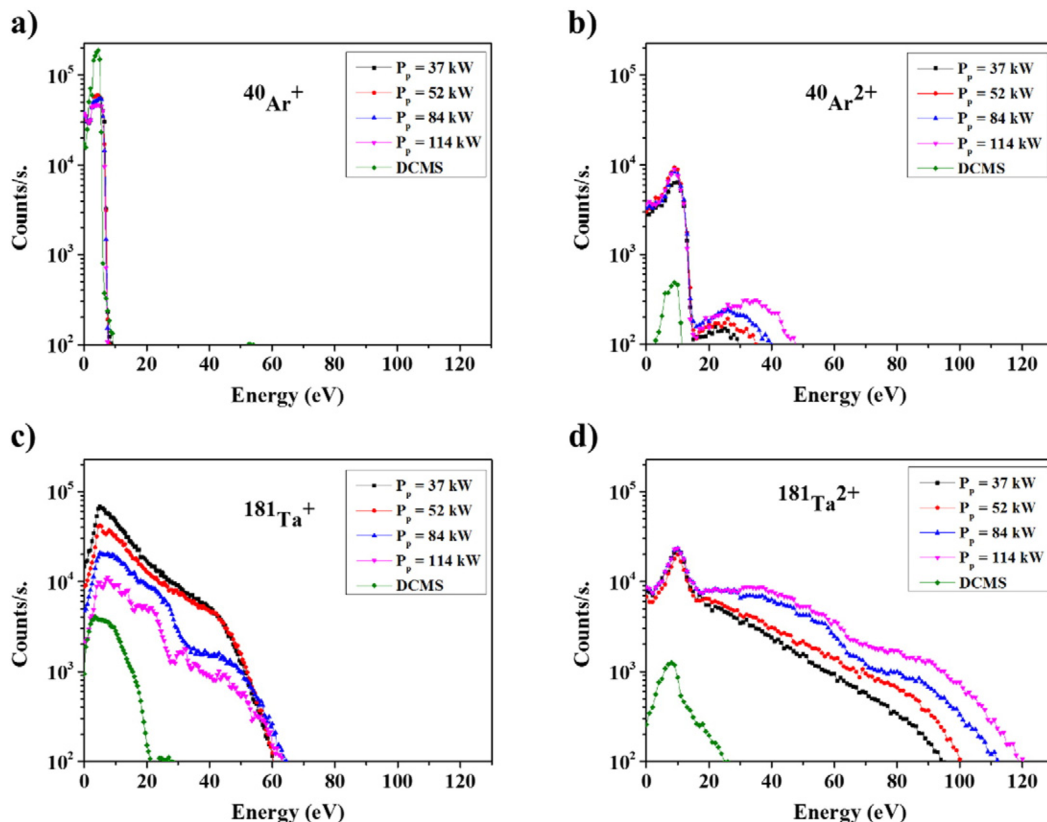

Fig. 2. Ion energy distributions (IEDs) of a) $^{40}Ar^+$; b) $^{40}Ar^{2+}$; c) $^{181}Ta^+$ and d) $^{181}Ta^{2+}$ species measured from DOMS plasma with different peak powers during sputtering a Ta target in pure Ar atmosphere. DCMS IEDs are also plotted for comparison.

in DOMS as the higher energy of the Ar^+ ions bombarding the target will translate to higher average energy of the sputtered Ta neutrals. However, the origin of the energetic metal species generated by HiPIMS is still an open issue [28]. Recently, Anders et al. proposed that ionization zones in HIPIMS are locations of locally enhanced potential, incorporating double layers (DL) which result in potential humps that could explain the relatively high energy of the ions at the substrate [29]. Maszl et al. [28] also concluded that energetic Ti^+ ions are created in the spokes region and subsequently accelerated inside the DL surrounding the spoke. A similar mechanism could also explained the highly energetic Ta ions produced by the DOMS discharges generated in this work. Note however that the total count of Ta^+ ions decreases with increasing peak power. Although the fraction of ionized sputtered metal species increases with increasing peak power [12], the total number of metal ions reaching the substrate can decrease due to several effects, such as back-attraction of ionized metal species and the yield effect, that also cause a deposition rate decrease with increasing peak power [30]. The Ta^{2+} IEDF in DCMS (Fig. 2d) exhibit a peak energy at 8 eV and a tail extending up to 25 eV. The amount of Ta^{2+} ions is much lower than Ta^+ ions while the more pronounced low energy peak shows that the Ta^{2+} are either more efficiently thermalized or generated outside accelerating field structures than the Ta^+ ions. In the DOMS discharge the Ta^{2+} IEDF exhibits a peak energy close to 10 eV and a tail extending to even higher energy than for the Ta^+ ions, i.e., reaching between 95 and 120 eV depending on the applied peak power. Furthermore, the ions count in the high-energy portion of the Ta^{2+} IEDF increases with increasing peak power.

The metal IEDFs (Ta^+ and Ta^{2+}) in DOMS exhibit much larger high energy tails than the process gas IDEFs (Ar^+ and Ar^{2+}) which suggest that a large fraction of the ion species within the plasma are energetic Ta ions. During a DOMS deposition the growing Ta film will be under intense and energetic bombardment of Ta ions while in DCMS most of the ions reaching the substrate are process gas ions with much lower energy.

3.2. Direct current magnetron sputtering (DCMS)

Fig. 3 shows the X-ray diffraction patterns (between 30° and 45°) of Ta thin films deposited by DCMS with increasing substrate bias (0, −30, −50, −80 and −120 V). The X-ray diffractograms exhibit β-Ta (002) peaks for all bias values. These results agree well with previous works [11,31,32]. The β-Ta (002) peak is shifted to higher diffraction angles (to smaller lattice spacing) as compared to the corresponding diffraction pattern standard, which is most probably due to the development of tensile stresses in the films. The peak shift decreases with increasing peak power and at the highest bias (−120 V) the β-Ta (002) peak is close to the unstressed position. This result is consistent with the increased energy of the Ar ions, which dominated DCMS as shown in the corresponding IEDF, as the bias is negatively increased. Despite of the increased energy of the ions bombarding the film, similar sharp β-Ta (002) peaks are observed irrespectively of the deposition bias. Dalla Torre et al. [33] have shown the importance of a mass match during growth of tantalum thin films by sputtering. The lower mass Ar ions as compared to the film-forming species are rather ineffective at influencing the Ta film structure.

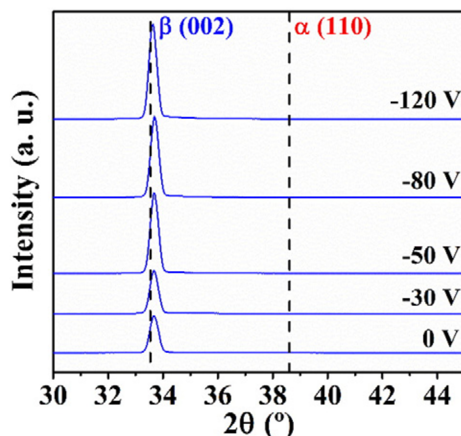

Fig. 3. X-ray diffraction patterns of the films prepared by DCMS with the increase of substrate bias.

Selected SEM micrographs of the Ta thin films deposited by DCMS with increase of substrate bias are shown in Fig. 4. All the films have a columnar morphology and exhibit brittle fractures typical of the β-phase. Similar Brittle fractures were also observed by Myers et al. [34] and corresponds to the T zone in Thornton's structure zone diagram [35]. The Ta thin films deposited with −30 and −80 V exhibit a surface with three-sided pyramidal structures. Increasing the substrate bias to −120 V resulted in the formation of structure with ellipsoidal morphology.

3.3. Deep oscillation magnetron sputtering (DOMS)

The deposition rate of the tantalum thin films deposited by DOMS is shown in Fig. 5. The deposition rate was calculated by dividing the film thickness (measured by SEM) by the deposition time. An increase of the peak power by a factor of almost three results in a loss of 43% in deposition rate. The loss of deposition rate in DOMS [20,21,24], and more generally in HIPIMS [30,36–39], as compared to DCMS, is well documented in the literature. The deposition rate decreases with increasing peak power in HIPIMS due to the back-attraction of some of the ionized sputtered metal species to the target, the so-called return effect. On the other hand, the yield effect results from the lower efficiency of the sputtering process at the typically higher process voltages in HIPIMS, as compared to DCMS, which originates in the sub-linear energy dependence of the sputtering yield [30,38]. Among other effects, Panjan et al. and Franz et al. also reported an increased flux of the sputtered species sideways, i.e., to higher angles with respect to target surface normal in HIPIMS than in DCMS [25,40].

Fig. 6 shows the X-ray diffraction patterns (between $2\theta = 30°$ and 45°) of Ta thin films deposited by DOMS with increase of peak power (P_p). All the diffractograms of Ta films deposited with a peak power up to 105 kW only exhibit the α-Ta (110) diffraction peak showing that pure α-Ta was deposited. In all the diffractograms the α-Ta (110) diffraction angle is lower than in the corresponding diffraction pattern

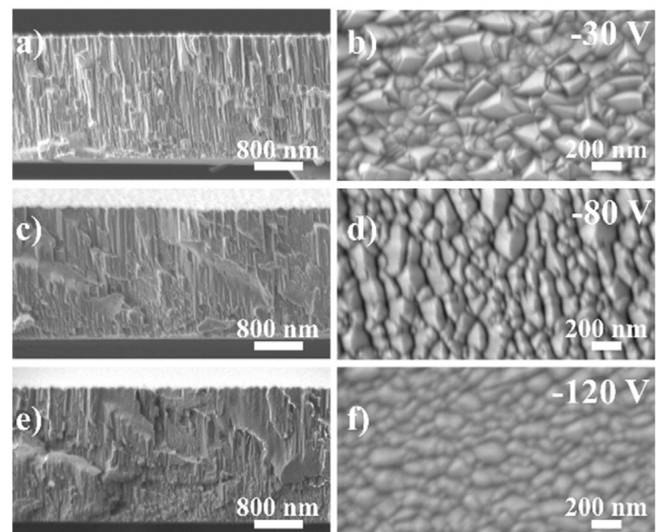

Fig. 4. SEM micrographs of Ta 2 μm thick films deposited by DCMS with substrate bias of a, b) −30 V; c, d) −80 V; e, f) −120 V.

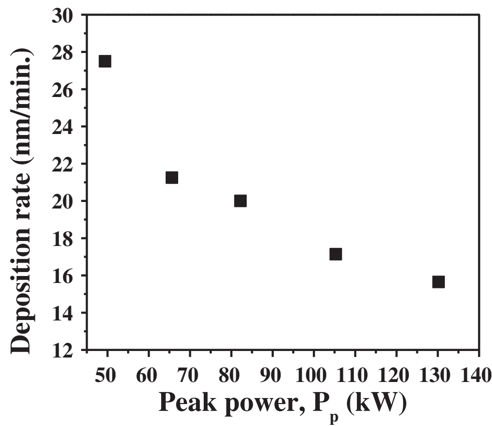

Fig. 5. Deposition rate of Ta thin films deposited by DOMS as function of P_p.

standard, which indicates the formation of compressive stresses. However, the shift of the α-Ta (110) peak to higher diffraction angles with increasing peak power shows that the compressive stress is partially relaxed at higher peak power. The α-Ta (110) diffraction peaks are broader than in DCMS indicating smaller grain sizes. Ren et al. proposed that small grain size of the α–Ta may be due to the high density of nucleation sites on the surface which is bombarded with energetic ions [41]. Increasing the peak power to 130 kW results in the deposition of mixed α- and β-Ta phases as confirmed by the presence of the corresponding diffraction peaks. However, the diffraction peaks are much broader and much less intense than at lower P_p, while the β-Ta (200) peak position coincides with the value in the corresponding diffraction pattern standard.

The cross-section and surface morphology of Ta thin films deposited by DOMS has been observed by SEM (Fig. 7). In cross-section all Ta thin films exhibit a columnar morphology with closely-packed columns and compact grain boundaries. This morphology corresponds to the T zone in the generalized structure zone diagram [42], and it was also observed in previous works with the use of DOMS power supply [20,21]. The Ta thin film deposited with 130 kW reveal two different types of fracture, the lower part of film (nearby the substrate) exhibits a brittle fracture while the upper part exhibits a ductile fracture. Myers et al. observed the same behaviour and attributed these different fractures types to the presence of different Ta phases [34]. This is in agreement with the X-ray diffractions which revealed a mixed phase structure. The surface of the film deposited with a peak power of 49 kW displays dense, regularly spaced grain facets similar to the ones reported by Ren et al. for α-Ta [41]. Increasing the peak power results in similar but lower sized

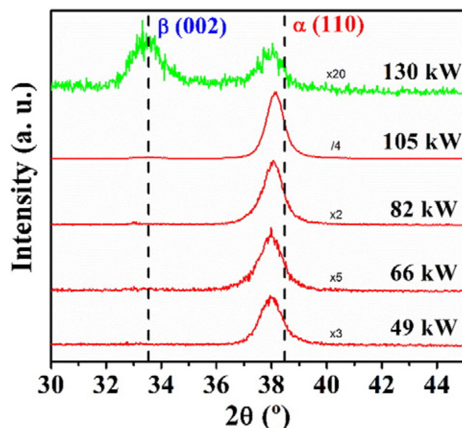

Fig. 6. XRD patterns of the films deposited by DOMS as function of P_p.

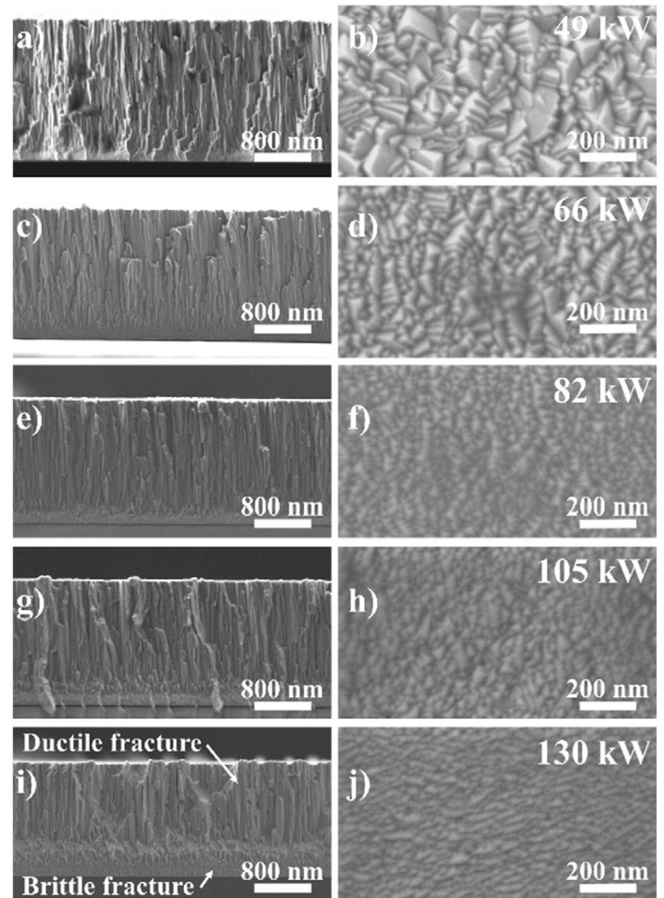

Fig. 7. SEM cross-section and surface micrographs of the Ta thin films deposited by DOMS with a P_p of a, b) 49 kW; c, d) 66 kW; e, f) 82 kW; g, h) 105 kW; i, j) 130 kW.

features on the film surface, even for the film deposited at 130 kW as α-Ta was deposited on the upper part of the film.

Fig. 8 shows the AFM 3D topographic images of Ta thin films of different P_p, deposited by DOMS. The AFM measurements were done in contact mode over 2 × 2 μm area. These analyses confirm what was observed in the SEM analyses. In AFM is also observed the surface structures downsize with the increase of the peak power. All the AFM images confirm the deposition of Ta films without significant defects.

The average roughness (measured by AFM) of Ta thin films deposited with increasing peak power is displayed in Fig. 9. The increase of peak power, i.e., increase of ion bombardment, results in a decrease of the roughness in two steps. This result agrees well with the decrease of the surfaces structures observed in SEM and AFM analyses.

Fig. 10 shows the hardness and Young's modulus of the DOMS Ta thin films deposited at different peak powers. The hardness values reported in the literature for α-Ta are between 8 and 12 GPa while higher hardness is reported for β-Ta (16 to 20 GPa) depending on the deposition method [43]. All the Ta thin films deposited between 49 and 105 kW have close to 11.5 GPa. All these films have pure α-Ta phase, therefore, this result agrees well with the hardness values mention above. The Ta thin film deposited with a peak power of 130 kW reveals a slightly higher hardness (12.7 GPa) which agrees well with the deposition of β-Ta mixed with α–Ta. The Young's modulus values of the Ta films range between 210 and 220 GPa.

4. Discussion

All the films deposited by DCMS consist only of the β-Ta phase and clearly have columnar microstructures. Increasing the bias voltage did not significantly change the films structure and microstructure although

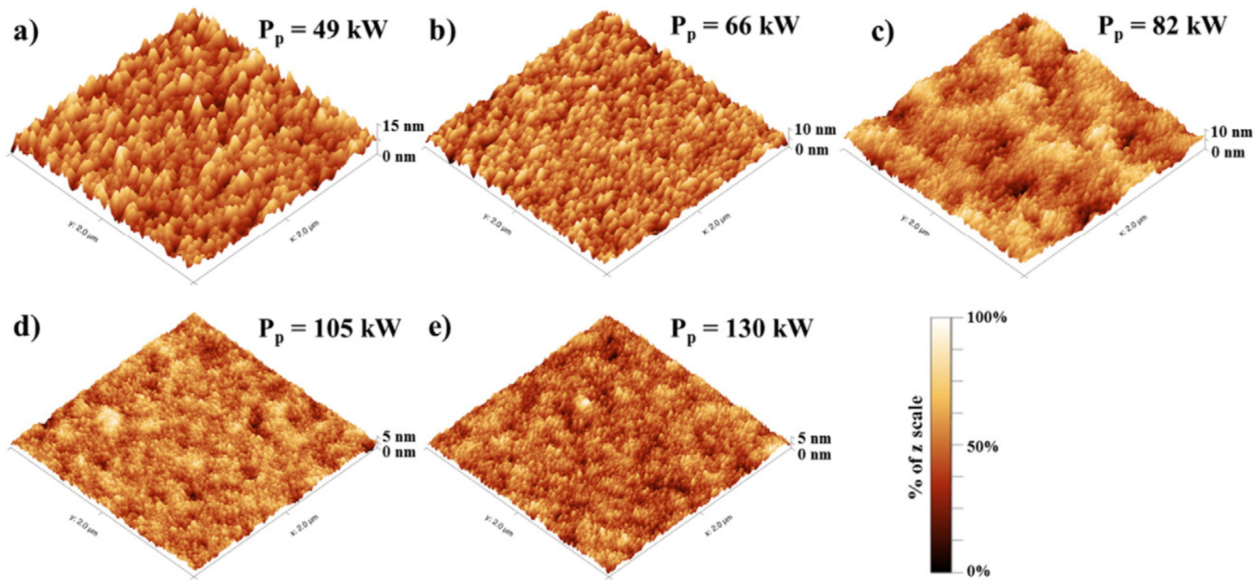

Fig. 8. Representative AFM scans (2 μm × 2 μm) showing the surface morphology of Ta thin films deposited by DOMS with a P_p of a) 49 kW; b) 66 kW; c) 82 kW; d) 105 kW; e) 130 kW.

bias voltages as high as −120 V were used in this work. As was shown in Section 3.1, the DCMS discharge consist mainly of process gas ions (Ar^+) which are extracted from the plasma and bombard the growing film after acceleration in the substrate sheath. Although very high energy ions were used during deposition at the highest bias, the momentum transfer to the growing film is rather ineffective as it is an indirect process which relies on collisions of the accelerated Ar ions with the Ta adatoms. Moreover, the mass mismatch between Ar and Ta further reduces the momentum transfer effectiveness. As a result the Ta thin films consist only of the β-Ta phase and even develop tensile stresses irrespective of the bias voltage. The deposition of pure α-Ta thin films by sputtering has been demonstrated by Ino et al. [8]. Pure α-Ta deposition was achieved at low bias voltages (between −5 and −25 V) but only at high Ar^+ fluxes which were achieved by using additional dual rf excitation of the plasma. In this work no additional plasma excitation sources were used in the DCMS depositions and the Ar^+ flux impinging on the growing film is insufficient to reach the pure α-Ta deposition region in the experimental phase formation diagram proposed by Ino et al. [8].

The Ta thin films deposited by DOMS up to 105 kW consist only of the α-Ta phase. Compressive stress are formed while the grain size is smaller than in the DCMS films. On the other hand, increasing the peak power leads to the deposition of more compact microstructures with much lower surface roughness. As was shown in Section 3.1, the DOMS plasma is dominated by highly energetic Ta^+ and Ta^{2+} ions which bombard the substrate during film grow. The momentum transfer to the film is then much more effective than in DCMS as it is directly carried out by the film-forming species. As a result, pure α-Ta is deposited while the films microstructure evolves according to the peak power, i.e., according to the energy and flux of the bombarding ions. The DOMS process allows us to deposit pure α–Ta without the addition of supplementary equipment, without substrate biasing and without substrate heating in contrast to previous works [5,19,41]. However, the energetic bombardment induced the formation of compressive stresses in the films as also found in previous works [5,8].

Lin et al. performed IEDFs measurements of Ar^+, Ta^+, and Ta^{2+} in a MPPMS discharge over a Ta target [19]. The IEFDs were shown to consist only in a low energy peak centred around 3 eV and with maximum energy of 12 eV for Ar^+ and Ta^+ and slightly lower (8 eV) for Ta^{2+} (however, no mention is made in this work about the charge state correction of energy, which, if it was omitted, would put the Ta^{2+} peak at 16 eV). In this work the IEDFs of the metallic ions also display a similar low energy peak, corresponding to thermalized species, but in all cases an additional high energy tail, extending up to 48 eV for Ta^+ and up to 120 eV for Ta^{2+}, is also detected. The negative target voltages are higher in the DOMS process (between −909 and −1296 V, Table 1) than in the MPPMS process used by Lin et al. (below −500 V). Thus, the Ar^+ ions

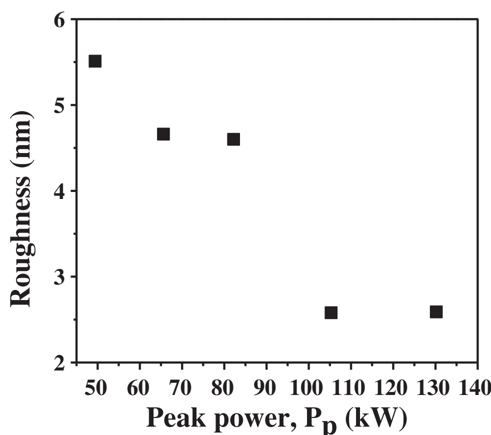

Fig. 9. Surface roughness calculated from the AFM scans of the films deposited by DOMS with increase of P_p.

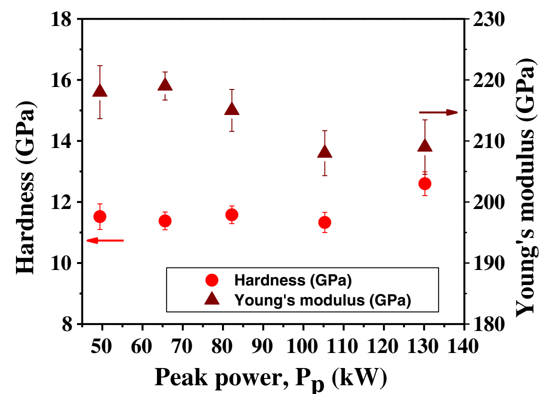

Fig. 10. Hardness and Young's modulus of the Ta thin films deposited by DOMS with the increase of P_p.

in DOMS gain more energy upon acceleration in the target sheath, and, although some of this energy will contribute to an increase of the sputtering yield this will also contribute to an increased energy of the sputtered species. As a result more energetic metallic ions will reach the substrate in DOMS as compared to MPPMS.

The XRD analyses shows that a mixed α- and β-Ta film was deposited by DOMS at the highest peak power (130 kW). Accordingly, the hardness of this film is higher than that of the pure α-Ta films deposited by DOMS at lower peak power. The SEM cross section of the film clearly shows that the film consists of β-Ta in the lower part while α-Ta is grown in the upper part. Alami et al. [11] reported on an energy window for the deposition of pure α–Ta by HIPIMS. The authors concluded that the window's higher energy limit was due to relaxation of the film stress under energetic ion bombardment. On the other hand, Ino et al. [8] found that the β-Ta phase is always formed at higher energies, i.e., when higher bias voltages (above 25 V) are used to accelerate the argon ions impinging on the growing film. The authors concluded that β-Ta formation was caused by the defects induced by the recoil implantation of Ta atoms in the excessive high-energy ion bombardment conditions. Both explanations cited above for the formation of the β-Ta phase under energetic bombardment during deposition are consistent with the results obtained in this work. A relaxation of the film stress with increasing peak power was observed by X-ray diffraction while the more compact microstructures and much lower roughness of the films deposited with increasing peak power could be explained by renucleation due to increasing defects formation, morphology that corresponds to the zone 3 in the generalized structure zone diagram [10].

5. Conclusions

The IEDFs measurement of the DCMS and DOMS discharges using a tantalum target revealed very different plasma environments for each deposition process. The DCMS plasma is dominated by low energy process gas ions while the DOMS discharge contains a large fraction of highly energetic (up to 120 eV) Ta ions. Although substrate biases up to −120 V were used in DCMS, all the deposited films consist in pure β-Ta. This result was attributed to the ineffective indirect momentum transfer from the Ar ions to the growing film that results in insufficient energy supply to grow the α-Ta phase. In contrast, α-Ta was formed in all films deposited by DOMS without the need of substrate biasing (samples at ground potential) and/or substrate heating. The momentum transfer to the film is much more effective than in DCMS as it is directly carried out by the film forming species. As a result, the films microstructure evolves according to the peak power, i.e., according to the energy and flux of the bombarding ions. The DOMS process allowed us to deposit pure α–Ta without the addition of supplementary equipment and without the need of substrate biasing as reported in previous works.

Acknowledgments

This research is sponsored by FLAD, FEDER funds through the program COMPETE – Programa Operacional Factores de Competitividade – and by national funds through FCT – Fundação para a Ciência e a Tecnologia –, under the projects: PTDC/EME-TME/122116/2010, PTDC/EMS-TEC/1805/2012 and PEst-C/EME/UI0285/2013, as well as the grant (SFRH/BD/68740/2010). Work at Lawrence Berkeley National Laboratory is supported by the U.S. Department of Energy under Contract No. DE-AC02-05CH11231.

References

[1] L. Gladczuk, A. Patel, C.S. Paur, M. Sosnowski, Tantalum films for protective coatings of steel, Thin Solid Films 467 (2004) 150–157.
[2] M. Grosser, U. Schmid, The impact of sputter conditions on the microstructure and on the resistivity of tantalum thin films, Thin Solid Films 517 (2009) 4493–4496.
[3] K. Holloway, P.M. Fryer, Tantalum as a diffusion barrier between copper and silicon, Appl. Phys. Lett. 57 (1990) 1736–1738.
[4] L. Liu, H. Gong, Y. Wang, J. Wang, A. Wee, R. Liu, Annealing effects of tantalum thin films sputtered on [001] silicon substrate, Mater. Sci. Eng. C 16 (2001) 85–89.
[5] S. Maeng, L. Axe, T. Tyson, P. Cote, Corrosion behaviour of electrodeposited and sputtered Cr coatings and sputtered Ta coatings with α and β phases, Surf. Coat. Technol. 200 (2006) 5767–5777.
[6] G. Chen, P. Lee, S. Chen, Phase formation behavior and diffusion barrier property of reactively sputtered tantalum-based thin films used in semiconductor metallization, Thin Solid Films 353 (1999) 264–273.
[7] L. Hallmann, P. Ulmer, Effect of sputtering parameters and substrate composition on the structure of tantalum thin films, Appl. Surf. Sci. 282 (2013) 1–6.
[8] K. Ino, T. Shinohara, T. Ushiki, T. Ohmi, Ion energy, ion flux, and ion species effects on crystallographic and electrical properties of sputter-deposited Ta thin films, J. Vac. Sci. Technol. A 15 (1997) 2627–2635.
[9] D.W. Matson, E.D. McClanahan, J.P. Rice, S.L. Lee, D. Windover, Effect of sputtering parameters on Ta coatings for gun bore applications, Surf. Coat. Technol. 133 (2000) 411–416.
[10] N. Schwartz, E. Feit, Impurity effects in the nucleation of alpha (bcc)-tantalum or Beta-tantalum films, J. Electrochem. Soc. 124 (1977) 123–131.
[11] J. Alami, P. Eklund, J.M. Andersson, M. Lattemann, E. Wallin, J. Bohlmark, et al., Phase tailoring of Ta thin films by highly ionized pulsed magnetron sputtering, Thin Solid Films 515 (2007) 3434–3438.
[12] A. Ehiasarian, R. New, W.-D. Münz, L. Hultman, U. Helmersson, V. Kouznetsov, Influence of high power densities on the composition of pulsed magnetron plasmas, Vacuum 65 (2002) 147–154.
[13] U. Helmersson, M. Lattemann, J. Bohlmark, A.P. Ehiasarian, J.T. Gudmundsson, Ionized physical vapor deposition (IPVD): a review of technology and applications, Thin Solid Films 513 (2006) 1–24.
[14] V. Kouznetsov, K. Macak, J.M. Schneider, U. Helmersson, I. Petrov, A novel pulsed magnetron sputter technique utilizing very high target power densities, Surf. Coat. Technol. 122 (1999) 290–293.
[15] D. Lundin, K. Sarakinos, An introduction to thin film processing using high-power impulse magnetron sputtering, J. Mater. Res. 27 (2012) 780–792.
[16] J. Lin, J.J. Moore, W.D. Sproul, B. Mishra, Z. Wu, Modulated pulse power sputtered chromium coatings, Thin Solid Films 518 (2009) 1566–1570.
[17] J. Lin, J. Moore, W. Sproul, B. Mishra, J. Rees, Z. Wu, et al., Ion energy and mass distributions of the plasma during modulated pulse power magnetron sputtering, Surf. Coat. Technol. 203 (2009) 3676–3685.
[18] J. Lin, W.D. Sproul, J.J. Moore, Z. Wu, S. Lee, R. Chistyakov, et al., Recent advances in modulated pulsed power magnetron sputtering for surface engineering, JOM 63 (2011) 48–58.
[19] J. Lin, J.J. Moore, W.D. Sproul, S.L. Lee, J. Wang, Effect of negative substrate bias on the structure and properties of Ta coatings deposited using modulated pulse power magnetron sputtering, IEEE transactions on plasma science 38 (2010) 3071–3078.
[20] F. Ferreira, R. Serra, J. Oliveira, A. Cavaleiro, Effect of peak target power on the properties of Cr thin films sputtered by HiPIMS in deep oscillation magnetron sputtering (DOMS) mode, Surf. Coat. Technol. 258 (2014) 249–256.
[21] F. Ferreira, J. Oliveira, A. Cavaleiro, CrN thin films deposited by HiPIMS in DOMS mode, Surf. Coat. Technol. 291 (2016) 365–375.
[22] J. Lin, W.D. Sproul, Structure and properties of Cr_2O_3 coatings deposited using DCMS, PDCMS, and DOMS, Surf. Coat. Technol. 276 (2015) 70–76.
[23] J. Lin, B. Wang, W.D. Sproul, Y. Ou, I. Dahan, Anatase and rutile TiO2 films deposited by arc-free deep oscillation magnetron sputtering, J. Phys. D. Appl. Phys. 46 (2013) 084008.
[24] J. Oliveira, F. Fernandes, F. Ferreira, A. Cavaleiro, Tailoring the nanostructure of Ti–Si–N thin films by HiPIMS in deep oscillation magnetron sputtering (DOMS) mode, Surf. Coat. Technol. 264 (2015) 140–149.
[25] R. Franz, C. Clavero, J. Kolbeck, A. Anders, Influence of ionisation zone motion in high power impulse magnetron sputtering on angular ion flux and NbO × film growth, Plasma Sources Sci. Technol. 25 (2016) 015022.
[26] A. Hecimovic, A.P. Ehiasarian, Spatial and temporal evolution of ion energies in high power impulse magnetron sputtering plasma discharge, J. Appl. Phys. 108 (2010) 063301.
[27] M. Thompson, II. The energy spectrum of ejected atoms during the high energy sputtering of gold, Philos. Mag. 18 (1968) 377–414.
[28] C. Maszl, W. Breilmann, J. Benedikt, A. von Keudell, Origin of the energetic ions at the substrate generated during high power pulsed magnetron sputtering of titanium, J. Phys. D. Appl. Phys. 47 (2014) 224002.
[29] A. Anders, M. Panjan, R. Franz, J. Andersson, P. Ni, Drifting potential humps in ionization zones: the “propeller blades” of high power impulse magnetron sputtering, Appl. Phys. Lett. 103 (2013) 144103.
[30] A. Anders, Deposition rates of high power impulse magnetron sputtering: physics and economics, J. Vac. Sci. Technol. A 28 (2010) 783–790.
[31] H. Högberg, L. Tengdelius, M. Samuelsson, J. Jensen, L. Hultman, β-Ta and α-Cr thin films deposited by high power impulse magnetron sputtering and direct current magnetron sputtering in hydrogen containing plasmas, Phys. B Condens. Matter 439 (2014) 3–8.
[32] A. Jiang, T.A. Tyson, L. Axe, L. Gladczuk, M. Sosnowski, P. Cote, The structure and stability of β-Ta thin films, Thin Solid Films 479 (2005) 166–173.
[33] J. Dalla Torre, G. Gilmer, D. Windt, R. Kalyanaraman, F. Baumann, P. O'Sullivan, et al., Microstructure of thin tantalum films sputtered onto inclined substrates: experiments and atomistic simulations, J. Appl. Phys. 94 (2003) 263–271.
[34] S. Myers, J. Lin, R.M. Souza, W.D. Sproul, J.J. Moore, The β to α phase transition of tantalum coatings deposited by modulated pulsed power magnetron sputtering, Surf. Coat. Technol. 214 (2013) 38–45.

[35] J.A. Thornton, Influence of apparatus geometry and deposition conditions on the structure and topography of thick sputtered coatings, J. Vac. Sci. Technol. 11 (1974) 666–670.
[36] J. Alami, K. Sarakinos, G. Mark, M. Wuttig, On the deposition rate in a high power pulsed magnetron sputtering discharge, Appl. Phys. Lett. 89 (2006) 154104.
[37] D. Christie, Fundamentals of high power pulsed magnetron sputtering: visualization of mechanisms for rate reduction and increased ion fraction, Czechoslov. J. Phys. 56 (2006) B93–B97.
[38] J. Emmerlich, S. Mráz, R. Snyders, K. Jiang, J.M. Schneider, The physical reason for the apparently low deposition rate during high-power pulsed magnetron sputtering, Vacuum 82 (2008) 867–870.
[39] M. Samuelsson, D. Lundin, J. Jensen, M.A. Raadu, J.T. Gudmundsson, U. Helmersson, On the film density using high power impulse magnetron sputtering, Surf. Coat. Technol. 205 (2010) 591–596.
[40] M. Panjan, R. Franz, A. Anders, Asymmetric particle fluxes from drifting ionization zones in sputtering magnetrons, Plasma Sources Sci. Technol. 23 (2014) 025007.
[41] H. Ren, M. Sosnowski, Tantalum thin films deposited by ion assisted magnetron sputtering, Thin Solid Films 516 (2008) 1898–1905.
[42] A. Anders, A structure zone diagram including plasma-based deposition and ion etching, Thin Solid Films 518 (2010) 4087–4090.
[43] S. Lee, M. Doxbeck, J. Mueller, M. Cipollo, P. Cote, Texture, structure and phase transformation in sputter beta tantalum coating, Surf. Coat. Technol. 177 (2004) 44–51.

ANNEX C

F. Ferreira, J. Oliveira, and A. Cavaleiro, "CrN thin films deposited by HiPIMS in DOMS mode," Surface and Coatings Technology, vol. 291, pp. 365-375, 2016.

Surface & Coatings Technology 291 (2016) 365–375

Contents lists available at ScienceDirect

Surface & Coatings Technology

journal homepage: www.elsevier.com/locate/surfcoat

CrN thin films deposited by HiPIMS in DOMS mode

F. Ferreira *, J.C. Oliveira, A. Cavaleiro

SEG-CEMUC, Mechanical Engineering Department, University of Coimbra, Polo II, Rua Luís Reis Santos, 3030-788 Coimbra, Portugal

ARTICLE INFO

Article history:
Received 4 August 2015
Revised 2 February 2016
Accepted in revised form 29 February 2016
Available online 4 March 2016

Keywords:
CrN films
DOMS
Film growth
Mechanical properties

ABSTRACT

It is well known that increasing the energy of the bombardment species, whether by using a bias or an additional ion source in direct current magnetron sputtering (DCMS) or by optimizing the deposition conditions in mid-frequency bipolar magnetron sputtering, enables us to tailor the properties of the CrN thin films. In the last fifteen years, several magnetron sputtering deposition methods have been developed which have aimed to produce highly ionized fluxes of sputtered material, thus enabling increased control over the energy and impinging angle distributions of the bombarding species. In this study, CrN thin films were deposited by deep oscillation magnetron sputtering (DOMS), a variant of High-power Impulse Magnetron Sputtering (HiPIMS), in order to study the effect of the additional control of the energetic ion bombardment on the film properties. The structural properties of the CrN films (lattice parameter and preferred orientation) showed that an intense energetic bombardment is always present in the DOMS deposition irrespective of the deposition conditions. This energetic bombardment was attributed to energetic N neutrals which are reflected at the target surface upon impingement of N_2^+ ions. A change from a columnar growth mode to a featureless one was observed with an increasing peak power at both 0.3 and 0.7 Pa. At the same time, the hardness of the films increased from 21–22 GPa to 28–29 GPa. This transformation was attributed to the increasing fraction of ionized sputtered species with increasing peak power. The columnar growth is interrupted by preventing the shadowing effect, i.e., due to the higher ionization fraction at higher pressure and/or peak power, rather than by overcoming the shadowing effect by using more energetic bombardment.

© 2016 Elsevier B.V. All rights reserved.

1. Introduction

In the past few decades, CrN films have been widely used in many engineering applications due to their considerable hardness, resistance to wear, low friction coefficients and high temperature stability [1–9]. Nowadays, both DC magnetron sputtering (DCMS) [3–6] and mid-frequency bipolar magnetron sputtering [8] are well-established methods for the reactive magnetron sputtering of CrN thin films. From the process point of view, relatively low levels of ion bombardment result in CrN films with [111] preferred orientation, lower stresses, lower hardness and lower density. Increasing the bombardment level gradually changes the preferential orientation to [002] or [220], while denser, harder and smoother coatings are deposited. The [002] or [220] preferred orientations can be obtained, for example, by increasing the deposition bias [5–7] or by enhancing the energetic bombardment in mid-frequency bipolar magnetron sputtering [9]. However, improvement in the mechanical properties of the coatings brings about a simultaneous increase in the film compressive stresses, which are detrimental in service. Zou et al. [10] also showed that the hardness of CrN films deposited by mid-frequency bipolar magnetron sputtering could be increased from 13 to 25 GPa by using an additional ion source. Once again, the increase in hardness occurred simultaneously with a preferential orientation change from [111] to [002]. The above results show that careful control of the ion bombardment is crucial for optimizing the properties of the CrN films.

In the last fifteen years, several magnetron sputtering deposition methods have been developed with the aim of producing highly ionized fluxes of sputtered material, thus enabling increased control over the energetic ion bombardment (energy and direction of the deposited species). Two of these recent developments are: High-power Impulse Magnetron Sputtering (HiPIMS) [11–14] and Modulated Pulsed Power Magnetron Sputtering (MPPMS) [15–17]. Both HiPIMS and MPPMS rely on the application of very high target power densities to increase the plasma density and therefore ionize the sputtered material. Such deposition conditions have been shown to be very useful for the tailoring of the microstructure and properties of CrN coatings [18–25]. Ehiasarian et al. [18] deposited dense and columnar CrN films by HiPIMS, clearly harder than conventional PVD CrN and with superior corrosion and wear resistant properties. Paulitsch et al. [19] showed that HIPIMS is much more versatile than DCMS for process up-scaling. The hardness of the CrN films (≈23 GPa) was maintained even when a 3-fold substrate rotation was used, while the hardness of the films deposited by DCMS decreased to less than 15 GPa. Lin et al. [22] also demonstrate that MPPMS enables the deposition of CrN films with higher hardness (25–26 GPa) than their DCMS counterpart (16 GPa). In a series of

* Corresponding author.
E-mail address: fabio.ferreira@dem.uc.pt (F. Ferreira).

http://dx.doi.org/10.1016/j.surfcoat.2016.02.064
0257-8972/© 2016 Elsevier B.V. All rights reserved.

studies [23–25] these authors also showed that MPPMS allows for the deposition of thick films (up to 55 μm) with high deposition rates.

Recently, a new deposition process, called deep oscillation magnetron sputtering (DOMS), was developed, based on MPPMS [26–30]. This process uses large voltage oscillation packets in long modulated pulses in order to attain high peak target currents and voltages. Such a configuration has been reported to decrease arcing in reactive deposition of insulating films and even allow virtually arc-free depositions. In a previous publication, the authors have shown that the microstructure of TiSiN films can be effectively tailored by changing the peak power in the DOMS process [30]. Two deposition regimes were identified. At low peak power, stress-free TiSiN films with [002] preferred orientation and a high degree of hardness (nearly 25 GPa) could be deposited. Increasing the peak power, i.e. increasing the bombardment intensity, resulted in an increase in hardness of up to 30 GPa, albeit with a concomitant increase in the films' defects and compressive stress, in a very similar fashion to that in the DCMS process. The main objective of the present work was to study the effect of the energetic ion bombardment of the growing films on the properties of CrN thin films deposited by DOMS. The energetic ion bombardment was controlled by changing the peak power and the deposition pressure (0.3 and 0.7 Pa). The structure, morphology and mechanical properties of CrN coatings were characterized. A CrN thin film was also deposited by DC magnetron sputtering (DCMS), using previously optimized deposition conditions, for reference purposes.

2. Experimental procedure

CrN films were deposited in reactive mode by DOMS (HiPIMS Cyprium™ III plasma generator, Zpulser Inc.) and DCMS (Hüttinger PFG 7500 DC). In both cases a square (150 × 150 mm) high purity Cr (99.9%) target was sputtered in reactive mode. Typical examples of the discharge voltage and current oscillating waveforms of the DOMS process are shown in Fig. 1. A DOMS pulse is made of a packet of 25 sequential single oscillations. In each oscillation both the voltage and the current gradually increase during the on-time (t_{on}) until they reach their maximum value (V_p and I_p). Then, both the voltage and current gradually decay, reaching zero before the end of the oscillation period (T). The DOMS depositions were performed using constant on-time (t_{on}), oscillation period (T) and pulse duration (D) of 6, 40 and 1000 μs respectively. The average power was controlled by the DOMS power supply software by automatic adjustment of the pulse frequency (F). A constant average power (Pa) of 1200 W was used in all depositions. In this study the peak voltage (V_p) and peak current (I_p) were calculated as the average value of the maximums of the voltage and current, respectively, in each oscillation, taking all the oscillations into account. The peak power (P_p) is defined as the product $V_p \times I_p$. A CrN film was deposited by DCMS using the same time average power (1200 W) as was used in the DOMS depositions. The DCMS film was deposited at 0.3 Pa with a bias of −80 V, resulting in a deposition voltage of −412 V and a 3 A.

All coatings were deposited onto (100) silicon samples. Prior to depositions, the substrates were ultrasonically cleaned in acetone for 15 min and [in] alcohol for 10 min. They were then fixed to a rotating substrate holder which revolved at 23.5 rev/min around the central axis of the chamber. Prior to all depositions a base pressure lower than 5×10^{-3} Pa was attained in the deposition chamber. The target to substrate distance was 80 mm. All the depositions were performed in reactive mode in an Ar + N_2 discharge gas. The Ar:N_2 gas flow ratio was maintained at 1:3. In order to enhance the adhesion of coatings a Cr adhesion layer of approximately 0.2 μm was deposited on the substrates before the final CrN layers.

The peak power was varied by progressively increasing the charging voltage (DC_{int}) of the DOMS power supply from 250 to 400 V. To further diversify the bombarding conditions on the growing films, two different deposition pressures were used (0.3 and 0.7 Pa). The main DOMS deposition parameters are compiled in Table 1. As shown in Fig. 2 using the values from Table 1 for the films deposited at 0.3 Pa, both I_p and V_p increased almost linearly with increasing peak power. A similar behaviour was found for the films deposited at 0.7 Pa (not shown).

The structure of CrN coatings was characterized by X-ray diffraction (XRD) (PANalytical X'Pert PRO MPD) with Cu Kα radiation (45 kV and 40 mA) using a parallel beam in symmetrical θ–2θ geometry. The XRD spectra were fitted using a pseudo-Voigt function to calculate both the area and the position (2θ) of the peaks. The lattice parameter was calculated by applying the Bragg's equation and using the geometrical relationship between the lattice parameter and the interplanar distance and Miller indices. The fracture cross section and surface morphologies of the coatings were examined by scanning electron microscopy (SEM). The composition of the CrN films was evaluated by Energy Dispersive Spectroscopy (EDS) using a CrN thin film previously studied by Electron Probe Micro-Analysis (EPMA) as standard. The hardness and Young's modulus of the films were evaluated by the depth-sensing indentation technique (Micro Materials NanoTest) using a Berkovich diamond pyramid indenter. A load of 8 mN was used in all the tests, in order to ensure an indentation depth of less than 10% of the coating's thickness. 16 hardness measurements were performed on each specimen.

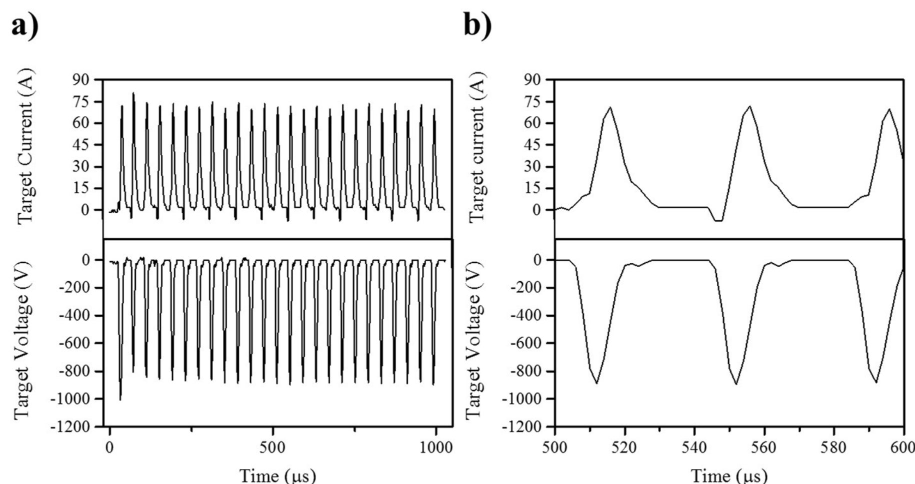

Fig. 1. a) The target voltage and current oscillation waveforms measured during the CrN coating depositions. b) Small oscillation pulses within one long pulse (P = 0.7 Pa; DC_{int} = 300 V; F = 233 Hz; D = 1000 μs; t_{on} = 6 μs; T = 40 μs).

Table 1
Deposition conditions used to deposit CrN films by DOMS.

Pressure (Pa)	V_p (V)	I_p (A)	P_p (kW)	F_i (Hz)	DC_{int} (V)	Dep. time (min)	Thickness (nm)
0.3 Pa	−908	46	42	275	250	90	1380
	−975	58	57	224	300	110	1361
	−1073	70	75	186	330	135	1323
	−1152	84	97	160	360	120	1140
	−1287	112	144	119	400	180	1265
0.7 Pa	−773	44	34	287	250	90	1760
	−878	72	63	233	300	110	1300
	−940	88	83	194	330	135	1135
	−1012	102	103	167	360	165	1205
	−1119	129	144	114	400	180	1010

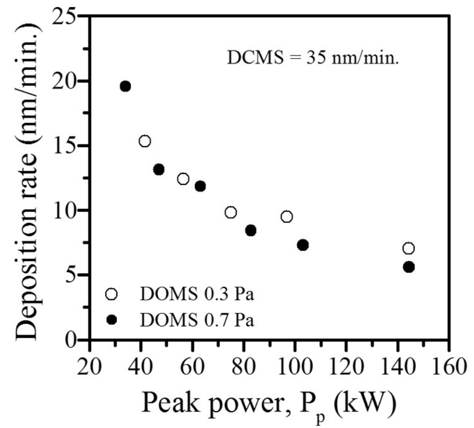

Fig. 3. Deposition rate of the HiPIMS-DOMS and DCMS CrN films as a function of P_p at 0.3 and 0.7 Pa.

3. Results

3.1. Deposition rate and composition

The deposition rate decreases markedly with the increase in the peak power at both pressures used in this work (Fig. 3). In the DOMS process, increasing the peak power increases both the peak current and the peak voltage (see Fig. 2). Alami et al. [20] have shown that increasing the peak current in HiPIMS of CrN thin films enhances the fraction of metal ions in front of the target. As part of the ionized metal ions are back-attracted to the Cr target [31,32], and therefore do not contribute to the deposition rate, a higher ionization fraction of the Cr species contributes to a lower deposition rate ("return effect"). On the other hand, the higher peak voltage at higher peak power translates into a less efficient sputtering process, due to the sub-linear energy dependence of the sputtering yield [32,33] ("yield effect"), and also contributes to the deposition rate loss. The similar deposition rates measured at 0.3 and 0.7 Pa for similar average peak powers (Fig. 3) show that the "return effect" and the "yield effect" mostly cancel each other out upon pressure variation.

Depending on the peak power, the deposition rate of the film deposited by DOMS lies at between 44 and 84% of the deposition rate of the CrN film deposited by DCMS (35 nm/min). The loss of the deposition rate in HiPIMS, as compared to DCMS, is well documented in the literature and several possible causes have been identified. Besides the "return effect" and the "yield effect" already mentioned above, other less obvious effects are also known to contribute to the deposition rate loss in HiPIMS [32].

The nitrogen content of the CrN thin films, as measured by EDS, is shown in Fig. 4. As expected, the CrN film deposited by DCMS has a chemical composition close to stoichiometric CrN. Taking into account the large systematic experimental error associated with light element evaluation by EDS, the nitrogen content of the films deposited by DOMS is also consistent with the deposition of stoichiometric CrN, regardless of the deposition conditions. However, the nitrogen content in the films deposited by DOMS is consistently higher than in the films deposited by DCMS, as can be concluded from the small standard deviation of the N content measured in the films deposited by DOMS (±0.89 at.%). Increasing the bias, i.e. increasing the energy of the bombarding ions, has been reported to induce a loss of nitrogen in CrN films deposited by both DCMS and ARC, due to the preferential re-sputtering of the lighter element [5,6]. The amount of nitrogen in the CrN films deposited by DOMS is very similar, indicating that preferential re-sputtering did not occur upon an increase in the peak power.

3.2. Microstructure and morphology (SEM)

As expected, the CrN thin film deposited by DCMS using a relatively low deposition pressure (0.3 Pa) and bias (−80 V) has a compact microstructure (Fig. 5). Although the film cross section reveals a columnar morphology, the columns are closely-packed with compact boundaries. The film surface consists of elongated features of different sizes resulting from the stacking of several columns. This type of morphology corresponds to the T zone in the Thornton structure diagram [34] and Type G in the work of Gerbig et al. [35].

The morphology evolution of the films deposited by DOMS at low pressure (0.3 Pa) as a function of P_p is shown in Fig. 6. The film deposited with P_p = 42 kW has a columnar morphology (Fig. 6a and b) similar to

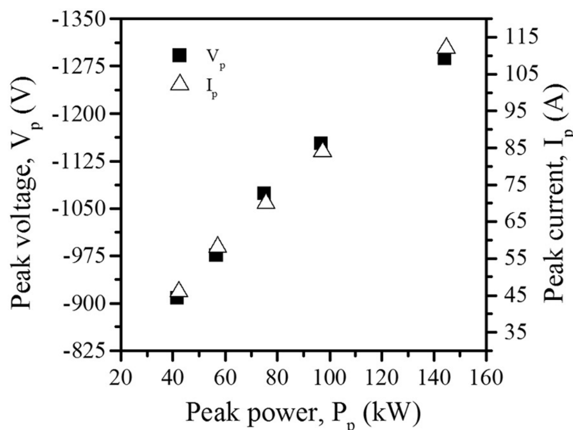

Fig. 2. Peak voltage (V_p) and peak current (I_p) as a function of peak power (P_p) for the CrN coatings deposited at 0.3 Pa by DOMS.

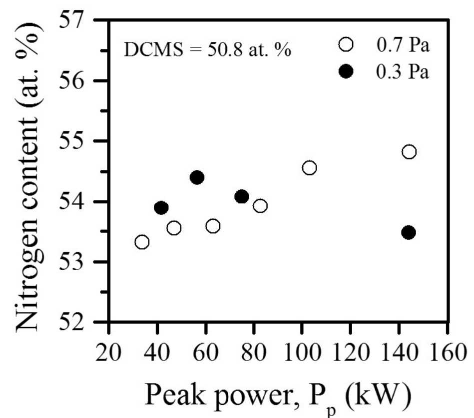

Fig. 4. Nitrogen atomic content in the films deposited by HiPIMS-DOMS at 0.3 and 0.7 Pa (the N content of the film deposited by DCMS was plotted at P_p = 0 kW to facilitate comparison).

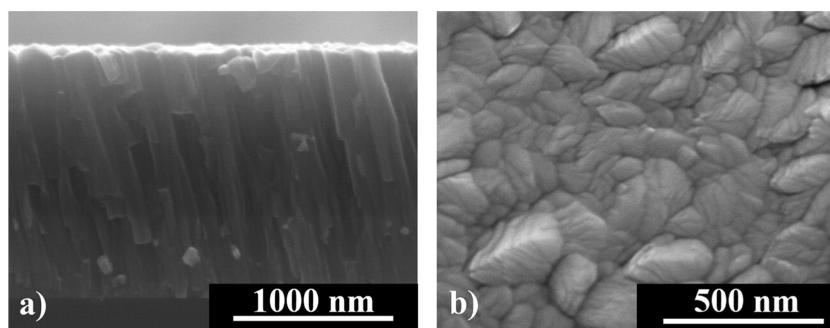

Fig. 5. SEM a) cross-section and b) surface micrograph of the CrN film deposited by DCMS.

that deposited by DCMS. Although the surface of the film also consists of elongated features resulting from aggregation of individual columns, the column tops are much more equiaxed and stacking is no longer observed. Increasing the peak power to 57 kW (Fig. 6c and d) completes the transformation to a columnar cauliflower-type morphology with protruding structures which consist of grains, 15–25 nm wide, that agglomerate to form larger surface structures, 70–150 nm wide. These types of structures are associated with unstable growth under surface diffusion limited conditions. Similar microstructures are also observed for the film deposited at 75 and 97 kW (Fig. 6f to h), although in the latter case both the cauliflower-like surface features and the columnar growth are much less evident. The cross section of the film deposited at the highest peak power (P_p = 144 kW) shows a featureless or columnar-free microstructure (Fig. 6i and j). The cauliflower-like surface morphology is no longer observed. Instead, the film surface displays strongly packed individual equiaxed features with smaller dimensions than those observed on the surface of the films deposited at lower P_p values.

The microstructure of the films deposited at 0.7 Pa also evolves from a columnar growth with cauliflower-type surface features to a featureless growth with a more granular surface morphology as the peak power increases (Fig. 7). However, the microstructural transition occurs at a lower peak power at high pressure (83 kW) than at low pressure (97 kW). However, the transition occurs at similar peak currents (just above 80 A) at both pressures (see Table 1).

Alami et al. [20] also reported a transition from a dense columnar microstructure to a nanocrystalline one as the peak target current was increased for CrN thin films deposited by HiPIMS at 0.8 Pa. The CrN films were deposited at a constant average target current (0.9 A) and the peak target current was increased from 6 to 180 A by decreasing the duty cycle from 25 to 2.5%. As pointed out by the authors, decreasing the duty cycle resulted in an increase in the average power with increasing peak current while low-energy ion-irradiation conditions were always observed. Therefore, the authors attributed the microstructural transformation to an increase in the total ion flux towards the target as well as to the increasing fraction of Cr^+ ions in the total flux. In this study the average power was kept constant for all depositions and therefore the microstructural transformation should be due to the increasing ionization fraction of Cr rather than to an increase in the total ion flux impinging on the growing film.

3.3. Structure (XRD)

The diffraction patterns of the films deposited in this work are shown in Figs. 8 and 9. Although most of the diffraction peaks of the films are close to those of both CrN and Cr_2N, as reported in the respective ICCD cards, the peak located nearest to $2\theta = 62°$ cannot be indexed to any of the diffraction peaks of the Cr_2N phase, as the closest Cr_2N diffraction peaks with significant intensity are the (300) peak at $2\theta = 67.35°$ and the (112) peak at $2\theta = 66.01°$ (ICCD card 00-035-0803). This peak can only be indexed to the (220) peak of the CrN phase (ICCD card 01-076-2494) with a shift to lower 2θ angles due to the presence of compressive stresses. On the other hand, all the diffraction peaks of the films are shifted towards lower 2θ values by similar amounts as compared to the CrN peaks' positions in the ICCD card. This is consistent with the deposition of CrN films with high homogeneous compressive stresses, as already concluded above. Note also that the diffraction peaks of the films are shifted in different directions and by different amounts as compared to the Cr_2N peaks' positions in the ICCD card, which rules out the deposition of this phase. In this work the Ar/N_2 gas flow ratio was chosen in order to deposit CrN thin films in both DCMS and DOMS depositions. As expected, besides the substrate and Cr interlayer diffraction features, all the diffraction peaks in Figs. 8 and 9 could be assigned to the NaCl type CrN phase.

The XRD pattern of the film deposited by DCMS at 0.3 Pa with a bias of −80 V is shown in Fig. 8. The film has a clear [220] preferential orientation, while the position of the XRD peaks is shifted to lower diffraction angles as compared to the corresponding ICCD pattern. These results were expected and are due to an intense bombardment of the growing film, which induces compressive stresses. The XRD patterns of the DOMS films deposited at 0.3 Pa are shown in Fig. 8. All the CrN diffraction peaks are broad and shifted to lower diffraction angles, as compared to the CrN ICCD card, showing that all the films have a low degree of crystallinity and that compressive stresses were formed. Similar conclusions can be drawn for the films deposited by DOMS at higher pressure (Fig. 9), except for the film deposited at the lowest peak power, which has somewhat narrower and more intense diffraction peaks, although also shifted to a lower diffraction angle.

According to the reference pattern of CrN (ICDD card n° 01-076-2494), the lattice parameter of unstrained CrN is 0.414 nm. It is well known that the lattice parameter of thin films deposited by magnetron sputtering can be influenced by both the thermal stresses that develop upon cooling of the films and the intrinsic stresses. Additionally, in the case of nitride films, the lattice parameter also depends on the films' compositions, i.e., on the deviation of the chemical composition from stoichiometry. In this study all the CrN films were deposited over Silicon substrates. As the thermal expansion coefficients for Si [36] and CrN [37] are very similar and as the deposition temperature is estimated to be around 150 °C, the influence of thermal stresses on the lattice parameter can be discarded. On the other hand, as shown above, the chemical composition of all the films is close to stoichiometry, enabling us to discard any influence on film stresses. It is then expected that the lattice parameter measured for the CrN films is mostly influenced by the intrinsic stresses that develop during film deposition.

The lattice parameter of the films deposited by DOMS at 0.7 and 0.3 Pa is shown in Fig. 10 as a function of the peak power. For comparison the lattice parameter of the film deposited by DCMS is also shown. The most striking feature in this figure is that the lattice parameter of all the films deposited by DOMS is clearly higher than the one referred to in the ICCD card and even higher than the lattice parameter of the film deposited by DCMS at low pressure (0.418 nm). As demonstrated by the authors [29], the lattice parameter of Cr thin films deposited by

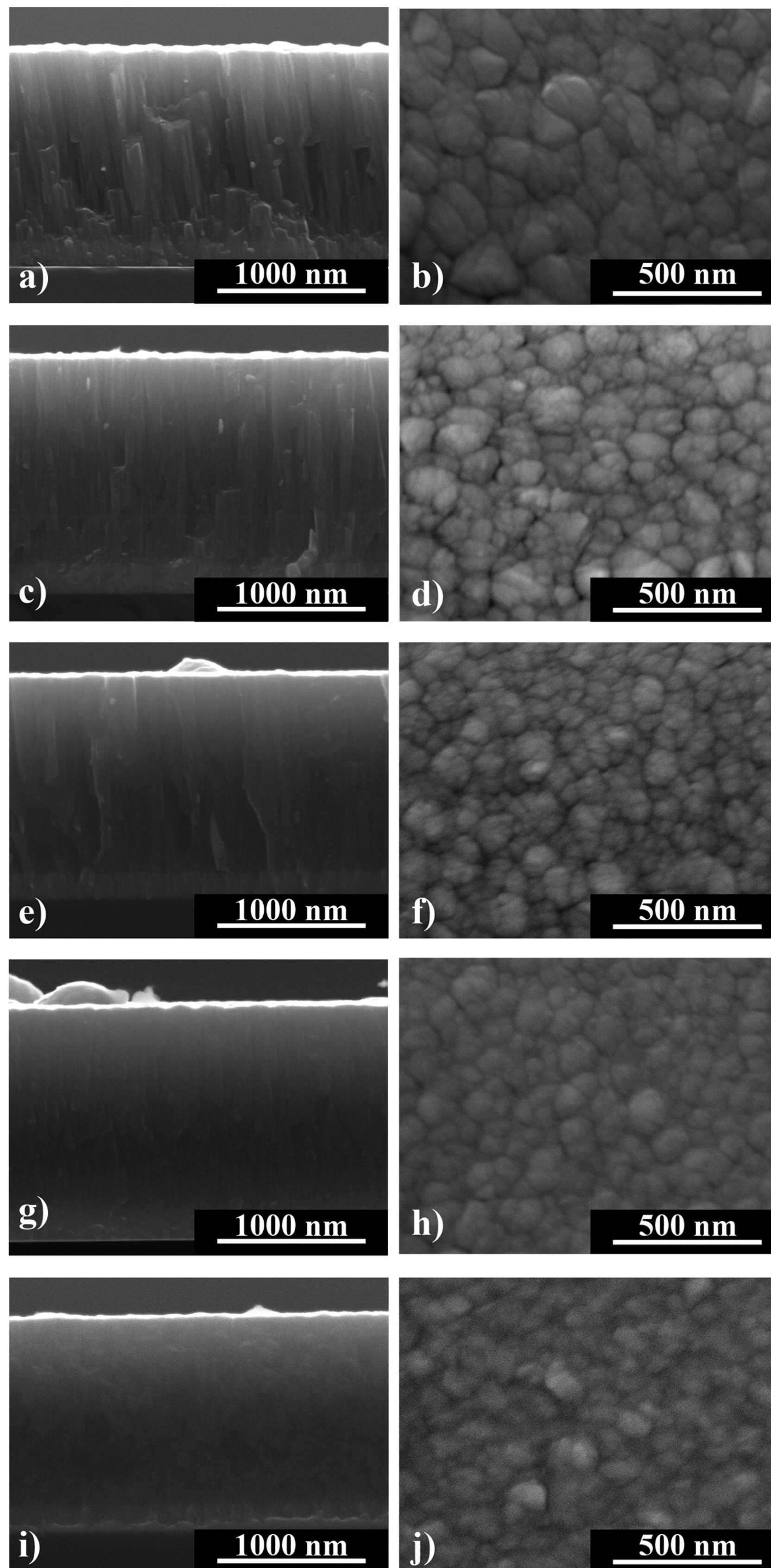

Fig. 6. SEM cross-section and surface micrographs of the films deposited by HiPIMS DOMS at 0.3 Pa with a P_p of a, b) 42 kW; c, d) 57 kW; e, f) 75 kW; g, h) 97 kW; i, j) 144 kW.

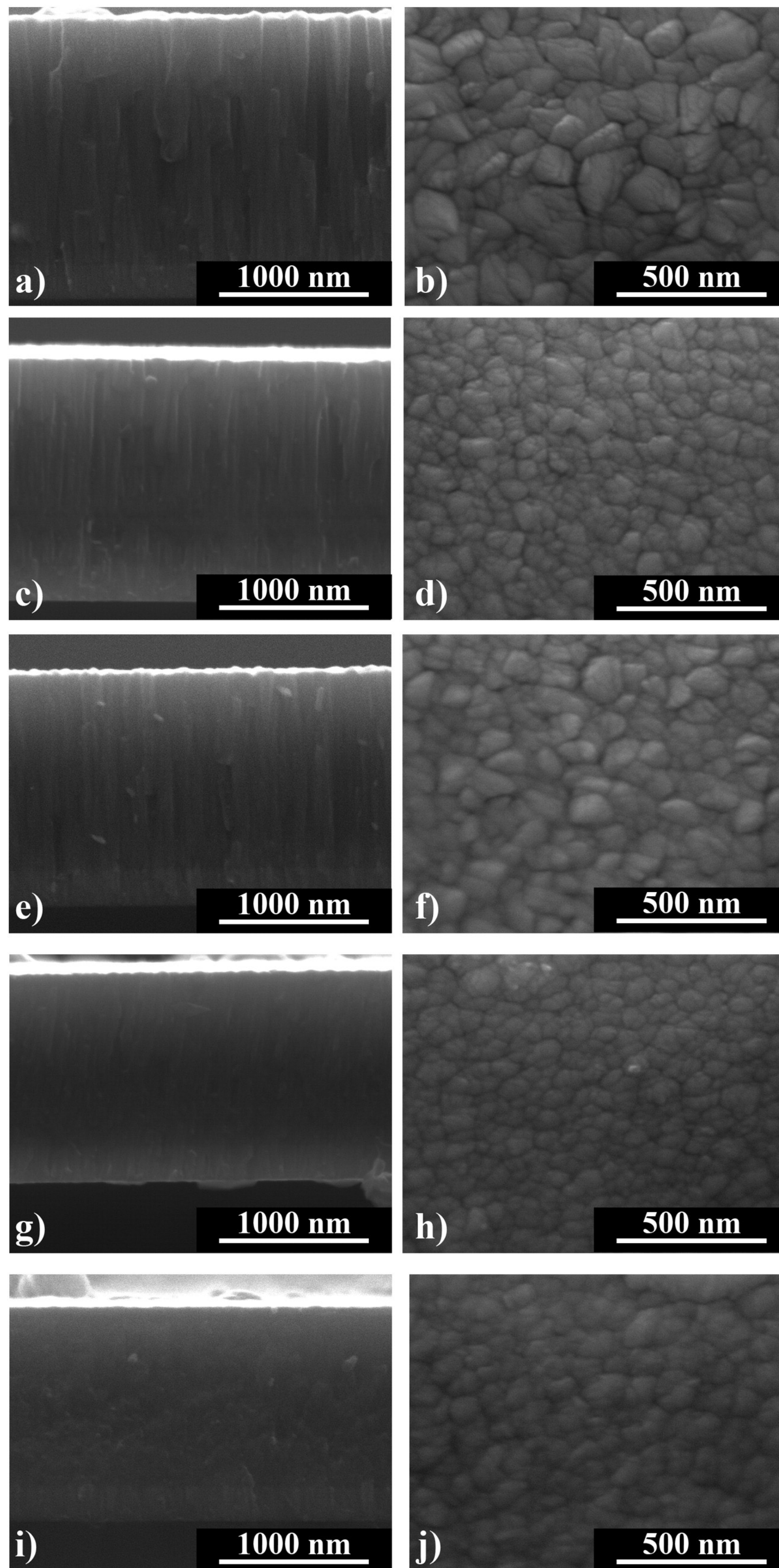

Fig. 7. SEM cross-section and surface micrographs of the films deposited by HiPIMS-DOMS at 0.7 Pa with a P_p of a, b) 34 kW; c, d) 47 kW; e, f) 63 kW; g, h) 83 kW; i, j) 103 kW; l, m) 144 kW.

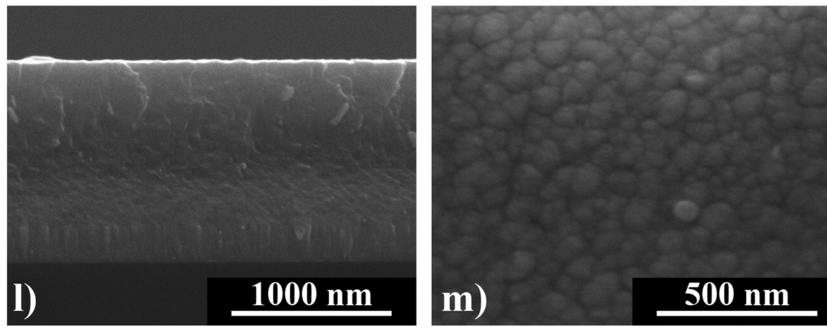

Fig. 7 (*continued*).

DOMS using deposition conditions similar to those used in this study steadily increased with increasing peak power, starting at values close to the unstrained material (0.2884 nm) at the lowest peak power. The lattice parameter of the CrN films deposited by DOMS in this work is already very high at low peak power, revealing that high compressive stresses are formed even at the lowest P_p. The lattice parameter remains fairly constant as the peak power is increased and only displays a weak tendency to increase at high peak power. The weak influence of the deposition conditions on the lattice parameter is somehow surprising, taking into account that both the deposition rate and the microstructure of the film are strongly influenced by the peak power, as shown previously.

CrN films deposited by HiPIMS usually have a high apparent lattice parameter. Ehiasarian et al. [18] reported lattice parameter values of between 0.419 and 0.421 nm for CrN films deposited using a high Ar/N_2 ratio in the discharge. The XRD CrN peaks of the film deposited at $Ar/N_2 = 0.5$ and without bias by Greczynski et al. [21] are also shifted to lower diffraction angles than the ICCD card. Although the authors did not calculate the lattice parameter, a rough estimation from the published XRD patterns resulted in a value close to 0.422 nm. Alami et al. [20] found that the CrN films deposited by HiPIMS had very broad diffraction peaks also shifted to lower 2θ values. In this case an estimation of the lattice parameter from the CrN diffractograms resulted in a lattice parameter close to 0.419 nm. Finally, an estimation of the lattice parameter of the films deposited by Lin et al. [22] by MPP resulted in values between 0.420 and 0.422 nm. Although high lattice parameters are also reported in the literature for CrN thin films deposited by DCMS [1,5,38], in most cases this is associated with the use of high bias voltages applied to the substrate.

The preferred orientation of the CrN films was evaluated from the XRD patterns obtained with symmetrical configuration (θ–2θ). The relative intensity of the XRD CrN peaks was divided by the relative intensity of the corresponding peaks in the ICCD card in such a way that a random orientation would result in a value of 1 for all peaks in Fig. 11, while any preferred orientation would result in a value higher than 1 for the corresponding peak.

The results obtained for the films deposited at 0.3 Pa are shown in Fig. 11a as a function of peak power. The CrN film deposited by DCMS has a clear [220] preferred orientation, as has already been mentioned. Although the film deposited at the lowest peak power by DOMS also has a [220] preferred orientation, the degree of preferential orientation is lower than for the film deposited by DCMS. Increasing the peak power results in a stronger [220] preferred orientation similar to the one obtained for the DCMS film. The film deposited by DOMS at 0.7 Pa using the lowest peak power has an almost random distribution of the crystallites as a value close to 1 was found for all peaks (Fig. 11b), i.e., the relative intensity of the diffraction peaks is close to the one mentioned in the ICCD card. Increasing the peak power results in a strong [220] preferred orientation which is maintained up to the highest peak power.

3.4. Mechanical properties (nanoindentation)

The Young's Modulus of the film deposited by DCMS (271 GPa) is slightly lower than the Young's Modulus of the films deposited by DOMS (Fig. 12). This result is most probably due to the presence of some porosity in the film. It is well known that the Young's Modulus of a material decreases with increasing porosity, although this relation depends not only on the amount of porosity but also on its distribution and on the shape of the pores. The Young's modulus of the films deposited by DOMS is always close to 300 GPa irrespective of the peak power and deposition pressure used in this work. This indicates that using

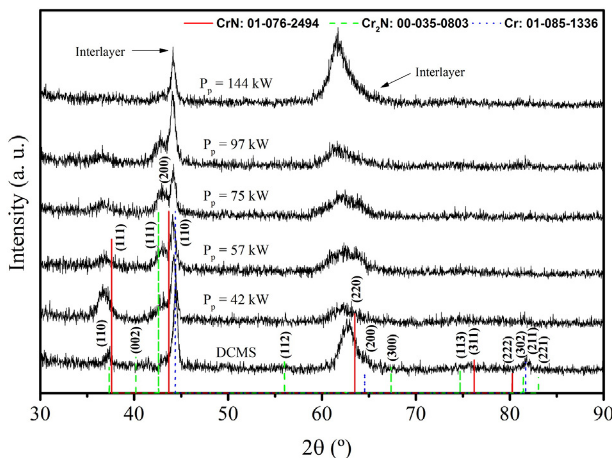

Fig. 8. XRD patterns of the films deposited by HiPIMS-DOMS at 0.3 Pa as a function of P_p. The figure also shows the CrN, Cr_2N and Cr standards.

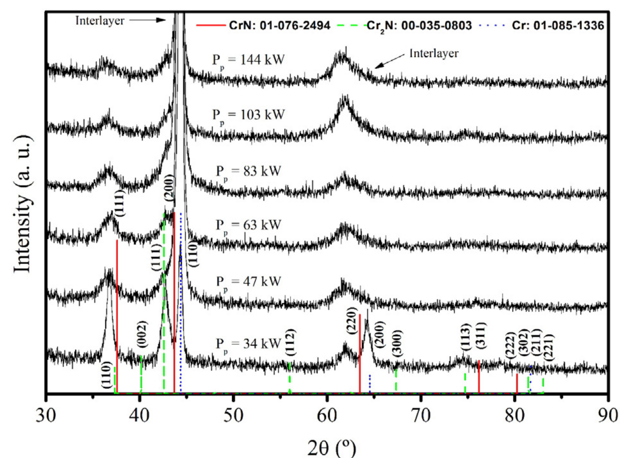

Fig. 9. XRD patterns of the films deposited by HiPIMS-DOMS at 0.7 Pa as a function of P_p. The figure also shows the CrN, Cr2N and Cr standards.

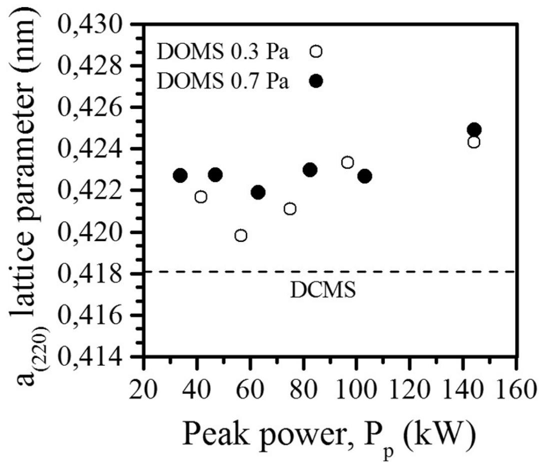

Fig. 10. Lattice parameter of the films deposited by HiPIMS-DOMS as a function of P_p (the dashed line is the film deposited by DCMS).

DOMS results in completely densified films in all deposition conditions. These results agree well with Ehiasarian et al. [18], who showed by TEM analysis that the CrN films deposited by DCMS still had some porosity and that fully densified films were obtained by HiPIMS, notwithstanding the deposition conditions.

The CrN film deposited by DCMS has a hardness close to 17 GPa (Fig. 13). Although the microstructure is columnar, the intense bombardment resulted in a dense film with tightly packed columns which are quite able to sustain plastic deformation. All the films deposited by DOMS show a hardness above 21 GPa, i.e. much higher than the film deposited by DCMS under intense bombardment conditions. The hardness of the films increases with increasing peak power at both 0.3 and 0.7 Pa. Furthermore, the range of variation of the hardness is similar for both pressures (from close to 20–21 GPa to nearly 28–29 GPa). However, at intermediate values of P_p (between 80 and 110 kW), the hardness of the films deposited at 0.7 Pa is higher than that of the films deposited at 0.3 Pa. These results show that their hardness is closely related to their microstructure. The hardness increases as denser films are deposited at both pressures, but it is higher at intermediate values of P_p at 0.7 Pa because the microstructural transformation from columnar to featureless occurs at lower values of P_p.

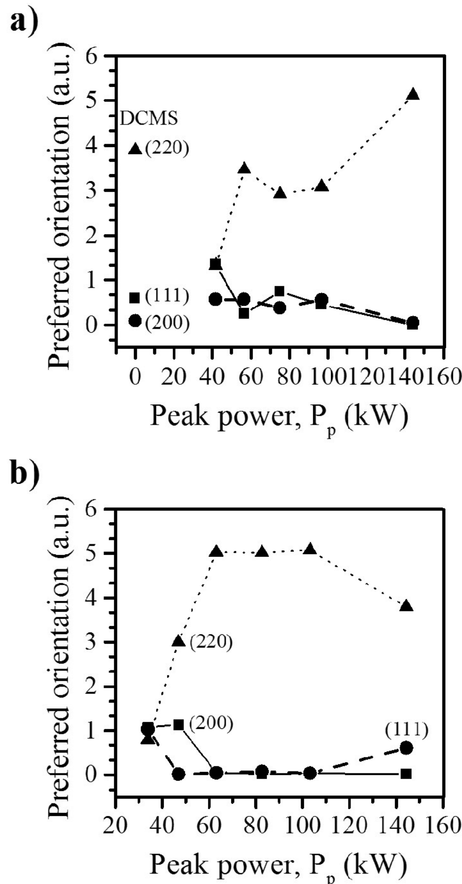

Fig. 11. Evolution of the preferred orientation of the DOMS coatings as a function of peak power at a) 0.3 Pa and b) 0.7 Pa (the value of the film deposited by DCMS at 0.3 Pa was plotted at P_p = 0 kW to facilitate comparison, the lines are guides to the eye).

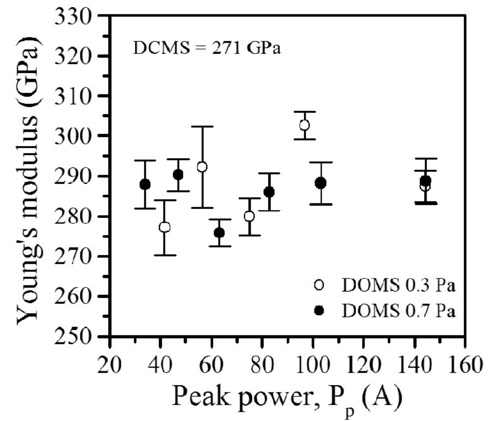

Fig. 12. Young's modulus of the films deposited by HiPIMS-DOMS as a function of P_p (Pa = 1.2 kW; P = 0.3 Pa; Di = 1000 μs; ton/T = 6/40 μs).

4. Discussion

The preferential orientation of transition nitride thin films deposited by PVD is a complex phenomenon involving an interplay between kinetics and thermodynamics which depends on the energy and flux of the species impinging on the substrate [39,40]. The [002] preferred orientation can be obtained under both kinetic and thermodynamic conditions. In the former case the films are free from compressive stress and therefore their lattice parameter is close to the ICCD card value. In the latter case compressive stresses and higher lattice parameters are usually found due to a gradual increase in subplantation of the impinging species with increasing energy. Although the preferred orientation model referred above was derived for TiN, it has also been used to successfully explain the preferred orientation of CrN thin films [41]. For both TiN and CrN the [220] preferred orientation is usually attributed

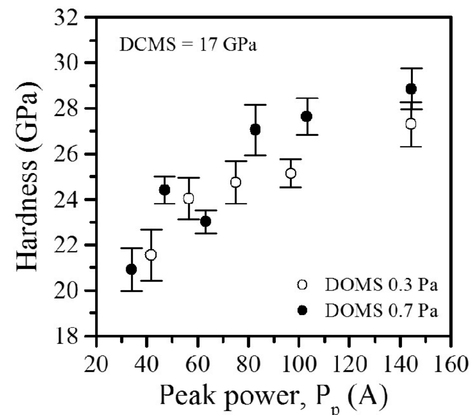

Fig. 13. Hardness of the films deposited by HiPIMS-DOMS as a function of P_p (Pa = 1.2 kW; P = 0.7 Pa; Di = 1000 μs; ton/T = 6/40 μs).

to the lower density of the (220) as compared to the (200) planes in the NaCl type structure [42]. Although both planes possess low surface energy, that of the (002) plane is the lowest, which favours the corresponding preferred orientation under thermodynamic considerations. However, under intense bombardment conditions the more open structure of the (220) planes is less prone to destruction, as it enables more "ion channelling" than the (002) planes. Under such conditions the [220] orientation has the fastest growth speed and the corresponding orientation develops.

According to the above discussion, the strong [220] preferred orientation of the film deposited by DCMS in this study indicates that it was subjected to an intense bombardment during growth. Regarding the CrN films deposited by DOMS, the same argument can be used with exception of the films deposited at the lowest peak powers, which do not have a strong [220] preferred orientation. Note that even in the case of the films deposited at low peak power, the random orientation and weaker [220] preferred orientation found at 0.3 and 0.7 Pa respectively also support the argument for intense bombardment, as otherwise [111] and/or [002] preferred orientations would have developed.

The CrN film deposited by DOMS at 0.7 Pa using the lowest peak power (34 kW) has a high lattice parameter (0.423 nm) and a [220] preferred orientation. These properties are typical of films grown under energetic bombardment, which brings about subplantation of the impinging species and consequent defect creation and formation of high compressive stresses. Accordingly, this film has a high hardness (21 GPa), as compared to the CrN film deposited by DCMS (17 GPa). Although the CrN film deposited using the lowest P_p (42 kW) and 0.3 Pa has a random preferred orientation, it also exhibits a high lattice parameter (0.422 nm) and a high hardness (22 GPa), suggesting that this film was also subjected to an energetic bombardment during growth. Similar conclusions can also be drawn for the remaining CrN films. Above the lowest P_p, the lattice parameter remains close to 0.422 nm, while the preferred orientation remains [220]. In fact, all the CrN films deposited by DOMS were subjected to an energetic bombardment during growth, regardless of the deposition conditions used in this work.

In a previous study [29] the authors have shown that the lattice parameter of Cr thin films deposited by DOMS at low peak power (39 kW) was close to the corresponding ICCD card value (0.288 nm). In other words, at low peak power the Cr film were only subjected to a weak bombardment unable to induce subplantation of the impinging species and consequent high compressive stress formation. The Cr films were deposited using deposition conditions similar to the ones used in this work, except of course for the addition of nitrogen to the Ar discharge in order to deposit the nitride thin films. These results enable us to conclude that, at least at low peak power, the energetic bombardment of the CrN films deposited in this research is caused by the presence of N_2 in the discharge gas.

The main sources for substrate bombardment during CrN deposition by reactive magnetron sputtering are the sputtered (Cr and N) and backscattered species (Ar and N). Sarakinos et al. [43] have shown that the high compressive stresses in CrN films deposited by DCMS could not be explained either by bombardment of the sputtered species or by formation of thermal stresses upon cooling of the films after the deposition stage. The authors used experimental techniques and simulations in order to study the role of backscattered species. They concluded that the energy of backscattered atomic nitrogen impinging on the substrate, resulting from neutralization and dissociation of the N_2^+ ions impinging on the target, was significantly higher than the energy of backscattered Ar atoms. Furthermore, the backscattering ratio of Ar impinging on a Cr target was very low (3%) due to the similar masses of the two elements. The out-of-plane lattice strain and compressive stresses were then attributed to the subplantation of the backscattered N species and consequent defect formation, as confirmed by simulation. The presence of energetic nitrogen neutrals in an HiPIMS discharge has been reported by Greczynski et al. [44]. The authors used mass spectroscopy to analyse the energy and composition of the ion flux in an HiPIMS discharge of a Cr target in both metallic and reactive mode with nitrogen. They found that the Ion Energy Distribution Function (IEDF) of singly charged Cr ions was similar to the one obtained in metallic mode, regardless of the N_2/Ar ratio in the discharge gas. On the contrary, the IEDF of the N^+ ions revealed not only the expected flux increase but also an increasing high energy tail, which was not present in the IEDF spectra of Ar^+ and N_2^+ ions. The authors concluded that an energetic stream of monoatomic nitrogen ions was created through the electron-impact ionization of the nitrogen atoms, either resulting from sputtering of the nitride portion of the target or from dissociation of back-attracted N_2^+ ions at the target surface.

The peak voltage during CrN films deposition by DOMS (above −773 V) is higher than the deposition voltage reported by Sarakinos et al. (−504 V) [43]. The energy of the N neutrals impinging on the growing film is proportional to the acceleration of N_2^+ ions from the plasma upon falling into the cathode potential. It is thus to be expected that bombardment with energetic nitrogen neutrals has an even stronger impact on the properties of CrN films deposited by DOMS. In this study it is argued that the CrN thin films deposited by DOMS are subjected to a strong bombardment by energetic nitrogen atoms, regardless of the deposition conditions used. The small tendency for the lattice parameter to increase at higher peak power can then be attributed to the higher deposition voltage and consequent higher energy of the nitrogen neutrals bombarding the substrate. Note however that the energetic flux of N species impinging on the growing film is unable to prevent the columnar growth at low peak power, showing that bombarding the growing films with energetic N species is ineffective at overcoming the shadowing effect.

Increasing the peak power has a significant effect on both the microstructure and the hardness of the CrN films deposited by DOMS. At both deposition pressures used in this research, increasing the peak power results in denser column-free rather than columnar films, while the hardness increases from 21–22 GPa to 28–29 GPa. As explained above, the bombardment by energetic backscattered nitrogen neutrals can be viewed as a "background" bombardment, almost independent of the deposition conditions, and thus cannot explain the observed microstructural transformation. One possible cause for this transformation could be the increase of the mean energy of the species impinging on the growing film. Increasing the deposition voltage increases the energy gain by the plasma ions upon acceleration in the cathode fall. However, most of the additional energy contributes to an increase of the sputtering yield rather than to an increase of the mean energy of the sputtered species. Therefore, although the peak voltage increases with peak power in DOMS, only a modest increase of the energy of the sputtered species is to be expected with increasing peak power. On the other hand, the energy gain upon acceleration in the vicinity of the substrate by both the ionized sputtered species and the Ar ions extracted from the plasma is small, as the self-bias is in the order of a few eVs only. On the overall, the energy of the species arriving at the substrate is not significantly increased by increasing the peak power, as also found by Alami et al. [20] for CrN films deposited by HIPIMS. We can then conclude that the microstructural transformation with increasing peak power observed in the CrN films deposited in this work is not likely to be due to an energy increase of the species impinging on the films during growth.

Another possible explanation for the microstructural change could be an increase of the flux of species impinging on the growing film with increasing peak power. Alami et al. [20] attributed the microstructural transition from columnar to columnar-free CrN films to an increase in the flux of the bombarding species. However, in that study the time averaged power was increased simultaneously with the peak current. In our work the time averaged power was kept constant in all depositions. Therefore, the average flux of particles impinging on the substrate cannot increase significantly with increasing peak power, since, as deduced above, the energy of the bombarding species is not significantly changed. In fact, the total flux of particles impinging on the substrate

decreases with increasing peak power, as shown by the decreasing deposition rate. We can then conclude that the CrN films' microstructural transformation with increasing peak power cannot be attributed to an increasing flux of the particles impinging on the substrate.

It is well known that the development of columnar structures is primarily due to the shadowing effect. Although the columnar growth can be overcome by increasing the energy and/or the flux of the bombarding species, it can also be avoided by decreasing or preventing the shadowing effect. Increasing the peak power increases the ionization fraction of the Cr species, which in turn increases their mean angle of incidence on the substrate, i.e., decreases the shadowing effect. Greczynski [45] et al. have shown that this can have a striking influence on the microstructure of Cr films by HiPIMS as the trajectory of the ions impinging on the substrate can be influenced significantly. In this study, the transition from columnar to columnar-free microstructures occurs at lower peak power for the CrN films deposited by DOMS at 0.7 Pa than for those deposited at 0.3 Pa. In fact at both deposition pressures the transition from the columnar to the columnar-free growth occurs at similar values of I_p (just above 80 A), although the peak voltage is higher by more than −200 V at low pressure (see Table 1). This result shows that the microstructure transformation is most probably triggered by an increase in the ionization fraction of the sputtered species and consequent weakening of the shadowing effect as the mean incidence angle of the species impinging on the growing film is shifted to values closer to the normal of the film.

As shown above, the bombardment of the growing films by energetic nitrogen neutrals enables us to provide a good explanation of the results obtained in this work for CrN deposition by DOMS. In fact it also explains why the lattice parameter of all the CrN films deposited by HiPIMS is always above 0.420 nm [18,20–22], i.e. it accounts for the presence of high compressive stresses in all the films deposited by HiPIMS. The main reason for this is the high voltage characteristic in HiPIMS depositions, as compared to DCMS depositions, which directly increases the energy of the backscattered nitrogen atoms impinging on the growing film. However, as demonstrated by Sarakinos et al. [43], the bombardment by energetic N neutrals also occurs in DCMS. For example, the lattice parameter of the CrN films deposited by He et al. [46] was always close to 0.422 nm and the films had a [220] preferred orientation regardless of the bias voltage used. These results may also be explained by the bombardment of energetic nitrogen neutrals, which override the effect of biasing. On the contrary, Kong et al. [7] found that the lattice parameter of CrN films deposited by DCMS increased from values below the ICCD standard (tensile stresses) only up to 0.415, i.e. close to the unstrained value. Furthermore, the preferred orientation was changed from [111] to [002] and not to [220]. In this case there is no evidence of the nitrogen neutrals bombardment. These results show that depending on the deposition conditions (and deposition systems) the energetic bombardment of nitrogen neutrals may or may not be present in CrN films deposition by DCMS.

One possible solution for overcoming the effect of the energetic nitrogen neutrals is to increase the deposition pressure. If the latter is high enough, most of the species travelling in the deposition chamber will be thermalized, including the energetic nitrogen neutrals. At the same time, more ionization of both Cr and N neutrals will occur, due to the higher I_p values, and the deposition voltage will be lower. It could then be possible to extract these ions from the plasma and control their energy by biasing the substrates. This solution could not be tested in the deposition system used in this study due to severe arcing above 0.8 Pa, mainly due to the occurrence of corona discharges at the back of the cathode.

5. Conclusions

The main objective of the present work was to understand the effect of the energetic ion bombardment of the growing films on the properties of CrN thin films deposited by DOMS. For this purpose two series of CrN films were deposited at different pressures and with increasing peak power, i.e., with increasing ionization of the bombarding species. The high lattice parameter and [220] preferred orientation of all the CrN films deposited by DOMS showed that an intense energetic bombardment occurred in all depositions irrespective of the deposition conditions (peak power and pressure). It is proposed that this “background” energetic bombardment is originated by the nitrogen neutral atoms which are backscattered at the target surface upon impingement of N_2^+ ions, as suggested in the literature for CrN films deposited by DCMS.

Although the structural properties of the films were mostly insensitive to the deposition conditions used in this work, the hardness and microstructure were influenced significantly. Increasing the peak power gradually changed the growth mode of the CrN films from columnar to nanocrystalline, enabling deposition of fully dense films at high peak power. On the other hand the hardness of the films increased from 21–22 GPa to 28–29 GPa when the peak power was increased. The transition from columnar to columnar-free mode of growth was triggered at lower peak power for the CrN films deposited at higher pressure (0.7 Pa) than those deposited at low pressure (0.3 Pa). It was concluded that the columnar growth was interrupted by preventing the shadowing effect, as a result of the higher ionization fraction of the sputtered species, rather than by overcoming the shadowing effect through more energetic bombardment.

Finally, it was pointed out that the energetic bombardment with nitrogen neutrals is more prone to occur in depositions by DOMS due to the characteristic high voltage used, as compared to DCMS. This conclusion can explain the high stresses always found in CrN films deposited by DOMS. It was also suggested that the apparently contradictory results regarding the effect of bias voltage on CrN thin films deposited by DCMS found in the literature could be due to the presence or absence of the energetic bombardment with nitrogen neutrals, depending on the deposition conditions and/or deposition systems used.

Acknowledgements

This research is sponsored by FEDER funds through the programme COMPETE – Programa Operacional Factores de Competitividade – and by national funds through FCT – Fundação para a Ciência e a Tecnologia –, under the projects: PTDC/EME-TME/122116/2010, PTDC/EMS-TEC/1805/2012 and PEst-C/EME/UI0285/2013, as well as the grant (SFRH/BD/68740/2010).

References

[1] Z. Zhao, Z. Rek, S. Yalisove, J. Bilello, Nanostructured chromium nitride films with a valley of residual stress, Thin Solid Films 472 (2005) 96–104.
[2] J. Xu, H. Umehara, I. Kojima, Effect of deposition parameters on composition, structures, density and topography of CrN films deposited by rf magnetron sputtering, Appl. Surf. Sci. 201 (2002) 208–218.
[3] C. Gautier, H. Moussaoui, F. Elstner, J. Machet, Comparative study of mechanical and structural properties of CrN films deposited by dc magnetron sputtering and vacuum arc evaporation, Surf. Coat. Technol. 86 (1996) 254–262.
[4] L. Chiu, C. Yang, W. Hsieh, A. Cheng, Effect of contact pressure on wear resistance of AISI H13 tool steels with chromium nitride and hard chromium coatings, Surf. Coat. Technol. 154 (2002) 282–288.
[5] T. Hurkmans, D. Lewis, H. Paritong, J. Brooks, W. Münz, Influence of ion bombardment on structure and properties of unbalanced magnetron grown CrN x coatings, Surf. Coat. Technol. 114 (1999) 52–59.
[6] C. Gautier, J. Machet, Study of the growth mechanisms of chromium nitride films deposited by vacuum ARC evaporation, Thin Solid Films 295 (1997) 43–52.
[7] Q. Kong, L. Ji, H. Li, X. Liu, Y. Wang, J. Chen, H. Zhou, Influence of substrate bias voltage on the microstructure and residual stress of CrN films deposited by medium frequency magnetron sputtering, Mater. Sci. Eng. B 176 (2011) 850–854.
[8] J.-W. Lee, S.-K. Tien, Y.-C. Kuo, The effects of pulse frequency and substrate bias to the mechanical properties of CrN coatings deposited by pulsed DC magnetron sputtering, Thin Solid Films 494 (2006) 161–167.
[9] S. Grasser, R. Daniel, C. Mitterer, Microstructure modifications of CrN coatings by pulsed bias sputtering, Surf. Coat. Technol. 206 (2012) 4666–4671.
[10] C. Zou, H. Wang, M. Li, C. Liu, L. Guo, D. Fu, Characterization and properties of CrN films deposited by ion-source-enhanced middle frequency magnetron sputtering, Vacuum 83 (2009) 1086–1090.

[11] V. Kouznetsov, K. Macák, J.M. Schneider, U. Helmersson, I. Petrov, A novel pulsed magnetron sputter technique utilizing very high target power densities, Surf. Coat. Technol. 122 (1999) 290–293.
[12] U. Helmersson, M. Lattemann, J. Bohlmark, A.P. Ehiasarian, J.T. Gudmundsson, Ionized physical vapor deposition (IPVD): a review of technology and applications, Thin Solid Films 513 (2006) 1–24.
[13] D. Lundin, K. Sarakinos, An introduction to thin film processing using high-power impulse magnetron sputtering, J. Mater. Res. 27 (2012) 780–792.
[14] A. Ehiasarian, R. New, W.-D. Münz, L. Hultman, U. Helmersson, V. Kouznetsov, Influence of high power densities on the composition of pulsed magnetron plasmas, Vacuum 65 (2002) 147–154.
[15] J. Lin, W.D. Sproul, J.J. Moore, Z. Wu, S. Lee, R. Chistyakov, B. Abraham, Recent advances in modulated pulsed power magnetron sputtering for surface engineering, JOM 63 (2011) 48–58.
[16] J. Lin, J.J. Moore, W.D. Sproul, B. Mishra, Z. Wu, Modulated pulse power sputtered chromium coatings, Thin Solid Films 518 (2009) 1566–1570.
[17] J. Lin, J. Moore, W. Sproul, B. Mishra, J. Rees, Z. Wu, R. Chistyakov, B. Abraham, Ion energy and mass distributions of the plasma during modulated pulse power magnetron sputtering, Surf. Coat. Technol. 203 (2009) 3676–3685.
[18] A. Ehiasarian, W.-D. Münz, L. Hultman, U. Helmersson, I. Petrov, High power pulsed magnetron sputtered CrN x films, Surf. Coat. Technol. 163 (2003) 267–272.
[19] J. Paulitsch, M. Schenkel, T. Zufraß, P. Mayrhofer, W.-D. Münz, Structure and properties of high power impulse magnetron sputtering and DC magnetron sputtering CrN and TiN films deposited in an industrial scale unit, Thin Solid Films 518 (2010) 5558–5564.
[20] J. Alami, K. Sarakinos, F. Uslu, M. Wuttig, On the relationship between the peak target current and the morphology of chromium nitride thin films deposited by reactive high power pulsed magnetron sputtering, J. Phys. D. Appl. Phys. 42 (2009) 015304.
[21] G. Greczynski, J. Jensen, J. Böhlmark, L. Hultman, Microstructure control of CrNx films during high power impulse magnetron sputtering, Surf. Coat. Technol. 205 (2010) 118–130.
[22] J. Lin, J.J. Moore, W.D. Sproul, B. Mishra, Z. Wu, J. Wang, The structure and properties of chromium nitride coatings deposited using dc, pulsed dc and modulated pulse power magnetron sputtering, Surf. Coat. Technol. 204 (2010) 2230–2239.
[23] J. Lin, W.D. Sproul, J.J. Moore, S. Lee, S. Myers, High rate deposition of thick CrN and Cr 2 N coatings using modulated pulse power (MPP) magnetron sputtering, Surf. Coat. Technol. 205 (2011) 3226–3234.
[24] J. Lin, W.D. Sproul, J.J. Moore, Microstructure and properties of nanostructured thick CrN coatings, Mater. Lett. 89 (2012) 55–58.
[25] J. Lin, W.D. Sproul, J.J. Moore, Tribological behavior of thick CrN coatings deposited by modulated pulsed power magnetron sputtering, Surf. Coat. Technol. 206 (2012) 2474–2483.
[26] J. Lin, B. Wang, W.D. Sproul, Y. Ou, I. Dahan, Anatase and rutile TiO_2 films deposited by arc-free deep oscillation magnetron sputtering, J. Phys. D. Appl. Phys. 46 (2013) 084008.
[27] J. Lin, W.D. Sproul, Structure and properties of Cr_2O_3 coatings deposited using DCMS, PDCMS, and DOMS, Surf. Coat. Technol. 276 (2015) 70–76.
[28] J. Lin, W.D. Sproul, R. Wei, R. Chistyakov, Diamond like carbon films deposited by HiPIMS using oscillatory voltage pulses, Surf. Coat. Technol. 258 (2014) 1212–1222.
[29] F. Ferreira, R. Serra, J. Oliveira, A. Cavaleiro, Effect of peak target power on the properties of Cr thin films sputtered by HiPIMS in deep oscillation magnetron sputtering (DOMS) mode, Surf. Coat. Technol. 258 (2014) 249–256.
[30] J. Oliveira, F. Fernandes, F. Ferreira, A. Cavaleiro, Tailoring the nanostructure of Ti–Si–N thin films by HiPIMS in deep oscillation magnetron sputtering (DOMS) mode, Surf. Coat. Technol. 264 (2015) 140–149.
[31] D. Christie, Target material pathways model for high power pulsed magnetron sputtering[a)], J. Vac. Sci. Technol. A 23 (2005) 330–335.
[32] A. Anders, Deposition rates of high power impulse magnetron sputtering: physics and economics, J. Vac. Sci. Technol. A 28 (2010) 783–790.
[33] J. Emmerlich, S. Mráz, R. Snyders, K. Jiang, J.M. Schneider, The physical reason for the apparently low deposition rate during high-power pulsed magnetron sputtering, Vacuum 82 (2008) 867–870.
[34] J.A. Thornton, Influence of apparatus geometry and deposition conditions on the structure and topography of thick sputtered coatings, J. Vac. Sci. Technol. 11 (1974) 666–670.
[35] Y. Gerbig, V. Spassov, A. Savan, D.G. Chetwynd, Topographical evolution of sputtered chromium nitride thin films, Thin Solid Films 515 (2007) 2903–2920.
[36] D.R. Lide, CRC handbook of chemistry and physics, CRC Press, 2004.
[37] S. Nagakura, T. Kusunoki, F. Kakimoto, Y. Hirotsu, Lattice parameter of the non-stoichiometric compound TiNx, J. Appl. Crystallogr. 8 (1975) 65–66.
[38] A. Barata, L. Cunha, C. Moura, Characterisation of chromium nitride films produced by PVD techniques, Thin Solid Films 398 (2001) 501–506.
[39] D. Gall, S. Kodambaka, M. Wall, I. Petrov, J. Greene, Pathways of atomistic processes on TiN (001) and (111) surfaces during film growth: an ab initio study, J. Appl. Phys. 93 (2003) 9086–9094.
[40] P. Patsalas, C. Gravalidis, S. Logothetidis, Surface kinetics and subplantation phenomena affecting the texture, morphology, stress, and growth evolution of titanium nitride films, J. Appl. Phys. 96 (2004) 6234–6246.
[41] R. Daniel, K. Martinschitz, J. Keckes, C. Mitterer, Texture development in polycrystalline CrN coatings: the role of growth conditions and a Cr interlayer, J. Phys. D. Appl. Phys. 42 (2009) 075401.
[42] W.-J. Chou, G.-P. Yu, J.-H. Huang, Bias effect of ion-plated zirconium nitride film on Si (100), Thin Solid Films 405 (2002) 162–169.
[43] K. Sarakinos, J. Alami, P. Karimi, D. Severin, M. Wuttig, The role of backscattered energetic atoms in film growth in reactive magnetron sputtering of chromium nitride, J. Phys. D. Appl. Phys. 40 (2007) 778.
[44] G. Greczynski, L. Hultman, Time and energy resolved ion mass spectroscopy studies of the ion flux during high power pulsed magnetron sputtering of Cr in Ar and Ar/N_2 atmospheres, Vacuum 84 (2010) 1159–1170.
[45] G. Greczynski, J. Jensen, L. Hultman, Mitigating the geometrical limitations of conventional sputtering by controlling the ion-to-neutral ratio during high power pulsed magnetron sputtering, Thin Solid Films 519 (2011) 6354–6361.
[46] X.-M. He, N. Baker, B. Kehler, K. Walter, M. Nastasi, Y. Nakamura, Structure, hardness, and tribological properties of reactive magnetron sputtered chromium nitride films, J. Vac. Sci. Technol., A 18 (2000).

ANNEX D

J. Oliveira, F. Fernandes, F. Ferreira, and A. Cavaleiro, "Tailoring the nanostructure of Ti–Si–N thin films by HiPIMS in deep oscillation magnetron sputtering (DOMS) mode," Surface and Coatings Technology, vol. 264, pp. 140-149, 2015.

Surface & Coatings Technology 264 (2015) 140–149

Contents lists available at ScienceDirect

Surface & Coatings Technology

journal homepage: www.elsevier.com/locate/surfcoat

Tailoring the nanostructure of Ti–Si–N thin films by HiPIMS in deep oscillation magnetron sputtering (DOMS) mode

J.C. Oliveira [a], F. Fernandes [a,*], F. Ferreira [a], A. Cavaleiro [a]

[a] SEG-CEMUC — Department of Mechanical Engineering, University of Coimbra, Rua Luis Reis Santos, 3030-788 Coimbra, Portugal

ARTICLE INFO

Article history:
Received 5 November 2014
Accepted in revised form 24 December 2014
Available online 3 January 2015

Keywords:
Nanocomposite TiSiN films
DOMS
Structure
Mechanical properties

ABSTRACT

Nanocomposite TiSiN films consist of nano-sized TiN crystallites surrounded by an amorphous Si–N matrix. Many works have shown that the hardness of nanostructured TiSiN films increases with increasing silicon content up to an optimal concentration. However, energetic ion bombardment of the growing film also influences the hardness and structure of TiSiN films. The main objective of the present work was to tailor the nanostructure of TiSiN films by using the highly ionized fluxes of sputtered material generated in a HiPIMS discharge. For this purpose TiSiN films were deposited by DOMS (deep oscillation magnetron sputtering) mode. The energetic ion bombardment of the growing films was controlled by changing the peak power.

The crystal structure of TiSiN films was analyzed by X-ray diffraction (XRD) with a parallel beam in both θ–2θ and GIXRD geometries. EDS and XPS were used to elucidate the chemical composition of the films and the nature of the chemical bonding, respectively. The microstructure of the films was characterized by SEM while their mechanical properties were measured by nanoindentation.

All the films deposited by DOMS have a nanocomposite microstructure consisting of two phases: f.c.c TiN and a-SiN. Although similar amounts of SiN were detected in the films, both the phase distribution and the properties of the f.c.c phase depend on the peak power. Two deposition regimes were identified. At low peak power (up to 44 kW) the growing film is bombarded with a high flux of low energy ionized sputtered species promoting the surface mobility of the ad-atoms and avoiding the atomic peening effect. At high peak power the energetic species impinging on the substrate are able to penetrate in the sub-surface of the growing film, resulting in an intense atomic peening effect which ultimately leads to secondary nucleation due to the high number of defects.

© 2014 Elsevier B.V. All rights reserved.

1. Introduction

Since Veprek and Reiprich reported the extremely high mechanical properties of the nanocomposite TiSiN system deposit by CVD [1], an extensive body of research works has been focused on the study and deposition of this system. Depending on the deposition conditions, these films have been reported consisting of: i) nano-sized TiN crystallites surrounded by an amorphous matrix of Si_3N_4 [1–6], or ii) substitutional solid solution of Si in TiN structure (not predicted by the Ti–Si–N phase diagram) [7–9]. The hardness of the films has been shown to increase with increasing silicon content up to an optimal concentration. Following the model proposed by Patscheider et al. [2], the maximum hardness corresponds to the formation of the nanocomposite phase with optimized sizes of both the TiN crystallites and the Si_3N_4 amorphous matrix. However, the friction coefficient of TiSiN films increases with increasing silicon content. Several works report friction coefficient values in the range 0.7–1.1 at room temperature [2,10,11]. This high friction coefficient implies that the Ti–Si–N films can hardly be used under conditions that require high surface quality of counterparts or products.

In the last decade, a new concept of lubrication based on the formation of lubricious oxides has been proposed. This is the case of the so-called Magnéli oxide phases based on Ti, Si, Mo, W and V, which have easy shear able planes [12–14]. Among these elements, particular attention has been given to the vanadium-containing films (Magnéli phases V_nO_{3n-1}), which showed interesting tribological properties in the temperature range 500–700 °C [15–18]. Since the addition of V has been shown to successfully decrease the friction coefficient of binary and ternary nitrides (down to reported values of 0.2–0.3 at temperatures between 550 and 700 °C), we reported in a previous work the effect of V-addition to TiSiN films [7]. Although the relative amounts of V_2O_5 detected at the oxidized surface of V rich TiSiN films was a promising result to achieve the envisaged tribological properties, the strong out-diffusion of V significantly degraded the oxidation resistance of the films. Control of the V out-diffusion could be achieved by changing the design of the films, i.e., by tailoring the nanostructure of the TiSiN films. As vanadium diffusion in the a-Si_3N_4 is much slower than in TiN, increasing the amount of the amorphous nitride phase while optimizing the size of the TiN grains could help to control the vanadium

* Corresponding author. Tel.: +351 239 790 745; fax: +351 239 790 701.
E-mail address: filipe.fernandes@dem.uc.pt (F. Fernandes).

http://dx.doi.org/10.1016/j.surfcoat.2014.12.065
0257-8972/© 2014 Elsevier B.V. All rights reserved.

diffusion in the nanocomposite TiSiN films. However, increasing the Si content in the films in order to achieve higher amounts of a-Si_3N_4 ultimately leads to the loss of the desired mechanical properties.

Energetic ion bombardment of the growing film has been shown to influence the hardness and structure of TiSiN films deposited by PVD. Nose et al. [19] found that the hardness of low Si content TiSiN films increases with substrate bias up to a maximum value. The resulting films consist of nano-columnar TiN grains with a small amount of a-Si_3N_4 phase. Zhang et al. [20] reported an increase of the hardness of TiSiN films with increasing bias up to a maximum of 46 GPa at − 100 V. The authors concluded that this high hardness was due to the formation of the nc-TiN/a-Si_3N_4 nanocomposite structure with complete phase separation and uniform crystallite size. This result was achieved without substrate heating showing that energetic ion bombardment effectively allows tailoring the nanostructure of the TiSiN films.

In the last decade, new magnetron sputtering deposition techniques have been developed to produce highly ionized fluxes of sputtered material and, hence, to allow an increased control over the energetic ion bombardment (energy and direction of the deposited species). Two of these recent developments are: High-power Impulse Magnetron Sputtering (HiPIMS) [21–23], also known as High-power Pulsed Magnetron Sputtering (HPPMS), and Modulated Pulsed Power Magnetron Sputtering (MPPMS) [24–26]. Both HiPIMS and MPPMS deposition techniques are characterized by the application of very high target power densities to achieve higher plasma densities and subsequent ionization of the sputtered material. The effect of Si additions to TiN films deposited by HiPIMS up to 8.8 at.%, has already been studied by Yazdi et al. [27]. Recently, a new design of the MPPMS process named deep oscillation magnetron sputtering (DOMS) was developed [28–30]. This process uses large voltage oscillation packets in long modulated pulses for achieving high peak target currents and voltages. Such configuration has been reported to allow virtually arc-free depositions for reactive deposition of insulating films [28].

The main objective of the present work was to tailor the nanostructure of TiSiN films with high amounts of the a-Si_3N_4 phase, i.e., with high Si content (near 11 at.%). TiSiN films where deposited by DOMS. The energetic ion bombardment of the growing films was controlled by changing the peak power. The structure, morphology and mechanical properties of TiSiN films were studied. Comparison with a film deposited by DC magnetron sputtering (DCMS), prepared as a reference, is also provided.

2. Experimental procedure

TiSiN films were deposited in reactive mode by DOMS (HiPIMS Cyprium™ III plasma generator, Zpulser Inc.) and DCMS (Hüttinger PFG 7500 DC). In both cases a square (150 × 150 mm) high purity Ti (99.9%) target with 16 holes (10 mm in diameter) uniformly distributed throughout the preferential erosion zone was used. The holes were filled with 11 pellets of high purity Si (99.9%) and 5 pellets of high purity Ti (99.9%) in order to achieve a Si content of about 11 at.%. The films were deposited onto polished high-speed steel (AISI M2, 20 × 3 mm) for mechanical property measurements, AISI 306 substrates (20 × 20 × 3 mm) for structure analysis and (111) silicon samples for cross section and surface morphology characterization. Prior to depositions, all the substrates were ultrasonically cleaned in acetone for 15 min and alcohol for 10 min. The substrates were fixed to a rotating substrate holder which revolved with 18 rev/min around the center axis of the chamber. The target to substrate distance was 100 mm. The chamber was evacuated down to 1.1×10^{-3} Pa. Before depositions an ion gun plasma was used to clean the substrates. The ion source consists of a tantalum (Ta) filament, a magnetic coil and an extraction electrode. The source is placed in a small dedicated vacuum chamber (contiguous to the main deposition chamber) which is filled with Ar at 0.13 Pa after the primary vacuum is reached. The electrons emitted by the Ta filament originate a plasma within the coil space. By applying a positive voltage to the extraction electrode, electrons are driven into the main deposition chamber and impinged on the substrate ("heating process"). By applying a negative voltage to the extraction electrode Ar ions are extracted and impinged on the substrate ("etching process"). The energy of both electrons and Ar ions is controlled by applying a suitable bias to the substrate holder. Before each deposition the substrates were first heated for 10 min and then etched for 10 min.

All the depositions (DOMS and DCMS) were performed in reactive mode in an Ar + N_2 discharge gas with a P_{N2}/P_{Ar} ratio of 1/4. In order to enhance the adhesion of films a Ti adhesion layer of approximately 0.4 and 0.3 μm for DOMS and DCMS, respectively, was deposited on the substrates. Furthermore, a gradient layer with increasing N content was deposited before TiSiN films. For all the films, the deposition time was set in order to obtain films with approximately 1 μm of thickness (excluding the interlayer). One TiSiN film was deposited by DCMS using previously optimized conditions for comparison purposes. The DCMS deposition was carried out at 0.3 Pa with a power of 1200 W applied to the target and a negative bias of 70 V applied to the substrates.

An example of the DOMS discharge voltage and current oscillating waveforms used in this work is shown in Fig. 1. Each DOMS pulse consists of a packet of single oscillations. The voltage and current gradually increase to their maximum value (V_p and I_p) during the voltage on-time (t_{on}), and then gradually decay, reaching zero before the end of the oscillation period (T). The DOMS depositions were performed using constant voltage on time (t_{on}), period (T) and pulse duration (D) of 6 and 80 and 1500 μs, respectively. In order produce films with increasing peak current, both the average power (Pa) and the charging voltage applied to the internal d.c. voltage source (DC_{int}) were progressively changed. Note that in this work P_p is defined as the maximum value of the $V_p \times I_p$ product calculated for each oscillation in a single pulse. The pulse frequency (F) was automatically adjusted by DOMS power supply software during each deposition in order to keep the set average power (Pa) constant. All DOMS depositions were performed at a relatively high working pressure (0.9 Pa) and without substrate biasing in order to increase the fraction of ionized sputtered species and to decrease the peak voltage. In this way bombardment of the growing films with a higher ion-to-neutral ratio was achieved while the energy of the bombarding ions was kept as low as possible.

Hereinafter, the DOMS deposited films will be designated as "DOxx", where xx is related to the peak power used in each deposition. The main deposition parameters used in DOMS depositions are compiled in Table 1.

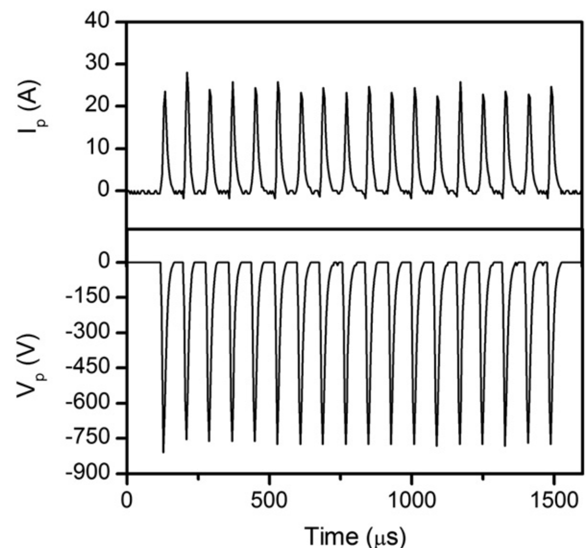

Fig. 1. Typical I–V waveforms of a DOMS pulse used on this work (P = 0.9 Pa; DC_{int} = 240 V; F = 312 Hz; D = 1500 μs; t_{on} = 6 μs; T = 80 μs).

Table 1
Deposition conditions used to deposit TiSiN films by DOMS.

Sample	V_p (V)	I_p (A)	P_p (kW)	P_a (W)	F_i (Hz)	DC_{int} (V)	Dep. time (min)
DO026	843	31	26	800	312	240	95
DO044	939	47	44	1000	290	270	98
DO065	1023	63	65	1200	312	300	104
DO102	1137	90	102	1200	258	350	108
DO148	1247	119	148	1200	198	400	114

As shown in Fig. 2 using the values in Table 1, both I_p and V_p increased almost linearly with increasing peak power. It is well known that the ionized fraction of the sputtered material in HiPIMS increases with I_p. On the other hand, increasing V_p results in an increasing energy of the species bombarding the film during growth.

The crystal structure of TiSiN films was analyzed by X-ray diffraction (XRD) (PANalytical X'Pert PRO MPD) using Cu Kα radiation (45 kV and 40 mA) with a parallel beam. Symmetric θ–2θ geometry was used to study the preferred orientations of the films while a grazing angle geometry (GIXRD) with an incident angle of 3° was used to calculate the lattice parameter and the grain size of the films. The XRD spectra were fitted by using a pseudo-Voigt function to calculate both the full width at half maximum (FWHM) and the peak position (2θ). The grain size was obtained by using the Scherrer's equation, while the lattice parameter was calculated by applying the Bragg's equation first, and then the geometrical relationship equation of lattice parameter with interplanar distance and Miller indices. Chemical bonding of films was characterized by X-ray photoelectron spectroscopy—XPS (Kratos AXIS Ultra HSA, with VISION software for data acquisition and CASAXPS software for data analysis). The analysis was carried out with a monochromatic Al Kα X-ray source (1486.7 eV), operating at 15 kV (90 W), in FAT (Fixed Analyser Transmission) mode, with a pass energy of 40 eV for region ROI and 80 eV for survey. Data acquisition was performed with a pressure lower than 1×10^{-6} Pa using a charge neutralization system. The effect of the electric charge was corrected using as reference the carbon peak (284.6 eV). The deconvolution of spectra was performed using the XPSPEAK41 program, in which an adjustment of the peaks was performed using peak fitting with Gaussian–Lorentzian peak shape and Shirley type background subtraction. Before measurements, the specimens were bombarded with a flux of Ar^+ ions (4 keV) during 45 min, in order to remove surface contaminations. The fracture cross section and surface morphologies of the films were examined by scanning electron microscopy (SEM). The chemical composition of the films was evaluated by energy-dispersive spectrometry (EDS) analysis. Three TiSiN films with Si contents ranging from 3.8 to 12.8 at.%, as measures by EPMA (Electron Probe Microanalysis), were used as reference for the EDS measurements. The hardness and Young's modulus of films were evaluated by depth-sensing indentation technique (Micro Materials NanoTest) using a Berkovich diamond pyramid indenter. In order to avoid the effect of the substrate, the applied load (10 mN) was selected to keep the indentation depth less than 10% of the film's thickness. 16 hardness measurements were performed in each specimen.

3. Results

3.1. Chemical composition and deposition rate

The deposition rate per kilowatt of average power of the DOMS films (hereafter simply referred as "normalized deposition rate") steadily decreases with increasing peak power as shown in Fig. 3. Increasing the peak power in the DOMS discharge simultaneously increases I_p and V_p, i.e., simultaneously increases the ionized fraction of the sputtered material and the energy of the sputtered species bombarding the film. It is well established in the literature that increasing the fraction of ionized sputtered flux results in a loss of deposition rate due to increasing metallic ion back-attraction to the target [31]. Moreover, the increase of V_p with increasing peak power also contributes to the loss of deposition rate due to the sub-linear evolution of the sputtering yield with discharge voltage [32]. Finally, the high voltages in DOMS (see Table 1) could also lead to some re-sputtering and consequent loss of deposition rate.

Although both the ionized fraction and the deposition voltage are much lower in the DCMS discharge, the normalized deposition rates of the films deposited with $P_p \leq 44$ kW are higher than the DCMS normalized deposition rate. Both the lower deposition pressure used in DCMS (0.3 Pa) and the applied bias (−70 V) contribute to a high energy of the bombarding specie. This results in an intense re-sputtering of the deposited species in DCMS and could account for the lower DCMS deposition rate. Increasing the peak power to 65 kW results in a steeper decrease of the normalized deposition rate to values below the DCMS normalized deposition rate. Further increasing P_p still results in a decreasing deposition rate but at a slower rate. As it will be shown later, the steep decrease in normalized deposition rate corresponds to a transition between two different deposition regimes.

The nitrogen content of both the DOMS and the DCMS films is close to 50 at.% (see Fig. 4) showing that a nitride phase with close to stoichiometric composition was deposited. Although all the films were produced using the same composite target, the Si content in the films produced by DCMS is higher than in the films deposited by DOMS by

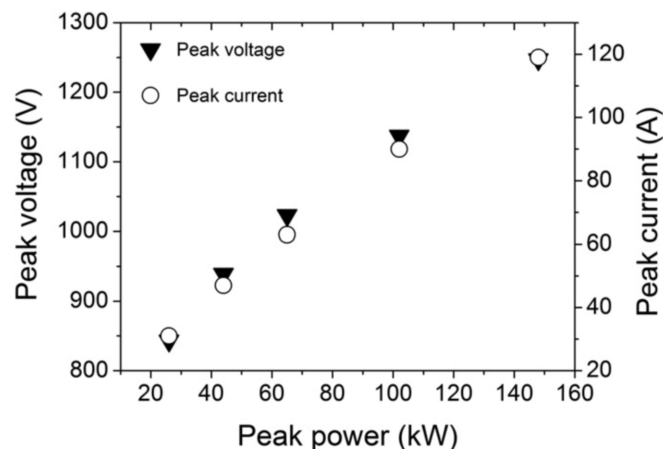

Fig. 2. Peak voltage (V_p) and peak current (I_p) as a function of peak power for the TiSiN films deposited by DOMS.

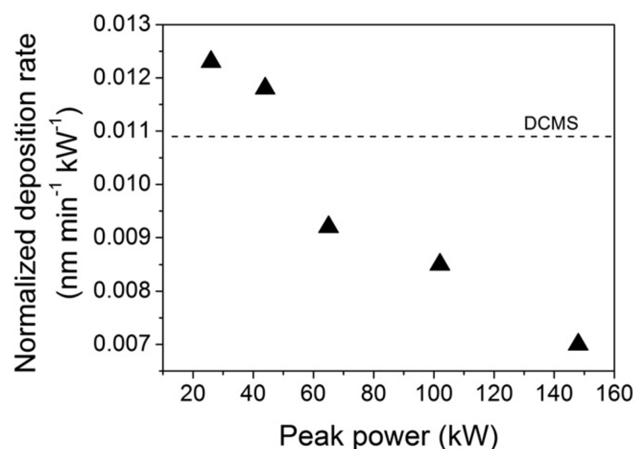

Fig. 3. Deposition rate of the DOMS films normalized to an average power of 1 kW (the dashed line indicates the DCMS value).

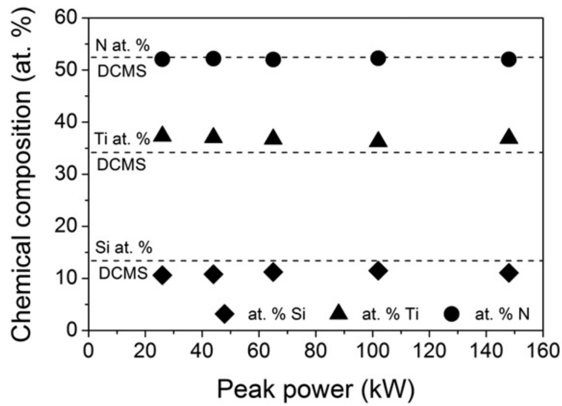

Fig. 4. Chemical composition of the different films. Dash lines give the elemental chemical composition of the DCMS film.

almost 2 at.% in average. The evolution of the sputtering yield of Ti and Si with increasing energy of impinging Ar^+ ions (i.e., with increasing discharge voltage) was simulated using the software package SRIM [33]. The sputtering yield of Ti increases with discharge voltage at a higher rate than the sputtering yield of Si which contributes to the loss of Si in DOMS as compared to DCMS. However, increasing the peak power in DOMS mode does not significantly influence the Si content in the films.

3.2. Structure (XRD)

The X-ray diffraction patterns of the TiSiN films obtained in θ–2θ configuration are shown in Fig. 5. Excluding the substrate contribution, all the diffraction peaks could be generally assigned to the f.c.c NaCl-type TiN phase. However, depending on the power supply used and the deposition conditions, different peak positions, intensities and broadening can be observed.

The XRD pattern of the film deposited by DOMS with the lowest peak target power (spectrum a) of Fig. 5) shows narrow diffraction peaks corresponding to a crystalline f.c.c TiN phase. The thermal expansion coefficient of the substrate (AISI 306) is almost double of TiN thermal expansion coefficient and therefore thermal compressive stresses should be formed upon cooling of the films. However all the TiN diffraction peaks of the film deposited with the lowest peak target power are located at slightly higher angles than referred in the ICCD card of TiN. As the nitrogen content in the films is close to 50 at.%, the most probable causes for the shift of the diffraction peaks are the formation of a solid solution of Si in TiN and/or the presence of tensile stresses. In the former case, as Si atoms are much smaller than Ti atoms, substitution of Ti by Si in the TiN lattice results in a smaller lattice parameter. In the latter case, although TiN films deposited by reactive magnetron sputtering usually have compressive stresses, tensile stresses may be formed if the films are deposited at relatively high pressure as in this work (0.9 Pa). For example, Abadias et al. [34] found that increasing the deposition pressure resulted in a shift to higher angles of the (111) TiN peak which was associated to a change in intrinsic stresses from compressive to tensile. A crystalline f.c.c TiN structure is still deposited when the peak target power is increased to 44 kW (spectrum b) of Fig. 5). However, the (002) diffraction peak is slightly broadened and its position is shifted to lower angles, being close to the value referred for unstrained TiN. Further increasing the Si content gradually shifts to position of the (002) diffraction peak to even smaller angles than the TiN standard and considerably broadens the XRD peaks (spectra c) to e) of Fig. 5). As the nitrogen content in the films remains the same, the most probable cause for the XRD peak evolution is the formation of increasing compressive stresses. Ultimately, the XRD pattern of the film deposited at the higher target peak power (148 kW) has low intensity diffraction peaks typical of a quasi-amorphous structure and is much more similar to the XRD pattern of the DCMS film (spectrum f)). The DCMS film was deposited at a lower pressure (0.3 Pa), i.e., with high energy of the sputtered species arriving at the substrate, and using a −70 V bias, i.e., with the additional bombardment of Ar ions from the plasma. The loss of bombardment intensity expected in the DOMS depositions which were carried at higher pressure (0.9 Pa) and without bias is completely counterpoint at high peak powers.

The preferred orientation of the films was evaluated from the XRD patterns obtained in θ–2θ configuration. Fig. 6 shows the measured relative intensities for the (111), (002) and (220) peaks divided by their relative intensities in the powder ICDD card of TiN. A value of 1 in this figure means that there is no preferential orientation while higher values indicate a preferred orientation. All the films deposited by DOMS have a strong [001] preferred orientation although a complete (001) texture is not achieved in the film deposited with the lowest peak power ($P_p = 26$ kW). The development of texture in TiN thin films deposited with relatively low intensity bombardment is a competitive process whose outcome depends on the relative growth rates of the (111) and (002) crystal faces. These grow rates are governed by surface chemistry processes, which in turn depend on the impinging flux. At low ion energies, increasing the ion to neutral ratios favors the (001) texture mainly due to the collisional enhancement of the surface mobility of adsorbed Ti [35]. Even at low peak target powers the fraction of ionized sputtered species in the DOMS discharge is significantly higher than in a DCMS discharge. On the other hand, the HiPIMS discharge also contributes to the activation of nitrogen by dissociation of nitrogen molecular ions in the plasma into atomic ionized species. In the presence of atomic nitrogen the ad-atom diffusion length on TiN (001) surfaces is considerably decreased also favoring a (001) texture. Both texture formation mechanisms contribute to the formation of the [001] preferred orientation observed in the DOMS film deposited at

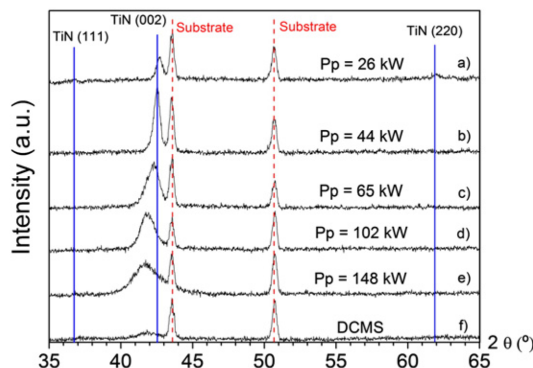

Fig. 5. XRD patterns of the DOMS films in θ–2θ configuration as a function of peak power (the DCMS pattern is also shown for comparison).

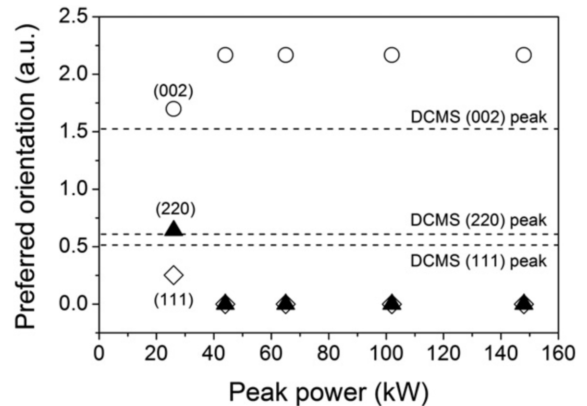

Fig. 6. Evolution of the preferred orientation of the DOMS films as a function of peak power (the dashed lines indicates the DCMS values).

low peak power. At relatively high ion energies TiN growth evolves towards the most open channeling direction, the (001) direction in the B1 NaCl structure, due to anisotropy in the collision cascades [36]. This texture formation mechanism should be dominant in the DOMS films deposited at the highest peak powers.

Grazing angle XRD diffraction (GIXRD) patterns were also acquired in order to obtained higher intensity peaks from the films and to avoid interference from the substrate and interlayer diffraction peaks. Once again, all the diffraction peaks could be assigned either to the substrate or to the TiN f.c.c structure (Fig. 7). The same qualitative conclusions already drawn from the XRD patterns obtained in θ–2θ configuration are also valid for the GIXRD patterns. However, the (220) peak is detected in all GIXRD patterns along with the (111) and the (002) peaks already detected in the θ–2θ configuration patterns.

The lattice parameters of the TiN grains were calculated from the GIXRD patterns using the Bragg equation. As shown in Fig. 8, the lattice parameter calculated from the (002) peak, $a_{(002)}$, increases almost linearly with increasing peak power. On the other hand, the lattice parameter calculated from the (220) diffraction peak, $a_{(220)}$, initially increases at low peak powers, reaches a maximum at 65 kW and decreases at higher peak powers. As a result two different regimes can be observed. At lower peak powers $a_{(002)}$ is similar to $a_{(220)}$ (within the experimental error) while both lattice parameters are close to unstrained TiN (0.4238 nm according to the ICDD card number 01-087-0633). At higher peak powers, $a_{(002)}$ is much higher than $a_{(220)}$ and also much higher than unstrained TiN. In GIXRD geometry the XRD azimuthal angle continuously increases with the diffraction angle. In an unstrained material similar lattice parameter values should be obtained from all XRD peaks excepting small differences due to the elastic anisotropy of the lattice. However if bi-axial in-plane stresses are present, significantly different values of the lattice parameter will be obtained from different planes depending on the azimuthal angle. Furthermore, bi-axial in-plane compressive stress will result in lower lattice parameter values calculated from higher 2θ angle planes and bi-axial in-plane tensile stresses will have the opposite effect. The above arguments allow us to conclude that the films deposited with pp ≥ 65 kW have in-plane bi-axial compressive stresses, which increase with increasing peak power, while no in-plane bi-axial stresses are detected in the films deposited at low peak power. Both the $a_{(220)}$ and $a_{(002)}$ lattice parameters are smaller than the lattice parameter in unstrained TiN for the film deposited at the lowest peak power. As referred above, smaller lattice parameters could originate either from the formation of in-plane bi-axial tensile stresses, as a result of the attractive forces between column and/or grain boundaries, or to the formation of a Si solid solution in the TiN grains. The above conclusions clearly advocate in favor of the later hypothesis. Note that $a_{(002)}$ is also much higher than $a_{(220)}$ in the DCMS films (see dashed lines in Fig. 8) while $a_{(002)}$ is much higher than in unstrained TiN, which shows that bi-axial in-plane compressive stresses were also formed in this film.

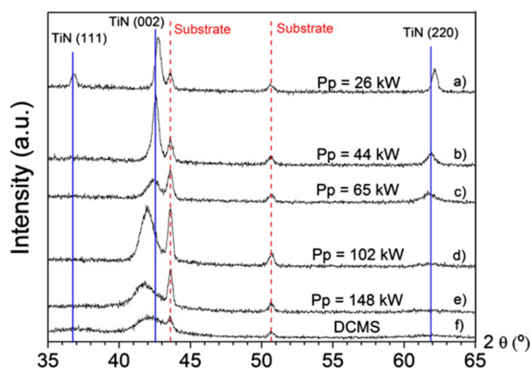

Fig. 7. XRD patterns of the DOMS films in GIXRD configuration as a function of peak power (the DCMS pattern is also shown for comparison).

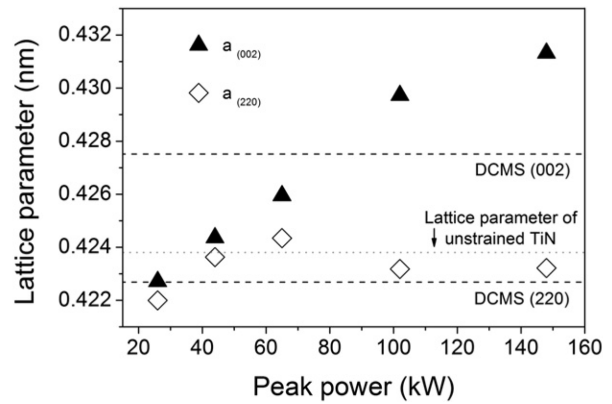

Fig. 8. $a_{(002)}$ and $a_{(220)}$ lattice parameters calculated from the GIXRD patterns of TiSiN films, as a function of peak power. Dashed lines indicate the lattice parameter of the film deposited by DCMS, for comparison purposes.

The TiN grain size was calculated from the GIXRD patterns using the Scherrer formula. The grain sizes calculated from the (001) and the (002) diffraction peaks agree well with each other. The grain size of the DOMS films decreases with increasing peak power from 25 nm to less than 5 nm (Fig. 9). (002) textured TiN films with a relatively large grain size (25 a 30 nm) were also deposited by Lattemann et al. [37] using HiPIMS under intense low-energy ion irradiation of the growing film. On the other hand, Chang et al. [38] found that the grain size of HiPIMS TiN films deposited under intense ion bombardment, i.e., low duty cycle, was less than 5 nm. Once again, two different deposition regimes can be identified for the DOMS films. The grain size of the films deposited by DOMS at the highest peak powers is close to the grain size of the film deposited by DCMS.

3.3. Chemical bonding (XPS)

It is well known that Si addition to TiN results in the formation of an amorphous phase which cannot be detected by XRD and is usually identified by XPS. Fig. 10 shows the N 1s XPS spectra of the DCMS and DOMS films deposited with a peak power of 26 and 102 kW after ion bombardment. All spectra were decomposed using a Shirley background and three Gaussian functions with the same full width at half maximum. Note that decomposition with only two Gaussian curves with the same width resulted in a bad agreement on the high binding energy side of the N 1s spectra. The lowest energy peak has a binding energy close to 397 eV which corresponds to the N 1s electrons in TiN [39]. The highest energy peak in all spectra is close to 400 eV and corresponds to N–O bonds [39], i.e., nitrogen atoms with only one oxygen atom as

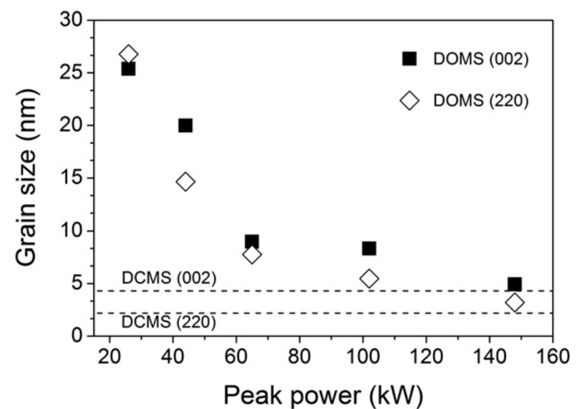

Fig. 9. Grain size of the TiSiN films deposited by DOMS calculated from the GIXRD patterns using the (002) and (220) diffraction peaks. Dashed lines indicate the grain size of the film deposited by DCMS.

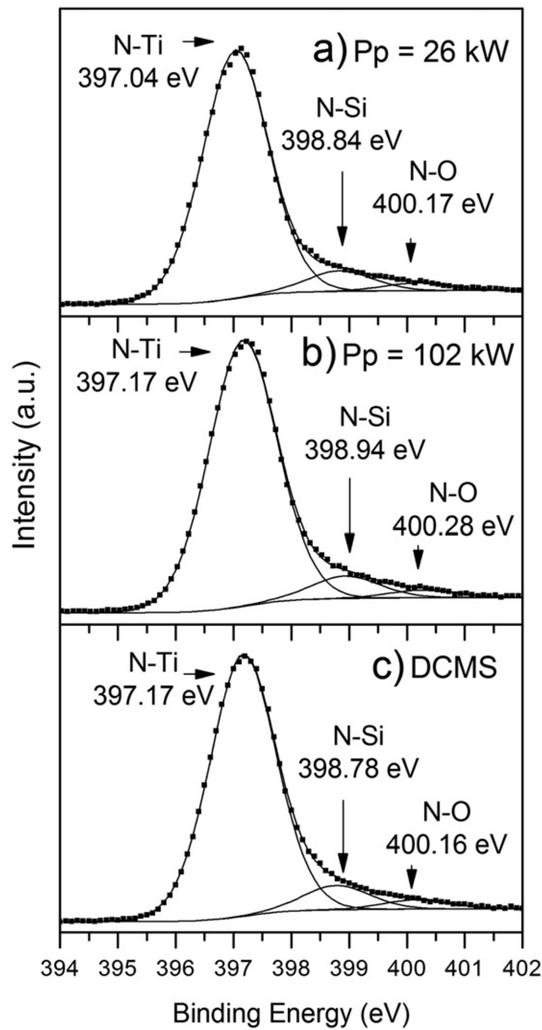

Fig. 10. XPS N 1s spectra of Ti–Si–N films deposited by DOMS (a) and b)) and DCMS (c)).

the first neighbor. This peak has very small intensity showing that only a minor amount of oxygen contamination remains in the samples after ion bombardment. The third peak is located near 399 eV in all spectra and corresponds to N–Si bonds in Si_3N_4 [40,41]. As expected the intensity of the peak corresponding to Ti–N bonds is much higher than that of the peak corresponding to N–Si bonds. Furthermore, as shown in Fig. 11, the relative amount of Ti–N and Si–N bonds in the DOMS films is similar, i.e., it does not depend on the peak power, while the amount of Si–N bounds is slightly higher in the DCMS film in agreement with its chemical composition.

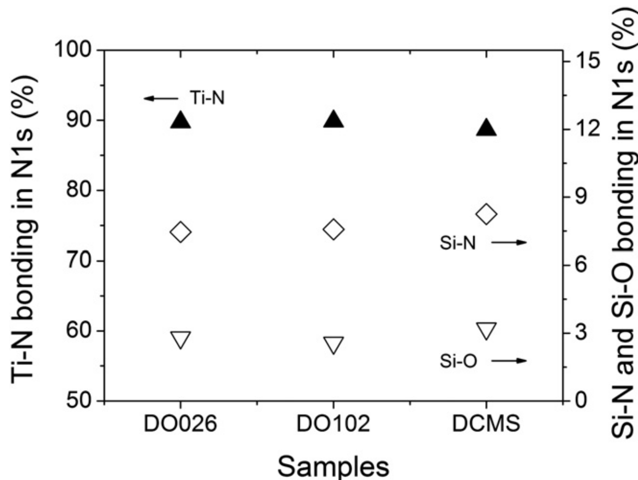

Fig. 11. Bonding percentage in the films calculated from the N 1s XPS spectra.

Fig. 12 shows the Si 2p XPS spectra of the same DCMS and DOMS films as in Fig. 10 also after ion bombardment. Once again, the XPS spectra could be fitted with three Gaussian functions with the same full with at half maximum. The highest energy peak, located near 103.5 eV was assigned to Si–O double bonds. The low intensity of this indicates that only minor amounts of oxygen were incorporated in the films. A small peak near the binding energy of free Si, 99 eV, is also detected in all spectra. The highest intensity peak is located near 101.5 eV, and has a full width at half maximum close to 2 eV while its base extended from 100 to 104 eV. Similarly shaped XPS peaks have been reported in the literature for TiSiN films in many works. In most cases this peak is associated with Si–N bonds in a-SiN. The position of the peak in the XPS spectra obtained in this work lies in the lower part of the range of values reported in the literature (between 101.5 and 101.8 eV [4,20,38,40,41]).

Regarding the formation of a Si solid solution in TiN, a similarly shaped peak has been fitted by 2 Gaussian contributions at 102.6 and 101.5 eV by Li et al. [9], the later one corresponding to Si in solid solution and the former to Si in a-SiN. This resulted in two peaks with much lower FWHM than in this work. In opposition, Li et al [8] found that Si in TiN resulted in a peak with the same shape as those obtained in this

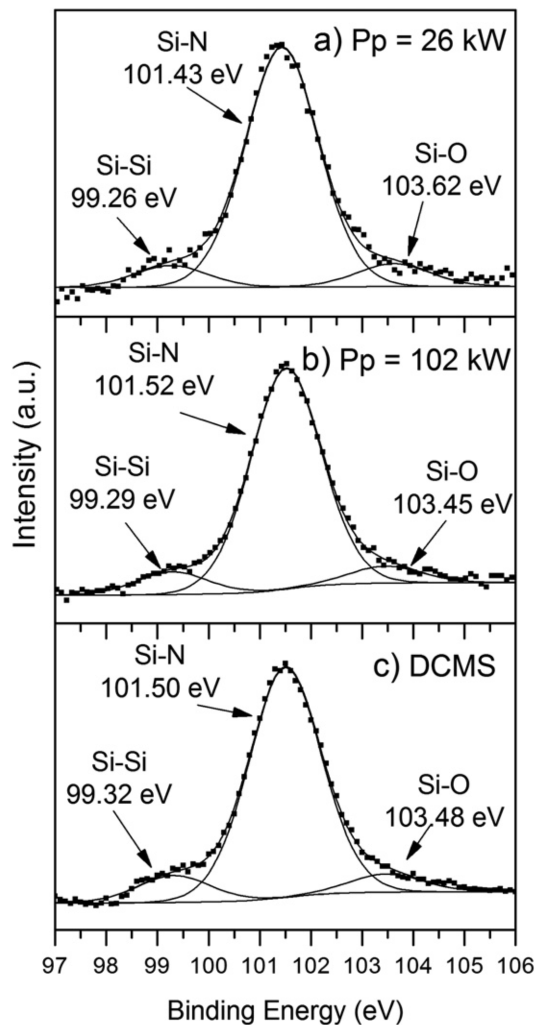

Fig. 12. XPS Si 2p spectra of the Ti–Si–N films deposited by DOMS (a) and b)) and DCMS (c)).

work but is located at a slightly higher energy (102.1 eV). This result was explained by the more electronegative ambient of Si in the solid solution than in the a-SiN (6 N neighbors against 4, respectively). However the film was XRD amorphous. The authors also found a similarly shaped peak at 101.7 eV in films consisting of a solid solution and a-SiN. Although it is clear that the XPS peak at 101.5 eV found in this work is associated with Si–N bonds in a-SiN, the available date do not allow us to argue about the possible formation of a solid solution.

3.4. Microstructure and morphology (SEM)

The TiSiN film deposited by DCMS has a compact microstructure with columns extending from the substrate to the top of the film (Fig. 13a)). The top-view micrographs show the characteristic dome-like endings of the columns although with a preferential elongation along one direction (Fig. 13a_1)). In this work the films were deposited using a rotating substrate holder which introduces an anisotropy in the deposition system. The spread of the incident angles of the sputtered species on the substrate surface is higher along the direction tangent to the substrate rotation than in the perpendicular direction. As a result a preferential in-plane elongation of the columns along the direction tangent to the rotation is observed.

The TiSiN films deposited by DOMS with the two lowest peak powers also show a compact columnar microstructure (Fig. 13b) and c)). However, the top-view micrographs show that the top of the columns have an equiaxed geometry, i.e., no preferential orientation is observed (Fig. 13b_1) and c_1)). The high plasma density achieved in the DOMS discharge results in an efficient ionization of the sputtered species by electron impact [23]. Even at low peak target powers the fraction of ionized sputtered species in the DOMS discharge is significantly higher than in the DCMS discharge. The effect of the deposition anisotropic geometry is suppressed in the films deposited by DOMS as the metallic ions are sensitive to the substrate self-bias and bombard the film at incident angles closer to the normal. The surface morphology of the film deposited with the lowest peak power resembles a cauliflower-type morphology with protruding structures which consists of grains, 15–25 nm wide, that agglomerate to form larger structures, 70–120 nm wide. These types of structures are associated with unstable growth under surface diffusion limited conditions. Increasing the peak power still results in the formation of cauliflower-type morphology but the characteristic dimensions of the agglomerates are considerably reduced due to increased surface diffusion (Fig. 13d_1)). Increasing the peak power to 102 kW significantly changes the morphology of the film (Fig. 13e)). Although some remains of columns are still observed, the morphology of the film is much more compact. On the other hand, a granular morphology is formed on the film surface. In this case, the grains do not aggregate to form larger structures as in the cauliflower like morphology. Further increasing the peak power confirms the previous trend (Fig. 13f)). The films deposited at the two highest peak powers have a completely dense morphology, without any columnar remains, while the granular morphology remains up to the highest peak power although with a small increase in granule size. Once again a clear transition of both the cross-section and surface morphologies is observed when the peak power increases from 44 to 65 kW.

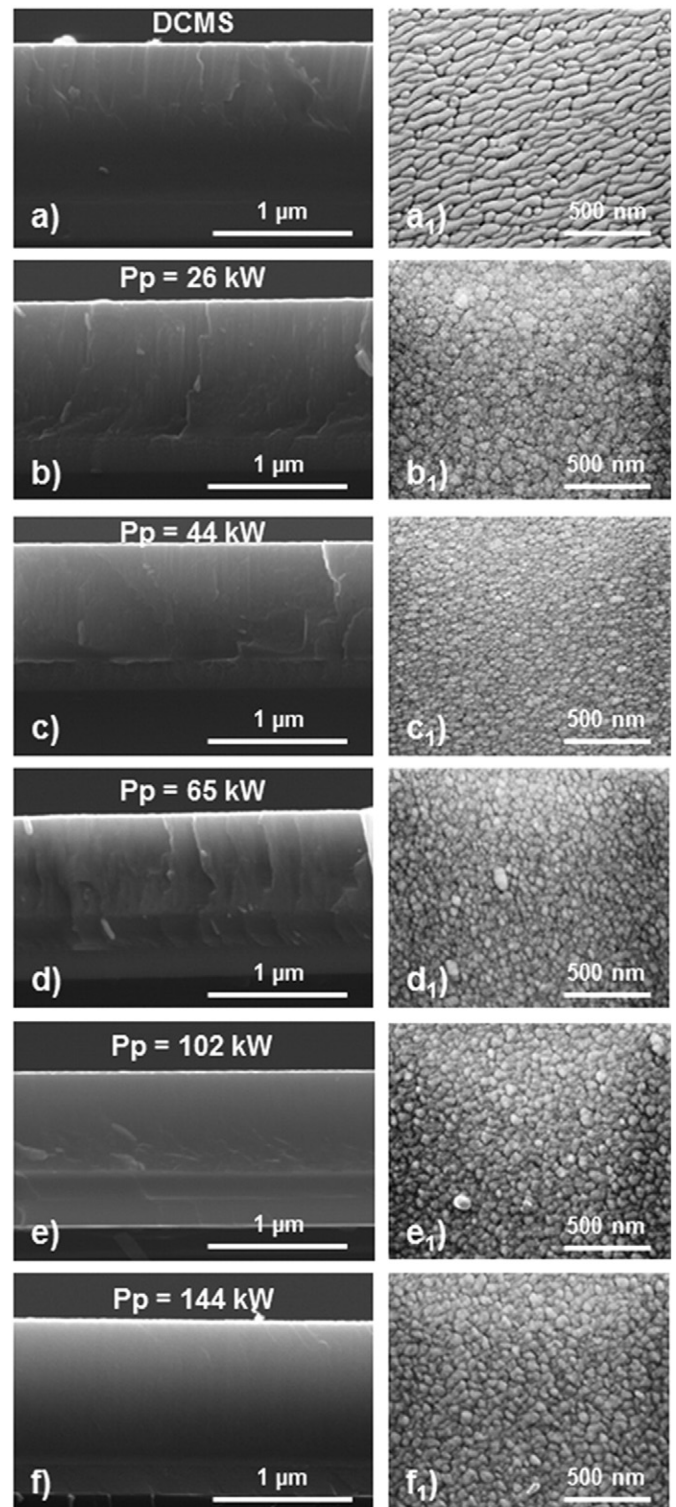

Fig. 13. SEM fracture cross section and surface micrographs of the TiSiN films deposited by DCMS (a)–a_1)) and DOMS (b)–b_1) to f)–f_1)).

3.5. Mechanical properties (nanoindentation)

The dependence of hardness and Young's modulus of DOMS TiSiN films with respect to peak power are displayed in Fig. 14. The hardness increases from 24 to 29 GPa with increasing peak power from 26 to 65 kW and remains fairly constant with further increasing the peak power. Once again, the evolution of the hardness with peak power shows two different trends switching at Pp = 65 kW. Many authors reported in the literature hardnesses for TiSiN films over 40 GPa [4,11,20,41]. The hardness of the films usually increases with increasing silicon content and reaches a maximum at an optimized content which corresponds to the formation of a nanocomposite. However, in this work the silicon content in the films is higher that the optimized content for maximum hardness. All the TiSiN films deposited by DOMS have a silicon content near 11 at.%, which is close to the percolation threshold of the a-SiN phase, resulting in lower hardness values. However, all the films deposited by DOMS have a significantly higher hardness than the film deposited by DCMS (dashed line in Fig. 14).

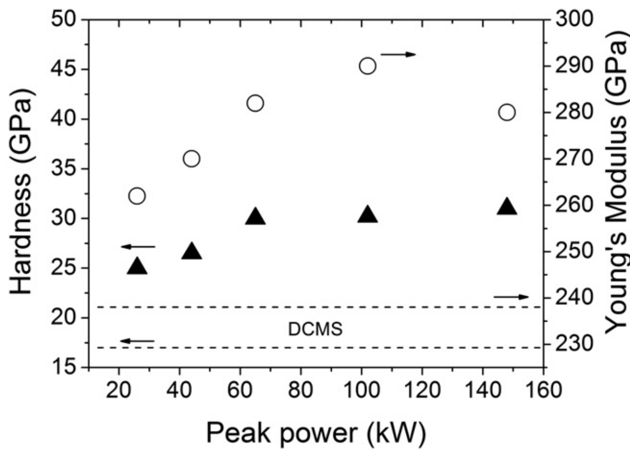

Fig. 14. Hardness and Young's modulus evolution of the DOMS films.

The Young's modulus increases from 260 to 290 GPa with increasing peak power up to 102 kW while a slight decrease to 285 GPa is observed at the highest peak power. The Young's modulus of the films deposited by DOMS is higher than for the films deposited by DCMS (see dashed line in Fig. 14) irrespective of the peak power.

4. Discussion

All the films deposited by DOMS have a nanocomposite structure consisting of two phases: f.c.c TiN, as detected by XRD, and a-Si_3N_4, as identified by XPS. Both the Si content measured by EDS and the amount of a-SiN evaluated by XPS are similar in the DOMS films irrespective of the deposition conditions. However, based on the presented results, a transition between two different deposition regimes can be identified between Pp = 44 kW and Pp = 65 kW: a steep decrease in deposition rate is observed, in plane bi-axial compressive stresses start to form, the TiN diffraction peaks start to broaden and the morphology of the films changes from columnar to featureless. The following discussion will first address these two deposition regimes, hereafter referred as low and high peak power regimes. Then the formation of the Si solid solution in TiN and the evolution of films microstructure with increasing peak power will be discussed. Finally some conclusions about the comparison of DCMS and DOMS processes will be drawn.

4.1. Low peak power deposition regime

All the TiSiN DOMS films were deposited at a relatively high deposition pressure (0.9 Pa) and without bias. TiN film deposited by DCMS in such conditions usually have a (111) preferred orientation and tensile stresses as shown for examples by Abadias et al. [34]. Both the energetic sputtered atoms and reflected neutrals experience a sufficient number of collisions to significantly decrease their kinetic energy and therefore the atomic peening effect is weak or non-existent. As a result, the attractive forces between column/grain boundaries are the dominant sources of stress. However, the DOMS films deposited in this work at low peak power have a preferred (002) orientation and a dense microstructure. Although, small tensile stresses may be present in the film deposited at the lowest peak power, the film deposited at 44 kW is stress free. The main advantage of the DOMS discharge as compared to the DCMS discharge is the ionization of the sputtered flux. Even at low peak target powers the fraction of ionized sputtered species in the DOMS discharge is significantly higher than in the DCMS discharge. As a result the ions to neutral ratio in the flux of particles impinging on the substrate is much higher, which improves the reactivity of the deposited species [23]. Additionally, the HiPIMS discharge also contributes to the activation of nitrogen by dissociation of nitrogen molecular ions in the plasma into atomic ionized species [42]. As shown by Gall et al. [43], in such conditions, and provided that the energy of the bombarding species is kept low, dense columnar TiN films without compressive stresses or defects and with a (002) preferred orientation can be deposited. The properties of the DOMS films deposited in at low peak power fit well this deposition regime. The films have a dense columnar morphology, relatively high grain sizes (20 to 30 nm), and at most small compressive stresses while the TiN grains have a (002) preferred orientation.

4.2. High peak power deposition regime

Increasing the peak power in the DOMS discharge increases the I_p and therefore, the ion to neutral ratio in the bombarding flux. As referred above, this increases the ad-atom mobility on the film surface and favors film densification and (002) preferred orientation. However, V_p also increases and therefore the energy of the bombarding species increases. It is well known that above a critical threshold of the bombarding species, the incident particles will penetrate in the subsurface of the growing film and will induced compressive stress and film defects through the atomic peening effect [44]. In this deposition regime the TiN films also have a (002) preferred orientation induced by ion channeling through the more open (002) planes in contrast to the denser (111) planes which are destroyed during growth. As a result dense defective films with a quasi-amorphous structure and high compressive stresses are deposited. Although careful optimization of the energy of the bombarding species can minimize the compressive stresses and defect formation, this is only possible in a narrow range of energies (if any) which makes the control of the process difficult. The film deposited at high peak power clearly fits this deposition regime. Above Pp = 65 kW high compressive stresses are formed, the film have a dense featureless morphology and the TiN grain size is smaller (5 nm). The high energy of the deposited species results in an intense atomic peening effect which ultimately leads to secondary nucleation due to the high number of defects. Note that the film deposited by DCMS also fits this deposition regime. In fact the properties of the DCMS film are similar than those of the DOMS films deposited with high peak power although a columnar morphology is formed in the DCMS film. In the DCMS case the high energy of the bombarding species is provided both by the low deposition pressure and the additional bombardment with argon ions from the plasma. In the DOMS case the increased energy provided at high peak power was enough to compensate the loss of energy due to high pressure and to the lack of bias. The atomic peening effect is even more intense than in the case of the DOMS films as higher compressive stress develop and secondary re-nucleation is initiated.

4.3. Solid solution of Si in TiSiN at low temperature

As it is well known, there is no metastable solid solution in the equilibrium diagram of TiSiN [45]. However, the deposition conditions provided by conventional magnetron sputtering may be very far from thermodynamic equilibrium. Houska et al. [46] performed classical molecular dynamics simulations of thermodynamically preferred structures of $Ti_{(50-x)}Si_xN_{50}$ ($x \leq 0.3$) nanocomposites of various compositions containing. They concluded that if the mobility of film-forming atoms is limited (which correspond to high quenching rates in their calculations) Si-containing TiN nanocrystals are formed. The lattice constant of the crystals decreases with increasing Si down to 98% of the Si free lattice and stabilizes at 4 at.% which is also the saturation composition of Si. If sufficiently low ion bombardment conditions are used during TiSiN film deposition by magnetron sputtering (high pressure, no bias, high target to substrate distance, etc), the formation of a solid solution can be expected due to the low ad-atom mobility and associates kinetics barriers. Such deposition conditions can be achieved by using positive bias of the substrate in order to irradiate the films with an electron flux instead of energetic ions as shown by Li et al. [9]. As expected for low ion bombardment, the preferred orientation of

the films was (111) up to 10 at.% Si. On the other hand, the lattice parameter of the films decreased from just above 0.423–0.424 to below 0.4195 nm always being lower than unstrained TiN. They concluded that a solution with a cubic B1 NaCl-type structure existed in the films containing <10 at.% Si. Formation of a solid solution when a positive bias is used was also suggested by Vaz et al. [47,48]. A solid solution in (111) TiN can also be obtained by using high target to substrate distance. Fernandes et al. [7] used a target to substrate distance of 175 mm in the deposition of TiSiN films. They found that the lattice parameter of all films was lower than unstrained TiN and that it decreased with increasing silicon content. All the films had a (111) orientation. A shift of the (111) peak to higher angles with increasing silicon content was reported by Chawla et al. [49] in the XRD patterns of TiSiN films with a (111) texture deposited at a relatively high pressure (0.5 Pa). Although the authors did not focused on this particular feature, they also reported lower lattice parameters than unstrained TiN in all films which decreased with increasing Si content. On the contrary, Zhang et al. [4] and Ding et al. [50] reported that the (111) peak position of TiN did not change with Si content also for (111) textured films. However, both authors measured lattice parameters higher than that of TiN and attributed this result to the formation of in plane bi-axial compressive stresses. In both cases a relatively high ion bombardment energy was used which was enough to overcome the kinetics barrier responsible for the formation of the solid solution. Li et al. [51] used a hybrid deposition configuration (inductively coupled plasma (ICP)-assisted magnetron sputtering) in order to irradiate the growing TiSiN films with a high-flux of low energy ions (20 eV). The films deposited at higher fluxes were found to shave a (002) preferred orientation and increasing lattice parameters up to the unstrained TiN value with increasing flux. They concluded that a solid solution of Si in TiN was formed at intermediate fluxes and that complete Si segregation was only achieved for the highest flux which has a complete (002) orientation and a lattice parameter close to TiN. These authors also investigate the effect of Si content using the same high flux as in the previous reference. They found that all films were (002) textured and that irrespective of the Si content the lattice parameter of the TiN structure was always close to unstrained TiN.

Resuming the above results found in the literature, Si solid solution in TiN can be formed by magnetron sputtering at low bombardment conditions which lead to (111) textured films. Increasing the energy of the bombarding ions suppresses the solid solution formation although the (111) texture may be retained. In this case the starting formation of compressive stress seems to be coincident to the loss of the solid solution. Increasing the flux of ions while keeping their energy low also results in suppression of the solid solution formation. However, in this case, Si free TiN grains are only deposited when the (111) to (002) texture turnover is completed. The TiSiN films in this work were deposited at a high pressure (0.9 Pa) and without bias which are clearly deposition conditions of low ion bombardment in DCMS. However, a solid solution was formed at the lowest peak power in a (002) textured film although the texture was not complete. On the other hand, increasing the peak power suppresses the solid formation simultaneously with complete (002) texture. These results agree well with the results reported by Li et al. [8] showing that a high flux of low energy ions was achieved in the DOMS discharge at low peak power, somewhat equivalent to the one used by the authors in their ICP assisted setup.

4.4. Nanocomposite TiN/a-SiN microstructure evolution with peak power

As already referred, all the films deposited by DOMS have a nanocomposite microstructure consisting of two phases: f.c.c TiN and a-SiN. Although similar amounts of SiN were detected in the DOMS films, both the phase distribution and the properties of the f.c.c phase depend on the peak power. At low peak power the nanocomposite is formed by a solid solution of Si in TiN and a-SiN. The columnar microstructure of the films and the cauliflower-like surface morphology suggest that this film is formed by nano-columnar TiN based grains while the a-SiN phase fills the inter-columnar spaces. Increasing the peak power suppresses the formation of the solid solution while decreasing the grain size. The higher peak power decreases the size of the TiN nano-columns although the nano-columnar nanocomposite microstructure still holds. As shown by Pei et al. [52], the inter-columnar regions can degrade the mechanical properties of the films. The lower size of the nano-columns in the film is responsible for the hardness increase in spite of the solid solution suppression. Further, increasing the peak power increases the bombarding species energy above the TiN critical threshold for implantation [36]. The higher energy ions are able to penetrate to the sub-surface of the growing films leading to the start of compressive stresses and defect formation. The morphology of the film is denser and globular structures are observed in the surface. Secondary nucleation starts and the film microstructure consists of equiaxed nanocrystalline TiN grains in an a-SiN matrix. Both the increase in hardness and Young's modulus agrees well with the concomitant densification of the film. The nanocomposite nanostructure of the films remains unchanged with further increasing the peak power and, consequently, both the hardness and Young's modulus also remain constant. As a result, DOMS allows us to tailor the microstructure of the TiSiN films by decreasing the TiN grain size while keeping the amount of a-SiN.

4.5. Comparison of the DOMS and DCMS deposition processes

One of the aims of this work was to compare the DCMS and DOMS discharge effects on the properties of the TiSiN films. Several differentiating characteristics were already pointed out in the previous discussion and will be summarized in this section.

The most striking difference is the ability of the DOMS discharge to overcome the degradation of the bombardment with increasing pressure. Although the DOMS films were deposited at a high pressure (0.9) and without bias, dense films with high hardness and (002) preferred orientation were deposited. The ability of the DOMS discharge to overcome pressure effects lies in the high ionization fraction of sputtered materials. Although the voltage peak decreases with pressure, as in DCMS, the fraction of ionized material increases with increasing pressure and efficiently delivers the needed energy to the growing films.

Another interesting feature of the present work is that at low peak power we were able to deposit TiSiN films with similar properties of TiSiN films deposited by ionized PVD methods. At low peak power sufficiently high ionization of the sputtered material is achieved to efficiently promote surface diffusion and a sufficiently low energy of the bombarding species to avoid the atomic peening effect. To our knowledge, this is not possible in magnetron sputtering. The fraction of ionization and the energy of the species, i.e., I_p and V_p, are not independent from each other in the DOMS discharge. However, it should be possible to tailor the ionization fraction independently of the ion energy by carefully choosing the pressure and substrate to target distances. Of course, the optimum conditions will also depend on the material properties.

Finally, as already pointed out by many authors for HiPIMS, the DOMS process also brings the dilemma between film properties and deposition rate. As for HiPIMS, DOMS allows the deposition of dense films with high hardnesses and better overall quality than DCMS. However, this is achieved at the expense of deposition rate which is one of the most important parameters from the technological point of view. The results obtained in this work point out that higher peak powers may not be the most interesting feature of DOMS as they also bring about higher energy of the bombarding species. In fact, using low peak powers and strategies to increase the ionization fraction of the sputtered materials (such as high pressure) may be much more interesting as we already concluded in a previous work about Cr deposition by DOMS [30].

5. Conclusions

Two distinct regimes were identified for the deposition of TiSiN by DOMS. The films deposited at low peak power (up to 44 kW) have a dense columnar morphology, relatively high grain sizes (20 to 30 nm), and at most small compressive stresses while the TiN grains have a (002) preferred orientation. In this regime the growing film is bombarded with a high flux of low energy ionized sputtered species promoting the surface mobility of the ad-atoms and avoiding the atomic peening effect. The films deposited at higher peak power have high compressive stresses, a dense featureless morphology and a smaller TiN grain size (≈5 nm). In this regime the high energy species impinging on the substrate are able to penetrate in the sub-surface of the growing film, resulting in an intense atomic peening effect which ultimately leads to secondary nucleation due to the high number of defects.

All the films deposited by DOMS have a nanocomposite microstructure consisting of two phases: f.c.c TiN and a-Si_3N_4. Although similar amounts of a-SiN were detected in the films, both the phase distribution and the properties of the f.c.c phase depend on the peak power. At low peak power the nanocomposite is formed by a solid solution of Si in large TiN grains imbibed in a-SiN matrix. Increasing the peak power suppresses the solid solution formation and decreases the size of the TiN grains. As a result, DOMS allows us to tailor the microstructure of the TiSiN films by decreasing the TiN grain size while keeping constant the amount of a-SiN.

DOMS allows the deposition of dense TiSiN films with good mechanical properties at a much higher pressure than DCMS. The ability of the DOMS discharge to overcome pressure effects lies in the high ionization fraction of sputtered materials. Another interesting feature of the present work is that at low peak power we were able to deposit TiSiN films with similar properties of TiSiN films deposited by ionized PVD methods. However, as for other HiPIMS processes, DOMS also brings the dilemma between film properties and deposition rate. DOMS allows the deposition of dense films with high hardnesses and better overall quality than DCMS at the expense of deposition rate which is one of the most important parameters from the technological point of view.

Acknowledgments

This research is sponsored by FEDER funds through the program COMPETE — Programa Operacional Factores de Competitividade — and by national funds through FCT — Fundação para a Ciência e a Tecnologia, under the projects: PTDC/EME-TME/122116/2010, PTDC/EMS-TEC/1805/2012 and PEst-C/EME/UI0285/2013, as well as the grant SFRH/BD/68740/2010.

References

[1] S. Veprek, S. Reiprich, Thin Solid Films 268 (1995) 64–71.
[2] J. Patscheider, T. Zehnder, M. Diserens, Surf. Films Technol. 146 (2001) 201–208.
[3] K.H. Kim, S. Choi, S. Yoon, Surf. Films Technol. 161 (2002) 243–248.
[4] C. Zhang, X. Lu, H. Wang, J. Luo, Y. Shen, K. Li, Appl. Surf. Sci. 252 (2006) 6141–6153.
[5] S.R. Choi, I.-W. Park, S.H. Kim, K.H. Kim, Thin Solid Films 447 (2004) 371–376.
[6] C.-L. Chang, C.-T. Lin, P.-C. Tsai, W.-Y. Ho, D.-Y. Wang, Thin Solid Films 516 (2008) 5324–5329.
[7] F. Fernandes, A. Loureiro, T. Polcar, A. Cavaleiro, Appl. Surf. Sci. 289 (2014) 114–123.
[8] Z. Li, Y. Wu, S. Miyake, J. Vac. Sci. Technol. A 25 (2007) 1524–1528.
[9] Z. Li, S. Miyake, M. Kumagai, H. Saito, Y. Muramatsu, Jpn. J. Appl. Phys. 42 (2003) 7510.
[10] D. Ma, S. Ma, K. Xu, Vacuum 79 (2005) 7–13.
[11] Y. Cheng, T. Browne, B. Heckerman, E. Meletis, Surf. Films Technol. 204 (2010) 2123–2129.
[12] N. Fateh, G. Fontalvo, G. Gassner, C. Mitterer, Wear 262 (2007) 1152–1158.
[13] E. Badisch, G. Fontalvo, M. Stoiber, C. Mitterer, Surf. Films Technol. 163 (2003) 585–590.
[14] E. Lugscheider, O. Knotek, K. Bobzin, S. Bärwulf, Surf. Films Technol. 133 (2000) 362–368.
[15] D. Lewis, S. Creasey, Z. Zhou, J. Forsyth, A. Ehiasarian, P.E. Hovsepian, Q. Luo, W.M. Rainforth, W.-D. Münz, Surf. Films Technol. 177 (2004) 252–259.
[16] K. Kutschej, P. Mayrhofer, M. Kathrein, P. Polcik, C. Mitterer, Surf. Films Technol. 200 (2005) 1731–1737.
[17] P. Mayrhofer, P.E. Hovsepian, C. Mitterer, W.-D. Münz, Surf. Films Technol. 177 (2004) 341–347.
[18] A. Glaser, S. Surnev, F. Netzer, N. Fateh, G. Fontalvo, C. Mitterer, Surf. Sci. 601 (2007) 1153–1159.
[19] M. Nose, Y. Deguchi, T. Mae, E. Honbo, T. Nagae, K. Nogi, Surf. Films Technol. 174 (2003) 261–265.
[20] Y. Zhang, Y. Yang, Y. Zhai, P. Zhang, Appl. Surf. Sci. 258 (2012) 6897–6901.
[21] V. Kouznetsov, K. Macák, J.M. Schneider, U. Helmersson, I. Petrov, Surf. Films Technol. 122 (1999) 290–293.
[22] U. Helmersson, M. Lattemann, J. Bohlmark, A.P. Ehiasarian, J.T. Gudmundsson, Thin Solid Films 513 (2006) 1–24.
[23] D. Lundin, K. Sarakinos, J. Mater. Res. 27 (2012) 780–792.
[24] J. Lin, W.D. Sproul, J.J. Moore, Z. Wu, S. Lee, R. Chistyakov, B. Abraham, JOM 63 (2011) 48–58.
[25] J. Lin, J.J. Moore, W.D. Sproul, B. Mishra, Z. Wu, Thin Solid Films 518 (2009) 1566–1570.
[26] J. Lin, J. Moore, W. Sproul, B. Mishra, J. Rees, Z. Wu, R. Chistyakov, B. Abraham, Surf. Films Technol. 203 (2009) 3676–3685.
[27] M. Arab Pour Yazdi, F. Lomello, J. Wang, F. Sanchette, Z. Dong, T. White, Y. Wouters, F. Schuster, A. Billard, Vacuum 109 (2014) 43–51.
[28] J. Lin, B. Wang, W.D. Sproul, Y. Ou, I. Dahan, J. Phys. D. Appl. Phys. 46 (2013) 084008.
[29] J. Lin, W.D. Sproul, R. Wei, R. Chistyakov, Surf. Coat. Technol. 258 (2014) 1212–1222.
[30] F. Ferreira, R. Serra, J.C. Oliveira, A. Cavaleiro, Surf. Coat. Technol. 258 (2014) 249–256.
[31] D. Christie, J. Vac. Sci. Technol. A 23 (2005) 330–335.
[32] J. Emmerlich, S. Mráz, R. Snyders, K. Jiang, J.M. Schneider, Vacuum 82 (2008) 867–870.
[33] J. Ziegler, SRIM 1 (1995) 1.
[34] G. Abadias, W. Leroy, S. Mahieu, D. Depla, J. Phys. D. Appl. Phys. 46 (2013) 055301.
[35] L. Hultman, J.-E. Sundgren, J. Greene, D. Bergstrom, I. Petrov, J. Appl. Phys. 78 (1995) 5395–5403.
[36] P. Patsalas, C. Gravalidis, S. Logothetidis, J. Appl. Phys. 96 (2004) 6234–6246.
[37] M. Lattemann, U. Helmersson, J. Greene, Thin Solid Films 518 (2010) 5978–5980.
[38] C.-L. Chang, S.-G. Shih, P.-H. Chen, W.-C. Chen, C.-T. Ho, W.-Y. Wu, Surf. Coat. Technol. 259 (2014) 232–237.
[39] D. Jaeger, J. Patscheider, J. Electron Spectrosc. Relat. Phenom. 185 (2012) 523–534.
[40] Y. Cheng, T. Browne, B. Heckerman, P. Gannon, J. Jiang, E. Meletis, C. Bowman, V. Gorokhovsky, J. Phys. D. Appl. Phys. 42 (2009) 125415.
[41] H.C. Barshilia, B. Deepthi, A. Arun Prabhu, K. Rajam, Surf. Films Technol. 201 (2006) 329–337.
[42] A. Ehiasarian, A. Vetushka, Y.A. Gonzalvo, G. Sáfrán, L. Székely, P. Barna, J. Appl. Phys. 109 (2011) 104314.
[43] D. Gall, S. Kodambaka, M. Wall, I. Petrov, J. Greene, J. Appl. Phys. 93 (2003) 9086–9094.
[44] H. Windischmann, Crit. Rev. Solid State Mater. Sci. 17 (1992) 547–596.
[45] X. Ma, C. Li, W. Zhang, J. Alloys Compd. 394 (2005) 138–147.
[46] J. Houska, J. Klemberg-Sapieha, L. Martinu, Surf. Films Technol. 203 (2009) 3348–3355.
[47] F. Vaz, L. Rebouta, S. Ramos, M. da Silva, J. Soares, Surf. Films Technol. 108 (1998) 236–240.
[48] F. Vaz, L. Rebouta, B. Almeida, P. Goudeau, J. Pacaud, J. Riviere, J. Bessa e Sousa, Surf. Films Technol. 120 (1999) 166–172.
[49] V. Chawla, R. Jayaganthan, R. Chandra, Surf. Films Technol. 204 (2010) 1582–1589.
[50] X.Z. Ding, X.T. Zeng, Y.C. Liu, Q. Yang, L.R. Zhao, J. Vac. Sci. Technol. A Vac. Surf. Films 22 (2004) 2351–2355.
[51] Z. Li, M. Mori, S. Miyake, M. Kumagai, H. Saito, Y. Muramatsu, Surf. Films Technol. 193 (2005) 345–349.
[52] Y. Pei, C. Chen, K. Shaha, J.T.M. De Hosson, J. Bradley, S. Voronin, M. Čada, Acta Mater. 56 (2008) 696–709.

ANNEX E

F. Ferreira, R. Serra, A. Cavaleiro, and J. Oliveira, "Additional control of bombardment by deep oscillation magnetron sputtering: Effect on the microstructure and topography of Cr thin films," Thin Solid Films, vol. 619, pp. 250-260, 2016.

Thin Solid Films 619 (2016) 250–260

Contents lists available at ScienceDirect

Thin Solid Films

journal homepage: www.elsevier.com/locate/tsf

Additional control of bombardment by deep oscillation magnetron sputtering: Effect on the microstructure and topography of Cr thin films

F. Ferreira *, R. Serra, A. Cavaleiro, J.C. Oliveira

SEG-CEMUC, Mechanical Engineering Department, University of Coimbra, Polo II, Rua Luís Reis Santos, 3030-788 Coimbra, Portugal

ARTICLE INFO

Article history:
Received 8 June 2016
Received in revised form 18 October 2016
Accepted 27 October 2016
Available online 28 October 2016

Keywords:
Cr films
HiPIMS
Surface topography
AFM
Mounted surface

ABSTRACT

In magnetron sputtering additional control of the bombarding species can be obtained by ionizing the sputtered flux as in high power impulse magnetron sputtering (HIPIMS). The main objective of this work is to evaluate the effectiveness of the additional control of bombardment in Deep Oscillations Magnetron Sputtering (DOMS), a variant of HIPIMS. For this purpose, Cr thin films were deposited by d. c. Magnetron Sputtering (DCMS), with and without substrate biasing, and by DOMS between 0.2 and 1.0 Pa. The microstructure and topography of the deposited films were characterized by SEM and AFM. It was found that the shadowing effect is the dominant film formation mechanism in DCMS and that it is stronger along the substrate rotation direction, resulting in anisotropic surfaces. The DOMS process allows to overcome the shadowing effect by decreasing the strength of the shadowing effect rather than by decreasing its effectiveness, as is usually the case in magnetron sputtering when using high energetic bombardment. It also allows to minimize the effect of geometrical asymmetries of the deposition system in the films properties, which is of paramount technological importance as large substrate batches with several rotation degrees are usually processed in industrial conditions.

© 2016 Elsevier B.V. All rights reserved.

1. Introduction

The so-called dynamic roughening of a growing thin film surface is often observed in magnetron sputtering [1,2]. After an initial "crystalline" roughening due to island formation and coalescence, roughening of the growing film surface proceeds mainly due to the shadowing effect [3,4]. Particles that approach the surface at oblique angles are captured by higher surface points (hills) leading to the formation of rougher surfaces and columnar microstructures. On the other hand, several mechanisms, such as ion-induced surface sputtering (re-sputtering) [5] and surface down-hill mass transport [6], can contribute to surface smoothening by redistributing the incoming flux of particles and filling shadowed region and thus counterbalance or even overcome the shadowing effect. Ultimately, the competition between roughening and smoothening effects will dictate both the final surface morphology evolution with time and, thus, the microstructure of a thin film.

In magnetron sputtering, the strength of the shadowing effect is primarily set by the geometry of the deposition system. At lower pressures, the sputtered particles travel to the substrate following mostly straight paths (line of sight) and, thus, the strength of the shadowing effect is related to the angle between the lines connecting the racetrack points to the substrate and the substrate normal. Increasing this angle by, for example, decreasing the substrate to target distance or using bigger targets strengthens the shadowing effect and vices-versa. As the deposition geometry is usually set by the physical dimensions of the deposition system, the ability to tailor the surface roughness and microstructure of a thin film depends on the effective control of the properties of the bombarding species: flux, average energy and impinging angle distribution. Increasing the deposition pressure increases the gas phase collisions and therefore, the low angle component of the angle distribution of the impinging species becomes stronger, i.e., the shadowing effect is enhanced [7–9]. Bombarding the growing surface with energetic sputtered atoms, or argon ions extracted from the plasma (substrate biasing), are commonly used methods to activate the smoothening mechanisms [8,10] and thus counterbalance the shadowing effect.

Additional control of the bombarding species can be obtained by ionizing the sputtered flux. When the deposited species consist of more ions than neutral the process is referred as ionized physical vapour deposition (IPVD) [11,12]. The ions can be controlled with respect to their energy and impinging direction and, thus, the control of films properties is improved. However, in most cases additional components have to be used in the deposition system which increases the system complexity and limits the industrial applications of IPVD. A high degree of ionization of the sputtered species can be achieved by applying short pulses with extremely high power densities to the target at low duty cycle (<10%). This deposition method, known as High-power Impulse Magnetron Sputtering (HiPIMS) [13–15], allows to achieve higher plasma densities and the consequent ionization of the sputtered material by

* Corresponding author.
E-mail address: fabio.ferreira@dem.uc.pt (F. Ferreira).

http://dx.doi.org/10.1016/j.tsf.2016.10.054
0040-6090/© 2016 Elsevier B.V. All rights reserved.

electron impact, without the need for additional components in the deposition system. Recently, a new design of the modulated pulse power magnetron sputtering (MPPMS) process named deep oscillation magnetron sputtering (DOMS) was developed [16–19]. This process uses large voltage oscillation packets in long modulated pulses for achieving high peak target currents and voltages. Such configuration has been reported to allow virtually arc-free depositions for reactive deposition of insulating films.

This work is the first part of a study aiming at evaluating the effectiveness of the DOMS technology as a tool to improve the control of the bombarding species during magnetron sputtering. Chromium was selected as a model material since, (i) it has a high melting point resulting in low values of the ratio between substrate and melting temperature (T_s/T_m) in magnetron sputtering without intentional substrate heating [20] and (ii) it has a low mobility which helps to preserve growing history and to expose the effects of substrate bombardment. On the other hand, Cr has a mass close to argon (52 and 40 a.m.u, respectively) which minimizes the influence of the neutralized Ar ions reflected at the target surface on the film formation [21]. Finally, HIPIMS discharges with a Cr target allow a high ionization degree of the sputtered species which helps controlling the direction of the species impinging on the substrate [22]. The main objective of this work is to evaluate the effectiveness of the additional control of bombardment in DOMS to shape the microstructure and surface topography of Cr thin films deposited in the pressure range from 0.2 to 1.0 Pa. In a companion paper, the effects of bombardment on the structural and mechanical properties of the Cr films will be reported.

2. Material and methods

2.1. Film deposition

The Cr films were deposited by d. c. Magnetron Sputtering (DCMS) and DOMS in a pure Ar discharge gas generated with a planar square Cr target (99.99%), with 150 × 150 × 10 mm. A base pressure lower than 9×10^{-4} Pa was achieved before all depositions. Si (100) wafers cleaned in acetone and alcohol ultrasonic baths were used as substrates. The substrate-to-target distance was 80 mm and the substrate rotation was kept at 23.5 rpm. In the following text, the direction on the film surface parallel to the rotation axis is labelled as Y while the rotation direction, which is perpendicular to the Y direction, is labelled as X direction. All the Cr films were deposited with a constant time averaged power in order to minimize temperatures variations during film growth.

Two series of Cr films were deposited by d.c. Magnetron Sputtering (DCMS) using a Hüttinger PFG 7500 DC power supply. In both series, the pressure was varied from 0.2 to 1.0 Pa while the substrates were kept at floating voltage (DCMS serie) or at −80 V (DCMS + bias serie). The deposition conditions used for the DCMS depositions and the thickness of the deposited films are shown in Table 1.

All the HIPIMS Cr films were deposited in DOMS mode using a Cyprium™ III plasma generator (Zpulser Inc.). Examples of the discharge voltage and current wave forms used in this study are shown in Fig. 1. Each DOMS pulse consists of a packet of single oscillations. The voltage and current gradually increase to their maximum value (V_p and I_p) during the voltage on-time (t_{on}), and then gradually decay, reaching zero before the end of the oscillations period (T).

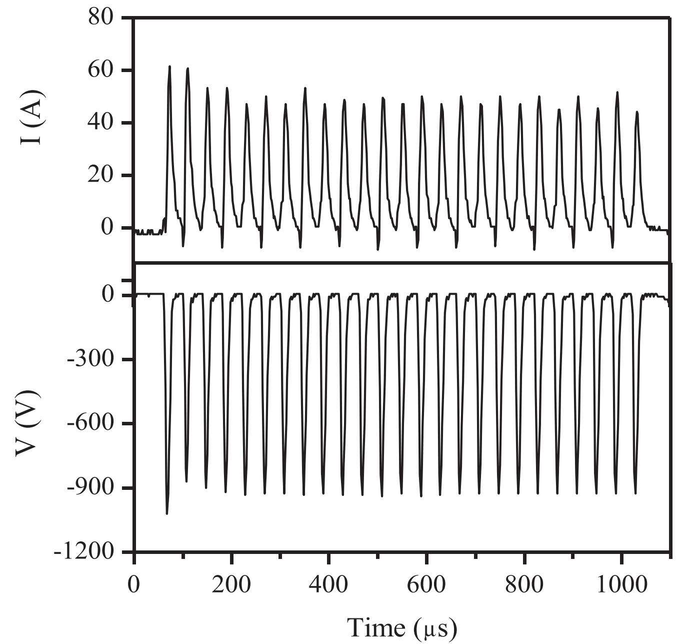

Fig. 1. Typical I-V waveforms of a DOMS pulse with DC_{int} = 300 V (P = 0.8 Pa; DC_{int} = 300 V; F = 217 Hz; D = 1000 μs; t_{on} = 6 μs; T = 40 μs).

The DOMS power supply is powered by an internal d.c. power supply. Two series of depositions were carried out in DOMS mode. First Cr films were deposited with a low Peak power (P_p) values (low P_p films series) by applying a voltage of 300 V to the internal DC power supply of the Cyprium plasma generator. Then depositions at higher peak power were carried out by using a voltage of 400 V (high P_p series). In both cases, the deposition pressure was varied between 0.2 and 1 Pa. The peak voltage (V_p) and peak current (I_p) were calculated as the average value of the maximums of the voltage and current in each oscillation, respectively, taking into account all the oscillations. All the films deposited by HiPIMS DOMS were deposited with floating substrate potential. The parameters t_{on} and T were kept constant for all DOMS depositions at 6 and 40 μs, respectively. The pulse duration (D) was also kept constant (1000 μs) while the pulse frequency (F) was automatically adjusted by the DOMS power supply software in order to keep a constant average power (P_a). The main DOMS deposition conditions are summarized in Table 2.

2.2. Film characterization

The thickness and morphology of the films were studied by scanning electron microscopy (SEM) using a Quanta 400FEG ESEM. The thickness

Table 1
Depositions conditions and thickness of the Cr thin films deposited by DCMS (Pa = 1.2 kW).

	DCMS			DCMS + Bias (−80 V)		
Deposition pressure (Pa)	V (V)	I (A)	Thickness (nm)	V (V)	I (A)	Thickness (nm)
0.2	427	2.9	770	427	2.9	800
0.4	412	3.0	850	412	3.0	870
0.6	400	3.1	950	400	3.1	900
0.8	378	3.4	1080	370	3.4	1030
1.0	355	3.5	1300	361	3.5	1280

Table 2
Deposition conditions and thickness of the Cr thin films deposited by DOMS (Pa = 1.2 kW; D = 1000 μs; t_{on} = 6 μs; T = 40 μs).

Regime	Pressure (Pa)	V_p (V)	I_p (A)	P_p (kW)	F_i (Hz)	Thickness (nm)
Low P_p (DC_{int} = 300 V)	0.2	1058	33	22	236	1000
	0.4	1006	38	28	217	1040
	0.6	945	43	30	217	1030
	0.8	916	50	35	220	890
	1.0	899	56	38	216	1110
High P_p (DC_{int} = 400 V)	0.2	1384	65	55	124	870
	0.4	1290	69	64	118	840
	0.6	1241	77	70	119	780
	0.8	1164	88	77	117	780
	1.0	1183	92	83	116	810

of the films was also confirmed with a stylus profilometer (MAHR Perthometer S4P). Several surface and cross-section micrographs of each film were acquired at similar amplifications. The films surface topography was characterized by AFM (Bruker Innova) with a Si tip of nominal 6 nm radius used in contact mode. Several 2 × 2 μm scans were acquired on the surface of each film to ensure surface representation. The Height-Height correlation functions (HHCFs), H(r), in the X and Y directions and the 2D auto-correlation function were calculated from the AFM scans using the Gwyddion [23,24] software (version 2.40) after leveling the surface. The HHCFs along the X and Y directions were calculated from different AFM scans in such a way that the fast scan axis was always aligned with the corresponding direction. For selected DCMS and DOMS films, the HHCFs were also calculated from scans after rotation by 45 and −45° with respect to the X direction. In all cases similar HHCFs were obtained allowing to confirm the surface orientation. The local slopes (m_x and m_y) [25] and the correlation lengths (ξx and ξy) [25] were calculated from the HHCFs in the corresponding directions. The methodology proposed by Bubendorff et al. [26] was used to extract the mean distance between adjacent surface features (D_x). For the surfaces exhibiting an oscillatory behavior in the cross-section of the 2D autocorrelation function along the X direction, D_x was taken as the wavelength of the oscillations.

2.3. Process simulation

The interaction of the Ar^+ plasma ions with the Cr target was modeled using the SRIM 2013 software package [27] in surface sputtering mode. The energy of the incident ions was set to be equal to the experimental target deposition voltage times the electronic charge. The impact of 10^6 argon ions was computed in each simulation. The computations provided a final list with the energy and direction of both backscattered (Ar) and sputtered (Cr) species leaving the target. The sputtering yield was computed from the ratio of impinging ions and sputtered atoms while the fraction of backscattered atoms in the sputtered flux was computed from the number of sputtered and backscattered atoms. Both the average energies and median energies were calculated from the output results of SRIM for each simulation.

The interaction of the sputtered species with the discharge gas along their path to the substrate were computed using the SIMTRA (version 2008(1)) software package [28]. Only neutral Ar was considered as buffer gas and gas heating was taken into account. The physical dimensions of the deposition system used in this work (chamber size and shape, target size and shape, substrate size and shape, target to substrate distance…) were inputted in the SIMTRA software in order to model the deposition process as close as possible. The initial energies and angles of the sputtered Cr atoms were taken from the results of the SRIM software. The average energy, median energy and fraction of thermalized atoms arriving at the substrate were calculated from the SIMTRA results.

3. Results

3.1. Simulation results

In order to estimate the energy and degree of thermalization of the Cr species arriving at the substrate during film growth by DCMS, a two-step simulation process was carried out. First the interactions of the Ar ions bombarding the target was simulated using the SRIM free software package. Then the transport of the sputtered flux trough the gas phase was simulated using the SIMTRA software package. The results of the DCMS process simulation are shown in Table 3. The sputtering yield (SY) increases as the pressure is decreased, i.e., it increases with increasing deposition voltage. The SY values (between 1.08 and 1.25) agree well with values published in the literature for similar energies of the impinging ions [29–30]. As the mass of Ar and Cr are similar, the number of Ar backscattered atoms is small and they only account for between 3.2 and 3.9% of the total number of species leaving

Table 3
Simulation results of Cr deposition by DCMS (deposition pressure (P) and voltage (V), fraction of backscattered Ar (B_{Ar}), sputter yield (SY), average energy Cr (E_{av}^{tar}) and median energy (E_{med}^{tar}) of the sputtered Cr leaving the target, average energy (E_{av}^{sub}) and median energy (E_{med}^{sub}) of sputtered Cr arriving at the substrate, fraction of thermalized Cr).

Deposition		Target				Substrate		
P (Pa)	V (V)	B_{Ar} (%)	SY	E_{av}^{tar} (eV)	E_{med}^{tar} (eV)	E_{av}^{sub} (eV)	E_{med}^{sub} (eV)	Therm. (%)
0.2	427	3.1	1.25	19.6	6.9	15.6	4.9	2.5
0.4	412	3.2	1.22	19.4	6.9	13.4	3.2	8.7
0.6	400	3.4	1.19	19.2	7.0	11.5	1.9	18.5
0.8	378	3.6	1.15	19.0	7.0	9.8	0.9	29.2
1	345	3.9	1.08	18.4	7.0	8.1	0.3	40.6

the target. The fraction of backscattered atoms is too small to significantly influence the properties of the deposited films and their effect on film growth will be discarded in the remaining discussion. The average energy of the sputtered atoms leaving the target increases with decreasing pressure as the deposition voltage increases. However, decreasing the pressure from 1.0 to 0.2 Pa only brings about a small variation of the average energy (close to 6%) while it has almost no effect on the median energy which remains close to 7 eV. Bombarding the target with higher energy Ar ions results mainly in more low-energy interactions with the target atoms rather than more energy transfer in each interaction. Therefore, a significant part of the additional energy contributes to the sputtering yield rather than to increase the energy of the sputtered atoms.

As expected, the energy of the sputtered species decreases along their path from the target to the substrate. At 0.2 Pa, the average energy decreases by 20% while at 1.0 Pa the loss is close to 50%. As a result, the average energy of Cr atoms arriving at the substrate is almost double at low pressure (15.6 eV) than at high pressure (8.1 eV). The higher loss of energy at 1.0 Pa is even more evidenced by the median energy which is 20 times higher at low pressure (4.9 eV) than at high pressure (0.28 eV). Finally, the fraction of thermalized Cr atoms arriving at the substrate increases from 2.5% at 0.2 Pa to 40.6% at 1.0 Pa.

The energy distribution of the sputtered Cr atoms leaving the target obtained with the SRIM simulations showed the presence of atoms with unrealistically high energies. The maximum energy of the a sputtered atom (E_{max}) is typically defined as $E_{max} = k\Lambda E_0 - U_s$ [31].

The K factor accounts for the fact that at normal incidence no Cr atoms can be sputtered by a head-on collision directly without further collisions, Λ is the maximum energy fraction loss for a head-on collision, E_0 is the energy of the bombarding Ar ions and U_s is the surface binding energy. For Cr under bombardment of Ar ions with $E_0 = 400$ eV and using $k = 0.4$ [31], $\Lambda = 0.983$ and $U_s = 4.12$ eV [32] a value of $E_{max} =$ 153 eV is obtained. However, sputtered Cr atoms with energy up to 365 eV were found in the SRIM simulation. The energy distribution of sputtered atoms follows a Thomson distribution which is asymmetric and has a high energy tail. As a result, the average energy is highly sensitive to the energies of the atoms in the tail and it significantly increases if a few additional sputtered high energy atoms are added. Note that the average energy is not the energy value that divides the distribution in two sets with equal number of atoms, as could be intuitively expected. In an asymmetric distribution, the energy that divides the atoms in two sets with equal number of atoms is the median energy. The median energy is thus much less sensitive to the presence of high energy particles. The median energy values in Table 3 are more realistic than the average energy value as the vast majority of sputtered atoms should leave the target with only a few eVs and most of them should be thermalized before arriving at the substrate at 1.0 Pa [31]. In the following text, the median energy is used to characterize the energy of the sputtered atoms unless otherwise stated.

The energy of the sputtered Cr atoms arriving at the substrate lies between 0.28 and 4.9 eV depending on the deposition pressure. The Cr atoms impinging on the surface may contribute to trigger local

smoothing mechanisms, such has surface diffusion, but their energy is well below the threshold to activate non-local smoothing mechanisms that could efficiently counterbalance the shadowing effect.

The peak voltage of the DOMS oscillations is much higher than the discharge voltage in DCMS (Tables 1 and 2). Even the average deposition voltage within each oscillation, which is more representative of the actual acceleration of the Ar ions, is higher than the DCMS voltage. A series of simulations were carried out using the average voltage within each oscillation to estimate the influence of the higher deposition voltages in DOMS (Table 4). These are not realistic simulations, as they do not simulate any actual deposition process. For example neither the back attraction of the ionized Cr atoms nor their acceleration in the substrate self-bias are taken into account. As can be concluded by comparing Tables 3 and 4, the higher deposition voltages involved in DOMS have almost no influence on the median energies of the sputtered Cr atoms independently of the peak power and deposition pressure. In fact, similar simulations computed using Vp instead of the average voltage of the oscillations resulted in similar conclusions. Considering that the energy of the sputtered Cr is maintained upon ionization by electron impact, the resulting Cr ions arrive at the substrate with an energy similar to the Cr atoms. However, unlike neutral atoms, the Cr ions are accelerated in the substrate self-bias and thus gain some energy. Typically, the plasma potential in an HIPIMS discharge is only a few eVs. For example, Leibig et al. [33] found that, for an MPPMS discharge with a chromium target at 0.53 Pa of Ar, the steady state plasma potential was 4.48 and 4.05 eV for the first and second step of excitation. The authors also found that the steady state floating potential, which is displaced from the plasma potential in proportion to the electron temperature, was close to 12 eV in both excitation steps of the MPPMS pulse. Even at lower pressure, the energy gain by the Cr ions upon acceleration by the substrate self-bias is then most likely higher than their median energy after traveling through the discharge gas.

3.2. Cr films microstructure (SEM)

The Cr film deposited by DCMS at 1.0 Pa has a well-developed columnar morphology with V-shaped columns extending from the substrate to the top of the film (Fig. 2a). The columns are separated by large channels of voids resulting in a saw-like pattern on the top of the film cross-section. This type of open columnar morphology is caused by the limited surface diffusion due to relatively low temperatures ($T/T_m \leq 0.15$) and low bombardment intensity during film growth. The pronounced V-shape of the columnar grains results from competitive growth, where grains with less preferable orientation are overgrown by grains with higher flux collection rate (shadowing effect). As a result, some of the columns end up before the top of the film and the smaller column tops in Fig. 2a correspond to columns that are about to be overcome. Most of the wider columns on the film surface end up with well-faceted three sided pyramidal-like shapes, although some are almost regular while others are clearly elongated along the Y direction. On the overall the surface morphology is anisotropic since most of the voids channels are preferentially oriented along the same direction.

The Cr film deposited at 0.8 Pa also has a columnar microstructure although with smaller columns than at higher pressure (Fig. 2b). Most

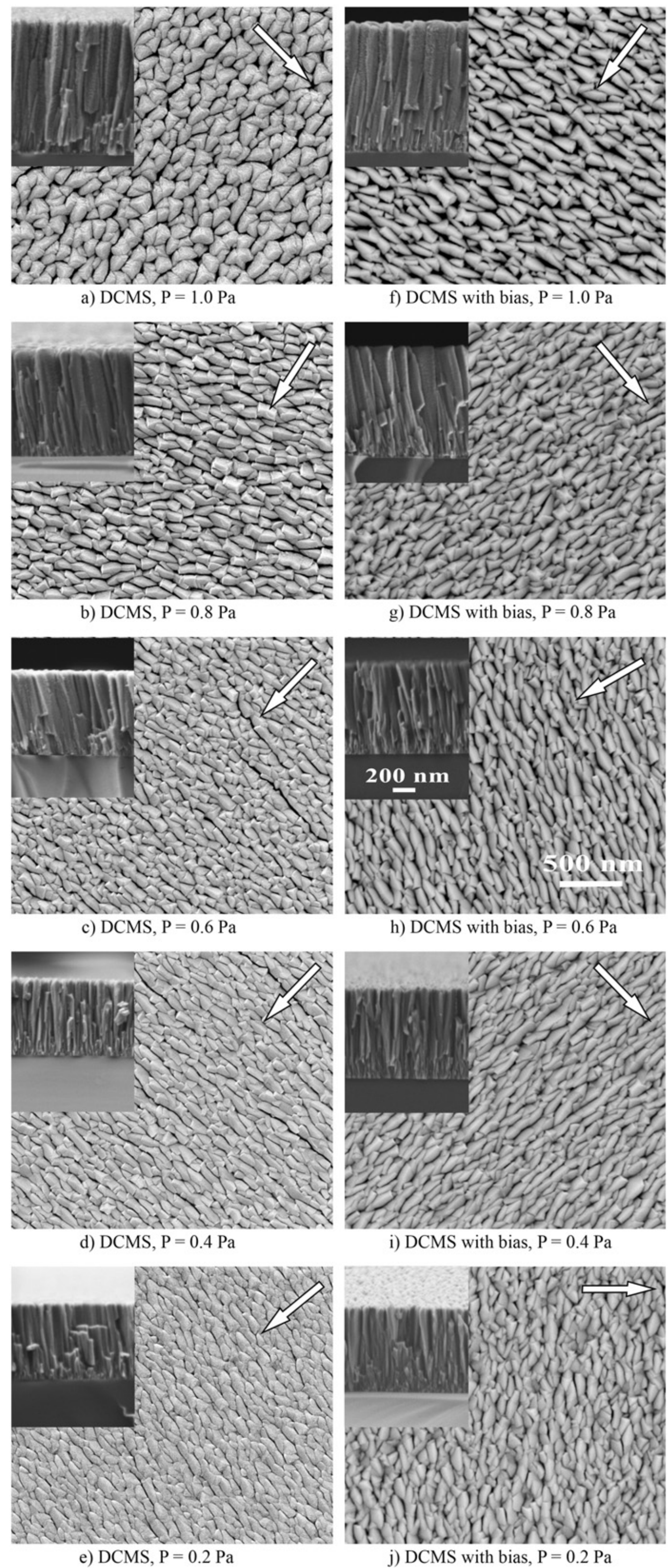

Fig. 2. SEM surface and cross-section micrographs (inset) of the Cr films deposited by DCMS with and without bias as a function of deposition pressure. The arrow approximately indicates the substrate rotation direction (X direction). Scales in panel h are valid for all the figures.

of the columns also have three-sided pyramidal-like tops although two of the sides are considerably elongated along the direction perpendicular to substrate rotation (Y direction). The columns tops are interconnected along the vertical direction (Y direction) while they are

Table 4
Results of the simulation using DOMS average voltage: Deposition pressure (P) and Voltage (V), Sputter Yield (SY), average energy of sputtered Cr (E_{av}), median energy of the sputtered Cr (E_{med}) and fraction of thermalized Cr.

	Deposition		Target		Substrate	
Process	P (Pa)	V (V)	SY	E^{tar}_{med} (eV)	E^{sub}_{med} (eV)	Therm. (%)
Low P_p	0.8	476	1.35	6.91	0.88	29.1
Low P_p	0.4	506	1.40	6.90	3.24	8.7
High P_p	0.8	567	1.51	6.90	0.85	29.4
High P_p	0.4	728	1.77	6.95	3.32	8.8

separated by large voids along the rotation direction. The surface morphology is highly anisotropic and may be described as ridges of columns separated by deep valleys of continuous voids oriented along the Y direction. The Cr films deposited at lower pressures also have a columnar microstructure and an anisotropic surface morphology (Fig. 2c to e). However, the width of the columns and the size of the pyramid-like tops decreases with decreasing pressure, shallower and thinner valleys and ridges are formed and denser films are deposited. The Cr film deposited at 0.2 Pa has the densest microstructure with smaller and tightly packed columns and almost no inter-columnar voids. The columns tops are less faceted with rounded borders, revealing the effect of bombardment during deposition.

All the Cr films deposited by DCMS with bias have a columnar structure as revealed by the cross-section micrographs in Fig. 2f to j. The column size decreases with decreasing pressure as was found for the films deposited without bias. The columns tops consist of highly distorted and faceted three-sided pyramidal-like shapes preferentially elongated along the Y direction. The column tops are also aligned along the Y direction, forming a pattern of ridges and valleys of voids as was observed for the films deposited by DCMS without bias. Decreasing the deposition pressure reduces the size of the inter-columnar voids although the morphology of the surface features and the size of the columns remains mostly the same. On the overall the microstructure of the Cr films deposited with bias is similar to the microstructure of the films deposited without bias at an immediately lower pressure. Bombarding the substrate with Ar ions results in slightly thinner columns separated by thinner valleys of voids although the columns geometrical anisotropy while the overall anisotropy of the surface remains mostly unchanged.

The Cr films deposited by DOMS at low P_p and high pressure (0.8 and 1 Pa) have a columnar microstructure with faceted three-sided pyramided-like column tops preferentially elongated along the Y direction on their surface (Fig. 3a and b). The surface morphology is anisotropic and similar to the one observed for the films deposited by DCMS at the same pressures. However, the size of the columns and corresponding pyramid-like tops are much smaller. In fact, the surface of both films is comparable to the surface of the films deposited by DCMS at lower pressures (0.2 and 0.4 Pa). The Cr film deposited by DOMS at low P_p and 0.6 Pa also has a columnar microstructure (Fig. 3c). However, its surface morphology is quite different from all the previous films, consisting of fine equiaxed features instead of faceted pyramid-like shapes. The features are randomly distributed and the resulting surface morphology is almost isotropic. Columnar films with equiaxed surface features are also deposited at low P_p and 0.2 and 0.4 Pa (Fig. 3d and e). However, the surface features are much more rounded resulting in an almost isotropic globular surface morphology. On the other hand, the size of both the columns and globular features is higher than at 0.6 Pa and increases with decreasing pressure. Although some remains of columnar growth are still detected in the cross-section micrographs of the films deposited by DOMS at high Pp, well defined columns extending from the substrate to the top of the film are no longer observed. Instead, the films cross-section is much more dense and irregular than in the previous films, similar to the ones found by Ferrec et al. [34] for Cr films also deposited by HIPIMS (Fig. 3f to i). The surface of the films is isotropic and consists of fine and highly compacted features, without clear borders.

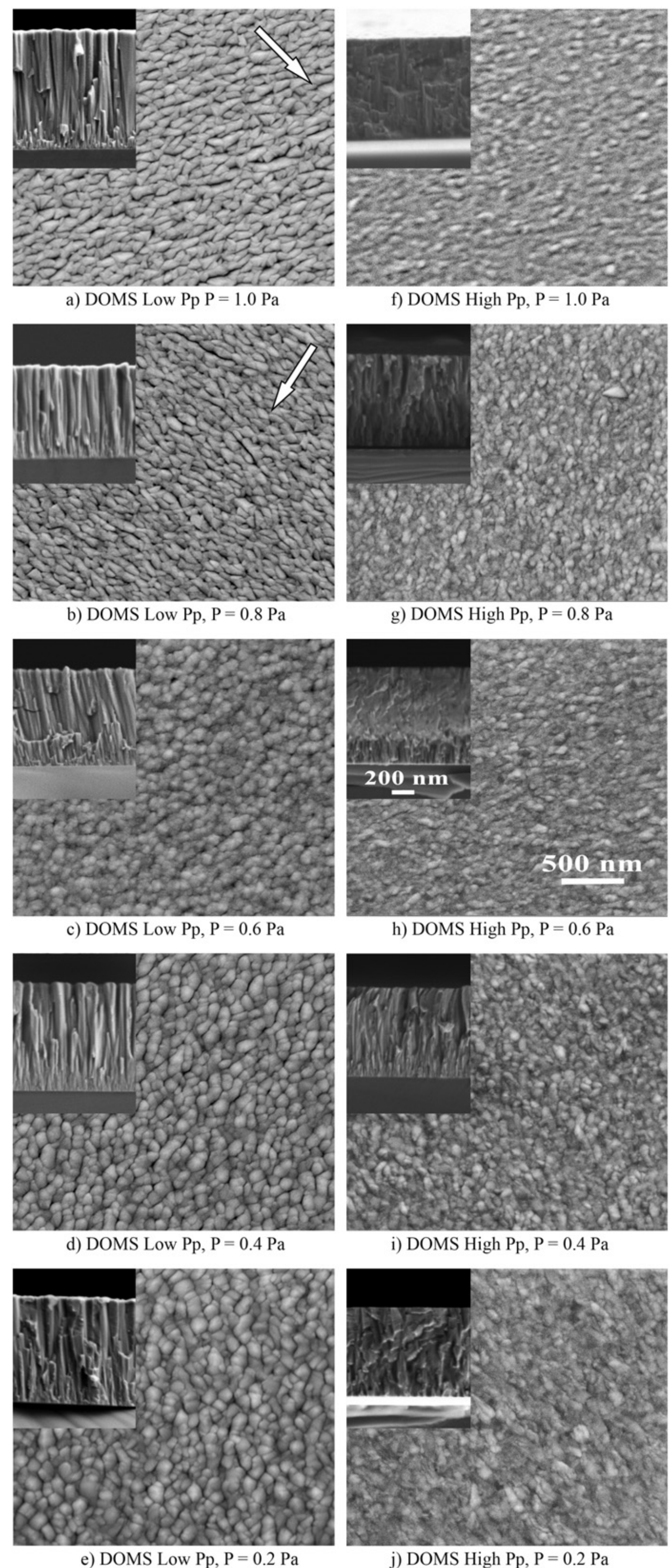

Fig. 3. SEM surface and cross-section micrographs of the Cr films deposited by DOMS at low and high P_p as a function of deposition pressure. The arrow approximately indicates the substrate rotation direction (X direction). Scales in panel h are valid for all the figures.

3.3. Surface topography (AFM)

AFM scans of some of the thin film surfaces obtained in this work are shown in Fig. 4. The same scale was use for the Z axis and, although the maximum value labelled in each scan is different, the height of the surface features can be compared by direct comparison of the scans. Decreasing the deposition pressure in DCMS significantly decreases the height of the surface features (Fig. 4a and b) while applying a bias only has a small effect on the surface morphology (Fig. 4b and c). On the other hand, the film deposited by DOMS show a much more isotropic surface morphology with rounded features and lower roughness (Fig. 4d to f). The height of the surface features is smaller at high P_p than at low P_p power, while finer surface features are developed (Fig. 4d and f). On the overall the AFM scans are in very good agreement with the SEM micrographs presented in Section 3.2.

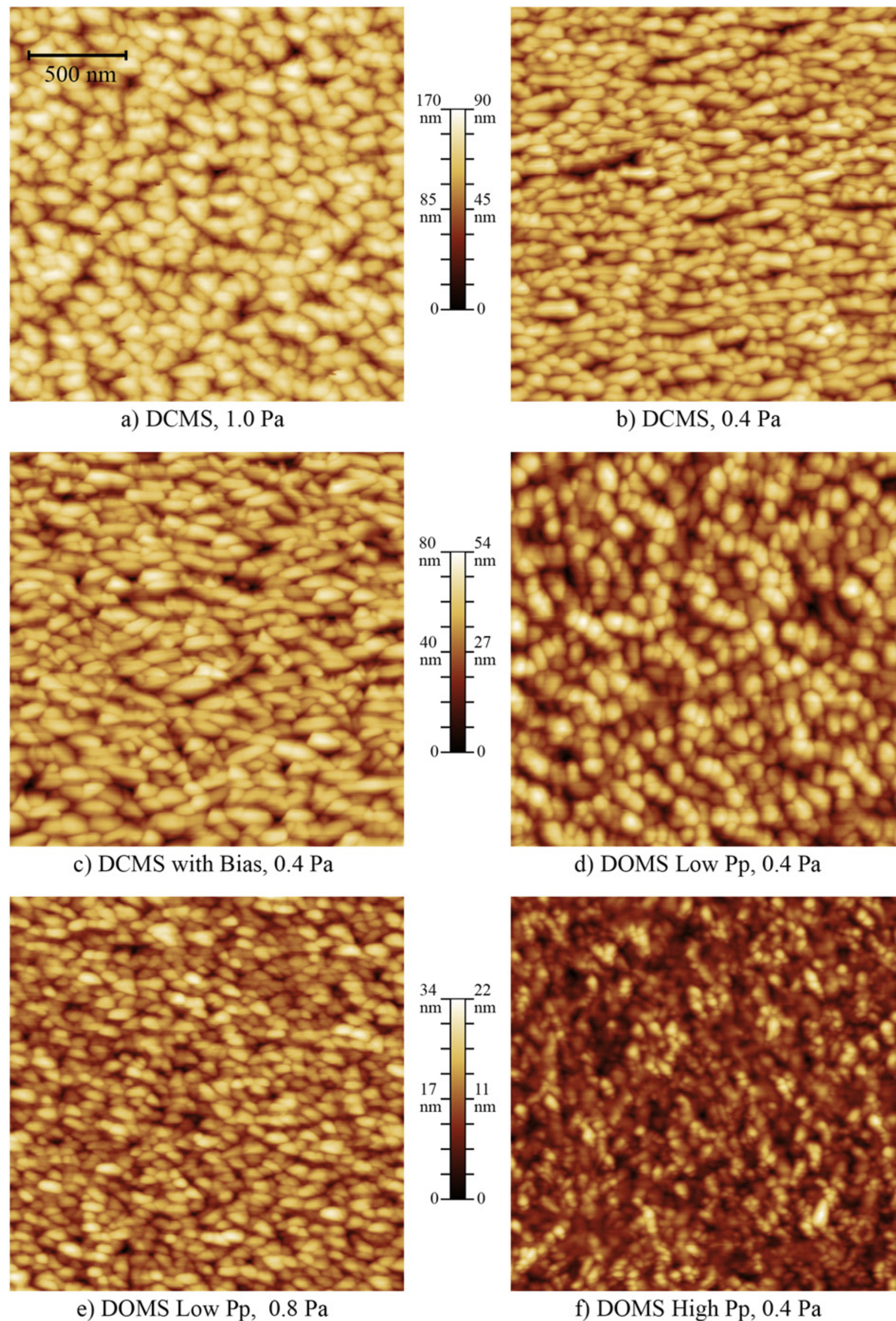

Fig. 4. Representative AFM scans (2 × 2 μm) showing the surface morphology of Cr thin films deposited by DCMS and DOMS.

The surface roughness (Ra) calculated from the AFM scans is shown in Fig. 5 as a function of the deposition pressure. The surface roughness of the films deposited by DCMS with and without bias increases significantly with increasing pressure. This is consistent with the formation of deeper grooves and higher hills on the films surface, as observed by SEM, due to the increasing strength of the shadowing effect. Bombarding the growing film with argons ions extracted from the plasma and accelerated at −80 V only has a small influence on the surface roughness, excepting for the films deposited at 1.0 Pa. The surface roughness of the films deposited by DOMS is much lower and much less influenced by the deposition pressure than that of the films deposited by DCMS. This is more evident at high deposition pressures, showing that the shadowing effect is effectively counterbalanced and/or prevented both at low and high P_p. On the other hand increasing the peak power decrease the surface roughness at all deposition pressures.

In order to quantify and gain a deeper understanding of the evolution of the Cr surface topography, the HHCF was calculated from the AFM scans of a representative set of films along both the X and Y directions. All calculations were performed keeping the AFM fast scan axis aligned with the studied direction. The HHCFs obtained from the AFM surface scans of the films deposited by DCMS are shown in Fig. 6 using double logarithmic and linear scales (in the inset).

The HHCF in both X and Y direction obtained for the film deposited at 0.4 Pa behave as a power-law for small values of r, i.e., a linear behavior in the log-log graph (with slope 2α) is observed in both directions. On the other hand, both functions stabilize at the same value (close to $2w^2$) at higher values of r. At intermediate values of r, the HHCF calculated along the X direction displays an oscillatory behavior before stabilizing which is typical of mounded surfaces [35]. Mounded surfaces possess characteristic length scales and result from growth mechanisms

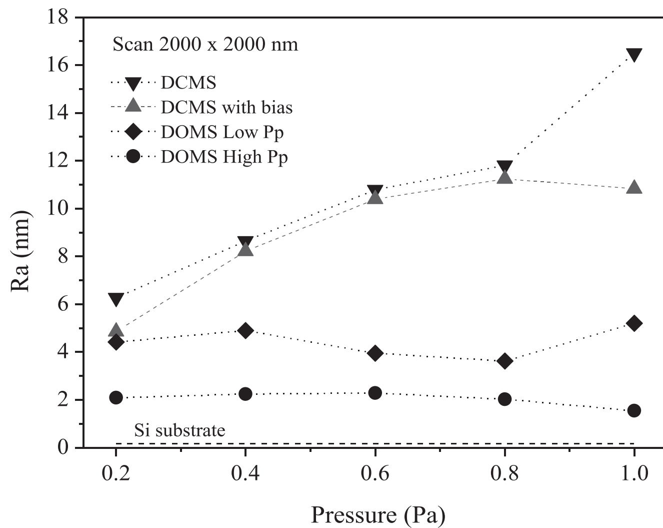

Fig. 5. Surface roughness calculated from the AFM scans of the films deposited by DCMS with and without bias and DOMS at low and high Peak power.

that are characteristically nonlocal in nature. In magnetron sputtering the primary nonlocal growing mechanism is the shadowing effect [5]. The characteristic length scale induces an oscillatory behavior of the HHCF, with exponentially decreasing amplitude, which results in a pronounced "bump" before stabilization at higher values of r. Such "bump" is most clearly seen in the inset of Fig. 2 for the HHCF along the X axis. On the contrary, the HHCF calculated along the Y direction monotonically increases up to its maximum value. The HHCF along the Y direction is similar to that of self-affine surfaces as it does not display an oscillatory behavior at intermediate values of r. These results show that the shadowing effect is effective only along the rotation direction (X).

The HHCFs obtained for the film deposited by DCMS at 0.8 Pa are similar to the ones obtained at lower pressure although shifted to higher values of H. Once again an HHCF typical of a mounded surface is found along the X direction while the HHCF along the Y direction is similar to that of a self-affine surface. Note however than the "bump" in the HHCF along the X direction has a higher amplitude and is shifted to higher values of r than at lower pressure, showing that increasing the pressure increases the effectiveness of the shadowing effect. Further

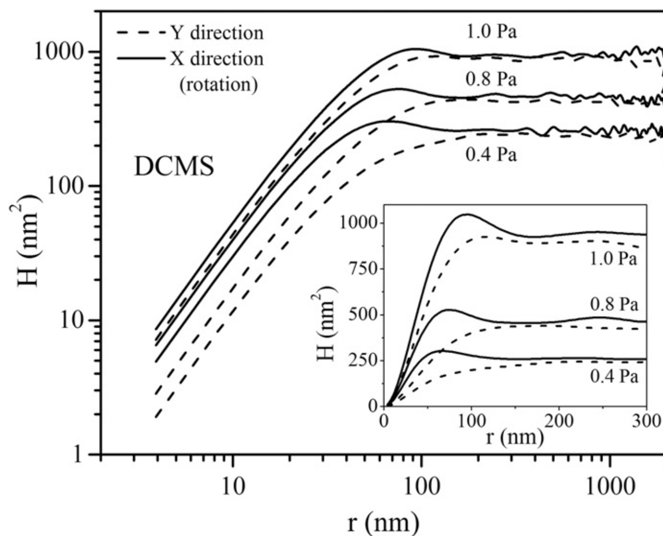

Fig. 6. Double logarithmic representation of the Height-Height correlation functions calculated for the Cr films deposited by DCMS. The HHCFs are represented with linear scales in the inset.

increasing the pressure results in mounded surfaces in both the X and Y directions. The "bump" in the HHCF along the X direction obtained at 1.0 Pa is further shifted to higher r values and also has a higher amplitude than at lower pressures. At 1.0 Pa the shadowing effect is effective along both the X and Y directions although it is more effective along the rotation direction (X).

All the HHCF have similar slopes at low values of r in the double logarithmic representations.

However, the HHCF along the X direction are shifted to higher values of r as compared to the respective HHCF in the Y direction which is a typical characteristic of correlation-length anisotropy [35]. The dissimilar HHCFs in the X and Y direction confirm the surface morphology anisotropy already observed by SEM. All the HHCFs values after stabilization, i.e., at high r values, increase with pressure showing that the interface width (RMS) increases. In all cases, the RMS values agree well with the Ra values calculated directly from the AFM scans.

The local slope and the correlation length calculated from the HHCFs of Fig. 6 are shown in Fig. 7 as a function of the deposition pressure. Both parameters increase with increasing pressure from 0.4 to 0.8 Pa. Bigger columns with deeper inter-columnar spaces are formed as the shadowing effect increases. On the other hand, the local slope is higher along the X direction while the correlation length is higher in the Y direction at both pressures. The columns are elongated along the Y direction and separated by deeper ridges in the X direction. Increasing the pressure from 0.8 to 1.0 Pa results in a steep increase of the local slope in both X and Y directions, showing that the height of the columns tops is significantly increased in both directions. However, this effect is more pronounced along the Y direction and the local slopes in X and Y are similar at 1.0 Pa. The correlation length along X also increases steeply while it decreases along the Y direction, resulting in similar values in both directions. More equiaxed columns are formed at higher pressure.

The distance between the columns centers (D_x), calculated from the 2D autocorrelation function of the AFM scans for the samples displaying mounded surfaces in the X direction, is shown in Table 5. As expected, for the DCMS films deposited without bias the separation between columns increases with increasing pressure (from 129 to 177 nm) in agreement with the more pronounced "bumps" observed in the corresponding HHCFs (Fig. 6).

The HHCFs (X and Y directions) obtained from the AFM scan of the surface of the film deposited by DCMS at 0.4 Pa with a −80 V bias (Fig. 8) are similar to the HHCFs obtained for the film deposited with the same conditions but without bias (Fig. 6). However, bombarding the surface of the growing Cr film with accelerated Ar ions resulted in

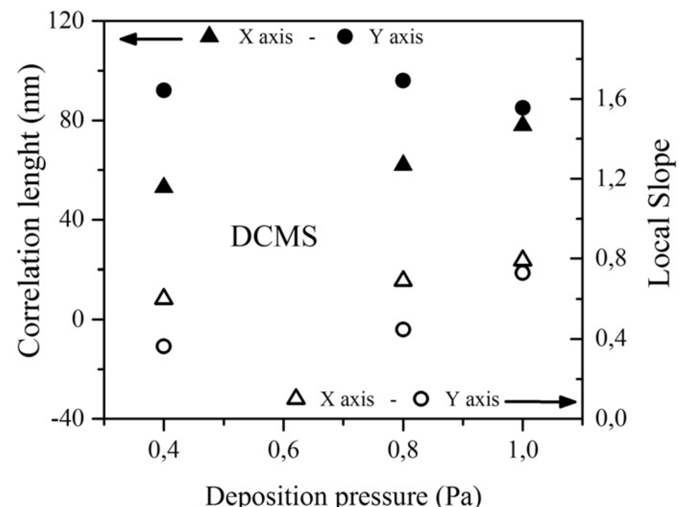

Fig. 7. Correlation length and local slope of the Cr films deposited by DCMS.

Table 5
Distance between columns centers (D_x) for the Cr films displaying mounded surfaces along the X direction.

D_x (nm)	0.4 Pa	0.8 Pa	1.0 Pa
DCMS	129	150	177
DCMS with bias	100	131	–
DOMS Low P_p	–	102	–

slightly more anisotropic columns (Fig. 9) and a significant decrease of the distance between columns centers (Table 5).

The HHCFs of the film deposited by DOMS at 0.4 Pa (Fig. 8) are shifted to lower values of the vertical scale confirming that lower roughness surfaces are formed as compared to DCMS with or without bias. The oscillatory behavior of the HHCF in the X direction is much less evident for the sample deposited by DOMS at low P_p and almost inexistent for the sample deposited by DOMS at high P_p. Ionizing the sputtered flux allows to efficiently decrease the shadowing effect and almost prevent its effects at high peak power.

The local slope of the films deposited by DOMS at 0.4 Pa is lower in both the X and Y directions as compared to the DCMS films (Fig. 9). However, this effect is much stronger for the rotation direction (X) resulting in similar local slopes in X and Y direction in both films deposited by DOMS. The correlation length anisotropy is significantly reduced for the films deposited by DOMS, as compared to DCMS, although anisotropic films are still deposited in DOMS.

As was found at lower pressure, the HHCFs (X and Y directions) of the surface of the film deposited at 0.8 Pa with bias (Fig. 10) and without bias (Fig. 6) are very similar. However, biasing the growing film at 0.8 Pa resulted in slightly smaller size columns (Fig. 11) and decreased the distance between column centers in the X direction from 150 to 131 nm (Table 5). In fact, the film deposited with substrate biasing has a D_x value similar to the value obtained for the DCMS film deposited at 0.4 Pa without substrate biasing ($D_x = 129$ nm), although bigger and more anisotropic columns were formed in the latter case.

In spite of the relatively high deposition pressure, the shadowing effect is effectively decreased in the films deposited by DOMS at 0.8 Pa, as already observed for the films deposited at 0.4 Pa. However, a low amplitude “bump” is still observed in the HHCF of the film deposited at low P_p (see inset in Fig. 10), revealing that the shadowing effect is not completely prevented. In fact, this film has $D_x = 102$ nm (Table 5) which is close to the value obtained for the film deposited by DCMS

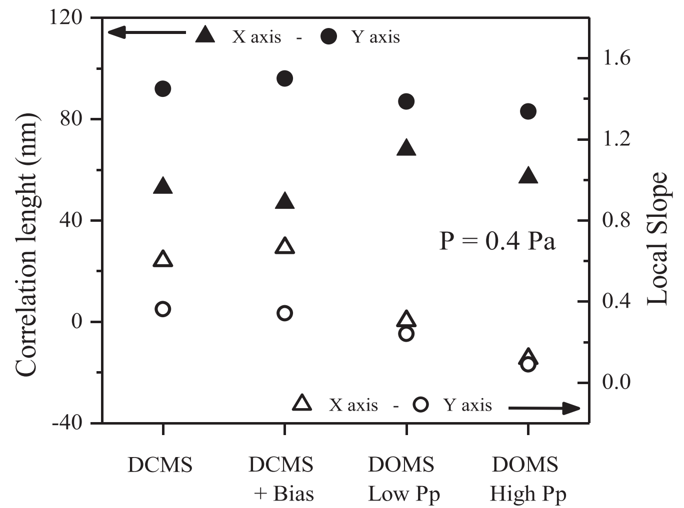

Fig. 9. Correlation length and local slope of the Cr films deposited at 0.4 Pa by DCMS and DOMS.

with bias at 0.4 Pa. As expected, the local slopes in both the X and Y directions of the films deposited at 0.8 Pa (Fig. 11) are higher than those measured at 0.4 Pa (Fig. 9), in agreement with the increased shadowing effect at higher pressure. Once again the local slopes of the films deposited by DOMS are significantly lower than those obtained for the films deposited by DCMS and are very similar in the X and Y directions. On the other hand, the correlation length anisotropy is also reduced in the films deposited by DOMS as compared to DCMS. However, at 0.8 Pa, this results is achieved mainly by a decrease of the correlation length in Y while at 0.4 Pa it was obtained through an increase of the correlation length along the X direction. Although increasing the pressure increases the average impinging angle of the species arriving at the substrate this effect is mostly counterbalanced by the higher ionization rate of the sputtered material. As a result, the DOMS depositions show a much lower dependence on the deposition pressure.

4. Discussion

One of the most striking results in this work is the deposition of highly anisotropic microstructures. The origin of this kind of

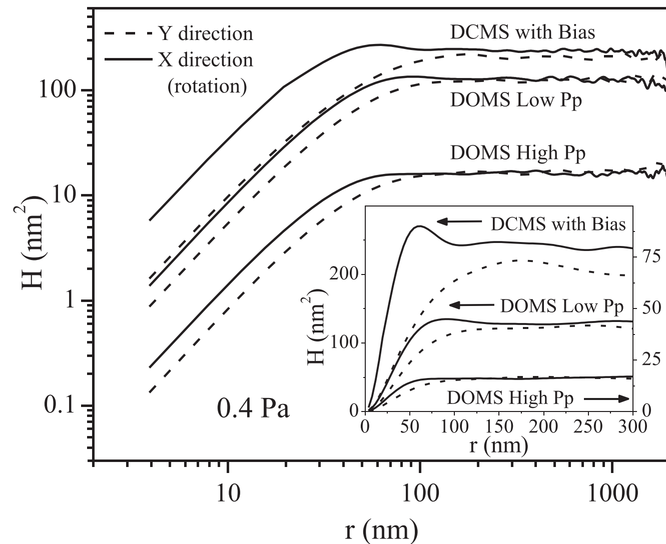

Fig. 8. Double logarithmic representation of the Height-Height correlation functions calculated for the Cr films deposited 0 t 0.4 Pa. The HHCFs are represented with linear scales in the inset.

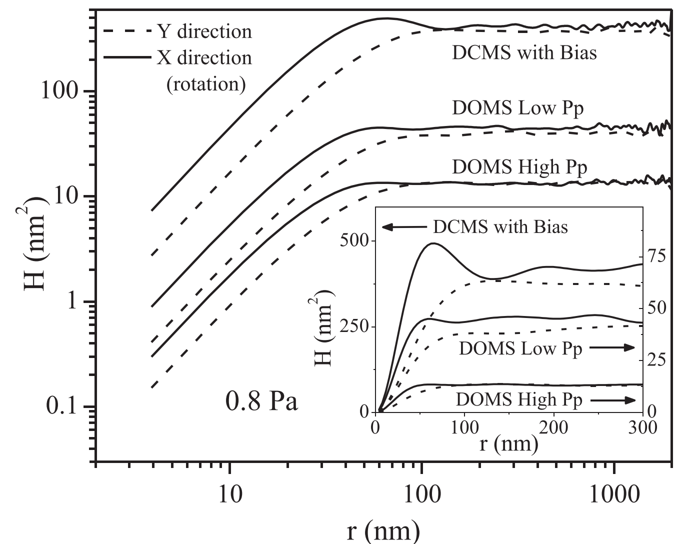

Fig. 10. Double logarithmic representation of the Height-Height correlation functions calculated for the Cr films deposited 0 t 0.8 Pa. The HHCFs are represented with linear scales in the inset.

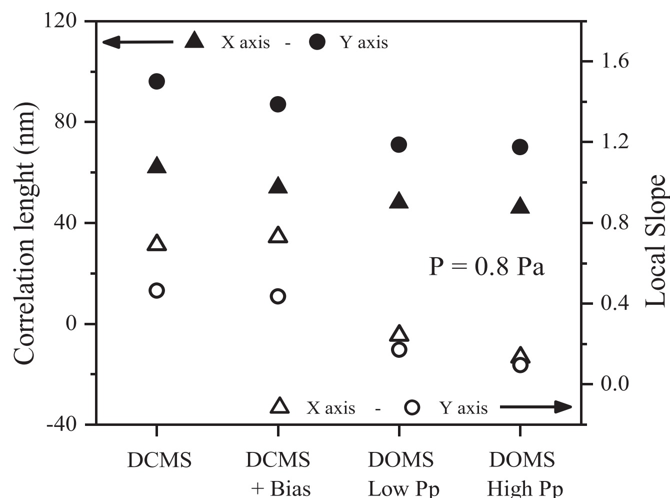

Fig. 11. Correlation length and local slope of the Cr films deposited at 0.8 Pa by DCMS and DOMS.

microstructures, as well as its dependence on the deposition conditions, are firstly discussed (Section 4.1). The relative influence of the shadowing effect and energy of the bombarding species on the surface topography and microstructure of the Cr films is then discussed in Section 4.2. Finally, in Section 4.3, the DCMS and DOMS processes are compared with regard to their ability to control the flux of bombarding species.

4.1. Anisotropic microstructures by DCMS

All of the Cr films deposited by DCMS with or without bias have an anisotropic columnar microstructure. Anisotropic microstructures have been reporter in the literature for Cr deposited by magnetron sputtering. Whitacre et al. [36] deposited Cr films on Si (100) wafers mounted on a platen which rotated beneath the sputter target. The resulting films displayed grain elongation in the plane of growth normal to the direction of substrate motion and faceted surface morphology. The authors related the anisotropic morphology to the asymmetric deposition system as there was on average more oblique flux in the rotation direction over any other. Similar results were also found for Mo, Ta and CrN thin films. Zhao et al. [37] performed a detail study of the evolution of anisotropic microstructure and residual stress in sputtered thin films. They also used a rotating substrate holder, in such a way that the center of the substrates passed beneath the cathode in each rotation. The Cr films developed well-organized microstructures which consisted of elongated grains separated with preferentially aligned inter-columnar voids. The direction of grain elongation coincided with direction perpendicular to substrate rotation. The surface morphology of the thicker Cr films deposited in that study is strikingly similar to the morphology of the films deposited by DCMS in this work. In another work, Zhao et al. [38] compared Mo films deposited by DCMS over moving and static substrates and found that anisotropic stresses and elongated grains were only formed in the former deposition case. Finally Jansen et al. [39] used a twofold rotation geometry with the substrates and target vertically aligned to deposit Cr thin films. They also found an anisotropic microstructure. In the vertical direction, which was perpendicular to substrate rotation, the grains formed ridges separated by large grain boundaries while they were separated by deep grooves in the horizontal direction.

In this work, the substrates were rotated in front of the target along the X direction. Although the average impinging angle of the incoming species should be the same in the rotation direction (horizontal direction) and the vertical direction, the spread of the angle distribution is considerably higher along the rotation direction. In this direction, glancing angle impingement is achieved both when the substrate enters and leaves the field of view of the target. As a result, the deposition conditions are asymmetric as the impinging flux has a higher angle component in the rotation direction. In such conditions, the shadowing effect is stronger along the rotation direction (X direction) resulting in HHCFs typical of mounded surfaces irrespectively of the deposition pressure. However, HHCFs similar to that of self-affine surfaces are found up to 0.8 Pa along the Y direction although the shadowing effect should also be active along this direction. On the other hand, the correlation length is higher along the Y direction showing that the columns are elongated in the direction perpendicular to the substrate rotation direction. Karpenko et al. [40] have shown that high-angle ion bombardment of a growing film results in grain elongation along the direction perpendicular to the bombardment direction. The grains whose fast crystallographic growth directions are aligned with the fast geometric growth direction have a growth advantage over grains of other orientations. As the Cr films deposited by DCMS in this work are subjected to a flux of impinging species with a stronger high-angle component along the X axis, this model explains the elongation of the columns along the Y direction. On the other hand, it also explains why HHCFs similar to those of self-affine surfaces are found in the Y direction even at 0.8 Pa. The additional material deposited along the Y direction due to the stronger shadowing effect along the X direction contributes to fill the inter-columnar voids otherwise created by the shadowing effect along the Y direction. At 1.0 Pa, the shadowing effect along the Y direction is strong enough to counteract the shadowing effect along the X direction and mounded surfaces are found along both directions while the anisotropy of the columns is reduced. This argument also explains why the correlation length along the Y direction decreases upon increasing the pressure from 0.8 to 1.0 Pa. The above conclusions show that the surface topography along one direction, X or Y, is influenced by the shadowing effect along both the X and Y directions. This conclusions is of paramount importance for simulation of the shadowing effect as it implies that 2D models have to be used in order to obtain realistic values for the surface properties such as the roughness.

4.2. Surface topography and microstructure vs. deposition conditions

The shadowing effect is the dominant deposition mechanism shaping the microstructure and surface topography of all the films deposited by DCMS. Almost all the films display a columnar growth with well-faceted three-sided pyramidal columns tops, while a network of inter-connected inter-columnar voids is developed. The films surface have a high roughness (Ra = 8 to 16 nm) and the HHCFs along the X direction are typical of mounded surfaces. Although the energy of the sputtered Cr atoms bombarding the substrate increases with decreasing pressure (up to 0.5 eV at 0.2 Pa), the shadowing effect is still effective, at least along the X direction, at 0.2 Pa. The bulk displacement energy for Cr (E_d^b) is 22.2 eV [41]. Owing to the lower coordination number of the surface atoms, the surface displacement energy (E_d^s) of Cr may be approximated to half of E_d^b, i.e., $E_d^s = 11.1$ eV [41]. According to the SRIM simulations carried out in this work, at 0.2 Pa, 28.5% of the Cr atoms impinging on the growing film have an energy higher than E_d^s while only 15.4% of such atoms have an energy higher than E_d^b. Note also that Cr atoms with much higher energy than E_d^b are necessary to promote long-range redistribution of the Cr atoms on the surface of the growing film. For example, for Cu thin films bombarding energies near 50 eV are necessary to activate re-emission processes and, thus, redistributing the flux of impinging species to shadowed regions [5]. In fact, the effectiveness of the shadowing effect is even higher for Cr films due to the lower mobility of the ad-atoms that mainly stick to the position where they arrive at the substrate. The Cr atoms impinging on the surface at 0.2 Pa may contribute to trigger local surface smoothing mechanisms, such has surface diffusion, but their energy is well below the threshold to activate non-local smoothing mechanisms that could efficiently counterbalance the shadowing effect. The topographical and microstructural

changes observed upon decreasing the deposition pressure are, thus, much more likely due to the weakening of the shadowing effect, as a consequence of a decreasing high angle component of the impinging angles distribution, than to the increase of the energy of the sputtered species arriving at the substrate.

It is well known that using a substrate bias, i.e., bombarding the growing film with energetic argon ions extracted from the plasma, generally allows the deposition of denser films. However, in this work, bombarding the films deposited by DCMS with Ar ions accelerated at −80 V does not bring about drastic microstructural changes. Well-defined columnar microstructure with anisotropic surface morphologies are still deposited irrespectively of the deposition pressure. This result agrees well with literature, since several works reported that the columnar structure of Cr films deposited by DCMS remains even if a much higher bias (up to 500 V) is used [42]. The well-faceted pyramid-like tops of the columns and the high roughness of the films surface clearly demonstrate that the films microstructure is still primary determined by the shadowing effect. However, substrate biasing decreases the shadowing effect as can be concluded from the decrease of the distance between column centers at both at 0.4 and 0.8 Pa. In this work a substrate bias of −80 V was used. The energy of the Ar ions (80 eV) bombarding the substrate is then well above the bulk displacement energy of Cr ($E_d^b = 22.2$ eV [41]) and, thus, re-sputtering of the Cr atoms on the film surface allows to redistribute the flux of impinging species to shadowed regions. On the other hand, only minor decreases of the local slopes and correlation lengths where found upon biasing. Slightly thinner and more tightly packed columns are formed and, thus, more compact films are deposited upon substrate biasing.

The Cr films deposited by DOMS at low P_p and high pressure (0.8 and 1.0 Pa) also display a surface topography consisting of ridges and valleys along the Y direction as was observed for the films deposited by DCMS. However, the width of the columns and valleys, the surface roughness and the local slope are much lower than for the film deposited at the same pressures by DCMS with or without bias. The DOMS discharge allows to substantially decrease the effectiveness of the shadowing effect. This result could be due to a higher energy of the Cr species bombarding the substrate as the deposition voltage in the DOMS process is higher than in DCMS. However, at high pressures most of the energy of the sputtered species is lost in collisions in the gas phase and almost half of the Cr species are thermalized before arriving at the substrate. On the other hand, the energy of the Cr ions generated in the DOMS process is increased in the vicinity of the substrate as they are accelerated in the electric field generated by substrate self-biasing. However, as discussed in Section 3.1, the energy gain is most likely of the order of 12 eV and, thus, it is insufficient to trigger the non-local smoothing mechanisms that could effectively weaken the shadowing effect. In fact, although the pattern of ridges and valleys in the films deposited at low P_p and high pressure is similar to the one obtained by DCMS at 0.2 Pa (similar sizes of ridges and columns), the columns tops are well faceted and without rounded borders confirming the lack of energetic bombardment.

Greczynski et al. [43] found that sputtered Cr films deposited by DCMS using a rectangular target exhibit high degree of in-plane alignment in addition to a (110) out-of-plane orientation. The former was assigned to the presence of an asymmetrical off-normal flux of sputtered species in the direction parallel to the longer side of the rectangular target that favors growth of grains with maximum capture cross section for incoming species. The biaxial alignment somewhat degraded at high bias voltage as the ionic portion of the incoming flux arrived close to the surface normal. However, a completely random distribution (fiber texture) was only obtained for Cr films deposited by HIPIMS under conditions when the incoming flux was dominated by ions. These results clearly show that ionization of the Cr sputtered species in the HIPIMS process allows to influence the impinging direction of the resulting ions on the substrate. In fact, the Cr ions are deflected in the self-bias and their impinging angles are shifted closer to the substrate normal. This effect is even more pronounced for the ions entering the substrate electrical fields at very high angles with respect to the substrate normal which are the main responsible for the shadowing effect. It is then argued that the lower effectiveness of the shadowing effect in the films deposited by DOMS at low P_p and high pressure (0.8 and 1.0 pa), as compared to DCMS, results from a decrease of the shadowing effect strength due to ionization of the sputtered Cr species.

Decreasing the deposition pressure at low P_p (0.2 and 0.4 Pa) still results in the deposition of a columnar microstructure showing that shadowing effect is still effective. However the columns are more tightly packed than at high pressure and the surface topography consists of rounded features instead of well faceted column tops deposited either at low P_p and higher pressure or by DCMS with or without bias at similar pressures. On the other hand, the HHCFs function no longer show the formation of mounded surfaces. Although the shadowing effect is not completely prevented, it is almost eliminated by both the low deposition pressure and the ionization of the Cr species. On the other hand, the energy of the Cr species impinging on the substrate is higher than at higher deposition pressure and also higher than in DCMS at similar pressures due to the acceleration of Cr ions in the substrate vicinity. As a result, the surface topography reveals the effect of ion bombardment by the formation of rounded features due to the activation of local smoothening mechanisms such as surface diffusion.

All the Cr films deposited at high P_p display much more dense and irregular microstructures and isotropic surface morphologies consisting of finer surface features without no inter-columnar voids. Accordingly, the films deposited by DOMS at high P_p have the lowest surface roughness measured in this work. On the other hand, the HHCFs of all the films no longer have the characteristic “bump” of mounded surfaces at intermediate values of r. Clearly the shadowing effect was almost completely prevented in all films irrespectively of the deposition pressure. At high pressure, the peak current is higher than for the films deposited at low P_p. The Cr ionization fraction is increased and, thus, the angle distribution of the species impinging on the growing film is shifted towards the substrate normal even more efficiently than at low P_p. Note, however, that increasing the ionization fraction of the Cr atoms also increases the average energy of the impinging species, since more ions are accelerated by the substrate self-bias.

4.3. Additional control of the impinging species in DOMS

In a DCMS deposition system the average intensity of the shadowing effect is firstly determined by the deposition geometry and depends on the average angle of the sputtered atoms coming from the race track and reaching the substrate without collisions with the gas phase. This effect can then be controlled mainly by changing the deposition pressure. In DOMS, the average angle of the impinging species can be additionally controlled by changing the peak current and, therefore, the fraction of ionized sputtered species. The DOMS process allows a new form of control of the average directions of impinging species, not available in DCMS. The DOMS process allows to decrease the strength of the shadowing effect or even to completely prevent it irrespectively of the deposition geometry. The most important consequence is that dense tightly packed microstructures can be deposited without the need of high energy bombardment, avoiding defect formation and compressive stresses development that are usually associated with high bombardment energy. On the other hand, the additional control of the impinging flux also allows to minimize the effects of geometrical asymmetries of the deposition system in the films properties. As pointed out by Greczynski et al. [43], this is an important issue at the technological level as thin films are usually deposited in large batches and several degrees of rotations are necessary to expose the substrate surface to the impinging flux of atoms coming from the target. In these conditions, the DOMS process, and more generally the HIPIMS process, allows to overcome the system asymmetries and to deposit thin films with much more uniform and similar properties.

Although the deposition rate of the Cr films was not studied in this paper, the authors have already shown that it is much lower in DOMS than in DCMS [19] for Cr films deposition. More generally, the lower deposition rate in HIPIMS as compared to the DCMS process is well documented in the literature [44–46]. The additional control of the impinging flux on the growing film which is made available by DOMS/HIPIMS processes is then achieved at the cost of the deposition rate. Depending on the specific applications, this cost can be a deal-breaker or not.

5. Conclusions

All the Cr films deposited by DCMS with or without bias have a columnar microstructure with elongated columns along the vertical direction and an anisotropic surface topography. It was shown that the formation of anisotropic films is a consequence of the asymmetric deposition conditions as the substrate is rotated in front of the target only in the horizontal direction. The shadowing effect is stronger along this direction, due to the stronger high-angle component of angle distribution of the species impinging on the substrate, resulting in mounded surfaces. It was also shown that the surface topography along one film surface direction is not only influenced by the shadowing in that direction but also by the shadowing effect in the orthogonal direction.

The DOMS process allows to overcome the shadowing effect, irrespectively of the deposition geometry, and, thus, to deposit dense tightly packed microstructures. This result was achieved by decreasing the strength of the shadowing effect, or even by completely prevent it, rather than by decreasing its effectiveness, as is usually the case in magnetron sputtering when using high energetic bombardment. The additional control of the flux of species impinging on the growing film, gain as a result of the ionization of the sputtered species, allows to minimize the effects of geometrical asymmetries of the deposition system in the films properties.

Acknowledgments

This research is sponsored by FEDER funds through the program COMPETE - Programa Operacional Factores de Competitividade - and by national funds through FCT - Fundação para a Ciência e a Tecnologia, under the projects: UID/EMS/00285/2013, as well as the grant SFRH/BPD/111958/2015 and SFRH/BPD/73827/2010.

References

[1] Y. Pei, K. Shaha, C. Chen, R. Van der Hulst, A. Turkin, D. Vainshtein, J.T.M. De Hosson, Growth of nanocomposite films: from dynamic roughening to dynamic smoothening, Acta Mater. 57 (2009) 5156–5164.
[2] T. Karabacak, Y.-P. Zhao, G.-C. Wang, T.-M. Lu, Growth-front roughening in amorphous silicon films by sputtering, Phys. Rev. B 64 (2001) 085323.
[3] M. Pelliccione, T. Karabacak, C. Gaire, G.-C. Wang, T.-M. Lu, Mound formation in surface growth under shadowing, Phys. Rev. B 74 (2006) 125420.
[4] A. Turkin, Y. Pei, K. Shaha, C. Chen, D. Vainshtein, J.T.M. De Hosson, On the evolution of film roughness during magnetron sputtering deposition, J. Appl. Phys. 108 (2010) 094330.
[5] T. Karabacak, Thin-film growth dynamics with shadowing and re-emission effects, J. Nanophotonics 5 (2011) 052501–052518.
[6] A. Redondo-Cubero, R. Gago, L. Vázquez, Ultrasmooth growth of amorphous silicon films through ion-induced long-range surface correlations, Appl. Phys. Lett. 98 (2011) 011904.
[7] J.A. Thornton, The microstructure of sputter-deposited coatings, J. Vac. Sci. Technol. A 4 (1986) 3059–3065.
[8] R. Roy, R. Messier, Preparation–physical structure relations in SiC sputtered films, J. Vac. Sci. Technol. A 2 (1984) 312–315.
[9] S. Mahieu, P. Ghekiere, D. Depla, R. De Gryse, Biaxial alignment in sputter deposited thin films, Thin Solid Films 515 (2006) 1229–1249.
[10] R. Alvarez, L. Vazquez, R. Gago, A. Redondo-Cubero, J. Cotrino, A. Palmero, Atomistic model of ultra-smooth amorphous thin film growth by low-energy ion-assisted physical vapour deposition, J. Phys. D. Appl. Phys. 46 (2013) 395303.
[11] J.A. Hopwood, Plasma physics, Thin Films 27 (2000) 181–207.
[12] U. Helmersson, M. Lattemann, J. Bohlmark, A.P. Ehiasarian, J.T. Gudmundsson, Ionized physical vapor deposition (IPVD): a review of technology and applications, Thin Solid Films 513 (2006) 1–24.
[13] V. Kouznetsov, K. Macak, J.M. Schneider, U. Helmersson, I. Petrov, A novel pulsed magnetron sputter technique utilizing very high target power densities, Surf. Coat. Technol. 122 (1999) 290–293.
[14] D. Lundin, K. Sarakinos, An introduction to thin film processing using high-power impulse magnetron sputtering, J. Mater. Res. 27 (2012) 780–792.
[15] J. Lin, J.J. Moore, W.D. Sproul, B. Mishra, Z. Wu, Modulated pulse power sputtered chromium coatings, Thin Solid Films 518 (2009) 1566–1570.
[16] J. Lin, B. Wang, W.D. Sproul, Y. Ou, I. Dahan, Anatase and rutile TiO_2 films deposited by arc-free deep oscillation magnetron sputtering, J. Phys. D. Appl. Phys. 46 (2013) 084008.
[17] Y. Ou, J. Lin, S. Tong, H. Che, W. Sproul, M. Lei, Wear and corrosion resistance of CrN/TiN superlattice coatings deposited by a combined deep oscillation magnetron sputtering and pulsed dc magnetron sputtering, Appl. Surf. Sci. 351 (2015) 332–343.
[18] J. Oliveira, F. Fernandes, F. Ferreira, A. Cavaleiro, Tailoring the nanostructure of Ti–Si–N thin films by HiPIMS in deep oscillation magnetron sputtering (DOMS) mode, Surf. Coat. Technol. 264 (2015) 140–149.
[19] F. Ferreira, R. Serra, J. Oliveira, A. Cavaleiro, Effect of peak target power on the properties of Cr thin films sputtered by HiPIMS in deep oscillation magnetron sputtering (DOMS) mode, Surf. Coat. Technol. 258 (2014) 249–256.
[20] J.A. Thornton, D. Hoffman, Stress-related effects in thin films, Thin Solid Films 171 (1989) 5–31.
[21] K. Sarakinos, J. Alami, P. Karimi, D. Severin, M. Wuttig, The role of backscattered energetic atoms in film growth in reactive magnetron sputtering of chromium nitride, J. Phys. D. Appl. Phys. 40 (2007) 778.
[22] J. Lin, J. Moore, W. Sproul, B. Mishra, J. Rees, Z. Wu, R. Chistyakov, B. Abraham, Ion energy and mass distributions of the plasma during modulated pulse power magnetron sputtering, Surf. Coat. Technol. 203 (2009) 3676–3685.
[23] D. Nečas, P. Klapetek, Gwyddion: an open-source software for SPM data analysis, Open Phys. 10 (2012) 181–188.
[24] P. Klapetek, Quantitative Data Processing in Scanning Probe Microscopy: SPM Applications for Nanometrology, William Andrew, 2012.
[25] M. Pelliccione, T.-M. Lu, Evolution of Thin-Film Morphology, Springer, 2008.
[26] J. Bubendorff, G. Garreau, S. Zabrocki, D. Berling, R. Jaafar, S. Hajjar, A. Mehdaoui, C. Pirri, Nanostructuring of Fe films by oblique incidence deposition on a $FeSi_2$ template onto Si (111): growth, morphology, structure and faceting, Surf. Sci. 603 (2009) 373–379.
[27] J.F. Ziegler, M.D. Ziegler, J.P. Biersack, SRIM — the stopping and range of ions in matter (2010), Nucl. Instrum. Methods Phys. Res., Sect. B 268 (2010) 1818–1823.
[28] K. Van Aeken, S. Mahieu, D. Depla, The metal flux from a rotating cylindrical magnetron: a Monte Carlo simulation, J. Phys. D. Appl. Phys. 41 (2008) 205307.
[29] A. Handoo, P. Ray, Sputtering yield of chromium by argon and xenon ions with energies from 50 to 500 eV, Appl. Phys. A 54 (1992) 92–94.
[30] W. Eckstein, Sputtering yields, Sputtering by Particle Bombardment, Springer 2007, pp. 33–187.
[31] D. Depla, W. Leroy, Magnetron sputter deposition as visualized by Monte Carlo modeling, Thin Solid Films 520 (2012) 6337–6354.
[32] M. Seah, C. Clifford, F. Green, I. Gilmore, An accurate semi-empirical equation for sputtering yields I: for argon ions, Surf. Interface Anal. 37 (2005) 444–458.
[33] B. Liebig, N.S.J. Braithwaite, P. Kelly, R. Chistyakov, B. Abraham, J. Bradley, Time-resolved plasma characterisation of modulated pulsed power magnetron sputtering of chromium, Surf. Coat. Technol. 205 (2011) S312–S316.
[34] A. Ferrec, J. Keraudy, S. Jacq, F. Schuster, P.-Y. Jouan, M. Djouadi, Correlation between mass-spectrometer measurements and thin film characteristics using dcMS and HiPIMS discharges, Surf. Coat. Technol. 250 (2014) 52–56.
[35] Y. Zhao, G.-C. Wang, T.-M. Lu, Characterization of Amorphous and Crystalline Rough Surface—Principles and Applications, Academic press, 2000.
[36] J. Whitacre, S. Yalisove, J. Bilello, In-plane texturing in sputtered films, Textures Microst. 34 (2000) 91–104.
[37] Z. Zhao, S. Yalisove, Z. Rek, J. Bilello, Evolution of anisotropic microstructure and residual stress in sputtered Cr films, J. Appl. Phys. 92 (2002) 7183–7192.
[38] Z. Zhao, S. Yalisove, J. Bilello, Stress anisotropy and stress gradient in magnetron sputtered films with different deposition geometries, J. Vac. Sci. Technol. A 24 (2006) 195–201.
[39] G. Janssen, P. Alkemade, V. Sivel, S.Y. Grachev, J.-D. Kamminga, Anisotropic growth of chromium films during sputter deposition on substrates in planetary motion, J. Vac. Sci. Technol. A 22 (2004) 1773–1777.
[40] O. Karpenko, J. Bilello, S. Yalisove, Growth anisotropy and self-shadowing: a model for the development of in-plane texture during polycrystalline thin-film growth, J. Appl. Phys. 82 (1997) 1397–1403.
[41] N. Ghafoor, F. Eriksson, P.Å. Persson, L. Hultman, J. Birch, Effects of ion-assisted growth on the layer definition in Cr/Sc multilayers, Thin Solid Films 516 (2008) 982–990.
[42] R. Bland, G. Kominiak, D. Mattox, Effect of ion bombardment during deposition on thick metal and ceramic deposits, J. Vac. Sci. Technol. 11 (1974) 671–674.
[43] G. Greczynski, J. Jensen, L. Hultman, Mitigating the geometrical limitations of conventional sputtering by controlling the ion-to-neutral ratio during high power pulsed magnetron sputtering, Thin Solid Films 519 (2011) 6354–6361.
[44] J. Emmerlich, S. Mráz, R. Snyders, K. Jiang, J.M. Schneider, The physical reason for the apparently low deposition rate during high-power pulsed magnetron sputtering, Vacuum 82 (2008) 867–870.
[45] M. Samuelsson, D. Lundin, J. Jensen, M.A. Raadu, J.T. Gudmundsson, U. Helmersson, On the film density using high power impulse magnetron sputtering, Surf. Coat. Technol. 205 (2010) 591–596.
[46] A. Anders, Deposition rates of high power impulse magnetron sputtering: physics and economics, J. Vac. Sci. Technol. A 28 (2010) 783–790.

ANNEX F

J. C. Oliveira, F. Ferreira, A. Anders, and A. Cavaleiro, "Reduced atomic shadowing in HiPIMS: Role of the thermalized metal ions," Applied Surface Science, vol. 433, pp. 934-944, 2018.

Applied Surface Science 433 (2018) 934–944

Contents lists available at ScienceDirect

Applied Surface Science

journal homepage: www.elsevier.com/locate/apsusc

Full Length Article

Reduced atomic shadowing in HiPIMS: Role of the thermalized metal ions

João Carlos Oliveira [a], Fábio Ferreira [a,b,*], André Anders [b], Albano Cavaleiro [a,c]

[a] SEG-CEMMPRE, Mechanical Engineering Department, University of Coimbra, Polo II, Rua Luís Reis Santos, 3030-788 Coimbra, Portugal
[b] Lawrence Berkeley National Laboratory, 1 Cyclotron Road, Berkeley, CA, 94720, USA
[c] LED&Mat-IPN, Instituto Pedro Nunes, Laboratório de Ensaios Desgaste e Materiais, Rua Pedro Nunes, 3030-199 Coimbra, Portugal

ARTICLE INFO

Article history:
Received 17 May 2017
Received in revised form 12 October 2017
Accepted 18 October 2017
Available online 18 October 2017

Keywords:
Cr films
DOMS
Surface topography
Shadowing effect
IEDFs

ABSTRACT

In magnetron sputtering, the ability to tailor film properties depends primarily on the control of the flux of particles impinging on the growing film. Among deposition mechanisms, the shadowing effect leads to the formation of a rough surface and a porous, columnar microstructure. Re-sputtered species may be re-deposited in the valleys of the films surface and thereby contribute to a reduction of roughness and to fill the underdense regions. Both effects are non-local and they directly compete to shape the final properties of the deposited films. Additional control of the bombarding flux can be obtained by ionizing the sputtered flux, because ions can be controlled with respect to their energy and impinging direction, such as in High-Power Impulse Magnetron Sputtering (HiPIMS). In this work, the relation between ionization of the sputtered species and thin film properties is investigated in order to identify the mechanisms which effectively influence the shadowing effect in Deep Oscillation Magnetron Sputtering (DOMS), a variant of HiPIMS. The properties of two Cr films deposited using the same averaged target power by d.c. magnetron sputtering and DOMS have been compared. Additionally, the angle distribution of the Cr species impinging on the substrate was simulated using Monte Carlo-based programs while the energy distribution of the energetic particles bombarding the substrate was evaluated by energy-resolved mass analysis. It was found that the acceleration of the thermalized chromium ions at the substrate sheath in DOMS significantly reduces the high angle component of their impinging angle distribution and, thus, efficiently reduces atomic shadowing. Therefore, a high degree of ionization in HiPIMS results in almost shadowing effect-free film deposition and allows us to deposit dense and compact films without the need of high energy particle bombardment during growth.

© 2017 Elsevier B.V. All rights reserved.

1. Introduction

In magnetron sputtering-based deposition processes the ability to tailor the properties of a thin film deposited under conditions of low temperature and low mobility of the ad-atoms depends primary on the effective control of the flux of particles arriving at the growing film surface. The flux intensity and composition, as well as the energy and impinging direction of the particles can trigger different deposition mechanisms to different extents [1,2]. Particles that approach the film surface at oblique angles are captured by higher surface points (hills) re-enforcing their preferential growth rate. As the heights of the hills increase, the neighbouring areas (valleys) are shadowed and capture even less particles from the deposition flux. The so-called shadowing effect promotes the formation of rougher surfaces and porous columnar microstructures [3,4]. This film formation mechanism is non-local as the capture of particles at the top of the hills also influence the film growth in the shadowed area, i.e., at considerable distance from their capture location [5,6]. If the energy of the bombarding particles is high enough, i.e., above the sputtering threshold, the film material will be re-sputtered, i.e., it will be sputtered in a similar way to the magnetron target process although at a lower extent as a much lower negative voltage is applied to the substrate. The re-sputtered species may then be directly re-deposited on the valleys of the surface and thus contribute to fill the underdense regions resulting from the atomic shadowing effect [5,6]. This so-called re-deposition process is also a non-local film formation mechanism as some of the

* Corresponding author at: SEG-CEMMPRE, Mechanical Engineering Department, University of Coimbra, Polo II, Rua Luís Reis Santos, Coimbra, 3030-788, Portugal.
E-mail address: fabio.ferreira@dem.uc.pt (F. Ferreira).

https://doi.org/10.1016/j.apsusc.2017.10.133
0169-4332/© 2017 Elsevier B.V. All rights reserved.

re-sputtered particles end up being re-captured at a significant distance of their emission location. The bombarding particles can also influence the films properties through other film formation mechanisms that increase the ad-atoms mobility in the vicinity of the impingement location, such as atomic peening [7] and atomic scale heating [8]. However, these mechanisms are local, i.e., they only operate in the vicinity of the impingement location and, thus, they are unable to counteract the atomic shadowing effect [5]. In fact, as shown by the authors in a previous work [9], applying a substrate bias of − 80 V during growth of Cr films by DCMS does not significantly change the columnar microstructure of the Cr films and only brings about a moderate decrease of the films roughness. This result suggests that atomic shadowing and re-deposition are the most prominent film formation mechanism operating during the growth of the Cr films deposited in this work. As they have opposite effects on the growing film, they directly compete to shape the final properties of the deposited films.

Traditionally, the most influential deposition parameters regarding both bombardment and shadowing effect are the process pressure and substrate biasing. In constant power mode, decreasing the process pressure results in an increased discharge voltage and less collisions with gas atoms and molecules and thus it increases the average energy of the sputtered species. On the other hand, the high-angle component of the angular distribution of the impinging species, as measured relatively to the substrate normal, also decreases thus weakening of the shadowing effect [10]. Substrate biasing allows us to bombard the growing film with ions extracted from the plasma with an energy proportional to the applied voltage (and ion charge state). This triggers re-sputtering if a high enough voltage is used.

Additional control of the bombarding flux can be obtained by ionizing the sputtered flux because ions can be controlled with respect to their energy and impinging direction. In the last decade, High-Power Impulse Magnetron Sputtering (HiPIMS) has been popularized for this purpose [11–15]. This deposition process relies on the application of very high power densities to the target during short periods to achieve higher plasma densities, and consequent ionization of the sputtered atoms by electron impact. In a previous paper it was shown that Deep Oscillation Magnetron Sputtering (DOMS), a variant of HiPIMS, allowed us to overcome the shadowing effect and, thus, to deposit Cr thin films with much smoother surfaces and densely packet columns even at relatively high pressure (up to 1 Pa) [9]. The main objective of the present work is to identify the mechanisms which effectively decreases the shadowing effect in DOMS. For this purpose the deposition conditions and properties of two Cr films deposited by DOMS at higher pressure (1.0 Pa) and DCMS at lower pressure (0.2 Pa) were studied and compared. In both cases the energy distributions of the energetic particles bombarding the substrate during film growth were evaluated by energy-resolved mass analysis (ERMS) and the angular distribution of the Cr species impinging on the substrate was simulated using Monte Carlo-based programs. The microstructure, structure and mechanical properties of the deposited Cr films were characterized by SEM and AFM, X-Ray diffraction and nano-indentation. It was found that in DOMS the acceleration of the chromium ions at the substrate sheath significantly reduces the high angle component of the angular distribution and, thus, efficiently reduces atomic shadowing. Hence, dense and compact films can be deposited without the need of high energy particles bombardment during growth.

Chromium has been chosen as a model material in this work since, (i) it has a high melting point resulting in low values of the ratio between substrate and melting temperature (T_s/T_m) and thus a low surface mobility which helps to preserve the film growth history [16], (ii) it minimizes the number of neutralized Ar ions reflected at the target surface [17] and (iii) it has a high ionization degree in HiPIMS [18].

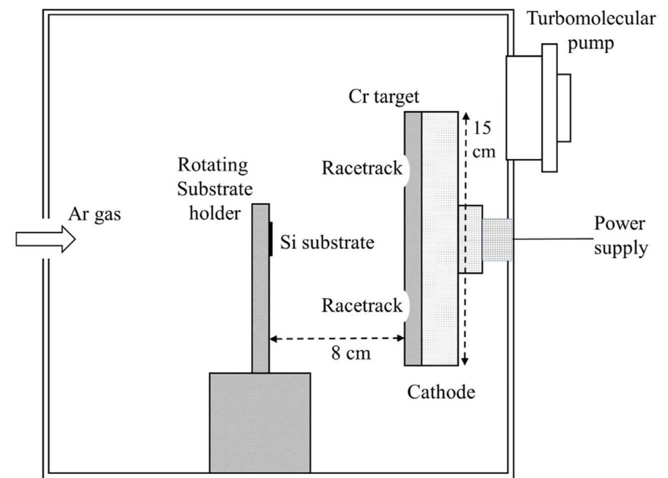

Fig. 1. Schematic diagram of the magnetron sputtering system.

2. Experimental details

Cr films were deposited by HiPIMS in DOMS mode using a Cyprium^{TM} III plasma generator (Zpulser Inc.) and by DCMS using a PFG 7500 d.c. power supply (Hüttinger). In both cases, a pure Cr (99.99%) target with dimensions of 150 mm × 150 mm × 10 mm was sputtered in a pure Ar discharge gas. The films were deposited onto (100) silicon samples with dimensions 20 mm × 20 mm. The substrates were ultrasonically cleaned in acetone for 15 min and in ethanol for 10 min. They were then fixed to a rotating substrate holder which revolved at 23.5 rev/min around the central axis of the chamber. The substrate-to-target distance was 80 mm. A schematic of the deposition system is shown in Fig. 1.

Prior to all depositions a base pressure lower than 5×10^{-4} Pa was attained in the deposition chamber using a turbomolecular pump. In this work two Cr films were deposited, one by DOMS at high pressure (1.0 Pa) and another by DCMS at low pressure (0.2 Pa) in order to identify the mechanism responsible for decreasing the shadowing effect in DOMS. Both films were deposited with floating substrate potential using the same averaged target power (1200 W). The main deposition conditions in DOMS and DCMS depositions are shown in Tables 1 and 2, respectively. More details about the oscillating current and voltage waveforms in DOMS can be found in references [9,19,20].

The ion energy distribution (IED) was measured using a combined particle spectrometer combining an energy and mass filter (EQP 300 by Hiden Ltd.) at the Lawrence Berkeley National Laboratory. This equipment can measure up to 1 kV/charge and is differentially pumped by a 70 l/s turbo pump. A chromium target with a diameter of 7.6 cm was mounted in front of the EQP at a distance of 2 cm from the EQP entrance orifice (100 μm diameter). A average target power of 600 W was used both for DOMS and DCMS. The IEDs scans were measured from 0 to 100 V with a step size of 0.5 V and a 1000 ms dwell time. The raw data were corrected for the double charged ions by multiplying the scan voltage by two and dividing the count rate by two to account for the energy bin width and height. It has to be mentioned that the here-presented energy distributions are skewed, over-representing lower energies, due to the energy-dependent acceptance angle. The experimental conditions used to generate the DOMS and DCMS discharges probed by the EQP are shown in Tables 1 and 2, respectively. In both tables the power density values were calculated taking into account the area of the racetrack in order to take into account the different shapes of the targets used for ERMS and thin film deposition. The experimental conditions for the DOMS plasma analysis were chosen such as to work at similar target peak power density (P_{pd}) and target

Table 1
Experimental conditions used for the Cr film deposition by DOMS and EMRS measurements of the DOMS plasma. (V_p = peak target voltage, I_p = peak target current, I_{pd} = peak target current density, P_p = peak target power, P_{pd} = peak target power density, P_{av} = averaged power).

	Pressure (Pa)	V_p (V)	I_p (A)	I_{pd} (A/cm^2)	P_p (kW)	P_{pd} (kW/cm^2)	P_{av} (kW)
Deposition	1.0	899	56	1.87	38	1.27	1.2
ERMS discharge	1.0	711	40	1.77	28	1.26	0.6

Table 2
Experimental conditions used for the Cr film deposition by DCMS and energy-resolved mass spectrometry measurements of the DCMS plasma. (V = target voltage, I = target current, I_d = target current density, P = power, P_d = power density).

	Pressure (Pa)	V (V)	I (A)	I_d (A/cm^2)	P (kW)	P_d (W/cm^2)
Deposition	0.2	427	2.9	0.10	1.2	41.3
ERMS discharge	0.2	338	1.8	0.08	0.6	31.9

peak power current (I_{pd}) as those used during film deposition. Since these parameters are the most influential ones regarding the degree of ionization of the sputtered species, it is expected that the energy-resolved mass analysis results obtained at the Lawrence Berkeley National Laboratory are representative of the experimental conditions during Cr films deposition at the University of Coimbra. Thus, in the following sections we assume that the plasma conditions in both chambers are comparable.

The DCMS depositions were simulated using two Monte Carlo-based software packages. The interaction of the Ar^+ plasma ions with the Cr target was modelled using the SRIM 2013 software package [21] in surface sputtering mode. The energy of the incident ions was set to be equal to the experimental target deposition voltage times the ion charge state. The impact of 10^6 argon ions was computed in each simulation. The interaction of the sputtered species with the discharge gas along their paths to the substrate were computed using the SIMTRA (version 2008) software package [22]. Only neutral Ar was considered as buffer gas and gas heating was taken into account. The real physical dimensions of the deposition system used in this work (chamber size and shape, target size and shape, substrate size and shape, target to substrate distance) were entered in the SIMTRA software. In order to model the deposition process as realistic as possible, the shape of the racetrack was also taken into account by measuring an actual profile which was also used as input to the SIMTRA program. The initial energies and angles of the sputtered Cr atoms were taken from the results of the SRIM simulations. In the SIMTRA software the particle trajectories are followed until their energy falls below 0.0385 eV, after which they are considered thermalized and diffuse to the substrate without further energy variation. In this work all particles with energies above this value were taken as non-thermalized.

The crystal structure of Cr films was analysed by X-ray diffraction (XRD) (PANalytical X'Pert PRO MPD) using Cu Kα radiation (45 kV and 40 mA) with a parallel beam in θ–2θ geometry. The incident beam optics consisted of a hybrid monochromator (with a Cu W/Si mirror and a double crystal Ge (220). A parallel plate collimator (0.7°) and Soller slits (0.004°) were mounted in the path of the diffracted beam. A PIXcel detector in receiving slit mode was used for X-ray collection.

The thickness and morphology of the films were studied by scanning electron microscopy (SEM) using a Quanta 400 FEG ESEM. The films' surface topography was characterized by AFM (Bruker Innova) with a Si tip of nominal 6 nm radius used in contact mode. Several 2 μm × 2 μm scans were acquired on the surface of each film to ensure surface representation. The 2D auto-correlation function was calculated from the AFM scans using the Gwyddion [23,24] software (version 2.40) after levelling the surface. The methodology proposed by Bubendorff et al. [25] was used to extract the mean distance between adjacent surface features (D_x).

The hardness and Young's modulus of films were evaluated by depth-sensing indentation technique (Micro Materials NanoTest) using a Berkovich diamond pyramid indenter. In order to avoid the effect of the substrate, the applied load (10 mN) was selected to keep the indentation depth to less than 10% of the film's thickness. 16 hardness measurements were performed for each specimen.

3. Results

3.1. Ion flux characterization

The time-averaged ion energy distributions functions (IEDFs) for Cr^+, Cr^{2+}, Ar^+ and Ar^{2+} ion species obtained from the DCMS plasma at 0.2 Pa and from the DOMS plasma at 1.0 Pa during Cr sputtering are shown in Fig. 2. In both cases the IEDFs are dominated by singly charged ions. However, the DCMS plasma is dominated by Ar^+ ions, which account for approximately 94% of the ion flux, while the DOMS plasma is dominated by Cr^+ ions which account for approximately 66% of the ion flux, more than twice the Ar^+ contribution. As expected, many more Cr^+ ions are generated in DOMS than in the DCMS (note that the Cr^+ ion counts obtained in DCMS were multiplied by 10 in Fig. 2 to make them better visible). The doubly charged ions only account for a minor contribution to the ion flux (≈3% of the ion flux in both DCMS and DOMS). Thus, these ions hardly have any influence on chromium film properties and are not further discussed in the following text.

The Ar^+ IEDFs exhibit a single narrow low-energy peak extending up to ≈7 eV corresponding to thermalized ions after being accelerated in the sheath between the plasma to the EQP's entrance plate. The energetic position of the peak, which approximately corresponds to the plasma potential, is slightly higher in DCMS (4.4 eV) than in DOMS (3.5 eV). Besides a similar low energy peak corresponding to thermalized ions, high energy tails are also observed in the IEDFs of the Cr^+ ions. The origin of the high energy tails usually found in the IEDFs of many metallic ions sputtered by HiPIMS is still an open issue. Several mechanisms have been proposed to explain the presence of energetic metal species, including high energy sputtered atoms, reflected ions at the target or spoke-related effects [26].

To facilitate the direct comparison, the Cr^+ IEDFs obtained in DOMS and DCMS after normalization to unit area are shown in Fig. 3. Both normalized IEDFs extend up to 20 eV and in both cases the vast majority of ions have energies less than 15 eV. The contribution from thermalized and energetic Cr^+ ions are clearly separated in DOMS, as the low energy peak associated with thermalized ions is dominant. Although the contributions from thermalized and energetic Cr^+ ions are also discernable in DCMS, they account for similar fractions of the IEDF and thus are much more difficult to resolve. In order to quantitatively compare the

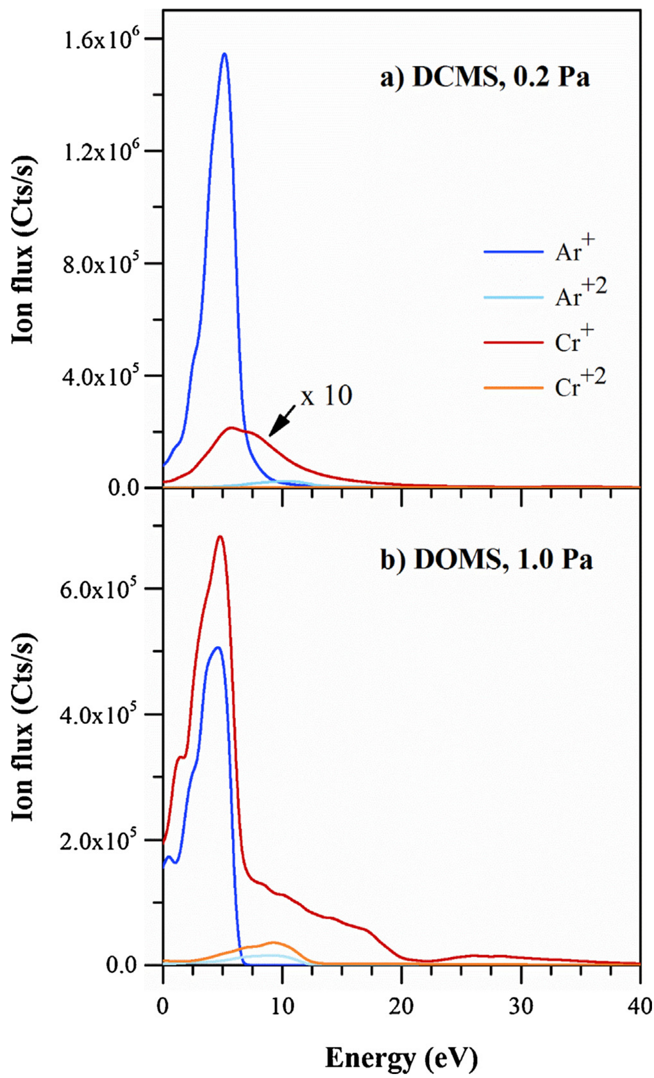

Fig. 2. IEDFs of $^{40}Ar^+$; $^{40}Ar^{2+}$; $^{52}Cr^+$ and $^{52}Cr^{2+}$ species measured in a) DCMS at 0.2 Pa and b) DOMS at 1.0 Pa during sputtering a Cr target in pure Ar atmosphere.

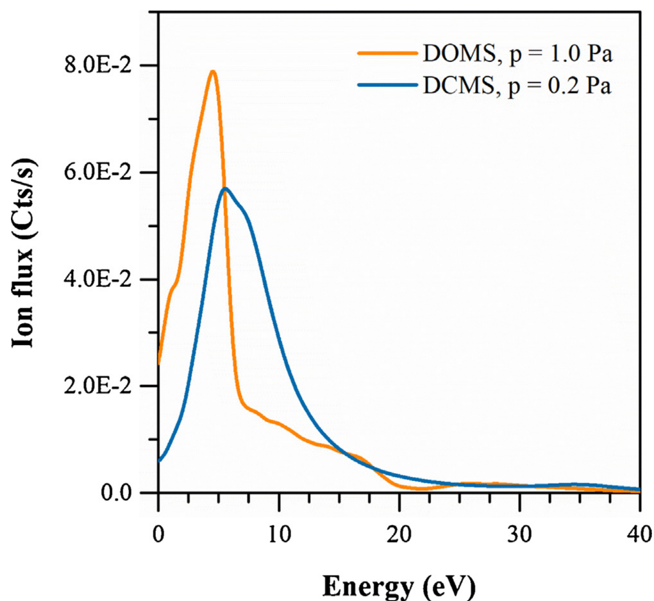

Fig. 3. IEDFs of the Cr^+ ions obtained from the DOMS and DCMS plasmas normalized to unit area.

Table 3
Average energy of the Cr^+ ions total (E_{Cr+}), ballistic ($E_{Cr+}{}^{energ}$) and diffusive ($E_{Cr+}{}^{therm}$) fluxes and% of ballistic Cr^+ ions in the total flux.

Sample	E_{Cr+} (eV)	$E_{Cr+}{}^{energ}$ (eV)	$E_{Cr+}{}^{therm}$ (eV)	% of ballistic Cr^+ ions
DCMS02	9.2	13.2	4.8	53%
DOMS10	6.8	14.9	3.7	28%

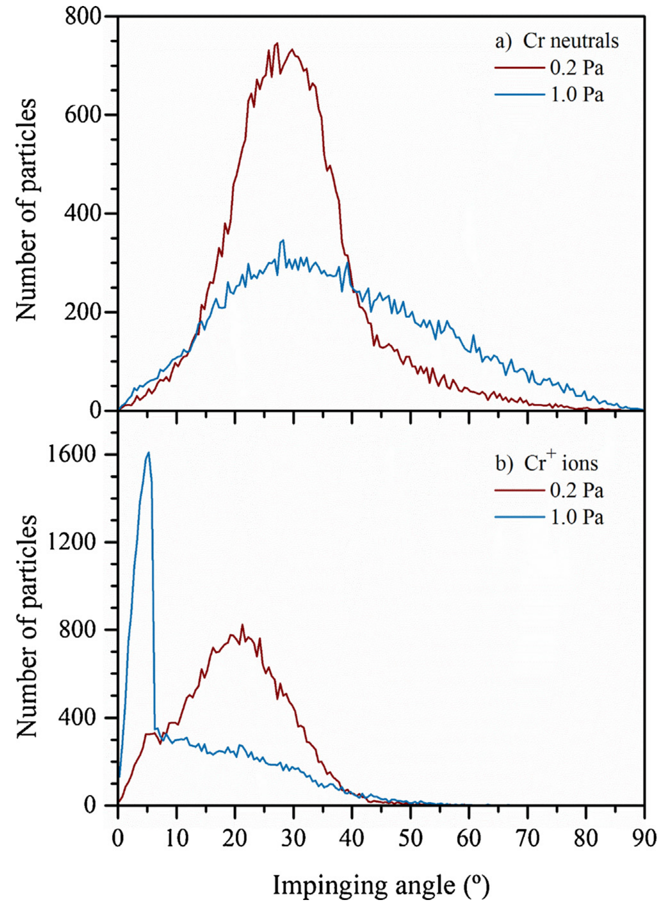

Fig. 4. Simulation of the angle distribution of the a) Cr neutrals and b) Cr^+ ions upon impinging on the growing film at 0.2 and 1.0 Pa.

thermalized and energetic Cr^+ contributions they were fitted using a Maxwell-Boltzmann and a Thompson distribution [27], respectively. The average energy of the Cr^+ ions, Cr^+ thermalized ions and Cr^+ energetic ions are shown in Table 3 together with the percentage of energetic Cr^+ ions in the total Cr^+ flux.

3.2. Angle distributions of the impinging Cr species

In DCMS at low pressure the Cr species flux is dominated by particles that travel along the line-of-sight between the racetrack and the substrate. For these particles the impinging angle relative to the substrate normal (α) is limited by the dimensions and relative positions of the substrate and racetrack, varying between 5.5 and 45.5° due to the off-axis positioning of the substrate in relation to the racetracks (see Fig. 1). The angle distributions of the Cr species impinging on the substrate obtained by simulation of the DCMS depositions are shown in Fig. 4a. Taking into account that the initial emission angle is also influenced by the shape of the racetrack, which was accounted for in the simulations, the simulation results confirm the above considerations as the majority of the Cr species impinge on the substrate in the angle range between 12° and 45°. Most of the Cr species impinging on the substrate at angles out-

side of this range are thermalized particles which can impinge on the substrate at any incident angle between 0 and 90°. Increasing the process pressure to 1.0 Pa results in a much broader impinging angle distribution with far fewer particles arriving at the substrate by line-of-sight and a well-developed high angle component. This result reflects the decrease of the mean free path for Cr species and the higher number of collisions with the gas neutrals (Ar) at higher pressure.

In DCMS the vast majority of the Cr species arriving at the substrate are neutrals and thus they are not influenced by the potential difference across the substrate sheath. In DOMS, in contrast, a substantial part of the Cr species is ionized by electron impact near the ionization zone, and, thus, the resulting ions are attracted towards the growing film in the substrate sheath and arrive at the substrate at angles β such that β < α. In order to investigate the effect of the sheath acceleration on the Cr^+ ions trajectory, their impinging angle distribution was calculated by assuming that (i) they arrive at the substrate's sheath edge with identical energy and impinging angle as the Cr neutrals and that (ii) they are then accelerated in a collisionless sheath. The incident angle of the Cr^+ ions (β) was calculated from classical equations for the motion of a charged particle in a uniform electric field using the following relation:

$$\tan\left(\beta\right) = \frac{\sin\left(\alpha\right)}{\sqrt{\cos^2\left(\alpha\right) + \frac{Qe\Delta V}{E_0}}}$$

where E_0 is the initial energy of the ions, ΔV the potential drop at the substrate and Q the ion charge state number ($Q = 1$ for Cr^+ ions). An explicit derivation of Eq. (1) is given in Appendix A. The resulting impinging angle distributions at 0.2 and 1.0 Pa, assuming that the potential drop at the substrate is equal to the plasma potential in DOMS ($\Delta V = 3.5$ V, see section 3.1), are shown in Fig. 4b. The impinging angle distribution at 0.2 Pa is strongly "compressed" to smaller angles as compared to the angle distribution obtained for the neutrals. Although the trajectories of all ions are deflected to smaller impinging angles by the Coulomb force, this effect is more pronounced for ions with higher initial angles since they are accelerated for a longer time. Besides being "compressed" to smaller angles, the impinging angle distribution of the ions at 1.0 Pa also develops an intense narrow peak at small angles (centered close to 5°). As will be shown later, this peak is associated with thermalized Cr^+ ions. At both pressures, there are almost no ions impinging on the substrate at angles greater than 60°, i.e., the large-angle component of the impinging angle distribution is suppressed by ion acceleration in the electric field of the sheath.

The impinging angle distribution of the thermalized and energetic (non-thermalized) Cr neutrals and ions obtained at 1.0 Pa are shown in Fig. 5(a) and (b), respectively. To facilitate comparison, the overall angle distributions already shown in Fig. 4 were also plotted. As expected, the angle distribution of the thermalized neutrals (Fig. 5(a)), which account for 37% of the total Cr species, is symmetrical and peaks at 45°, in accordance to their diffusive path to the substrate. Also as expected, the angle range corresponding to Cr energetic neutrals traveling along line-of-sight trajectories from the target to the substrate is much better defined than in the overall distribution. Note that the thermalized Cr species account for more than 2/3 of the Cr neutrals impinging on the substrate at angles greater than 70°, i.e., they account for most of the large angle component of the overall Cr distribution.

As can be observed in Fig. 5(b), the acceleration in the substrate's sheath has dramatic effect on the angle distribution of thermalized ions. Their impinging angle after acceleration is close to 5° irrespectively of their initial trajectories and, thus, they are responsible for the intense and narrow peak in the overall ions angle distributions. This is due to their very low initial velocity that give rise to a longer acceleration period, much like in the case of high impinging angles mentioned above. Note that a narrow peak near 5° is also observed in the impinging angle distribution of the ions at 0.2 Pa (Fig. 4(b)) although with a low intensity as a much smaller number of thermalized Cr^+ ions arrive at the substrate at low pressure. The angle distribution of the non-thermal ions is also considerably compressed to lower impinging angles although it still extends to slightly greater than 50°.

Table 4
Thickness, roughness (R_a) and distance between columns centres (D_x) in the rotation direction for the Cr films.

Sample	Thickness (nm)	R_a (nm)	D_x (nm)
DCMS02	770	6.3	102
DOMS10	1110	5.2	106

3.3. Microstructure and surface morphology

Top-view and cross-section micrographs of the Cr films deposited by DOMS at 1.0 Pa and DCMS at 0.2 are shown in Fig. 6. The arrows in the surface micrographs indicate the direction in the film surface tangent to the circular motion of the substrate during deposition, which will be referred to hereafter as the X or rotation direction. The direction in the film surface parallel to the substrate rotation axis will be referred to as the Y-direction. The cross-section micrographs of the films show well-defined columns of comparable widths which extend from the bottom to the top of the films. Most of the columns end up in three-sided pyramidal-like tops although two of the sides are considerably elongated along the direction perpendicular to substrate rotation. The inter-column distance is larger along the X-direction while the columns tops are interconnected along the Y-direction.

AFM scans of the surface of the Cr films (not shown here) were acquired in order to characterize in a more quantitative way the surface morphology of the Cr films. The surface roughness (Ra) calculated from the AFM scans is shown in Table 4 along with the distance between the column centres (D_x) in the rotation direction (X-direction) calculated from the 2D autocorrelation function of the AFM micrographs. Additionally, the thickness of the films is also reported in Table 4.

A value of D_x close to 100 nm was found for both films, confirming the similar separation distance between column centres inferred from the films' surface micrographs. In spite of the higher process pressure, the Cr film deposited by DOMS has a significantly lower roughness than the roughness of the DCMS film.

3.4. Structure

Besides the Si substrate peaks, all the peaks in the XRD patterns of the Cr films studied in this work (Fig. 7) could be indexed to the b.c.c. Cr phase (ICCD card n° 21-1457). The Cr (110) peak is dominant in both the XRD spectrum of the film deposited at 0.2 Pa by DCMS and that of the film deposited by DOMS at 1.0 Pa. The Cr (211) peak is also detected in both diffractograms although with much lower intensity in the DCMS diffractogram. The preferred orientation (PO) of the films was evaluated by dividing the measured intensity of each peak by the sum of experimental intensities and then by the intensity fraction of each peak in the Cr ICCD card. The PO coefficients for each peak are shown in Table 5. A PO coefficient higher than 1 indicates a preferred orientation along the corresponding direction. The lattice parameter of the film calculated from the Cr (110) is also shown in Table 5.

The Cr film deposited by DCMS has a well-developed [110] PO characteristic of Cr thin films deposited by DCMS without substrate heating. The (110) planes have the lowest energy in the b.c.c.-based structures [28] and, for Cr, the (110) PO develops in the

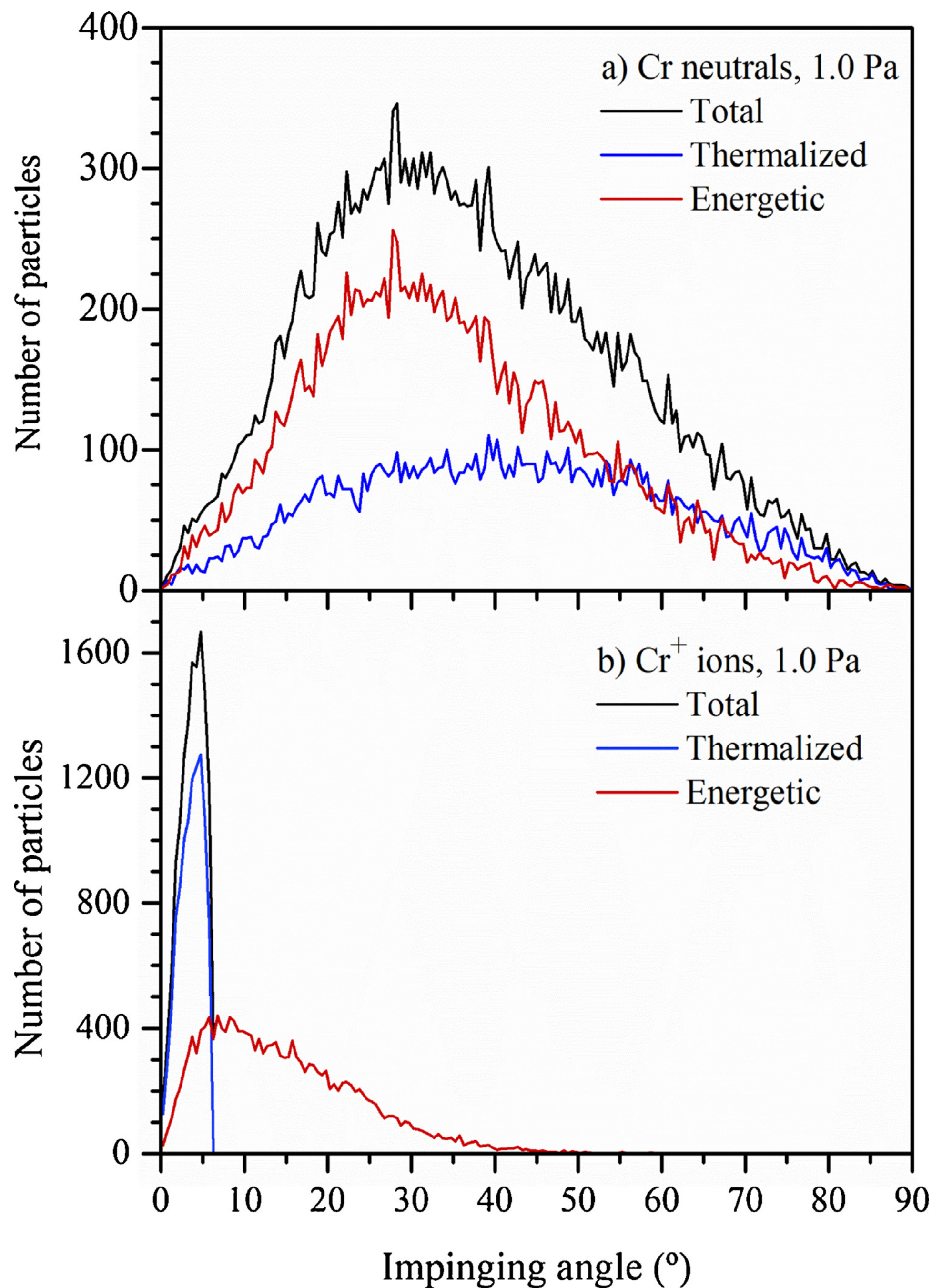

Fig. 5. Simulation of the angle distributions of the thermalized and energetic a) neutrals and b) ions upon impinging on the growing film at 1.0 Pa.

Table 5
Preferred orientation (PO) coefficients and a(110) lattice parameter for the Cr films.

Sample	PO coefficients			$a_{(110)}$ (nm)
	(110)	(211)	(222)	
DCMS02	1.29	0.11	0.46	0.2890
DOMS10	0.92	0.80	3.33	0.2889

early stages of the film growth, either due to energy minimization before island coalescence or by competitive growth in the subsequent stages of film growth [29]. The $a_{(110)}$ lattice parameter (i.e. in the growth direction) of this film is significantly higher than the lattice parameter of the unstrained material (a = 0.2885 nm) indicating that compressive stresses were form during the growth process. The Cr (110) is also the most intense diffraction peak in the diffractogram of the film deposited by DOMS. The (111) family of plans of the b.c.c. lattice of Cr does not diffract and thus the PO of the films has to be evaluated taking into account the (222) diffraction peak. As the Cr (222) peak intensity is only 6% of the intensity of the Cr (110) in the Cr ICCD card, the Cr film deposited by DOMS has a well-developed [111] PO.

The [111] PO is characteristic of Cr films deposited at higher pressure or with higher thickness and is generally associated with the deposition of an open, porous microstructure unable to sustain stress. The $a_{(110)}$ lattice parameter of this film is similar to that

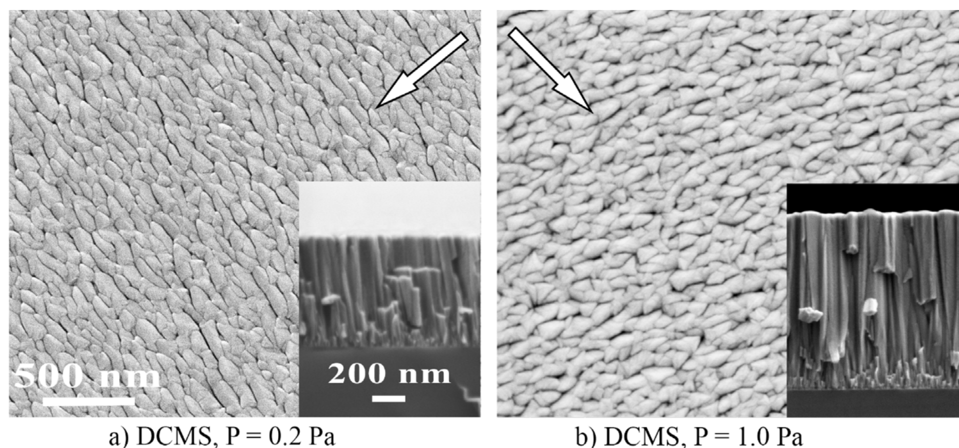

Fig. 6. SEM micrographs of the Cr films deposited by DOMS at 1.0 Pa and DCMS at 0.2 Pa.

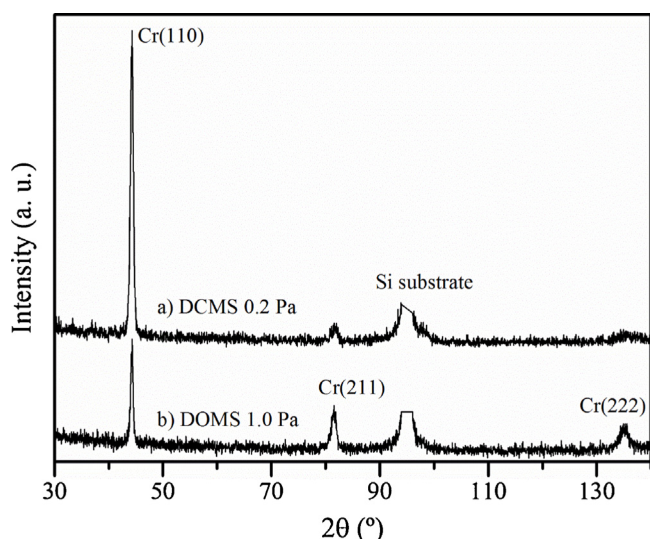

Fig. 7. Diffractograms of the Cr thin films deposited by DOMS and DCMS at 0.2 and 1.0 Pa.

Table 6
Deposition rate and mechanical properties (Youngís modulus and hardness) of the Cr films.

Sample	Dep. Rate (nm/min)	Youngís Mod. (GPa)	Hardness(GPa)
DCMS02	64.2	228	12.2
DOMS10	37	260	12.3

obtained for the film deposited by DCMS, i. e., the film deposited by DOMS is also under compression.

3.5. Deposition rate and mechanical properties

The deposition rate, hardness and Young's modulus of the Cr films studied in this work are compiled in Table 6. The deposition rate of the Cr film deposited by DOMS is only 58% of the deposition rate of the film deposited by DCMS. The loss of deposition rate in HiPIMS, as compared to DCMS, is a well-known result and can be attributed to several effects [30–32]. The most influential ones are the back attraction of the sputtered material after ionization in the target sheath (”return effect”) and the loss of sputtering efficiency due to the higher voltages typically used in HiPIMS deposition (“yield effect”). Lintymer et al. [33] have shown that porosity is the dominant microstructural feature influencing the Young modulus of sputtered Cr thin films. The Cr film deposited by DCMS in this work has a much lower Young's modulus than the bulk material (280 GPa) and thus it contains some porosity. As the film was deposited at low pressure and, as shown above, it is under compression, most of the porosity should be intra-granular rather than inter-columnar [34]. The Youngís modulus of the film deposited by DOMS is much closer to that of bulk Cr indicating that a denser film was deposited. Note that the higher density of the Cr film deposited by DOMS also contributes to the loss of deposition rate, as compared to DCMS, since the deposition rate was calculated by dividing the film thickness by the deposition time. It is well known that the hardness of Cr films deposited by DCMS decreases with increasing pressure due to the development of a porous microstructure under a more intense shadowing effect [35]. For example, the hardness of Cr films deposited by DCMS at 1.0 Pa by the authors in another study was close to 6 GPa [9], i.e, much lower than the hardness of the film deposited in this work at 0.2 Pa by DCMS (12.2 GPa). However, the hardness of the Cr film deposited by DOMS at 1.0 Pa in this work (12.3 GPa) is similar to that obtained at 0.2 Pa by DCMS.

4. Discussion

In thin film deposition by magnetron sputtering-based processes at low T_s/T_m, which is the case for the films deposited in this work, the mobility of the ad-atoms on the growing film surface is low and the impinging species tend to stick close to their point of impact. In such systems, the properties of the films are mostly dictated by the shadowing effect and re-deposition, as mentioned in the introduction section. Until now, the term "shadowing effect" has been used in this work to denote both the deposition mechanism responsible for column formation, which does not change during film growth, and the actual shadowing effect by the hills on the film surface which increases during film growth as the height of the hills increases. In the following discussion, the former will be explicitly referred as "shadowing mechanism" while the later will be referred as "shadowing effect", as is usually the case. Accordingly, the shadowing effect at any film growth stage is the result of the interplay between the shadowing mechanism and the bombardment-induced deposition mechanisms, such as re-deposition.

The aim of the present work was to identify the main deposition mechanism responsible for the quite different surface properties of Cr films deposited by DOMS and DCMS as shown in a previous work [9]. In the following discussion, the characteristics of the chromium ion fluxes produced in DOMS and DCMS are first discussed, aiming at comparing the bombardment that the Cr films

undergo. Then the effect of ionizing the sputtered Cr on the angle distribution of the bombarding species is evaluated in view of its implications regarding the shadowing mechanism. The properties of the Cr films deposited by DOMS and DCMS are then compared in order to elucidate the role of the different deposition mechanisms in each deposition process. Finally, some of the implications of the results obtained in this work are also discussed.

4.1. Average energy and re-sputtering mechanism

Although the average energy is not a universal parameter for describing ion-assisted film growth [36], the IEDFs of the Cr^+ ions obtained in this work in DCMS and DOMS are similar and thus this parameter will be used in the following discussion. The average energy of the Cr^+ ions is higher by 2.4 eV in DCMS than in DOMS (Table 3). However, the lower average energy measured for the Cr^+ ions in DOMS is mainly due to the lower fraction of energetic ions in the overall Cr^+ flux, 28% in DOMS as compared to 53% in DCMS, which is a consequence of the shorter mean free path of the Cr species at higher pressure. In fact, the energetic Cr^+ ions average energy in DOMS is even higher than in DCMS although by only 1.7 eV. Even after taking into account the higher plasma potential in DCMS, the average energy difference between energetic Cr^+ ions in DOMS and DCMS at the EQP location should not exceed $\approx$ 3 eV. Similar average values of the Cr^+ ions in DOMS and DCMS are not surprising. DOMS deposition was deliberately performed at the lowest peak target power that still allowed us to operate the power supply in DOMS mode in order to minimize the difference between the average Cr^+ ion energy in DOMS and DCMS modes.

As mentioned in the Introduction, re-deposition is a non-local deposition mechanism and, as such, it reduces the shadowing effect during film growth. The occurrence of re-sputtering during film deposition depend mainly on two factors: the sputtering threshold of the material being deposited and the average energy of the energetic species imping on the growing films. As shown in section 3.2, the chromium ion flux generated in both DOMS and DCMS are composed of thermalized and energetic species. The former have very low average energies, well below the threshold energy for Cr self-sputtering (which is close to 22 eV [37]) and, thus, they cannot trigger the re-sputtering mechanism. Assuming a similar potential drop at the EQP and substrate sheath, the average energy of the energetic Cr^+ ions in Table 3 may be taken as the average energy of the Cr^+ ions impinging on a substrate placed at 2 cm from the target, the distance between the location of EQP collection orifice and the target. Although energy-resolved mass analysis measurements and the Cr film depositions were carried out in different deposition systems, the experimental conditions were chosen in order to achieve similar ionization degrees of the sputtered material and similar energies of the sputtered species, as explained in section 2. Since the chromium ions lose energy upon traveling inside the deposition chamber due to collisions with the process gas, their average energies upon impinging on the substrate placed at 8 cm from the target during the deposition process are lower than those reported in Table 3. Therefore, they are also considerably lower than the threshold energy for Cr self-sputtering and thus the energetic Cr^+ ions impinging on the growing cannot trigger the re-sputtering mechanism. The same conclusion applies to the Cr neutrals as they are not sensitive to the electric field at the substrate sheath and thus they do not gain energy upon acceleration in the substrate sheath like the Cr^+ ions do. Since the substrates were not biased during deposition and the flux of neutralized Ar ions reflected at the target is less than 3% of the sputtered Cr flux, as shown in the SRIM simulations, none of the species impinging on the growing film can trigger the re-sputtering mechanism. Therefore, the properties of the Cr films are mostly determined by the strength of the shadowing mechanism during deposition.

4.2. Impinging angle distribution and atomic shadowing mechanism

The impinging angle distributions of the Cr atoms upon colliding with the substrate at 0.2 and 1.0 Pa obtained from the simulations using the SRIM and SIMTRA software packages agree well with the general picture about metal film deposition by DCMS. The flux of particles arriving at the substrate can be viewed as the sum of two fluxes: a ballistic flux comprising of the particles that travelled by line-of-sight to the substrate, and a diffusive flux, encompassing particles that were thermalized due to collisions in the gas phase and subsequently travelled to the substrate by diffusion [38]. Increasing the pressure – distance product ($p \times d$) increases the diffusive flux component in the overall flux, whereas decreasing this product results in a flux of particles with ballistic trajectories. The results presented in section 3.2 show that ionizing the sputtered material strongly affects the interaction of both fluxes with the growing film. The Cr^+ ions are deflected towards the substrate and, thus, their impinging angle distribution is shifted to lower impinging angles. This effect is more pronounced for ions arriving at the sheath at higher impinging angles and/or with lower energies as they are accelerated for a longer period of time. Therefore, due to their much lower velocity, the trajectories of thermalized Cr^+ ions are most efficiently deflected towards the substrate and they all impinge on the growing film at angles close to the substrate normal, irrespectively of their direction upon arrival at the sheath.

According to the simulation results for the deposition system used in this work, almost all of the ions impinge on the substrate at angles smaller than 50° (Fig. 4). The atomic shadowing mechanism relies on the capture of particles on the top of the hills that form during growth, particles that would otherwise end up filling the valleys, i.e., the underdense regions. This effect is more pronounced if the particles arrive at the growing film at high impinging angles relative to the substrate normal. For example, in the work of Bubendorff et al. [25], who studied the effect of substrate tilting on the microstructure of Fe films deposited by DCMS, the distance between column centres exponentially raised at tilting angles above 60°, indicating an exponential dependence of the shadowing effect on the impinging angles of the particles. Assuming a similar relationship in our deposition system, both the ballistic and diffusive Cr^+ fluxes will have almost no contribution to the shadowing effect due to the loss of the high-angle component in their impinging angle distributions upon acceleration of the ions in the sheath. Note, however, that the ballistic Cr^+ can contribute to the shadowing effect in depositions systems with higher line-of-sight angles between the target and the substrate such as, for example, when bigger targets or shorter substrate to target distances are used. On the contrary, the impinging angle distribution of thermalized Cr^+ ions is always close to the substrate normal irrespectively of the geometrical setup in the deposition chamber.

Of course, not all the sputtered species are ionized when using HiPIMS. Although high ionization degrees were reported in the literature for metals, such as 80% for Ti [39], in most cases the ionization degree is much lower. The Cr film growth by DOMS in this work made use of a relatively low peak power in order to achieve a low average energy of the Cr species, comparable to the average energy of the Cr species in DCMS. However, the degree of ionization in the DOMS plasma is still significant as the flux of Cr^+ is close to two orders of magnitude higher than in DCMS (see Fig. 4). It is then plausible that the ionization of the sputtered material during the growth of the Cr film deposited by DOMS in this work could significantly decrease the shadowing effect.

4.3. Cr films properties and atomic shadowing

The surface morphology of the Cr films is highly anisotropic and may be described as ridges of well-packed columns separated by deep valleys extending along the Y-direction. As shown in a previous work, this anisotropic microstructure is a direct result of the higher shadowing effect along the rotation direction [9]. The microstructure and properties of the Cr film deposited by DOMS at high pressure (1.0 Pa) are very similar to those of the film deposited by DCMS at low pressure (0.2 Pa). Both films have well-packed columnar microstructures with similar distances between column centres. They also have similar values of the $a_{(110)}$ lattice parameter, which are higher than in unstrained Cr. Finally, the films have similar hardness (close to 12 GPa), higher than most values reported in the literature for Cr films deposited by DCMS [9]. These results show that the shadowing effect in the films is not much different despite the much higher pressure used in DOMS. Furthermore, it is well known that the shadowing effect increases with increasing pressure and thus leads to the deposition of films with higher roughness at similar thicknesses. Taking into account the significantly greater thickness of the Cr film deposited by DOMS (Table 4), the strength of the shadowing mechanism is even lower in DOMS at high pressure as confirmed by the lower surface roughness (Table 4) and the higher Young's modulus (Table 6).

In spite of the similar properties listed above, the Cr films develop completely different POs during growth. Zhao et al. [34] reported a texture turnover from a complete [110] PO at small thickness to a complete [111] PO at large thickness for a Cr thin film deposited by DCMS under conditions similar to the ones used in this work. The [111] PO of the film deposited by DOMS in this work may be due to its greater thickness, allowing the texture to change. Note however that the Cr film deposited by DOMS in this work has a dense and compact microstructure in contrast to the Cr film deposited by Zhao et al. [34], which had a pronounced porous columnar microstructure and was unable to sustain stress.

4.4. Atomic shadowing control in DOMS (HiPIMS)

Taking into account that the energy of the Cr species impinging on the growing film is not high enough to trigger re-sputtering, as discussed in section 4.1, and that the shadowing mechanism strength is even lower in DOMS at high pressure than in DCMS at low pressure, as concluded in the previous section, a mechanism has to be effective in DOMS that is specific to the DOMS deposition process and able to efficiently undermine the strength of the shadowing mechanism. This mechanism is most probably the acceleration of the Cr^+ ions at the substrate sheath which, as explained in section 4.2, significantly reduces the high angle component of the ions impinging angle distribution and, thus, efficiently reduces the atomic shadowing mechanism strength. The atomic shadowing effect which develops during film growth, is thus prevented not by counteracting the atomic shadowing mechanism, as is usually the case in DCMS upon substrate biasing or upon another kind of high energy particle bombardment, but rather by decreasing the strength the atomic shadowing mechanism itself. Although both the energetic (ballistic) Cr ions and the thermalized ones contribute to weaken the shadowing mechanism, the later assume a much more prominent role. On one hand, thermalized neutrals are the primary particles influencing the strength of the atomic shadowing mechanism since the majority of particles impinging on the growing film at high angles in DCMS are thermalized. On the other hand, the thermalized ions are most efficiently influenced by the electric field at the substrate sheath. They end up impinging on the substrate at angles near the normal, and thus, they have almost no contribution to the shadowing effect. As a result, ionizing the sputtered species is an efficient way of decreasing the shadowing mechanism, especially at higher pressure since the sputtered flux arriving at the substrate's sheath edge has a higher diffusive (thermalized) component and lower energy ions.

In a previous study [40] we have shown that dense and hard CrN films could only be obtained by DCMS in the same deposition system used in this work when working at low pressure (0.3 Pa) and high substrate biasing (−80 V). In contrast, the CrN films deposited by DOMS at 0.3 and 0.7 Pa without substrate biasing had very similar and dense microstructures and, accordingly, similarly high hardness. In DOMS, and more generally in HiPIMS, the shadowing mechanism is mostly controlled by the ionization degree of the sputtered material and can even decrease with increasing pressure, as both the fraction of thermalized ions and the degree of ionization of the sputtered material increase. In fact, in HiPIMS at high ionization degree, substrate biasing may even be superfluous with regard to controlling the atomic shadowing effect as the shadowing mechanism is already efficiently prevented. Therefore, in DOMS or, more generally in HiPIMS, the shadowing effect is regulated by the ionization degree of the sputtered material instead of process pressure and substrate biasing as is usually the case in DCMS.

Finally, another interesting point is that the reduced shadowing effect at high ionization degree of the sputtered species also contributes to the deposition of characteristically denser films in HiPIMS than in DCMS [9], although the increased energy of the film-forming species is more frequently invoked in the literature. In fact, a high degree of ionization could even result in almost shadowing effect-free films deposition, as can be inferred from Fig. 4(b), and, thus, allow us to deposit dense and compact films without the need of high energy particles bombardment during growth. Note however, that increasing the ionization degree in HiPIMS also brings about an increase of the average energy of the ionized species, in an analogous way as decreasing the process pressure also increases the average energy of the deposited particles in DCMS. Accordingly, Cr films deposited by DOMS at high pressure and high peak power also develop high compressive stresses, as previously shown [9]. Nevertheless, a proper balance of the ionization degree vs. average energy of the ionized species in HIPIMS allows us to grow thin films under deposition conditions which are not available in DCMS, such as the Cr film deposited by DOMS at 1.0 Pa in this work.

5. Conclusions

As shown by Monte Carlo simulations and ERMS measurements, the chromium ion flux generated in both DOMS and DCMS is composed of thermalized and energetic species. In both cases, the average energies of the Cr^+ ions are well below the threshold energy for Cr self-sputtering and, thus, they cannot trigger the re-sputtering mechanism. The same conclusion applies to the Cr neutrals as the Cr^+ ions lose less energy upon traveling inside the chamber, due to their lower collision cross-section with gas neutrals (Ar). Therefore, the properties of the Cr films deposited in this work are mostly determined by the strength of the shadowing mechanism during deposition.

The microstructure and properties of the Cr film deposited in this work by DOMS at high pressure (1.0 Pa) are very similar to those of the film deposited by DCMS at low pressure (0.2 Pa). Although the Cr film deposited by DOMS developed a [111] PO, this film has a dense and compact microstructure in contrast to the pronounced porous columnar microstructure usually obtained in Cr films with [111] PO deposited by DCMS. These results show that the shadowing effect in the films is not much different despite the much higher pressure used in DOMS.

Ionizing the sputtered material strongly affects the interaction of both thermalized and energetic species fluxes with the growing film. The acceleration of the Cr^+ ions in the substrate sheath

significantly reduces the high angle component of the ions angle distribution and, thus, efficiently reduces the atomic shadowing mechanism strength. Although both the energetic Cr ions and the thermalized ones contribute to weakening the shadowing mechanism, the latter assumes a much more prominent role because ions end up impinging on the substrate at angles near the normal, and thus, they have almost no contribution to the shadowing effect.

In DOMS, and more generally in HiPIMS, the shadowing mechanism is mostly controlled by the ionization degree of the sputtered material and can even decrease with increasing pressure. In fact, in HiPIMS at high ionization degree, substrate biasing may even be superfluous with regard to controlling the atomic shadowing effect as the shadowing mechanism is already efficiently prevented. Thus, a high degree of ionization could even result in almost shadowing effect-free films deposition and allow us to deposit dense and compact films without the need of high energy particles bombardment during growth.

Acknowledgments

This research is sponsored by FEDER funds through the programCOMPETE – Programa Operacional Factores de Competitividade – and by national funds through FCT– Fundação para a Ciência e a Tecnologia, under the project: UID/EMS/00285/2013 and the Postdoc grant SFRH/BPD/111958/2015. Work at Lawrence Berkeley National Laboratory was supported by the U.S. Department of Energy, under Contract No. DE-AC02-05CH11231.

Appendix A. Derivation of the angle of ion impingement.

The height above the substrate (y) of an ion after penetrating the substrate sheath is given by the following projectile-like equation of motion:

$$y = d + V_{0y}t - \frac{1}{2}at^2 \quad (1)$$

where d is the sheath thickness, V_{0y} if the velocity of the ion in the y direction when arriving at the sheath and $\boldsymbol{a}$ is the acceleration due to the electrical field at the sheath. The velocities of the ion in the x and y directions at any point within the substrate sheath are given by:

$$V_x = V_{0x} = V_0 \sin\alpha \quad (2)$$

$$V_y = V_{0y} - at = V_0 \cos\alpha - at \quad (3)$$

where α is the angle relative to the substrate normal of the ion trajectory when arriving at the sheath and V_o its initial velocity. From Eqs. (1) and (3) it is possible to deduce that:

$$V_y^2 = (V_0 \cos\alpha)^2 - 2a(y - d) \quad (4)$$

Then the angle of impingement of the ion on the substrate (β) is given by:

$$\tan\beta = \frac{V_y}{V_x} = \frac{V_0 \cos\alpha}{\sqrt{(V_0 \cos\alpha)^2 - 2a(y - d)}} \quad (5)$$

The acceleration by the electric field is given by

$$a = \frac{Qe\Delta V}{md} \quad (6)$$

where e is the electronic charge, m the mass of the ion, ΔV the potential drop at the substrate and Q the ion charge state (Q = 1 for Cr^+ ions). On the other hand, the initial energy of the ion arriving at the sheath (E_0) is given by:

$$E_0 = \frac{1}{2}m\,V_0^2 \quad (7)$$

Using Eqs. (6) and (7), (5) can be reformulated as follow:

$$\tan\beta = \frac{\sin\alpha}{\sqrt{cos^2\alpha + \frac{qe\Delta V}{E_0}}} \quad (8)$$

This equation gives the angle of impingement of the ion at the substrate surface (β) as a function the angle of the ion trajectory when arriving at the sheath (α).

References

[1] J.A. Thornton, The microstructure of sputter-deposited coatings, J. Vac. Sci. Technol. A 4 (1986) 3059–3065.
[2] B.A. Movchan, A.V. Demchishin, Investigation of the structure and properties of thick vacuum-deposited films of nickel, titanium, tungsten, alumina and zirconium dioxide, Fizika Metallov i Metallovedenie (Phys. Met. Metall.) 28 (1969) 653–660.
[3] K.H. Müller, Molecular dynamics and collision cascade studies of ion-assisted thin film deposition, J. Vac. Sci. Technol. A 5 (1987) 2161–2162.
[4] R. Karunasiri, R. Bruinsma, J. Rudnick, Thin-film growth and the shadow instability, Phys. Rev. Lett. 62 (1989) 788–791.
[5] T. Karabacak, Thin-film growth dynamics with shadowing and re-emission effects, J. Nanophotonics 5 (2011), 052501-052501–18.
[6] M. Pelliccione, T. Karabacak, C. Gaire, G.-C. Wang, T.-M. Lu, Mound formation in surface growth under shadowing, Phys. Rev. 74 (2006) 125420.
[7] G. Janssen, J.-D. Kamminga, Stress in hard metal films, Appl. Phys. Lett. 85 (2004) 3086–3088.
[8] A. Anders, Atomic scale heating in cathodic arc plasma deposition, Appl. Phys. Lett. 80 (2002) 1100–1102.
[9] F. Ferreira, R. Serra, A. Cavaleiro, J. Oliveira, Additional control of bombardment by deep oscillation magnetron sputtering: effect on the microstructure and topography of Cr thin films, Thin Solid Films 619 (2016) 250–260.
[10] A. Myers, J. Doyle, J. Abelson, D.N. Ruzic, Monte Carlo simulations of magnetron sputtering particle transport, J. Vac. Sci. Technol. A 9 (1991) 614–618.
[11] J.A. Hopwood, The role of ionized physical vapor deposition in integrated circuit fabrication, Thin Films 27 (2000) 1–7.
[12] U. Helmersson, M. Lattemann, J. Bohlmark, A.P. Ehiasarian, J.T. Gudmundsson, Ionized physical vapor deposition (IPVD): a review of technology and applications, Thin Solid Films 513 (2006) 1–24.
[13] J. Bohlmark, M. Lattemann, J.T. Gudmundsson, A.P. Ehiasarian, Y. Aranda Gonzalvo, N. Brenning, U. Helmersson, The ion energy distributions and ion flux composition from a high power impulse magnetron sputtering discharge, Thin Solid Films 515 (2006) 1526.
[14] G. Greczynski, J. Jensen, L. Hultman, Mitigating the geometrical limitations of conventional sputtering by controlling the ion-to-neutral ratio during high power pulsed magnetron sputtering, Thin Solid Films 519 (2011) 6354–6361.
[15] J. Alami, P.O.Å. Persson, D. Music, J.T. Gudmundsson, J. Bohlmark, U. Helmersson, Ion-assisted physical vapor deposition for enhanced film properties on nonflat surfaces, J. Vac. Sci. Technol. A 23 (2005) 278–280.
[16] G. Janssen, A. Dammers, V. Sivel, W. Wang, Tensile stress in hard metal films, Appl. Phys. Lett. 83 (2003) 3287–3289.
[17] K. Sarakinos, J. Alami, P. Karimi, D. Severin, M. Wuttig, The role of backscattered en- ergetic atoms in film growth in reactive magnetron sputtering of chromium nitride, J. Phys. D 40 (2007) 778–785.
[18] G. Greczynski, J. Jensen, L. Hultman, Films prepared by DC magnetron sputtering and high-Power pulsed magnetron sputtering: a comparative study, IEEE Trans. Plasma Sci. 38 (2010) 3046–3056.
[19] F. Ferreira, R. Serra, J. Oliveira, A. Cavaleiro, Effect of peak target power on the properties of Cr thin films sputtered by HiPIMS in deep oscillation magnetron sputtering (DOMS) mode, Surf. Coat. Technol. 258 (2014) 249–256.
[20] Y. Ou, J. Lin, S. Tong, H. Che, W. Sproul, M. Lei, Wear and corrosion resistance of CrN/TiN superlattice coatings deposited by a combined deep oscillation magnetron sputtering and pulsed dc magnetron sputtering, Appl. Surf. Sci. 351 (2015) 332–343.
[21] J.F. Ziegler, M.D. Ziegler, J.P. Biersack, SRIM The stopping and range of ions in matter (2010), nuclear instruments and methods in physics research section B, Beam Interact. Mater. Atoms 268 (2010) 1818–1823.
[22] K. Van Aeken, S. Mahieu, D. Depla, The metal flux from a rotating cylindrical magnetron: a Monte Carlo simulation, J. Phys. D Appl. Phys. 41 (2008) 205307.
[23] D. Nečas, P. Klapetek, Gwyddion: an open-source software for SPM data analysis, Open Phys. 10 (2012) 181–188.
[24] P. Klapetek, Quantitative Data Processing in Scanning Probe Microscopy: SPM Applications for Nanometrology, William Andrew, 2012.
[25] J. Bubendorff, G. Garreau, S. Zabrocki, D. Berling, R. Jaafar, S. Hajjar, et al., Nanostructuring of Fe films by oblique incidence deposition on a $FeSi_2$ template onto Si (111): Growth, morphology, structure and faceting, Surf. Sci. 603 (2009) 373–379.
[26] C. Maszl, W. Breilmann, J. Benedikt, A. von Keudell, Origin of the energetic ions at the substrate generated during high power pulsed magnetron sputtering of titanium, J. Phys. D Appl. Phys. 47 (2014) 224002.

[27] M.W. Thompson, The energy spectrum of ejected atoms during the high energy sputtering of gold, Philos. Mag. 18 (1968) 377–414.
[28] B.-Q. Fu, W. Liu, Z.-L. Li, Calculation of the surface energy of bcc-metals with the empirical electron theory, Appl. Surf. Sci. 255 (2009) 8511–8519.
[29] Y. Feng, D. Laughlin, D. Lambeth, Formation of crystallographic texture in rf sputter-deposited Cr thin films, J. Appl. Phys. 76 (1994) 7311–7316.
[30] M. Samuelsson, D. Lundin, J. Jensen, M.A. Raadu, J.T. Gudmundsson, U. Helmersson, On the film density using high power impulse magnetron sputtering, Surf. Coat. Technol. 205 (2010) 591–596.
[31] A. Anders, Deposition rates of high power impulse magnetron sputtering: physics and economics, J. Vac. Sci. Technol. A 28 (2010) 783–790.
[32] D. Christie, Fundamentals of high power pulsed magnetron sputtering: visualization of mechanisms for rate reduction and increased ion fraction, Czech. J. Phys. 56 (2006) B93–B97.
[33] J. Lintymer, N. Martin, J.-M. Chappé, P. Delobelle, J. Takadoum, 'Nanoindentation of chromium zigzag thin films sputter deposited', Surf. Coat. Technol. 200 (2005) 269–272.
[34] Z. Zhao, S. Yalisove, Z. Rek, J. Bilello, Evolution of anisotropic microstructure and residual stress in sputtered Cr films, J. Appl. Phys. 92 (2002) 7183–7192.
[35] S.Y. Grachev, F. Tichelaar, G. Janssen, Stress in sputter-deposited Cr films: influence of Ar pressure, J. Appl. Phys. 97 (2005) 073508.
[36] I. Petrov, F. Adibi, J.E. Greene, L. Hultman, J.E. Sundgren, Average energy deposited per atom: a universal parameter for describing ion-assisted film growth, Appl. Phys. Lett. 63 (1993) 36–38.
[37] R. Stuart, G. Wehner, Sputtering yields at very low bombarding ion energies, J. Appl. Phys. 33 (1962) 2345–2352.
[38] J. Keller, R. Simmons, Sputtering process model of deposition rate, IBM J. Res. Dev. 23 (1979) 24–32.
[39] J. Bohlmark, J. Alami, C. Christou, A.P. Ehiasarian, U. Helmersson, Ionization of sputtered metals in high power pulsed magnetron sputtering, J. Vac. Sci. Technol. A 23 (2005) 18–22.
[40] F. Ferreira, J. Oliveira, A. Cavaleiro, CrN thin films deposited by HiPIMS in DOMS mode, Surf. Coat. Technol. 291 (2016) 365–375.

ANNEX G

F. Ferreira, A. Aijaz, T. Kubart, A. Cavaleiro, and J. Oliveira, "Hard and dense diamond like carbon coatings deposited by deep oscillations magnetron sputtering," Surface and Coatings Technology, 2017.

Surface & Coatings Technology xxx (xxxx) xxx–xxx

Contents lists available at ScienceDirect

Surface & Coatings Technology

journal homepage: www.elsevier.com/locate/surfcoat

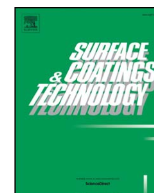

Hard and dense diamond like carbon coatings deposited by deep oscillations magnetron sputtering

Fábio Ferreira[a,*], Asim Aijaz[b], Tomas Kubart[b], Albano Cavaleiro[a,c], João Oliveira[a]

[a] SEG-CEMUC - Department of Mechanical Engineering, University of Coimbra, Rua Luis Reis Santos, 3030-788 Coimbra, Portugal
[b] The Ångström Laboratory, Uppsala University, P.O. Box 534, SE-751 21 Uppsala, Sweden
[c] LED&Mat-IPN, Instituto Pedro Nunes, Laboratório de Ensaios Desgaste e Materiais, Rua Pedro Nunes, 3030-199 Coimbra, Portugal

ARTICLE INFO

Keywords:
DLC
DOMS
Mass density
Hardness
Temperature stability

ABSTRACT

Recent developments in the automotive industry to improve engine efficiency and minimize pollutant emissions are driving the need for higher operating temperatures and loading densities in internal combustion engines. Future engines for internal combustion engines will require coatings with increased temperature stability (up to 500 °C) and wear resistance as compared to present day solutions. Hard tetrahedral DLC coatings (ta-C coatings) very low coefficient of friction and performed very well under mixed and boundary lubrication, and, thus, they are very attractive for automotive industry. In this work, DLC coatings were deposited by deep oscillations magnetron sputtering (DOMS), a variant of high power magnetron sputtering (HiPIMS). The main objective is to increase the sp^3 content in the films, as compared to d.c. magnetron sputtering (DCMS), and thus extend their operating range to higher temperatures. Increasing the bias voltage results in denser and smoother films with increasing hardness, as measured by nano-indentation, and increasing mass density, as measured by x-ray reflectivity. Accordingly, the UV Raman spectroscopy analysis of the films shows that the sp^3/sp^2 ratio in the films increases with increasing substrate biasing. However, the sp^3 bonds convert back to sp^2 upon annealing. Never the less, a significantly higher amount of sp^3 bonds is formed in the DLC films deposited by DOMS, as compared to the DCMS ones, showing that DOMS is a promising path for the development of hard DLC films.

1. Introduction

Recent developments in the automotive industry to improve engine efficiency, such as downsizing, start-stop engines, turbo-charging and the use of lower viscosity oils, all have similar effects on requirements for engine parts: operating temperatures and loading densities on components are getting increasingly higher [1]. Future engines for internal combustion engines (ICE) will require coatings with increased temperature stability (up to 500 °C) and wear resistance as compared to present day solutions. Hard tetrahedral DLC coatings (ta-C coatings) which are hydrogen-free and have a high amount of carbon sp^3 bonds. Besides their extremely smooth surfaces and their very low coefficient of friction [2–7], these coatings also performed very well under mixed and boundary lubrication and, thus, are very attractive for automotive industry [8]. They are very resistant to abrasive and adhesive wear, making them suitable for use in applications that involve extreme contact pressures, such as the piston's ring/cylinder wall interface in ICEs. The main limitation of hard hydrogen-free ta-C coatings is related to the high internal stresses, often in excess of 5–10 GPa [2]. The stress limits the maximum film thickness to a few hundred nanometres as delamination occurs when the internal stress exceeds a critical value.

Hard DLC (ta-C) coatings can only be deposited by highly ionized physical vapor deposition (PVD) deposition techniques, such as Cathodic Arc deposition, as the sp^3 content depends critically on the bombardment of ions with hyper-thermal energy during the deposition [7]. The main drawback of this deposition process is the ejection of “macro-particles” from the target which degrade films mechanical properties and increase the surface roughness beyond industry acceptable standards [9]. This drawback can be overcome by filtering the plasma. However, this solution is expensive and strongly decreases the deposition rate. DLCs with smooth surface can commonly be deposited by d.c. magnetron sputtering (DCMS), another PVD technique [10]. However, the present DLCs deposited by conventional magnetron sputtering have low sp^3 content (up to 45%) and, therefore, much lower film density (1.8–2.3 g/cm^3) and hardness (< 20 GPa) than DLCs deposited by Cathodic Arc [11–13]. This is due to the low ionization of carbon typical for standard magnetron sputtering deposition processes.

A recently developed technique called High Power Impulse Magnetron Sputtering (HiPIMS) has been proposed for hard DLC deposition [14–16]. In HiPIMS, a large fraction of sputtered atoms is

* Corresponding author.
E-mail address: fabio.ferreira@dem.uc (F. Ferreira).

https://doi.org/10.1016/j.surfcoat.2017.10.055
Received 18 June 2017; Received in revised form 30 September 2017; Accepted 17 October 2017
0257-8972/ © 2017 Published by Elsevier B.V.

ionized, thanks to 2–3 orders of magnitude higher plasma densities than in DCMS [17,18]. However, in the standard HiPIMS process based on Ar, the ionized fraction of C is very low (few percent), due to the low carbon ionization cross section by electron impact [19]. Recently, Konoshi et al. [20] have reported that the use of very short high voltage pulses in HiPIMS efficiently increased the sp^3/sp^2 fraction in the DLC films. On the other hand, Lin et al. [21] reported that hard DLC films could be deposited by Deep Oscillations Magnetron Sputtering (DOMS), a variant of HiPIMS [22–27]. Each DOMS pulse consists of a packet of very short high voltage single oscillations and, thus, the deposition process is well suited for the deposition of DLC films with high sp^3 content. In this work DLC films were deposited by DOMS and DCMS in the same deposition system and using the same time-averaged power in order to evaluate the potential of DOMS for hard DLC synthesis. The mass density of the films was evaluated by using X-ray reflectivity, their structure and temperature stability were studied by UV Raman spectroscopy, their morphology was examined by scanning electron microscopy (SEM) and their hardness was measured by nano-indentation.

2. Experimental procedure

DLC coatings were deposited onto 20 × 20 mm Si (100) substrates using a DOMS power supply (HiPIMS Cyprium™ plasma generator, Zpulser Inc.). An example of the DOMS discharge voltage and current wave forms used in this work is shown in Fig. 1. More details about the oscillating current and voltage waveforms in DOMS can be found in reference [23]. The depositions were performed using constant voltage on time (t_{on}), period (T) and pulse duration (D) of 6, 130 and 1690 μs, respectively, while the pulse frequency (F) was automatically adjusted by the DOMS power supply software in order to maintain the time-averaged power (Pa) equal to 1.3 kW.

The apparatus used in this work is shown in Fig. 2. The deposition chamber is made of high grade stainless steel with 400 × 400 × 400 mm dimensions. Pure graphite (99.95%) and chromium (99.99%) targets (150 × 150 mm and 10 mm of thickness) were used. The graphite target was connected to the DOMS power supply and the chromium target was connected to the D.C. power supply. The targets were sputtered in pure Ar (99.999%) discharge gas at 0.8 Pa. In all depositions, the substrate-to-target distance was kept at 80 mm. Prior to the depositions the Si substrates were ultrasonically cleaned in a sequence of acetone and ethanol solutions baths, for 15 min each. They were then glued with silver glue (99.9% purity) onto a rotating aluminium substrate holder revolving at 23.5 rev/min around the central axis of the chamber. A base pressure lower than 3×10^{-4} Pa was achieved before all depositions using a system constituted by a rotary and a turbomolecular pump. Prior to all depositions an etching treatment using an ion gun was performed during 40 min with a − 150 V bias.

The effect of substrate biasing was studied within the range from − 40 to − 100 V. DLC films with thicknesses of 150, 600 and 1200 nm were deposited for mass density, UV Raman spectroscopy and mechanical properties characterization, respectively. Prior to the films deposition a ∼50 nm C interlayer was deposited without substrate biasing for the films deposited with 150 and 600 nm thickness. A Cr adhesion interlayer with 250 to 300 nm was deposited by DCMS to enhance the adhesion of the DLC films deposited with a thickness of 1200 nm. The main deposition parameters used for the deposition of DLC films with a thickness of 600 nm are shown in Table 1. In this work, the peak power (P_p) is defined as the product $V_p \times I_p$. One DLC film with a thickness of 150 nm was deposited using a continuous D.C. power source (Huttinger PFG 7500 DC) and a substrate bias of − 60 V for comparison purpose. The voltage and current target were 333 V and 3.75 A, respectively.

The thickness and morphology of the films were studied by scanning electron microscopy (SEM) using a Quanta 400FEG ESEM. The SEM images obtained for the cross section and surface area in this work were achieved with a 2 keV acceleration voltage. The hardness of the films was measured by nano-indentation (MicroMaterialsNano Tester) using a Berkovich diamond indenter. The hardness was evaluated from load–displacement curves using the depth-sensing method. Hardness measurements were done with 10 mN loads in order to ensure an indentation depth < 10% of the coating's thickness. 16 hardness measurements were performed on each specimen. The mass density of the resulting films was evaluated by using an X-ray diffractometer (Philips Xpert) operated in reflection geometry using Cu-K (λ = 0.15406 nm) monochromatic radiation. A simulated curve was generated using the Xpert reflectivity software [28] and was fitted to the measured curve to obtain film density. The structural investigation of the deposited films was performed by employing UV Raman spectroscopy using a Renishaw inVia Raman microscope equipped with a He-Cd laser of 325 nm. In order to investigate the thermally induced structural changes in the films, Raman spectroscopic measurements were performed on the films annealed in vacuum at temperatures of 250 and 500 °C.

3. Results and discussion

The cross-section and surface morphology of DLC coatings deposited by DOMS are shown in Fig. 3 as a function of substrate bias. As mentioned in the experimental section, a Cr interlayer with a thickness close to 400 nm was deposited over the Si substrate. As can be observed in all the cross section micrographs, the Cr interlayer has an open columnar microstructure which is known to form tensile stresses [29] that

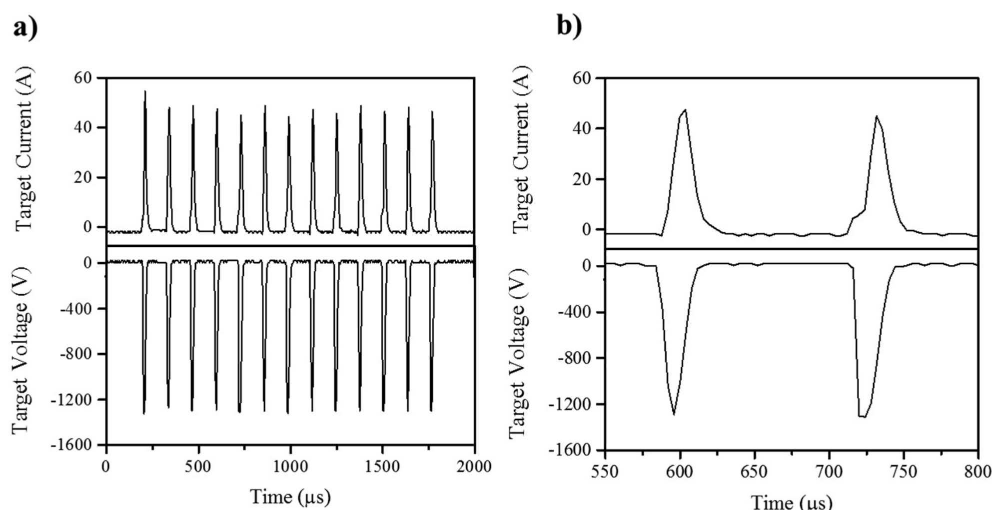

Fig. 1. a) The target voltage and current oscillation waveforms measured during the DLC coatings depositions. b) Small oscillation pulses within one long pulse.

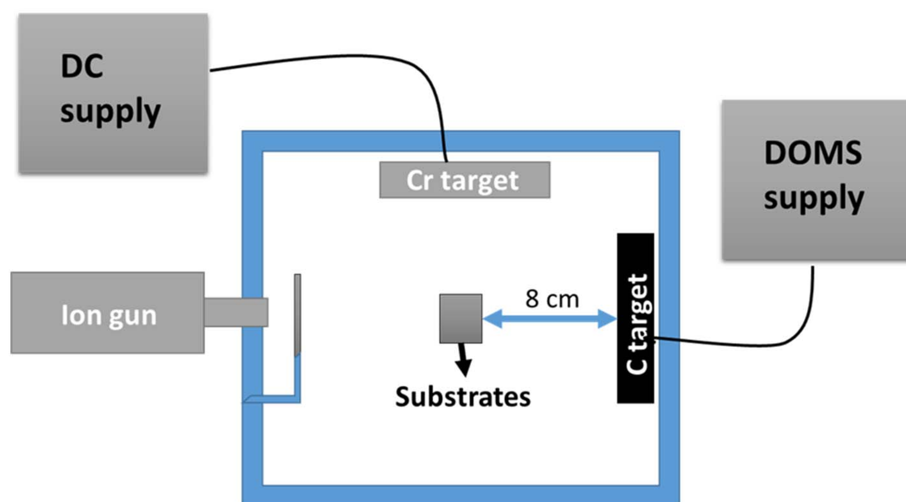

Fig. 2. Apparatus used in this work.

Table 1
Deposition conditions used to deposit DLC coatings by DOMS with 600 nm of thickness.

Substrate bias (V)	V_p (V)	I_p (A)	P_p (kW)
–	1399	65	91
− 40	1409	66	93
− 60	1401	61	86
− 80	1400	63	87
− 100	1399	62	87

contribute to counteract the compressive stress formed upon DLC films deposition. The surface morphology of the films deposited with a bias up to − 60 V consist of small grains, 10–20 nm wide, that agglomerate to form larger protruding structures, 50–160 nm wide. Such cauliflower-type morphologies were previously observed for films deposited by DOMS without substrate biasing [22,23], being associated with unstable growth under surface diffusion limited conditions. Increasing the substrate bias (− 80 V) still results in the formation of cauliflower-type morphology but the characteristic dimensions of the grains inside the agglomerates are considerably reduced due to increased surface diffusion. Further increasing the substrate bias to − 100 V results in a much smoother surface with almost imperceptible structures. The cross section of the films deposited without bias and with a bias of − 40 V reveals a dense columnar microstructure, which is typical of the T zone in the generalized structure zone diagram [30]. Increasing the bias voltage results in more compact microstructures as can be concluded from the feature-less cross section of the film deposited at the highest bias. On the overall, increasing the substrate bias clearly results in the deposition of smoother and denser DLC films.

The DLC properties are largely controlled by the amount of sp^2 and sp^3 hybridized bonds [12,13]. Raman spectroscopy is a popular and effective tool to characterize the carbon bonding in DLC films mainly due to the thigh sensitivity of the technique to carbon-based materials in general. Raman spectra of DLC usually exhibit at least two distinct broad bands, the "graphitic carbon" (G) band located above 1500 cm^{-1} and the "disordered carbon" (D) band, located at lower Raman shifts than the G band. The absolute and relative features of these bands, such as position and full with at half maximum, can be used to gain information about the structure of the films. However, both bands convey information mainly about sp^2-bonded carbon atoms and only indirect information about sp^3-bonded carbons can be inferred. The main advantage of using UV radiation instead of visible light in Raman spectroscopy is that the higher energy photons are able to directly probe the sp^3-bonded carbon atoms and thus originate a third broad band located near 1040 cm^{-1}, the so-called T band. The presence of this band is usually taken as an indication of a high sp^3 content in DLC films. Fig. 4 shows the Raman spectra for DLC coatings deposited by DOMS with biasing (− 40, − 60 and − 80 V) obtained using UV radiation. Each spectrum can be deconvoluted into only two Raman peaks, located close to 1438 and 1580 cm^{-1}, which were identified as the D and G bands, respectively. The so-called T band is not observed in the measured Raman spectra, irrespectively of the applied bias. Therefore, as referred above, only indirect information about the sp^3-bonded carbons, inferred from the characteristics of the D and G peaks, can be extracted from the Raman spectra of the deposited films. In this work, the intensity ratio I_D/I_G was used to probe the sp^3 to sp^2 ratio in the DLC films following the Ferrari three-stage model [12]. The D peak is due to the breathing modes of sp^2 atoms in rings, and the G peak is due to bond stretching of sp^2 pair atoms in both rings and chains. Thus, the band intensity ratio I_D/I_G is inversely proportional to the sp^3/sp^2 ratio of carbon bonding. The D and G peaks were fitted using Lorentzian and Breit-Wigner-Fano (BWF) line shapes respectively, Fig. 4. The I_D/I_G ratio obtained from the fitted spectra (see Fig. 5) exhibit a decrease with increasing bias voltage. The formation of sp^3 bonds in DLC films is achieved by subplantation of energetic carbon species into the sub surface region of the growing film which promotes the formation of dense amorphous films [31,33]. In classical magnetron sputtering-based deposition with substrate biasing most of the energetic species impinging on the growing film are Ar ions from the process gas as the sputtered carbon species are not significantly ionized. Thus sp^3 bonding is only achieved indirectly, as the energy of Ar ions energy must be transferred to the film forming species, and thus high substrate biasing is needed. The most plausible explanation for the formation of sp^3 bonds in the films is that a significant ionization of the sputtered carbon species is achieved in DOMS and, thus, that the growing film is bombarded by both C and Ar ions with hyper thermal energy.

The mass density of the DLC films deposited by DOMS with the lowest thickness as evaluated by XRR is shown in Fig. 6 as a function of the substrate bias potential. For comparison purposes, the density of a film deposited by DCMS with a bias of − 60 V is also shown in the figure. The mass density of the films deposited by DOMS increases with increasing bias from close to 1.8 g/cm^3 to almost 2.5 g/cm^3. As shown by Robertson et al. [11], the mass density of DLC films is directly correlated to their sp^3 content (linear relationship). Thus, the increase in film density with increasing bias agrees well with the formation of an increasing number of sp^3 bonds as concluded from the UV Raman analysis. The mass density of the film deposited with the highest bias is significantly higher that the values usually obtained for DLC films deposited by DCMS (in the range between 1.6 and 2.2 g/cm^3 [12]), although it is still short of the values routinely achieved in DLC films deposited by FCVA (up 3.2 g/cm^3 [34]). Note that the mass densities of

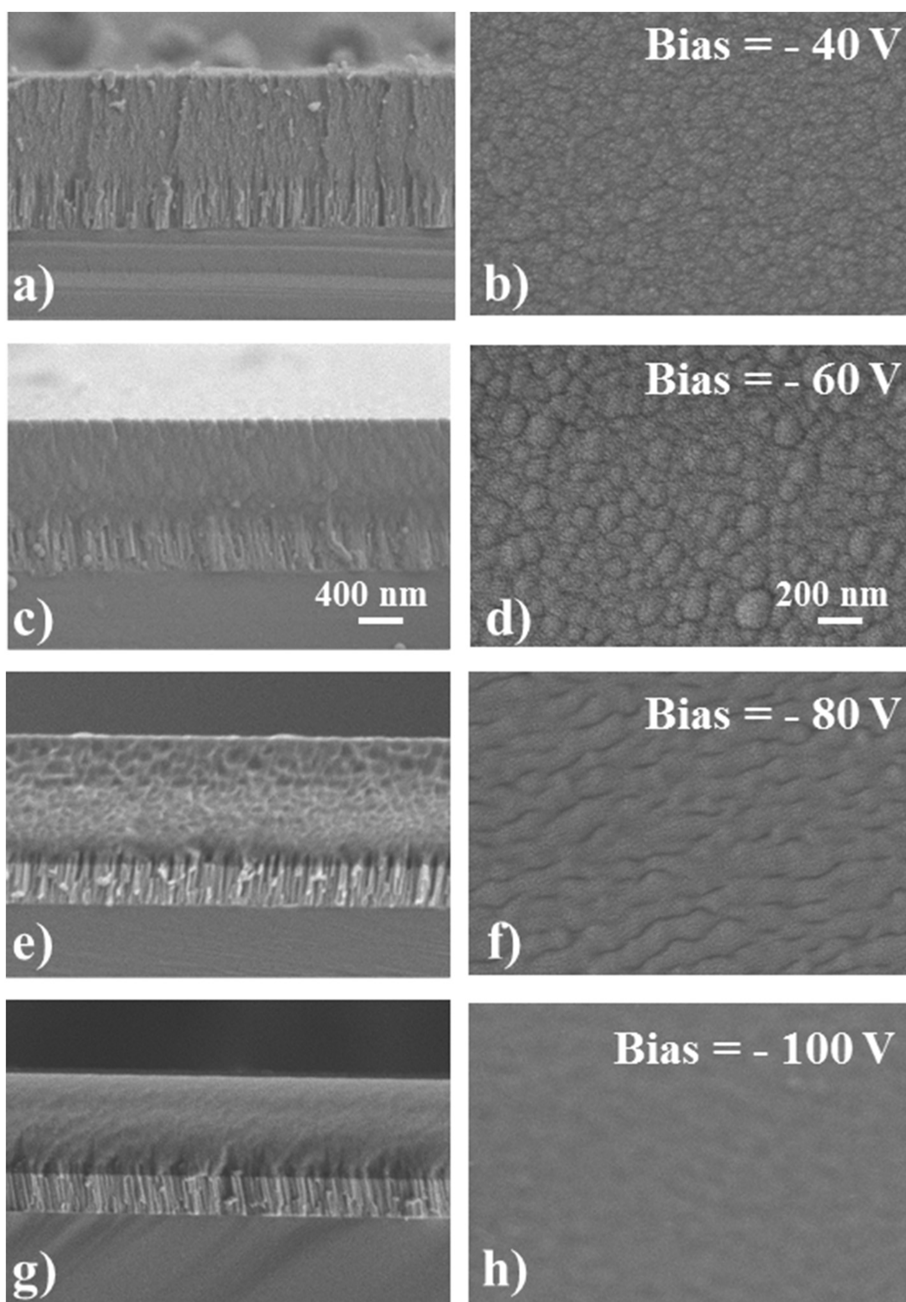

Fig. 3. SEM cross-section and surface micrographs of the DLC coatings deposited by DOMS with biasing of a, b) − 40 V; c, d) − 60 V; e, f) − 80 V; g, h) − 100 V.

the films deposited by DOMS in this work are slightly under estimated as a thin carbon layer was deposited without substrate biasing between the Cr adhesive interlayer and the DLC films. The mass density of the film deposited by DCMS (2.1 g/cm^3) with a substrate bias of − 60 V is lower than the value of the corresponding film deposited by DOMS (close to 2.3 g/cm^3). The higher density of the film deposited by DOMS is most probably due to the higher fraction of ionization of the carbon sputtered species in DOMS and thus to an increased number of hyper thermal C ions bombarding the substrate. The density of the film deposited by DCMS is higher than that of the films deposited by DOMS without and with a bias of − 40 V. This results shows that increasing the bias voltage also increases the density of the films even in DCMS. However, in DCMS the increase in density is achieved by bombarding the films almost exclusively with energetic Ar ions from the background gas. Thus, the energy/momentum transfer to the film forming species is indirect and much less effective than bombarding the growing film with C ions.

Fig. 7 shows the hardness and Young's modulus of the DLC films deposited by DOMS. The hardness increases from 15 to 23 GPa with increasing bias voltage from − 40 to − 80 V. The hardness of DLC films is highly influence by their sp^3 content. The strong and directional sp^3 bonding of carbon atoms results in the formation of a three-dimensional (tetrahedral) network of σ bonds which increases the hardness of DLC films [35,36]. Thus, the increasing hardness of the DLC films deposited by DOMS with increasing substrate biasing correlates well with the increasing sp^3 content in the films previously inferred from the mass density measurements. On the other hand, the hardness of the film deposited with a bias voltage of − 80 V is higher than that of the hardest DLC films deposited by DCMS as reported in the literature (20 GPa, [11–13]). This result correlates well with the density of the film is lightly above the range of densities reported in the literature for DLC films deposited by DCMS.

The hardness of the film deposited with a substrate bias of − 100 V is lower (21 GPa) than that of the film deposited with a substrate bias of

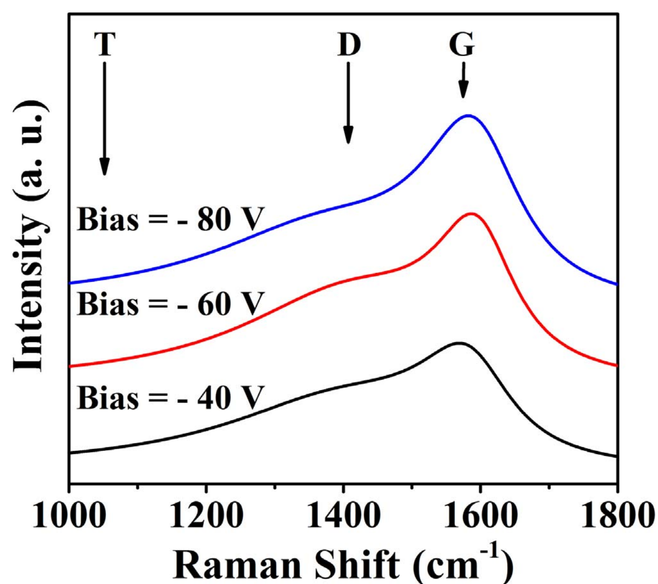

Fig. 4. Experimental UV Raman spectra of DLC coatings (1200 nm of thickness) deposited by DOMS with biasing (− 40, − 60 and − 80 V). Approximate positions of the T, D and G peaks are indicated. Excitation wavelength is 325 nm.

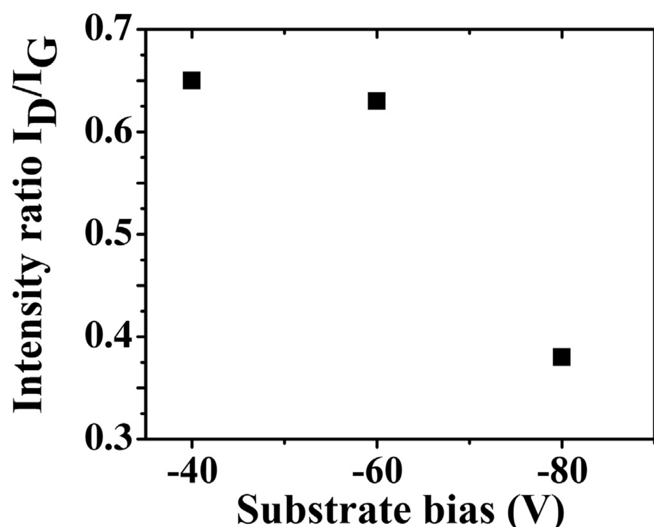

Fig. 5. Experimental values of the intensity ratios of the peaks I_D/I_G for the samples (1200 nm of thickness) deposited by DOMS as a function of the bias voltage.

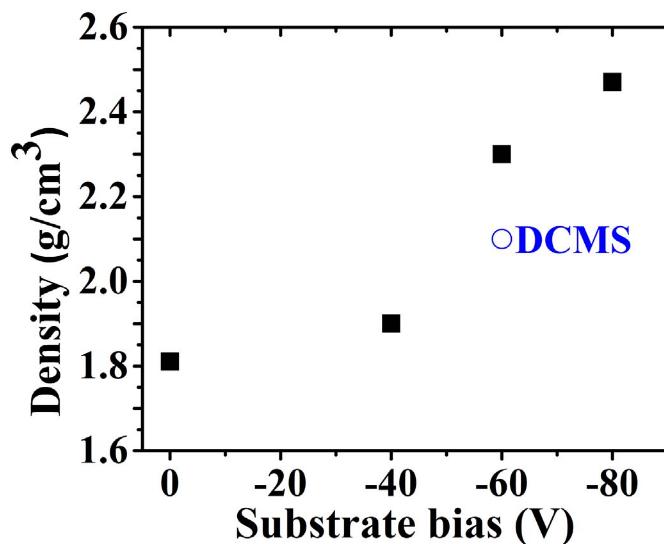

Fig. 6. Film density of the DLC films as a function of the deposition substrate bias obtained from UV Raman. The density of a DCMS film deposited with a bias of − 60 V of bias is also displayed for comparison.

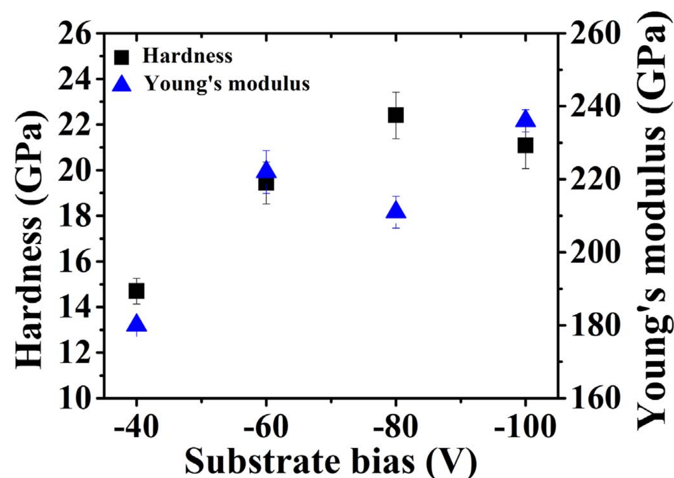

Fig. 7. Hardness and Young's modulus of the DLC coatings deposited by DOMS with the increase of bias voltage.

− 80 V. McKenzie et al. found that at very high bombarding energies, thermal spikes can occur [37]. The excess thermal energy in such conditions promotes a bond relaxation from sp^3 to sp^2. The authors reported an optimum energy for the impinging C ions of 100 eV in order to maximise the sp^3 content in the films. The thermal spike mechanism is probably at the origin of the decrease in hardness observed in this work upon increasing the bias voltage from − 80 to − 100 V. Thus a somewhat lower optimum bombarding energy for maximum sp^3 formation than reported by McKenzie et al. is found in this work. Overall the Young's modulus of the films increases with increasing bias voltage (from 180 GPa to 240 GPa), which is consistent with the general trend of increasing sp^3 content in the films with increasing bias deduced form the previous results.

As discussed in the introduction, the temperature stability of the DLC films is a critical parameter in view of their use as protective coatings in piston's rings. Therefore, the DLC coatings were annealed in vacuum at different temperatures and their Raman spectra was measured before and after the annealing process. Note however that the temperature stability during annealing is not necessarily a good indicator of the coatings performance in real applications, as in the latter case the coatings are additionally subjected to mechanical solicitations. Nevertheless, the effect of annealing on the structure of the DLC films is a good starting point to evaluate their temperature stability.

The Raman measurements were performed on coatings deposited with a − 60 V bias by DCMS and DOMS at room temperature and after annealed at 250 °C and 500 °C. In order to facilitate the comparison, the Raman spectra presented in Fig. 8 have been normalised to 1. Again, all spectra can be deconvoluted into two broad bands corresponding to the D and G peaks. Although the general shape of all spectra is similar, at room temperature the D and G peaks are less well resolved in the spectrum of the film deposited by DOMS. The D peak is clearly distinguished in the spectrum of the DLC deposited by DCMS while it is almost completely convoluted with the G peak in the Raman spectrum of the DLC film deposited by DOMS. Increasing the temperature does not significantly change the resolution of the D and G peaks for the film deposited by DCMS. However, it results in better separated peaks in DOMS, in such a way that at 500 °C the Raman spectra of the DCMS and DOMS films are very similar. These results agree well with the transformation of the sp^3 bonds present in the film deposited by DOMS into

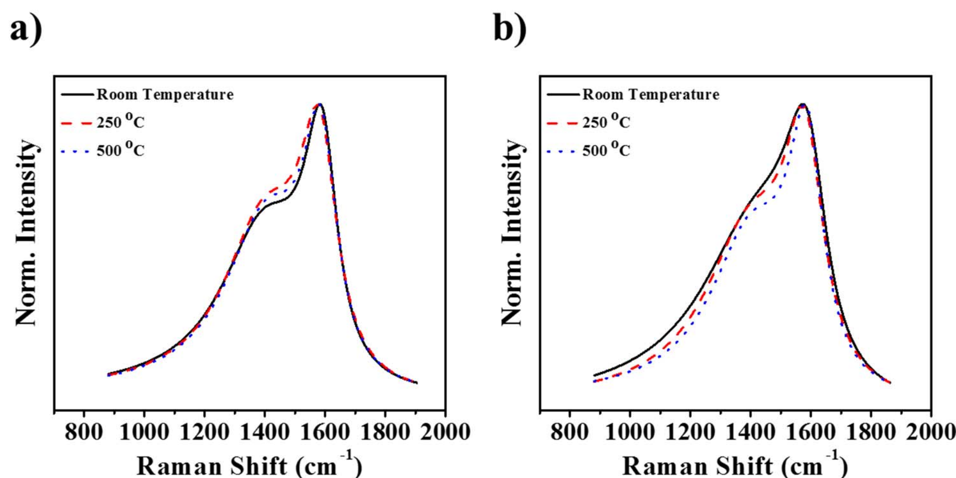

Fig. 8. Raman spectra recorded for DLC films (600 nm of thickness) deposited with a bias of − 60 V by a) DCMS and b) DOMS at room temperature and after annealed at 250 and 500 °C.

sp^2 bonds upon annealing. The shape of the Raman spectrum of the DOMS deposited film tends to that of the Raman spectrum of the DCMS film with increasing temperature as the later only have sp^2 bonds even at ambient temperature. Note also that the slightly higher intensity at low Raman shifts of the spectra obtained at room temperature for the DOMS film may also be interpreted as the presence of a weak T peak that disappears with increasing temperature. The Raman spectra in Fig. 8 confirm the previous conclusions that only a small amount of sp^3-bonded carbons are present in the films deposited by DOMS. On the other hand, they also show that the structure of the films is not stable upon annealing even at 250 °C. Although the DLC films deposited by DOMS have high hardness and mass density, they lack the temperature stability indispensable for their application in piston rings of internal combustion engines. Nevertheless, a significantly higher amount of sp^3 bonds was form in the DLC films deposited by DOMS, as compared to the DCMS ones, resulting in better mechanical properties. These results show that DOMS is a promising path for the development of hard DLC (ta-C) films.

4. Conclusions

In this work DLC films were deposited by DOMS with increasing substrate biasing voltage. Increasing substrate biasing results in the deposition of smoother and denser DLC films. The compact columnar microstructure observed at lower values of substrate biasing is gradually replaced with a featureless microstructure while the cauliflower-type surface morphology is replaced by an almost featureless surface. The so-called T band, which is associated to sp^3 bonding in carbon films, is not observed in the UV Raman spectra of the films deposited by DOMS. The intensity ratio I_D/I_G was used to probe the sp^3 to sp^2 ratio in the films following the Ferrari three-stage model. The I_D/I_G ratio decreases with increasing bias voltage which indicates an increasing sp^3/sp^2 ratio in the films. The mass density of the films deposited by DOMS increases with increasing substrate biasing from close to 1.8 g/cm^3 to almost 2.5 g/cm^3. On the other hand, the hardness of the films increases from 15 to 23 GPa with increasing bias voltage from − 40 to − 80 V. Both results are consistent with the formation of an increasing amount of sp^3 bonds in the films with increasing substrate bias and thus agree well with the conclusions obtained from UV Raman spectroscopy. The slight hardness decrease measured upon increasing the substrate bias from − 80 to − 100 V was attributed to relaxation of part of the sp^3 bonds back to sp^2 bonds due to the thermal spike mechanism. The optimum substrate bias for the maximum sp^3 content in the films was thus found to be slightly lower than the 100 eV usually referred in the literature. The Raman spectra of the film deposited by DOMS with a bias of − 60 V show that the sp^3 bonds convert back to sp^2 upon annealing and, thus, that the structure of the films is not stable upon annealing. A significantly higher amount of sp^3 bonds was form in the DLC films deposited by DOMS, as compared to the DCMS ones, resulting in better mechanical properties. These results show that DOMS is a promising path for the development of hard DLC (ta-C) films.

Acknowledgments

This research is sponsored by FEDER funds through the program COMPETE – Programa Operacional Factores de Competitividade – and by national funds through FCT – Fundação para a Ciência e a Tecnologia, under the projects UID/EMS/00285/2013 and M-ERA-NET/0003/2015 (TANDEM – “Thick, adherent stress-free DLC coatings for demanding applications”).

References

[1] K. Holmberg, P. Andersson, A. Erdemir, Global energy consumption due to friction in passenger cars, Tribol. Int. 47 (2012) 221–234.
[2] Ruud Jacobs, 10 - Industrial development of carbon-based coatings, Oral presentation at the International Conference on Metallurgical Coatings and Thin Films (ICMCTF), 2017.
[3] R. Rahmani, H. Rahnejat, B. Fitzsimons, D. Dowson, The effect of cylinder liner operating temperature on frictional loss and engine emissions in piston ring conjunction, Appl. Energy 191 (2017) 568–581.
[4] P. Mutafov, J. Lanigan, A. Neville, A. Cavaleiro, T. Polcar, DLC-W coatings tested in combustion engine—frictional and wear analysis, Surf. Coat. Technol. 260 (2014) 284–289.
[5] M. Evaristo, R. Azevedo, C. Palacio, A. Cavaleiro, Influence of the silicon and oxygen content on the properties of non-hydrogenated amorphous carbon coatings, Diam. Relat. Mater. 70 (2016) 201–210.
[6] C. Donnet, A. Erdemir, Tribology of Diamond-like Carbon Films: Fundamentals and Applications, Springer Science & Business Media, 2007.
[7] S.C. Tung, H. Gao, Tribological characteristics and surface interaction between piston ring coatings and a blend of energy-conserving oils and ethanol fuels, Wear 255 (2003) 1276–1285.
[8] J. Fontaine, C. Donnet, A. Erdemir, Fundamentals of the Tribology of DLC Coatings, Tribology of Diamond-like Carbon Films, Springer, 2008, pp. 139–154.
[9] A. Erdemir, C. Donnet, Tribology of diamond-like carbon films: recent progress and future prospects, J. Phys. D. Appl. Phys. 39 (2006) R311.
[10] D. Lundin, K. Sarakinos, An introduction to thin film processing using high-power impulse magnetron sputtering, J. Mater. Res. 27 (2012) 780–792.
[11] J. Robertson, Plasma deposition of diamond-like carbon, Jpn. J. Appl. Phys. 50 (2011) 01AF01.
[12] A.C. Ferrari, A. Libassi, B.K. Tanner, V. Stolojan, J. Yuan, L. Brown, et al., Density, sp 3 fraction, and cross-sectional structure of amorphous carbon films determined by X-ray reflectivity and electron energy-loss spectroscopy, Phys. Rev. B 62 (2000) 11089.
[13] A. Grill, Diamond-like carbon: state of the art, Diam. Relat. Mater. 8 (1999) 428–434.
[14] S. Nakao, K. Yukimura, S. Nakano, H. Ogiso, DLC coating by HiPIMS: the influence of substrate bias voltage, IEEE Trans. Plasma Sci. 41 (2013) 1819–1829.
[15] M. Tucker, R. Ganesan, D. McCulloch, J. Partridge, M. Stueber, S. Ulrich, et al., Mixed-mode high-power impulse magnetron sputter deposition of tetrahedral amorphous carbon with pulse-length control of ionization, J. Appl. Phys. 119 (2016) 155303.
[16] M. Lattemann, B. Abendroth, A. Moafi, D. McCulloch, D. McKenzie, Controlled glow

ARTICLE IN PRESS

to arc transition in sputtering for high rate deposition of carbon films, Diam. Relat. Mater. 20 (2011) 68–74.

[17] U. Helmersson, M. Lattemann, J. Bohlmark, A.P. Ehiasarian, J.T. Gudmundsson, Ionized physical vapor deposition (IPVD): a review of technology and applications, Thin Solid Films 513 (2006) 1–24.

[18] A. Anders, A review comparing cathodic arcs and high power impulse magnetron sputtering (HiPIMS), Surf. Coat. Technol. 257 (2014) 308–325.

[19] A. Aijaz, K. Sarakinos, D. Lundin, N. Brenning, U. Helmersson, A strategy for increased carbon ionization in magnetron sputtering discharges, Diam. Relat. Mater. 23 (2012) 1–4.

[20] T. Konishi, K. Yukimura, K. Takaki, Fabrication of diamond-like carbon films using short-pulse HiPIMS, Surf. Coat. Technol. 286 (2016) 239–245.

[21] J. Lin, W.D. Sproul, R. Wei, R. Chistyakov, Diamond like carbon films deposited by HiPIMS using oscillatory voltage pulses, Surf. Coat. Technol. 258 (2014) 1212–1222.

[22] F. Ferreira, R. Serra, J. Oliveira, A. Cavaleiro, Effect of peak target power on the properties of Cr thin films sputtered by HiPIMS in deep oscillation magnetron sputtering (DOMS) mode, Surf. Coat. Technol. 258 (2014) 249–256.

[23] J. Oliveira, F. Fernandes, F. Ferreira, A. Cavaleiro, Tailoring the nanostructure of Ti–Si–N thin films by HiPIMS in deep oscillation magnetron sputtering (DOMS) mode, Surf. Coat. Technol. 264 (2015) 140–149.

[24] F. Ferreira, J. Oliveira, A. Cavaleiro, CrN thin films deposited by HiPIMS in DOMS mode, Surf. Coat. Technol. 291 (2016) 365–375.

[25] R. Chistyakov, B. Abraham, SVC Bull. Spring (2012) 26–31.

[26] J. Lin, B. Wang, W.D. Sproul, Y. Ou, I. Dahan, Anatase and rutile TiO_2 films deposited by arc-free deep oscillation magnetron sputtering, J. Phys. D. Appl. Phys. 46 (2013) 084008.

[27] J. Lin, X. Zhang, P. Lee, R. Wei, Thick diamond like carbon coatings deposited by deep oscillation magnetron sputtering, Surf. Coat. Technol. 315 (2017) 294–302.

[28] Philips X'PERT Reflectivity, The Netherlands: PANalytical B.V, (2012).

[29] F. Ferreira, R. Serra, A. Cavaleiro, J. Oliveira, Additional control of bombardment by deep oscillation magnetron sputtering: effect on the microstructure and topography of Cr thin films, Thin Solid Films 619 (2016) 250–260.

[30] A. Anders, A structure zone diagram including plasma-based deposition and ion etching, Thin Solid Films 518 (2010) 4087–4090.

[31] J. Robertson, The deposition mechanism of diamond-like aC and aC: H, Diam. Relat. Mater. 3 (1994) 361–368.

[33] Y. Lifshitz, Diamond-like carbon—present status, Diam. Relat. Mater. 8 (1999) 1659–1676.

[34] S. Xu, B. Tay, H. Tan, L. Zhong, Y. Tu, S. Silva, et al., Properties of carbon ion deposited tetrahedral amorphous carbon films as a function of ion energy, J. Appl. Phys. 79 (1996) 7234–7240.

[35] Y. Lifshitz, S. Kasi, J. Rabalais, W. Eckstein, Subplantation model for film growth from hyperthermal species, Phys. Rev. B 41 (1990) 10468.

[36] S. Chowdhury, M. Laugier, I. Rahman, Characterization of DLC coatings deposited by rf magnetron sputtering, J. Mater. Process. Technol. 153 (2004) 804–810.

[37] D. McKenzie, D. Muller, B. Pailthorpe, Compressive-stress-induced formation of thin-film tetrahedral amorphous carbon, Phys. Rev. Lett. 67 (1991) 773.